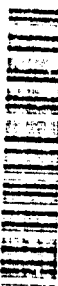


1958 Vol. 1

SN-3389
1958 Vol. 1

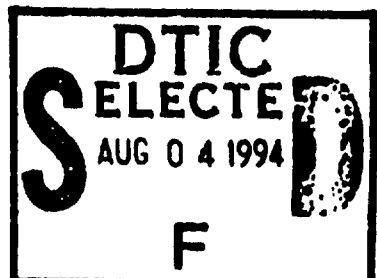
AD-A286 704



3RD Symposium

HIGH-SPEED AERODYNAMICS AND STRUCTURES

SAN DIEGO, CALIF



This document has been approved
for public release and sale; its
distribution is unlimited.

JOINT SPONSORSHIP

AIR RESEARCH AND DEVELOPMENT COMMAND
UNITED STATES AIR FORCE
UNIVERSITY OF CALIFORNIA
THE RYAN AERONAUTICAL COMPANY
CONVAIR
A DIVISION OF GENERAL DYNAMICS CORPORATION

94-24356



VOLUME 1

MARCH 25-27, 1958

94 8 02 034

Copy No. _____

3 RD SYMPOSIUM ON HIGH-SPEED AERODYNAMICS AND STRUCTURES

Held at San Diego, California
March 25-27, 1958

Joint Sponsorship

Air Research and Development Command
United States Air Force
University of California
The Ryan Aeronautical Company
Convair, A Division of General
Dynamics Corporation

Accession For	
NTIS	CRA&I
DTIC	TAB
Unannounced	
Justification	
By _____	
Distribution / _____	
Availability Codes	
Dist	Avail and/or Special
A-1	

VOLUME 1

prepared by

CONVAIR A Division of General Dynamics Corporation SAN DIEGO

TABLE OF CONTENTS - VOLUME I

	Page No.	
Foreword	1	
Technical Program	3	
Conference Organization	9	
Gas Dynamics		
Gas Physics of High-Altitude High-Speed Flight	Dr. S.A. Schaaf	13
One-Dimensional Unsteady Gas Dynamics by Hydraulic Analogue	Dr. W.H.T. Loh	33
High-Temperature Gas Dynamics Phenomena in Hypersonic Flight	W. H. Wurster C. E. Treanor	91
Generation of Pressure Wave Forms Through the Detonation of Explosive Charges	D. C. Anderson	109
Materials		
Criteria in the Selection of Materials for High Temperature Structures	W. H. Steurer	181
Ceramic Materials for Use in Hypersonic Aircraft	J. M. Nowak	229
Thermal Properties of Nose Cone Materials	I. B. Fieldhouse J. I. Lang A. N. Takata T. E. Waterman	253
Heat Transfer		
The Approach to Thermal Equilibrium in a Hypersonic Laminar Boundary Layer	Dr. D. E. Knapp	279
Mass Transfer Cooling in High-Velocity Flight	Dr. C. Gazley Dr. J. Gross Dr. D. J. Masson	295
A Technique for Experimental Investigation of Heat Transfer from a Surface in Supersonic Flow at Large Surface-to-Free-Stream Temperature Ratios	W. S. Bradfield A. R. Hansom J. J. Sheppard R. E. Larson	349
Structures:		
High-Temperature Structures	Dr. N. J. Hoff	383

FOREWORD

The material presented herein contains the formal proceedings of the Third Symposium on High Speed Aerodynamics and Structures. This Symposium was jointly sponsored by the U.S. Air Force Air Research and Development Command, Convair - A Division of General Dynamics Corporation, Ryan Aeronautical Company, and the University of California at Los Angeles. As in previous Symposia, the meeting was arranged to stimulate the exchange of ideas by engineers and scientists engaged in research on both high speed flight within the atmosphere; and on the problems of manned and unmanned vehicles entering the earth's atmosphere at near-satellite velocities. All sessions were held in a classified (Secret) atmosphere to permit a free and formal exchange of classified information. The formal proceedings, however, in many instances are of lower classification or in some instances are unclassified. For this reason, these papers have been published in three volumes; Unclassified, Confidential, and Secret, in order to achieve the broadest dissemination of information possible in academic, government, and industrial circles.

Charles W. Frick
Chairman
Program Committee

TECHNICAL PROGRAM

Vol. No.*

TUESDAY - MARCH 25, 1958

SESSION I

Opening Ceremonies

Chairman - R.C. Sebold, Vice-President - Engineering, Convair

Orientation Col. D.D. McKee, ARDC, USAF

Welcome Dr. L.M. K. Boelter, Dean of Engineering,
University of California at Los Angeles

Keynote Address: Lt. Gen. Samuel E. Anderson

ARDC Objectives Commander, ARDC, USAF

SESSION I (Cont'd)

Chairman - Col. D. D. McKee, ARDC, USAF

(a) Gas Physics of High Altitude-High-Speed Flight

By: Dr. S. A. Schaaf - University of California

(b) High-Temperature Structures

By: Dr. N.J. Hoff - Stanford University

SESSION II

(A) Gas Dynamics

Chairman - Dr. H. H. Kurzweg, Naval Ordnance Laboratory, USN

- I (a) One-Dimensional Unsteady Gas Dynamics by Hydraulic Analogue
By: Dr. W.H.T. Loh - Chance Vought
- (b) High Temperature Gas Dynamics Phenomena in Hypersonic Flight
By: W. H. Wurster and C.E. Treanor - Cornell Aeronautical Laboratory
- V (c) Aerodynamic Studies of Blunt Bodies in Dissociated Air at High Mach Numbers
By: W.R. Warren, A.J. Vitale, and E.M. Kaegi - General Electric Company
- I (d) Generation of Pressure Wave Forms Through the Detonation of Explosive Charges
By: D.C. Anderson - Armour Research Foundation

*The Proceedings are published in five volumes: Volume I, II, III, Unclassified; Volume IV, Confidential; Volume V, Secret.

Vol. No.*

V (e) Gas Dynamics of Under-expanded Rocket Jets
By: J. Ballinger - Convair-Astronautics and K. Hendershot,
Convair-San Diego

(B) Materials

Chairman - Dr. W.H. Steurer, Army Ballistics Missile Agency, USA

IV (a) Heat Transfer and Material Investigations in Aerodynamics Heating Simulation Tests
By: H. Connell, Jr. - Army Ballistic Missile Agency

V (b) Behavior of Reinforced Plastics at Very High Temperatures
By: I.J. Gruntfest, L.H. Shenker, and S. Zirinsky - General Electric Company

V (c) The Effect of Extremely High Temperature Environments on Materials
By: M. Annis - Allied Research Associates

I (d) Ceramic Materials for Use in Hypersonic Aircraft
By: J. M. Nowak - Bell Aircraft

I (e) Thermal Properties of Nose Cone Materials
By: I.B. Fieldhouse, J.I. Lang, A.N. Takata, and T.E. Waterman - Armour Research Foundation

WEDNESDAY - MARCH 26, 1958

SESSION III

Chairman - Dr. E.R. van Driest, North American Aviation

V (a) On Minimizing the Heat Transfer to a Hypersonic Vehicle
By: Dr. J. Farber - General Electric Company

V (b) High-Temperature Facilities
By: Lt. Col. A.R. Swansen - USAF, Department of Defense

IV (c) Unsteady Flow and Instability of Lifting Surfaces
By: Dr. Holt Ashley and Garabed Zartarian - Massachusetts Institute of Technology

I (d) Material Problems
By: Dr. W.H. Steurer - Army Ballistic Missile Agency

IV (e) Similarity Parameters for Surface Melting
By: Dr. Lester Lees - Ramo-Wooldridge Corporation and the California Institute of Technology

*The Proceedings are published in five volumes: Volume I, II, III, Unclassified; Volume IV, Confidential; Volume V, Secret.

SESSION IV

(A) Heat Transfer

Chairman - Dr. E.R.G. Eckert, University of Minnesota

- I (a) The Approach to Thermal Equilibrium in a Hypersonic Laminar Boundary Layer
By: Dr. D.E. Knapp - Douglas Aircraft
- I (b) Mass-Transfer Cooling in High-Velocity Flight
By: Dr. C. Gazley, Dr. Joseph Gross, and Dr. Davis J. Masson - The Rand Corporation
- V (c) Transpiration Cooling in Hypersonic Flow
By: Dr. S.M. Scala - General Electric Company
- I (d) A Technique for Experimental Investigation of Heat Transfer from a Surface in Supersonic Flow at Large Surface-to-Free-Stream Temperature Ratios
By: W.S. Bradfield, Convair Scientific Research and Dr. A.R. Hanson, J.J. Sheppard, and R.E. Larson, Dept. of Aerodynamics Engineering, University of Minnesota
- IV (e) Mass Transfer Cooling of Re-Entering Vehicles
By: E.R.G. Eckert, T.F. Irvine, J.P. Hartnett, and P.J. Schneider - University of Minnesota
- V (f) The Combustion of a Carbon Nose Cone During Re-Entry
By: Dr. G.M. Boobar - General Electric Company

(B) Structures

Chairman - Dr. John Brahtz, University of California, Los Angeles

- II (a) Optimum Design of Sandwich Structural Elements at Elevated Temperatures
By: G. Strasser - Bell Aircraft
- II (b) Primary Creep in Aircraft Design
By: B.B. Muvdi - The Martin Company and C.J. Giemza - Convair-Astronautics
- II (c) Stability of Wing Surface Elements in the Presence of Thermal Gradients
By: Dr. C. Riparbelli and L. Minkler - Convair - San Diego
- II (d) A Typical Long Range Hypersonic Rocket Glider and Its Structural Problems
By: V. Gradecak - The Ryan Aeronautical Company

*The Proceedings are published in five volumes: Volume I, II, III, Unclassified; Volume IV, Confidential; Volume V, Secret.

Vol. No. *

(C) High-Speed Aerodynamics I

Chairman - Prof. W.G. Vincenti - Stanford University

- II (a) Theoretical Evaluation of the Performance of Air-Breathing Hypersonic Airplanes
By: B.S. Baldwin, Jr. - NACA, Ames Laboratory
- II (b) Effects of Roughness on Supersonic Skin Friction
By: Dr. F. Goddard - Jet Propulsion Laboratory
- II (c) Wings with Minimum Induced Drag in Supersonic Flow
By: Dr. I. Ginzel and H. Multhopp - The Martin Company
- I (d) Aerodynamic Applications of Diabatic Flows at High Mach Numbers
By: T. Falk - Convair-San Diego (Not Published)
- III (e) Slender Wings - Some Aerodynamic Considerations
By: E.C. Maskell and J. Weber - Royal Aircraft Establishment

THURSDAY - MARCH 27, 1958

SESSION V

Chairman - Dr. N. J. Hoff, Stanford University

- IV (a) Some Recent Studies of Boundary Layer Transitions
By: Dr. E.R. van Driest and W.D. McCauley - North American Aviation
- II (b) High Temperature Flight Safety Factors
By: A.T. Clemen - Convair-Ft. Worth
- II (c) Minimum Weight Analysis Based on Structural Reliability
By: Dr. H.H. Hilton - University of Illinois and Dr. M. Feigen - Hughes Weapons Systems Development Laboratories
- II (d) A Structural Design Approach for High-Speed Flight
By: D. V. O'Brien and R.R. Drummond - The Martin Company
- IV (e) Compatability Requirements of High Performance Naval Aircraft and Guided Missiles
By: LTG W.J. Thompson, USNR - Bureau of Aeronautics, USN

SESSION VI

(A) High-Speed Aerodynamics II

Chairman - Prof. E.V. Laitone - University of California at Berkeley

- III (a) Phugoid Motion of Hypervelocity Vehicles
By: G. Breaux - Convair-Ft. Worth

*The Proceedings are published in five volumes: Volume I, II, III, Unclassified; Volume IV, Confidential; Volume V, Secret.

V (b) Problems Encountered in the Study of Aircraft Dynamic Stability at High Mach Numbers and Altitudes
 By: S. Starr - Convair-San Diego

III (c) Some Considerations on the Recovery of Satellite Vehicles
 By: S. Cohen - Republic Aviation

III (d) Aerodynamic Force Coefficients on the Yawed Slender Body at Hypersonic Speeds
 By: Dr. L. Trilling and J. W. Clark - Massachusetts Institute of Technology

IV (e) Coupling Between Inlet Stability and Airplane Stability
 By: R. Heppe, H. Drell, and L. Celniker - Lockheed Aircraft

(B) Testing Techniques

Chairman - Dr. B. Goethert - ARO, Inc.

(a) Hypersonic Shock Tunnel
 By: Dr. H. T. Nagamatsu and R. E. Geiger - General Electric Company (Not Published)

III (b) A General Technique for Evaluating Thermal Shock Characteristics of Materials Subjected to Temperature Gradients
 By: D. Horowitz - Armour Research Foundation

IV (c) Aerodynamic Testing at Hypervelocities
 By: W. N. MacDermott and R. W. Perry - ARO, Inc.

III (d) Experimental Techniques at Elevated Temperature
 By: C. J. VanDerMaas - The Martin Company

(C) Aeroelasticity and Flutter

Chairman - Dr. Holt Ashley - Massachusetts Institute of Technology

III (a) The Influence of Elevated Temperatures on the Static Aeroelastic Behavior of a Wing
 By: Dr. J. W. Mar, W. R. Mills, and L. A. Schmidt, Jr.
 Massachusetts Institute of Technology

III (b) Panel Flutter in the Presence of a Boundary Layer
 By: Dr. J. W. Miles - University of California and
 Ramo-Wooldridge Corporation

IV (c) Supersonic Static Aeroelasticity
 By: M. B. Zisfein and V. W. Donato - Bell Aircraft Corporation

III (d) Aerodynamic Loads on Swept Wings Due to Gust Entry
 By: R. A. Granger II - The Martin Company

III (e) Analytical and Experimental Deformation Studies of Low Aspect-Ratio Wings Including the Effects of Aerodynamic Heating
 By: I. Rattinger and R. H. Galagher - Bell Aircraft Corp.

*The Proceedings are published in five volumes: Volume I, II, III, Unclassified; Volume IV, Confidential; Volume V, Secret.

Representing
HEADQUARTERS AIR RESEARCH
and
DEVELOPMENT COMPANY

Colonel Daniel D. McKee, USAF
Chief, Aeronautics and Propulsion Division
Deputy Commander/Research and Development

CONFERENCE COMMITTEES

Executive Committee

Chairman, R. F. Robinson, Headquarters Air Research
and Development Command

Chairman, Technical Program Committee: C. W. Frick,
Convair-San Diego, A Division of General Dynamics Corporation

Chairman, Arrangement Committee: Wm. D. Logan,
Convair-San Diego, A Division of General Dynamics Corporation

Technical Program Committee

C. W. Frick, Convair-San Diego, Chairman

Dr. John Brahtz, University of California

Dr. E. Laitone, University of California

Dr. H. Yoshihara, Convair-San Diego

M. Rogers, Office of Scientific Research - ARDC

R. Fuhrman, Ryan Aeronautical Company, San Diego

Arrangements Committee

Wm. D. Logan, Convair-San Diego, Chairman

Ned Root, Convair-San Diego

Jack Porterfield, Convair-San Diego

Dr. Sam Houston, University of California

John W. Lent, Ryan Aeronautical Company, San Diego

John Bradbeer, Ryan Aeronautical Company, San Diego

Russ Glick, Convair-San Diego

Warren Kemmer, Convair-San Diego

GAS DYNAMICS

GAS PHYSICS OF HIGH-ALTITUDE-HIGH
SPEED FLIGHT

S. A. Schaaf

GAS PHYSICS OF HIGH ALTITUDE-HIGH SPEED FLIGHT

S. A. Schaaf

The purpose of this paper is to give a brief review of the current state of knowledge in the general field of rarefied gas dynamics and to present some of the more recent experimental and theoretical results obtained at the University of California pertaining to high altitude aerodynamics.

Free molecule flow, i. e. highly rarefied flow for which the molecular mean free path is large compared to the model or vehicle dimension, is now well-understood at least for moderate speeds. The general theory is established, has been verified by experiment at both the Ames Laboratory by Stalder and his co-workers and at Berkeley, and a great number of results of aerodynamic interest are now available. Further work in this region will involve experiments on high energy molecule-surface interaction and extensions of the general theory to certain types of non-equilibrium for the incident gas. Perhaps the result of most aerodynamic interest in free molecule flow is the general one of very poor lift-drag ratios which, in fact, approach zero at high speeds in all practical cases.

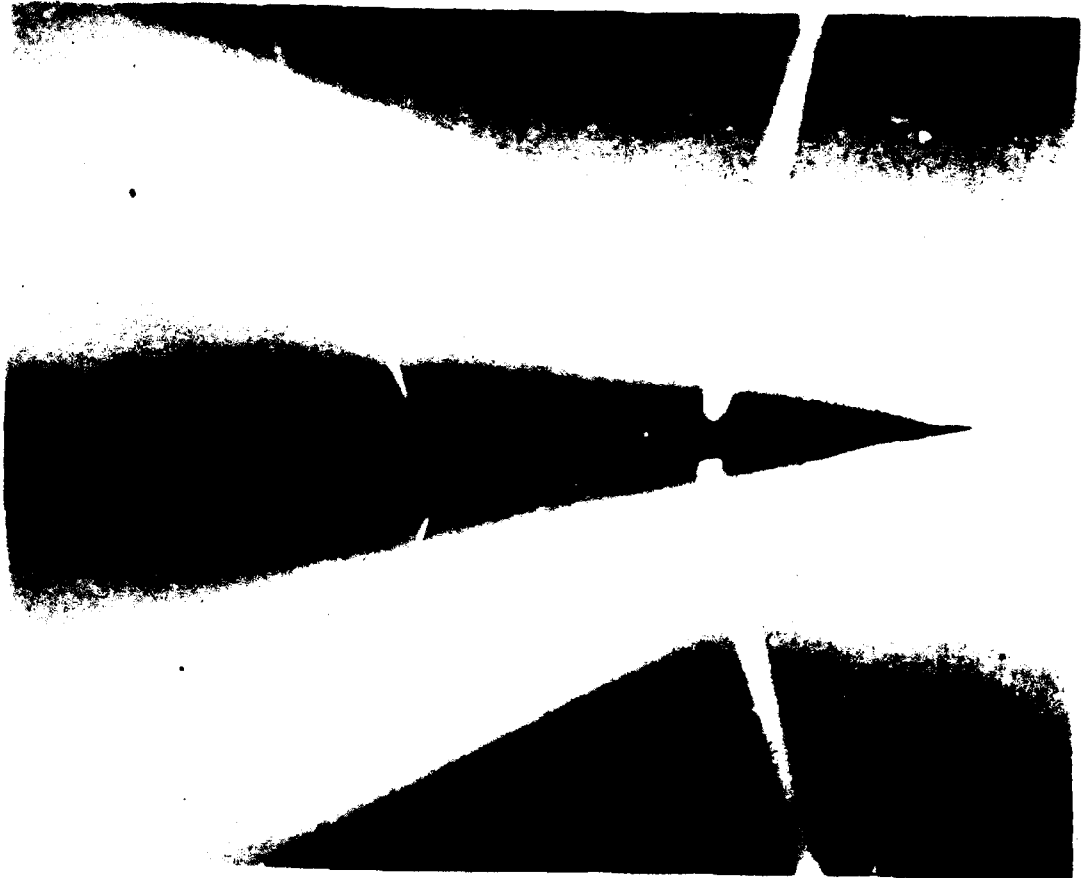
So-called slip flow, i. e. only moderately rarefied flow in which the molecular mean free path is a few percent of the vehicles' characteristic dimension, or of the boundary layer which forms on it, is considerably more complex. However, the basic physical formulation seems to have been pretty well established. Surprisingly enough, the standard Navier-Stokes equations, together with slip velocity and temperature jump boundary conditions seem valid for these densities. The main, if not only non-continuum effect, seems to be a straightforward alteration in the boundary conditions. Knowledge in the intermediate range of gas densities is still mostly empirical, and where available serves to provide an interpolation between slip flow on the one hand and free molecule flow on the other.

One of the most important general results of research in the slip flow to date has been to show that completely continuum boundary layer interaction effects are in most cases much more important than the non-continuum slip and temperature jump effects. Even small slip effects (to be thought of mostly as corrections to continuum results) are generally associated with moderate Mach numbers and very small Reynolds numbers - of the order of 5 and 1000 respectively, for example. But for such values as these for these parameters, the skin friction and induced pressures produced by the thick laminar boundary layers can be many times their normal values, enough to greatly alter low altitude aerodynamic characteristics. The relative importance of skin friction and induced pressure varies with vehicle geometry and orientation. In general, however, lift-drag ratios begin to deteriorate - usually because of the effect of skin friction on drag.

The slides depict views of the University of California Low Density wind tunnel, some of the experimental set-ups, and various as yet unpublished data on pressure distribution and aerodynamic coefficients in the slip and intermediate ranges. The flat plate and sphere-nosed cone pressure distributions were obtained by Drs. Hurlturt and Talbot and Mr. Aroesty; the sharp-tipped cone pressure distributions were obtained by Drs. Talbot and Koga and Mrs. Sherman; the cone-cylinder lift and drag coefficients were obtained by Mr. Nark. A very considerable body of additional similar data has already been published.

It will be observed that these results apply, for vehicles of the order of 1-10 feet in diameter, to altitudes and speeds with very little overlap with the "flight corridor," i. e. the corresponding atmospheric density is too low in most cases to provide sufficient dynamic pressure to generate adequate aerodynamic lift. It should also be noted that these are wind-tunnel experiments and correspond to adiabatic models and moderate gas stagnation temperatures, whereas

the free flight conditions would be for cooled surfaces and very high gas stagnation temperature. For blunt short bodies a tentative extrapolation of the wind tunnel data, based on matching only the Reynolds number behind the detached shock, has been suggested. Its validity has not yet been established one way or the other. There is clearly a great need, however, to extend slip flow research to higher velocities and gas temperatures at the same general density level.



McGraw-Hill
Book Company

Slide #1

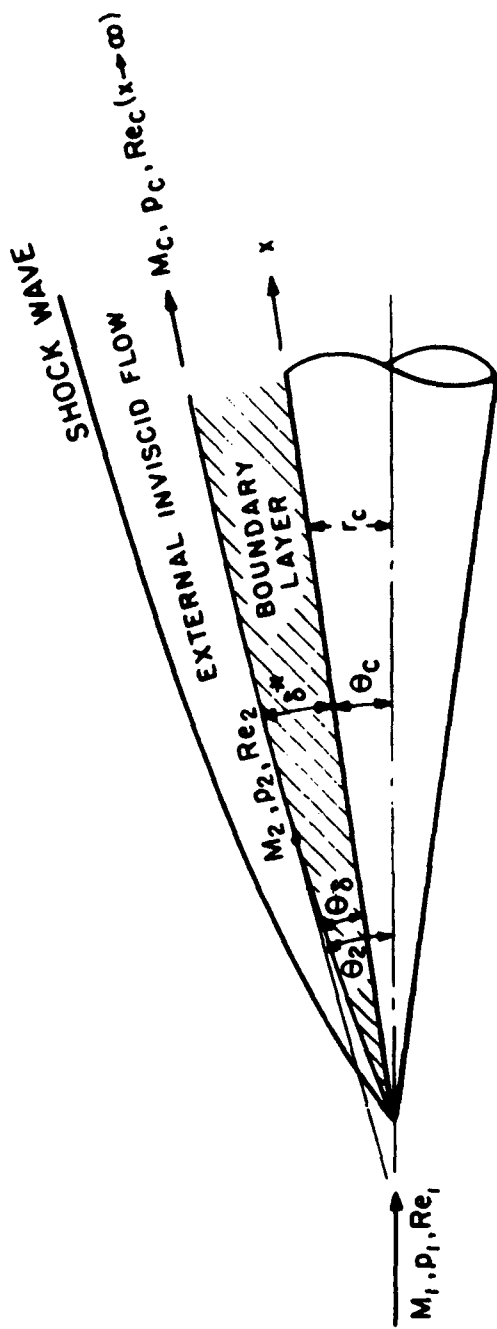
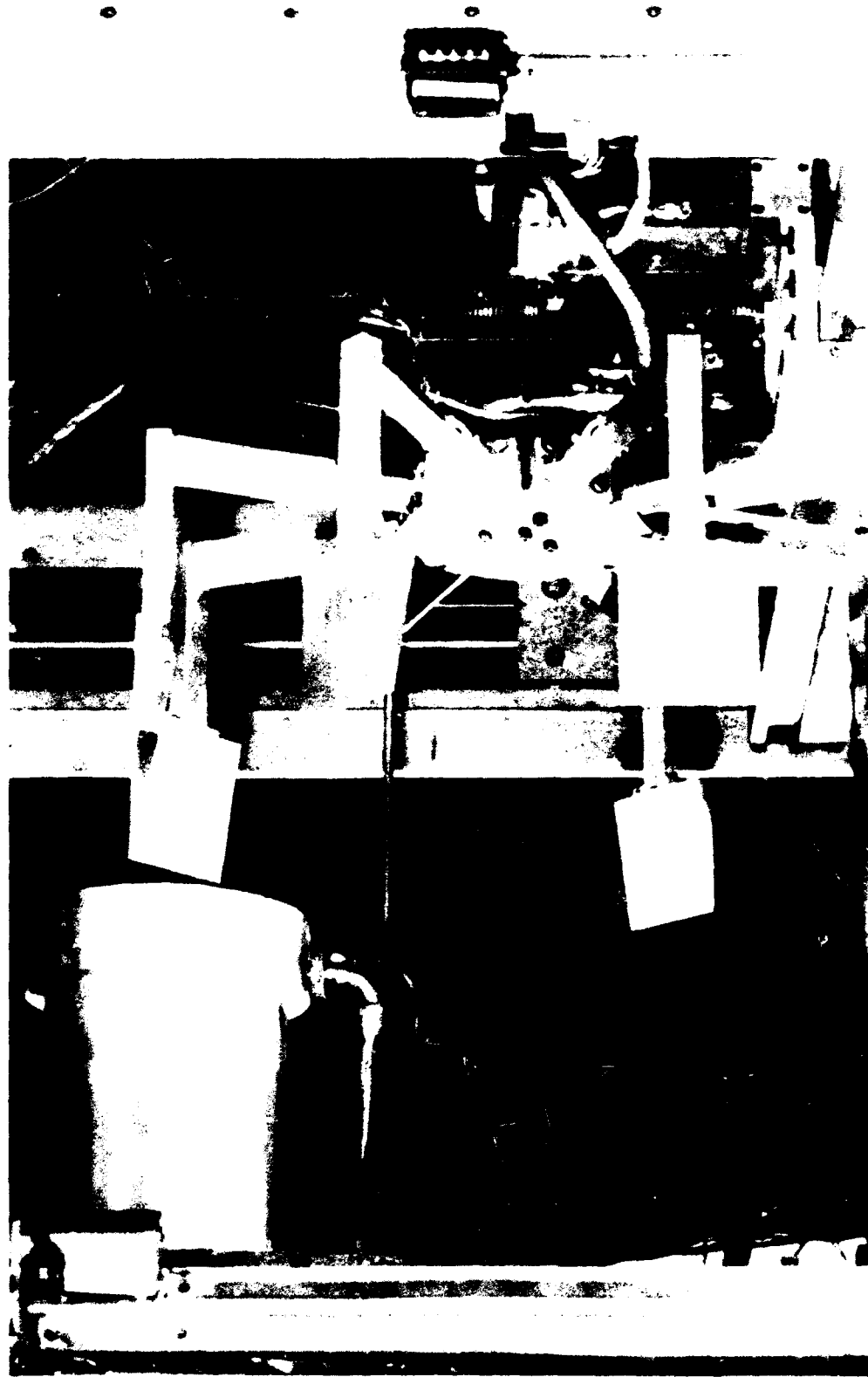


FIG. 1 SCHEMATIC OF VISCOUS FLOW OVER A CONE

HYD 6911-150-0

$$\frac{\delta p}{p_\infty} \sim \frac{M_\infty^3}{\sqrt{Re_{\infty,x}}}$$

$$\frac{\tau}{p_\infty} \sim \frac{M_\infty^2}{\sqrt{Re_{\infty,x}}}$$



Slide #4

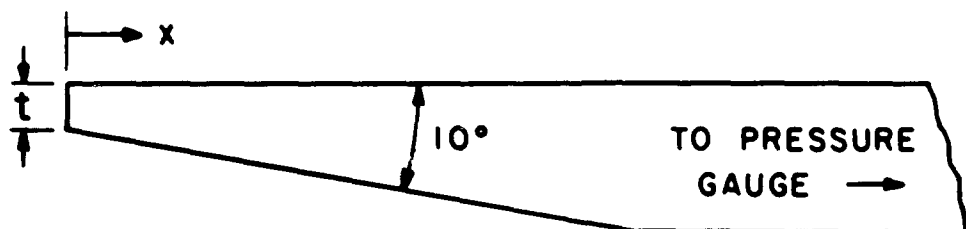
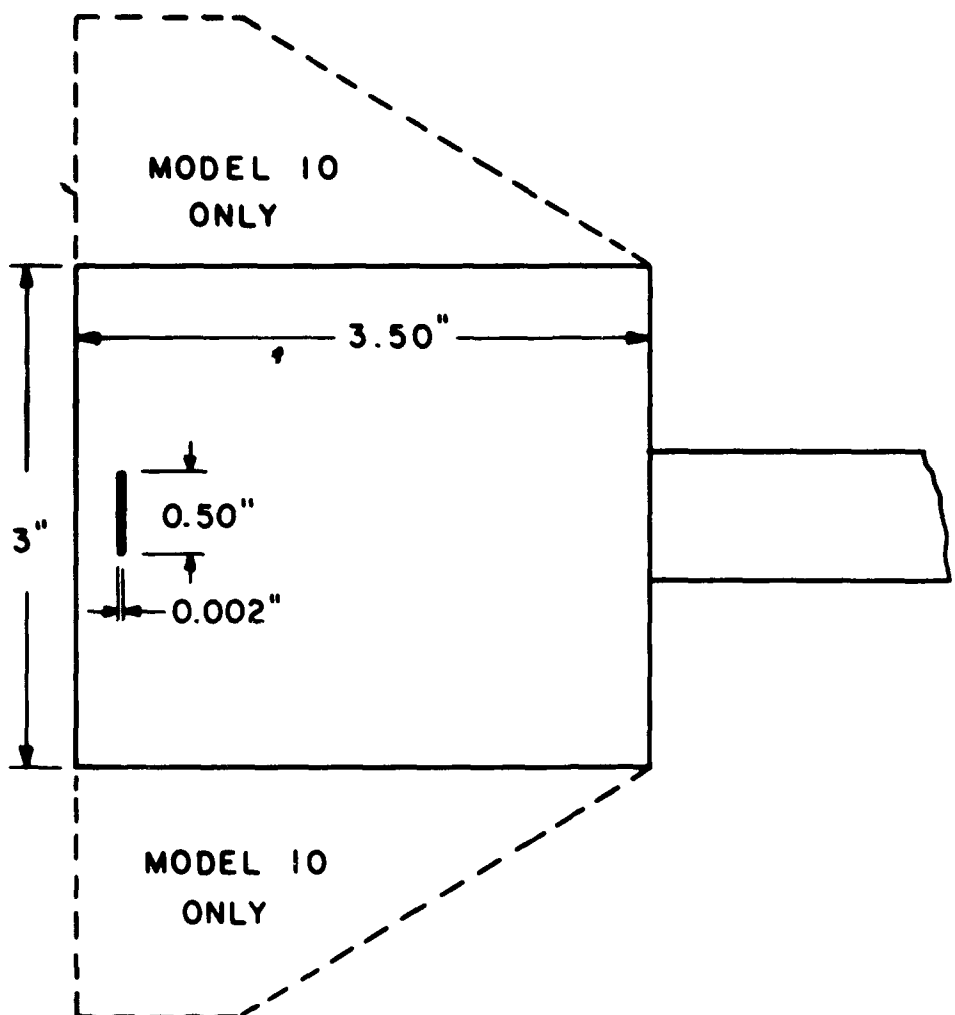
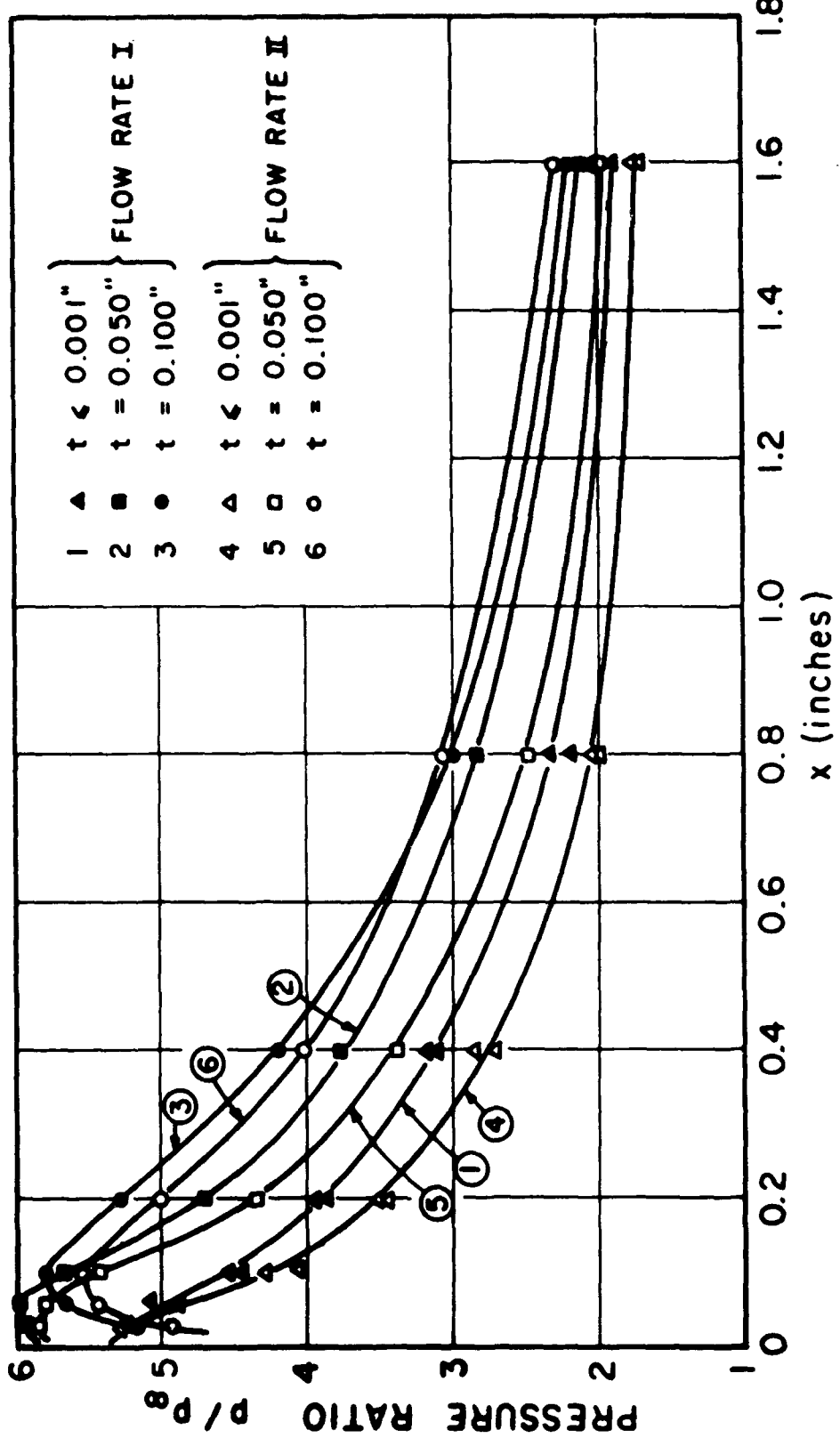
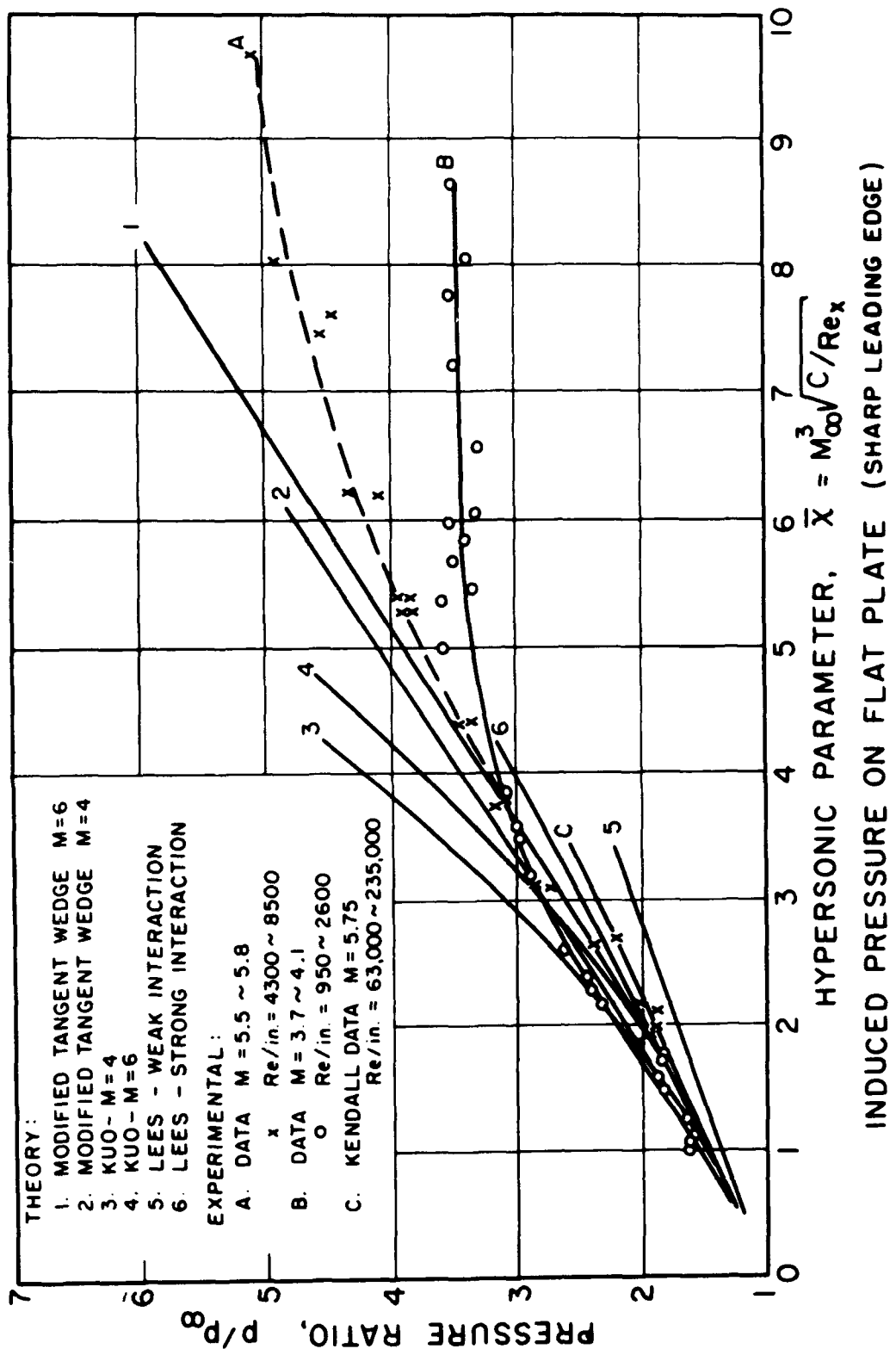


FIG. 1 PRESSURE MODELS



Slide #6



INDUCED PRESSURE ON FLAT PLATE (SHARP LEADING EDGE)

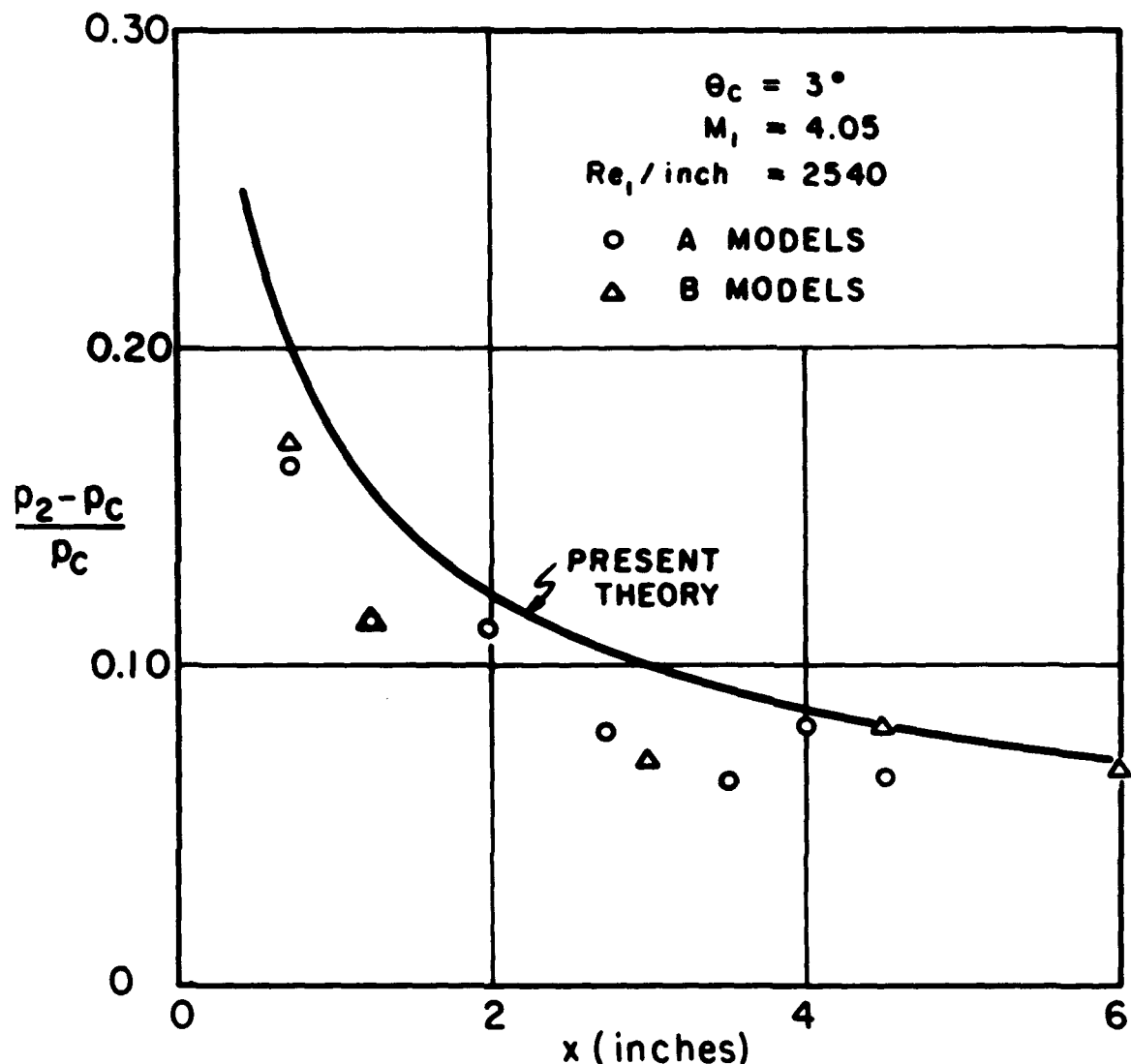


FIG. 7 INDUCED PRESSURE INCREMENT VS X

HYD 6917-150-0

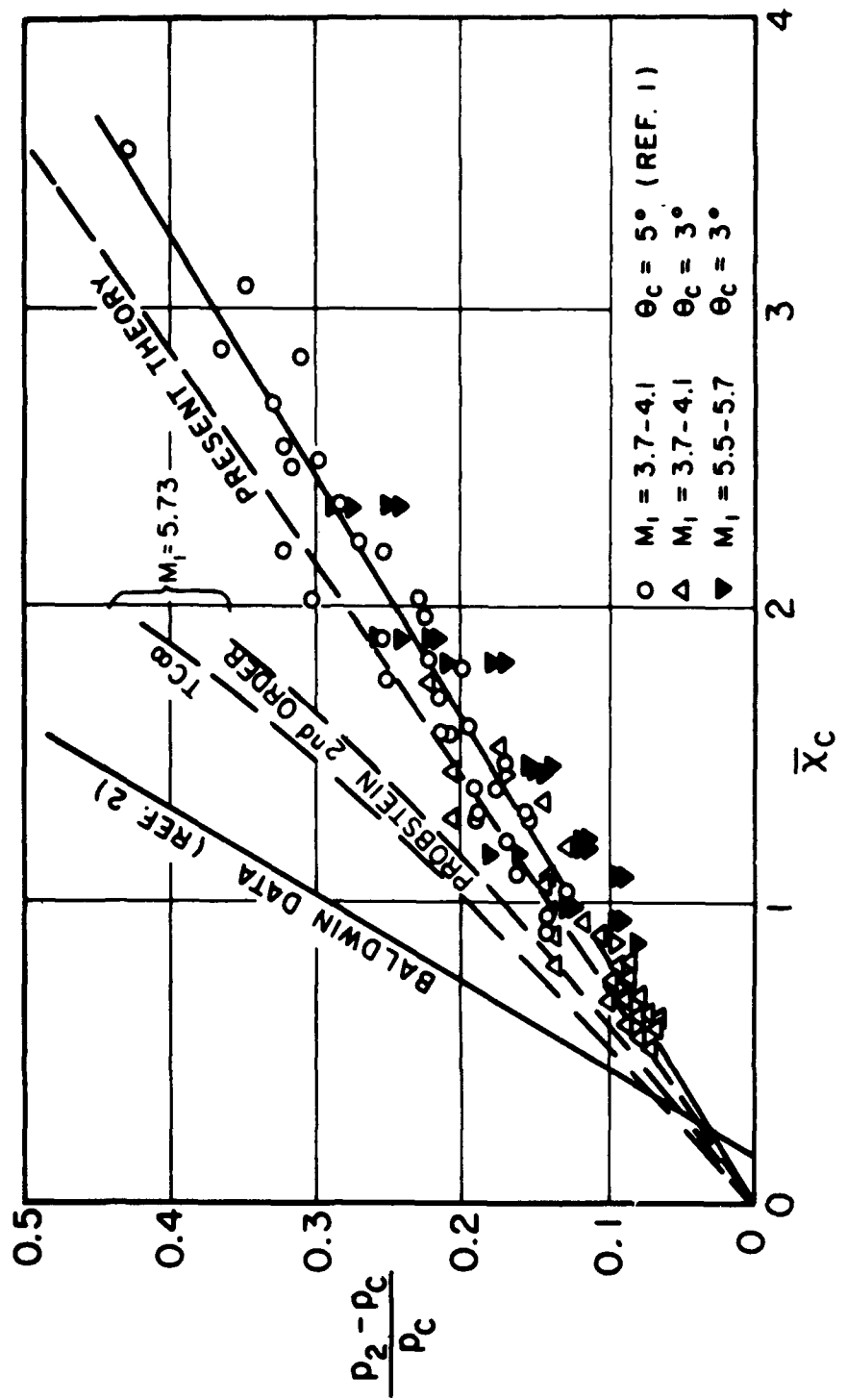
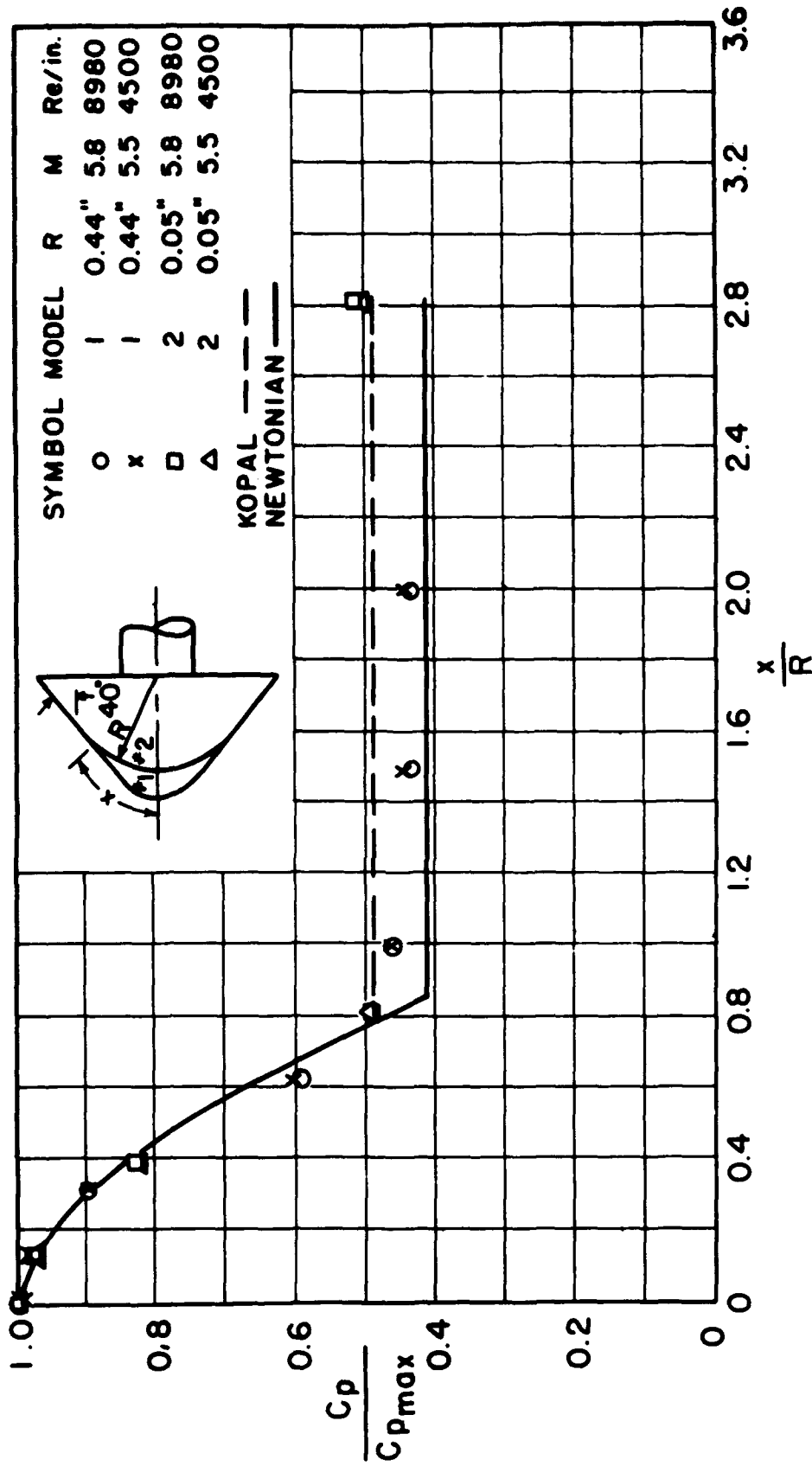


FIG. II INDUCED PRESSURE INCREMENT vs HYPERSONIC SIMILARITY PARAMETER $\bar{\chi}_c$

HYD 6921-150-0



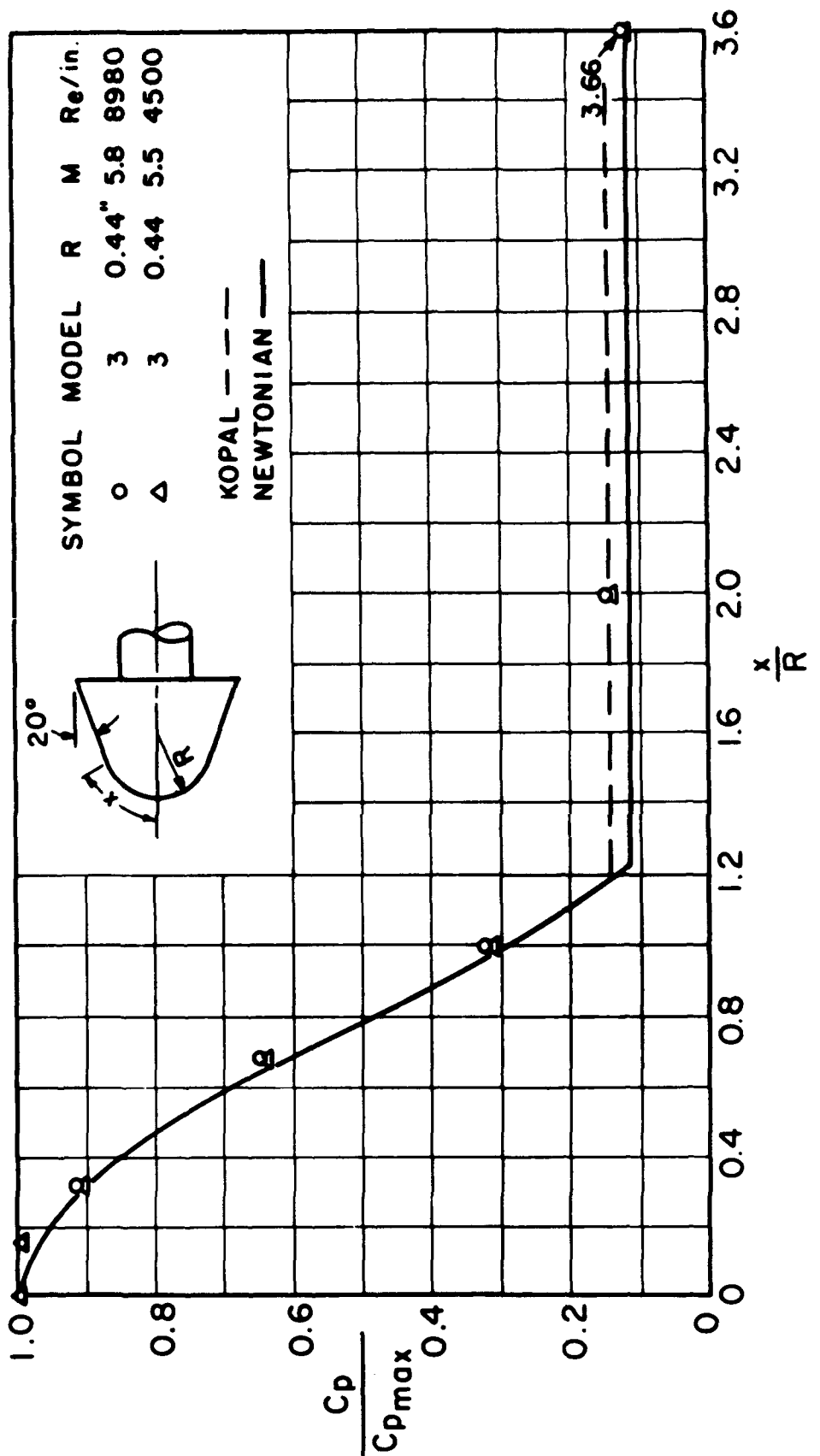
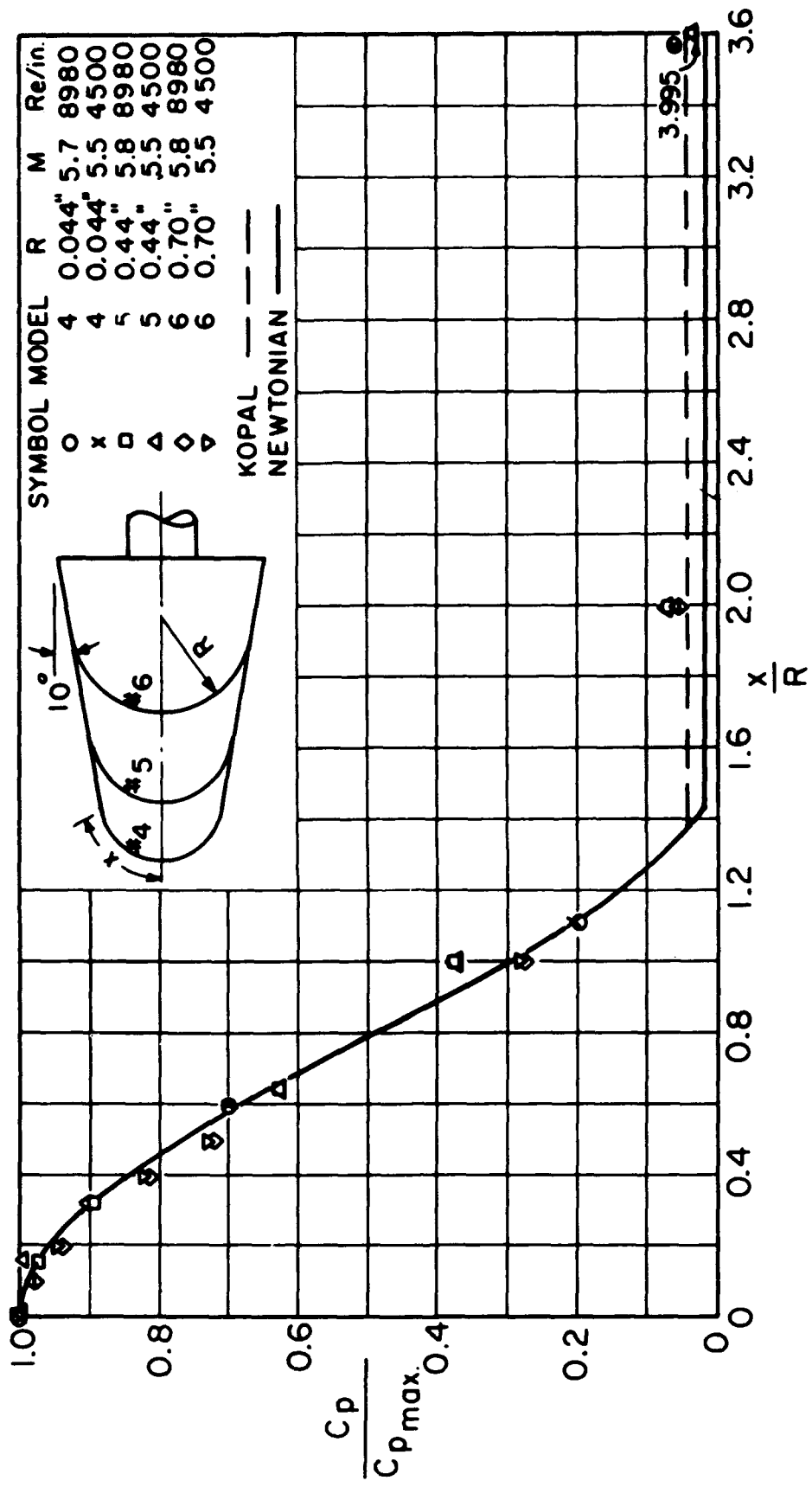


FIG. 7 SURFACE PRESSURE DISTRIBUTION, 20° CONE ANGLE



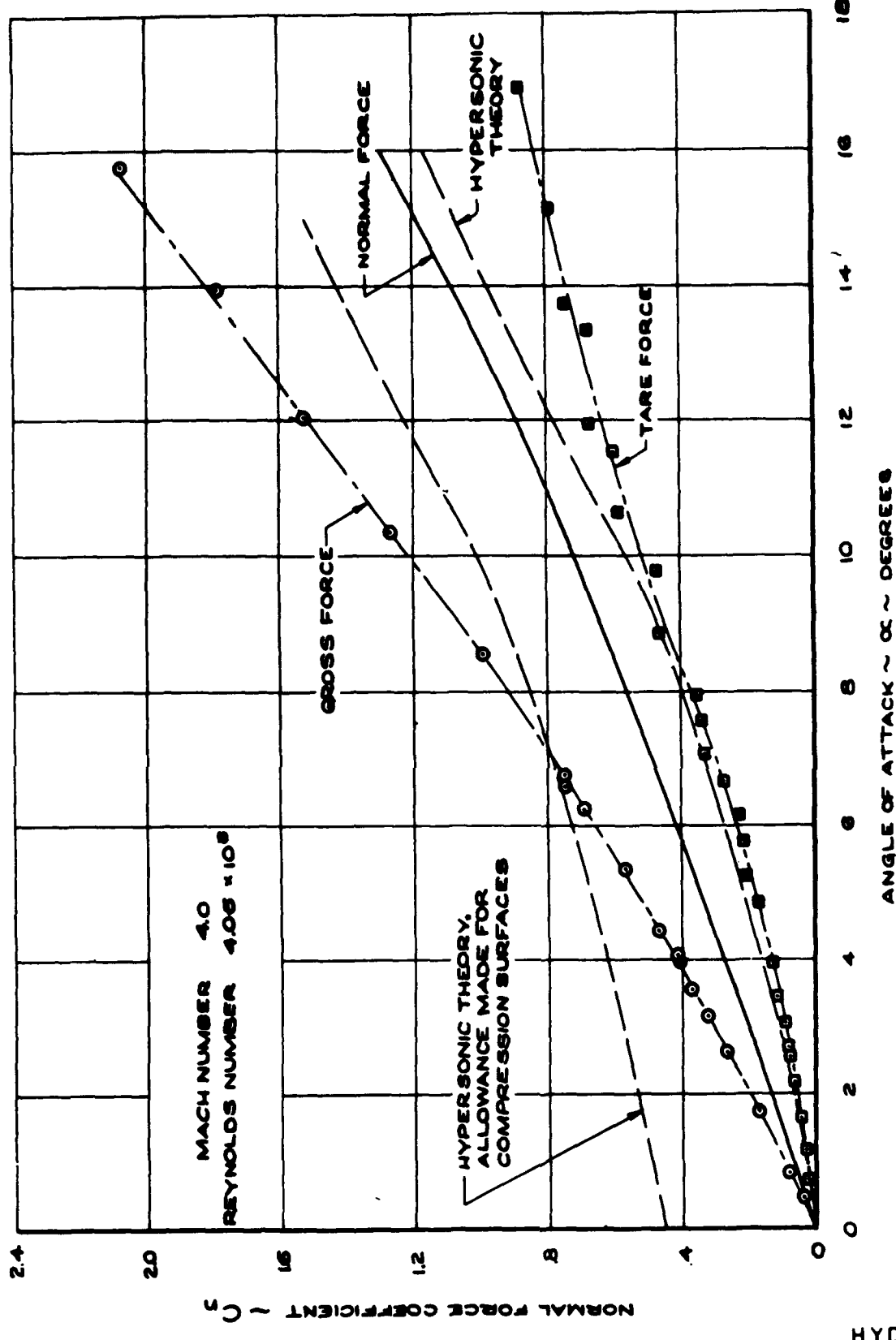


FIG. 7 NORMAL FORCE COEFFICIENT AT A NOMINAL MACH NUMBER OF 4.0

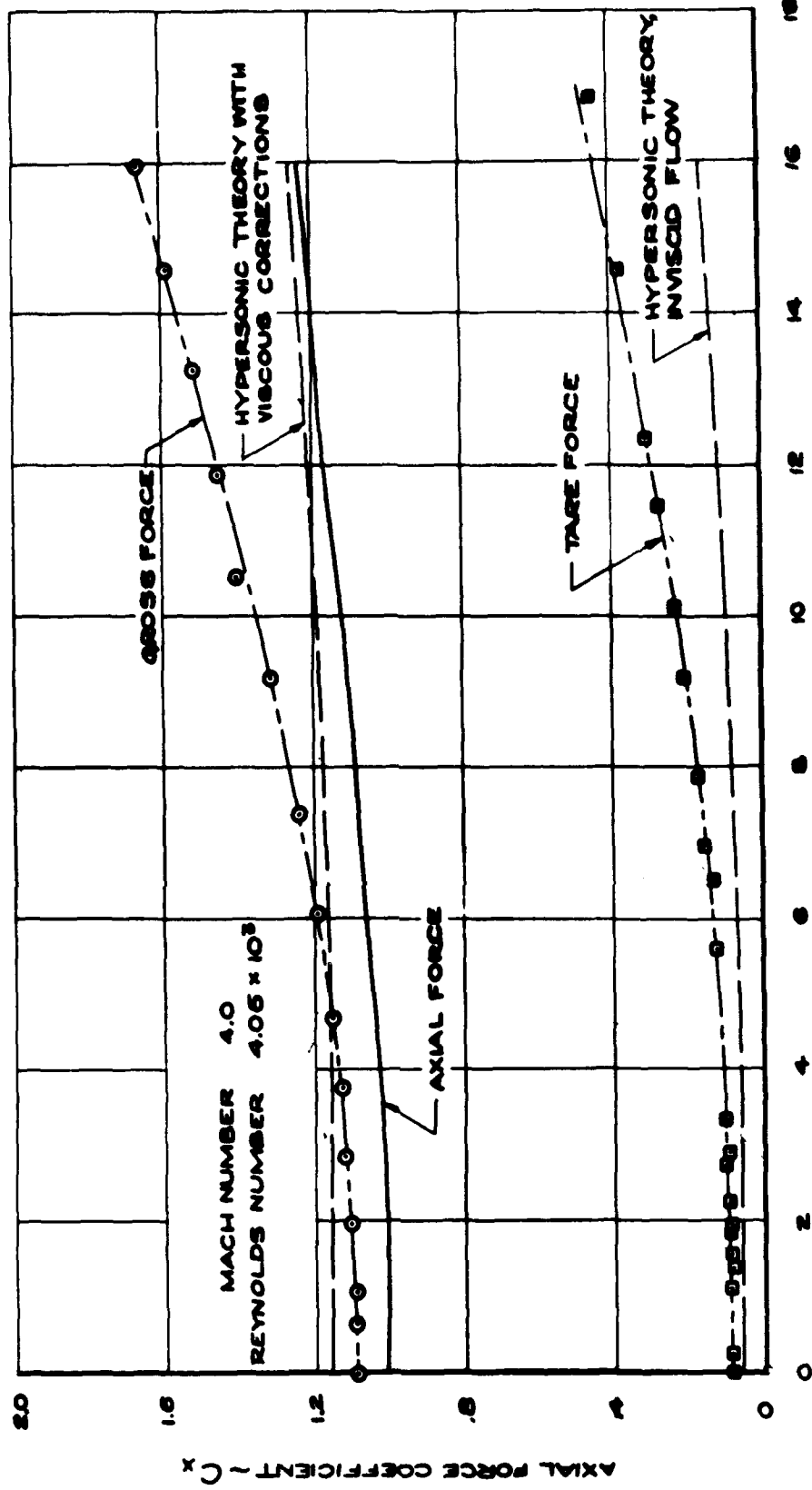
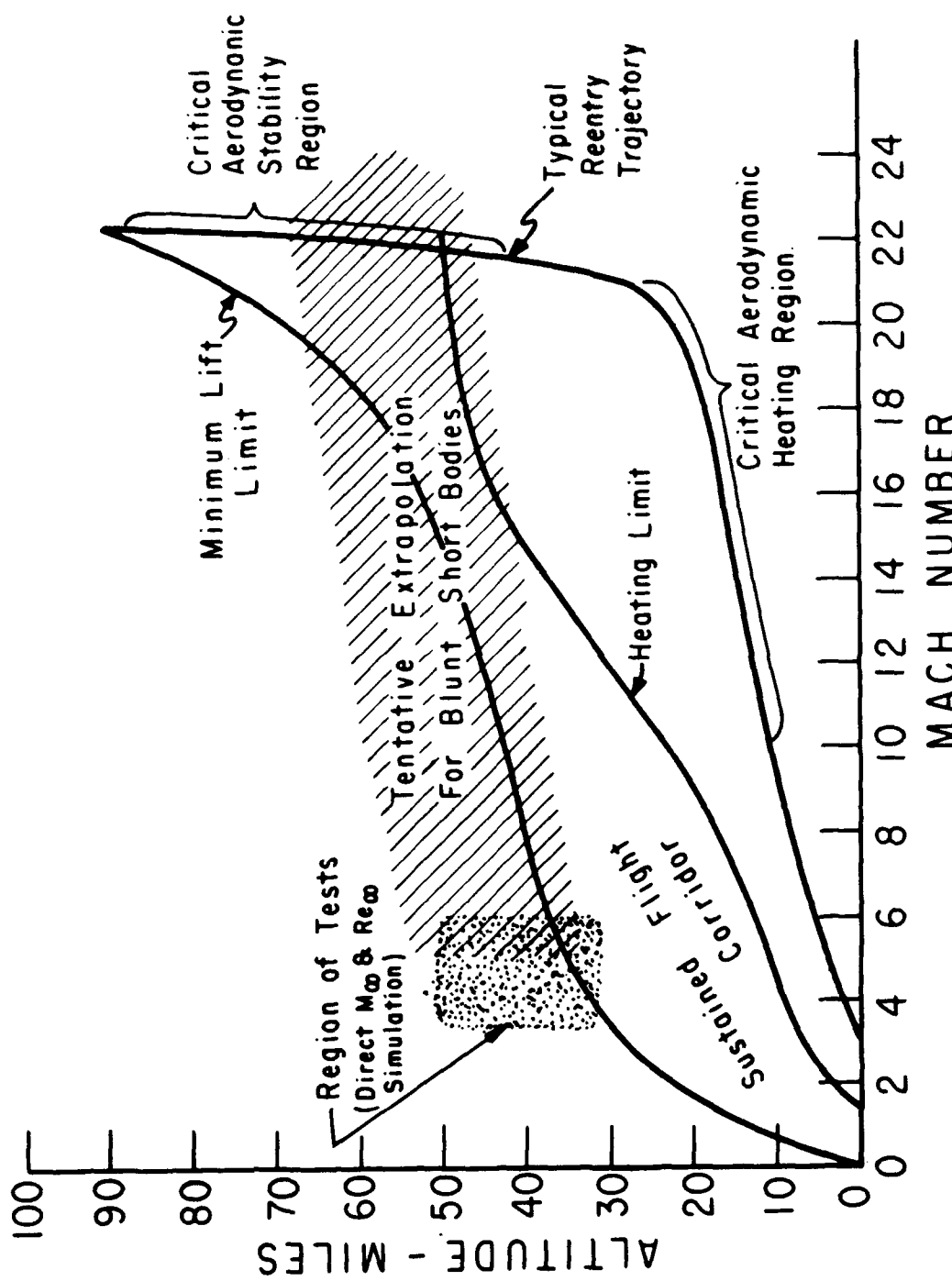


FIG. 8 AXIAL FORCE COEFFICIENT AT A NOMINAL MACH NUMBER OF 4.0

HYD 6988



PROTOTYPE vs MODEL CONSIDERATIONS

ONE DIMENSIONAL UNSTEADY GAS DYNAMICS BY
HYDRAULIC ANALOGUE

W. H. T. Loh
Chance Vought Aircraft

ONE DIMENSIONAL UNSTEADY GAS DYNAMICS BY
HYDRAULIC ANALOGUE

Dr. W. H. T. Lai

SUMMARY

Hydraulic analogy comes from the mathematical similarities of the basic equations. In two dimensional steady flow, the equations of continuity, momentum and energy were found to be identical in mathematical forms by many authors for an irrotational isentropic perfect gas flow with a specific heat ratio of 2 on one hand and an incompressible frictionless water flow in an open horizontal channel of a rectangular crosssection on the other hand. Pressure waves in the gas flow corresponds to gravity waves in the water flow. The shock waves of gas dynamics corresponds (although not rigidly) to hydraulic jump* of hydraulics. This is so called "water table", which has been used frequently in the past to study, in an analogical sense, the two dimensional steady subsonic and supersonic flows.

The present paper, instead of using two dimensional steady flow as done before, examined the problem of one dimensional unsteady flow. It was found here that (1) the equations of continuity, momentum and energy are identical in mathematical forms for an isentropic perfect gas flow of a specific heat ratio of any value, say K on one hand and an incompressible frictionless water flow

* NACA TM 934 and 935 "Application of the Methods of Gas Dynamics to Water Flows With Free Surfaces" by Ernest Preiswerk.

in an open horizontal channel of a crossectional shape, described by the equation $Z = Y^{\frac{2-K}{K-1}}$, on the other hand. Here Z is the local width and Y is the local height of the crossection, and (2) the equations of waves and wave propagation are also identical in mathematical forms for the two said flows. In the case of one dimensional unsteady flow, it was further found that the case of specific heat ratio of 2 in a rectangular channel is a special case of the general case when $n = 0$ (n is defined in the text).

TWO DIMENSIONAL STEADY FLOW

Let us start with the well known two dimensional steady flow case. This case was found and discussed by many many authors. This case will deal with the following two analogous flows. A flow of irrotational isentropic perfect gas of specific heat ratio equal to 2 and a flow of an incompressible frictionless water in an open horizontal channel of a rectangular crossection (slide). The equations of continuity, momentum and energy for the two flows are shown in the following:

Gas Flow

Water Flow

Continuity Equation:

$$u' \frac{\partial \rho'}{\partial x'} + \rho' \frac{\partial u'}{\partial x'} + v' \frac{\partial \rho'}{\partial y'} + \rho' \frac{\partial v'}{\partial y'} = 0 \quad u' \frac{\partial h'}{\partial x'} + h' \frac{\partial u'}{\partial x'} + v' \frac{\partial h'}{\partial y'} + h' \frac{\partial v'}{\partial y'} = 0$$

Momentum Equation

$$u' \frac{\partial u'}{\partial x'} + v' \frac{\partial v'}{\partial x'} = - \left(\frac{1}{k-1} \right) \frac{\partial p'}{\partial x'}^{k-1}$$

$$u' \frac{\partial u'}{\partial y'} + v' \frac{\partial v'}{\partial y'} = - \left(\frac{1}{k-1} \right) \frac{\partial \rho'}{\partial y'}^{k-1}$$

$$u' \frac{\partial u'}{\partial x'} + v' \frac{\partial v'}{\partial x'} = - \frac{\partial h'}{\partial x'}$$

$$u' \frac{\partial u'}{\partial y'} + v' \frac{\partial v'}{\partial y'} = - \frac{\partial h'}{\partial y'}$$

Energy Equation

$$\frac{u^2}{u_{\max}^2} = 1 - \left(\frac{T}{T_0} \right)$$

$$\frac{u^2}{u_{\max}^2} = 1 - \left(\frac{h}{h_0} \right)$$

Here the equations were shown in non-dimensional form, so identical terms in corresponding equations may be put equal numerically. Comparison of the corresponding equations show the following analogous terms:

Gas Flow

$$\rho' \left(= \frac{\rho}{\rho_0} \right)$$

$$p' \left(= \frac{\frac{k-1}{k} p}{\frac{k-1}{k} p_0} \right)$$

$$T' \left(= \frac{T}{T_0} \right)$$

$$u' \left(= \frac{u}{\sqrt{\frac{p_0}{\rho_0}}} \right)$$

$$\left(\frac{1}{k-1} \right)$$

Water Flow

$$h' \left(= \frac{h}{h_0} \right)$$

$$h' \left(= \frac{h}{h_0} \right)$$

$$h' \left(= \frac{h}{h_0} \right)$$

$$u' \left(= \frac{u}{\sqrt{g h_0}} \right)$$

1

The last condition specifies that the flow of water is comparable with the flow of a gas having a ratio of specific heats $k = \frac{C_p}{C_v} = 2$. Although no such gas with $k = 2$ was found in nature but the hydraulic analogue has been found useful in a qualitative manner for the studies of two dimensional steady subsonic and supersonic flows.

ONE DIMENSIONAL UNSTEADY FLOW

In a similar manner as done in the two dimensional steady flow case, the one dimensional unsteady flow is hereby presented. This case deals with the following two analogous flows (slide). A flow of isentropic perfect gas of any specific heat ratio, say k , and a flow of an incompressible frictionless water in an open horizontal channel of a crossectional shape, described by the equation $Z = Y^n$. The equations of continuity, momentum and energy for the two flows are derived in the following:

BASIC ASSUMPTIONS

1. The fluid is frictionless so that conservation of energy into heat is excluded both in gas and in water.
2. The flow is one dimensional and is in a duct (for gas) or channel (for water) of uniform crossection. This implies that v and w components of fluid velocity are negligible compared with u component of fluid velocity.
3. The vertical acceleration of the water is negligible compared with the acceleration of the gravity. Under this assumption the static pressure at a point of the field of flow depends linearly on the vertical distance under the free surface at that position. In otherwords, $p = \rho g(h-y)$. It is further assumed that the velocity is uniform and constant over any crossection in perpendicular to the flow direction. The justification of this assumption for the case of one dimensional unsteady flow is given in Appendix A.
4. In one dimensional unsteady gas flow, all parameters (pressure, temperature, velocity) are assumed to be uniform and constant across any section in perpendicular to the direction of flow.

THE EQUATION OF CONTINUITY

Gas Flow:

The well known equation of continuity for one dimensional unsteady flow has the following form:

$$\frac{\partial \rho}{\partial t} + u \frac{\partial \rho}{\partial x} + \rho \frac{\partial u}{\partial x} = 0$$

Putting into non-dimensional form by letting:

$$\frac{\rho}{\rho_0} = \rho'$$

$$\frac{u}{a_0} = u'$$

$$\frac{x}{l_a} = x'$$

$$\frac{t}{t_a} = t'$$

it becomes:

$$u' \frac{\partial \rho'}{\partial x'} + \rho' \frac{\partial u'}{\partial x'} + \left(\frac{l_a}{a_0 t_a} \right) \frac{\partial \rho'}{\partial t'} = 0$$

Water Flow:

The continuity equations says that the net mass rate of flow crossing the control surfaces must be equal to the net rate of change of mass inside the control volume. At a given instant, the mass rate of flow into the left boundary is $\rho A u$ and the mass within the control volume is $\rho A dx$. Hence we can write

$$-\frac{\partial (\rho A u)}{\partial x} dx = \frac{\partial}{\partial t} (\rho A dx)$$

Expanding this, and noting that ρ is constant for water flow, we get

$$u \frac{\partial A}{\partial x} + A \frac{\partial u}{\partial x} + \frac{\partial A}{\partial t} = 0$$

Putting into non-dimensional form and noting that $A = \int_0^h y^n dy = \left(\frac{h^{n+1}}{n+1} \right)$.

$$\frac{h}{h_0} = h'$$

$$\frac{A}{A_0} \approx h'^{n+1}$$

$$\frac{u}{\sqrt{\frac{gh_0}{n+1}}} = u'$$

$$\frac{x}{l_w} = x'$$

$$\frac{t}{t_w} = t'$$

it becomes

$$u' \frac{\partial h'^{n+1}}{\partial x'} + h'^{n+1} \frac{\partial u'}{\partial x'} + \left(\frac{l_w}{\sqrt{\frac{gh_0}{n+1}} t_w} \right) \frac{\partial h'^{n+1}}{\partial t'} = 0$$

THE EQUATION OF MOMENTUM

Gas Flow:

The well known equation of momentum for one dimensional unsteady flow has the following form:

$$\frac{\partial u}{\partial t} + u \frac{\partial u}{\partial x} = - \frac{1}{\rho} \frac{\partial p}{\partial x}$$

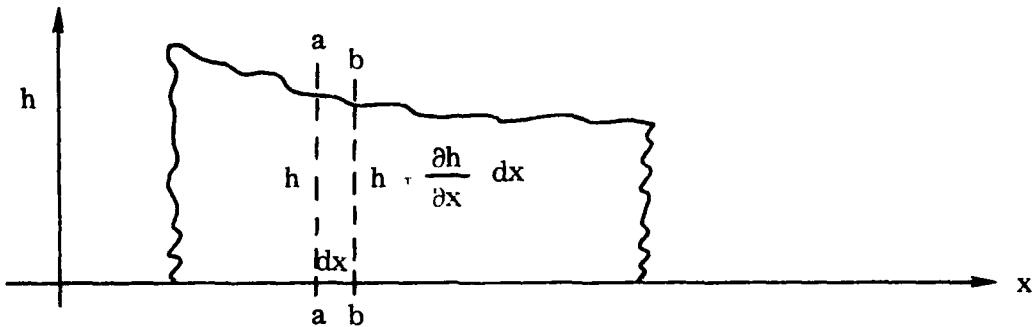
Putting into the same non-dimensional form and noting the isentropic

relationship $\frac{p}{\rho^k} = \frac{p_0}{\rho_0^k}$ we get:

$$\frac{\partial u'}{\partial t'} + \left(\frac{a_0 t_a}{l_a} \right) u' \frac{\partial u'}{\partial x'} = - \left(\frac{a_0 t_a}{l_a} \right) \left(\frac{1}{k-1} \right) \frac{\partial p}{\partial x'}^{\frac{k-1}{k}}$$

Water Flow:

Newton's law, as it applies to the fluid volume as shown, says that the net force to the right will be equal to the mass times the acceleration.



The net force is the difference of pressure forces on a - a and b - b, it is equal to:

$$\begin{aligned}
 F_{a-a} - F_{b-b} &= \int_0^h \rho g (h - y) z dy - \int_0^{h + \frac{\partial h}{\partial x} dx} \rho g (h - y) z dy \\
 &= - \frac{\rho g}{(n+1)(n+2)} [h^{n+2} - (h + \frac{\partial h}{\partial x} dx)^{n+2}]
 \end{aligned}$$

The mass between a - a and b - b is:

$$\rho \frac{[h^{n+2} - (h + \frac{\partial h}{\partial x} dx)^{n+2}]}{\frac{\partial h}{\partial x} (n+1)(n+2)} \quad (\text{derivation in Appendix B})$$

The acceleration is:

$$\frac{Du}{Dt} = \frac{\partial u}{\partial t} + u \frac{\partial u}{\partial x}$$

By Newton's law of motion, we get after simplification

$$\frac{\partial u}{\partial t} + u \frac{\partial u}{\partial x} = -g \frac{\partial h}{\partial x}$$

Putting into non-dimensional form as done before, we get:

$$\frac{\partial u'}{\partial t'} + \left(\frac{\sqrt{\frac{gh_0}{n+1}} t_w}{l_w} \right) u' \frac{\partial u'}{\partial x'} = - \left(\frac{\sqrt{\frac{gh_0}{n+1}} t_w}{l_w} \right) (n+1) \frac{\partial h'}{\partial x'}$$

EQUATION OF ENERGY

Gas Flow:

The well known one dimensional unsteady flow energy equation has the following usual form:

$$\frac{\partial E}{\partial t} + u \frac{\partial E}{\partial x} + p \frac{\partial (\frac{1}{\rho})}{\partial t} + pu \frac{\partial (\frac{1}{\rho})}{\partial x} = 0$$

Putting into non-dimensional form by letting

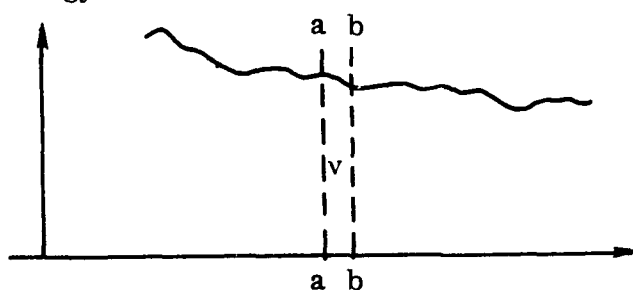
$$E' = \frac{E}{E_0} = \frac{C_v T}{C_v T_0} = \left(\frac{T}{T_0} \right)$$

in addition to the other non-dimensional quantities already shown previously, it becomes:

$$\frac{\partial E'}{\partial t'} + \left(\frac{a_0 t_a}{l_a} \right) u' \frac{\partial E'}{\partial x'} + (k-1) p' \frac{\partial (\frac{1}{\rho'})}{\partial t'} + (k-1) \left(\frac{a_0 t_a}{l_a} \right) p' u' \frac{\partial (\frac{1}{\rho'})}{\partial x'} = 0$$

Water Flow:

The law of conservation of energy requires that the difference in the rate of supply energy entering to a control volume V and the rate at which energy leaves V must be equal to the net rate of increase of energy in V.



Rate of energy entering at a - a

$$= \int \left(\frac{1}{2} u^2 \right) \rho u dA + \int (gy) \rho u dA + \int \rho u dA$$

Rate of energy leaving at b - b

$$= \left[\int \left(\frac{1}{2} u^2 \right) \rho u dA + \int (g y) \rho u dA + \int p u dA \right] \\ + \frac{\partial}{\partial x} \left[\int \left(\frac{1}{2} u^2 \right) \rho u dA + \int (g y) \rho u dA + \int p u dA \right] dx$$

Rate of energy increase in volume V.

$$= \frac{\partial}{\partial t} \left[\int \left(\frac{1}{2} u^2 \right) \rho dA dx + \int (g y) \rho dA dx \right]$$

Therefore, we may write the energy equation according to the law of conservation of energy as stated above:

$$- \frac{\partial}{\partial x} \left[\int \left(\frac{1}{2} u^2 \right) \rho u dA + \int (g y) \rho u dA + \int p u dA \right] dx \\ = \frac{\partial}{\partial t} \left[\int \left(\frac{1}{2} u^2 \right) \rho dA + \int (g y) \rho dA \right] dx$$

Expanding this relation by noting that $dA = y^n dy$, $p = \rho g (h-y)$ and further simplifying it by using the known relations of continuity and momentum equations already derived, we get:

$$\frac{\partial h}{\partial t} + u \frac{\partial h}{\partial x} + \left(\frac{h^{n+2}}{n+1} \right) \frac{\partial \left(\frac{1}{h^{n+1}} \right)}{\partial t} + \left(\frac{h^{n+2}}{n+1} \right) u \frac{\partial \left(\frac{1}{h^{n+1}} \right)}{\partial x} = 0$$

Putting into non-dimensional form, we get:

$$\frac{\partial h'}{\partial t'} + \left(\frac{\sqrt{gh_0} t_w}{\sqrt{n+1} l_w} \right) u' \frac{\partial h'}{\partial x'} + \left(\frac{h'^{n+2}}{n+1} \right) \frac{\partial \left(\frac{1}{h'^{n+1}} \right)}{\partial t'} \\ + \left(\frac{h'^{n+2}}{n+1} \right) \left(\frac{\sqrt{gh_0} t_w}{\sqrt{n+1} l_w} \right) u' \frac{\partial \left(\frac{1}{h'^{n+1}} \right)}{\partial x'} = 0$$

EQUATIONS OF STANDING WAVES

In order to make the hydraulic analogy more clear for the present case of one dimensional unsteady flow, it is best to check

further the mathematical similarities of fundamental wave equations. Only the simple equations of wave formation produced by some simple causes are considered here for simplicity, because otherwise the equations would be too complicated and difficult to operate. However, it is believed that the analogy of waves, which exist in those simple equations will also exist in complicated wave mechanisms. From this point of view, the following equations were derived in Appendix C and were given here for comparisons.

<u>Gas Flow</u>	<u>Water Flow</u>
$\frac{\partial^2 \xi}{\partial t^2} = -\frac{1}{k} a_0^2 \frac{\partial}{\partial x} \left[\left(\frac{p}{p_0} \right) - 1 \right]$	$\frac{\partial^2 \xi}{\partial t^2} = -\left(\frac{n+1}{n+2} \right) \left(\frac{gh_0}{n+1} \right) \frac{\partial}{\partial x} \left[\left(\frac{h}{h_0} \right)^{n+2} - 1 \right]$
$\frac{\partial^2 \xi}{\partial t^2} = a_0^2 \frac{\partial^2 \xi}{\partial x^2}$	$\frac{\partial^2 \xi}{\partial t^2} = \left(\frac{gh_0}{n+1} \right) \frac{\partial^2 \xi}{\partial x^2}$
$\frac{\partial^2}{\partial t^2} \left[\left(\frac{p}{p_0} \right) - 1 \right] = a_0^2 \frac{\partial^2}{\partial x^2} \left[\left(\frac{p}{p_0} \right) - 1 \right]$	$\frac{\partial^2}{\partial t^2} \left[\left(\frac{h}{h_0} \right)^{n+2} - 1 \right] = \left(\frac{gh_0}{n+1} \right) \frac{\partial^2}{\partial x^2} \left[\left(\frac{h}{h_0} \right)^{n+2} - 1 \right]$
$\frac{\partial^2}{\partial t^2} \left[\left(\frac{\rho}{\rho_0} \right) - 1 \right] = a_0^2 \frac{\partial^2}{\partial x^2} \left[\left(\frac{\rho}{\rho_0} \right) - 1 \right]$	$\frac{\partial^2}{\partial t^2} \left[\left(\frac{h}{h_0} \right)^{n+1} - 1 \right] = \left(\frac{gh_0}{n+1} \right) \frac{\partial^2}{\partial x^2} \left[\left(\frac{h}{h_0} \right)^{n+1} - 1 \right]$
$a = \left(\frac{dp}{d\rho} \right)^{\frac{1}{2}} = \sqrt{K \frac{p}{\rho}} = \sqrt{KRT}$	$c = \left(\frac{gA}{b} \right)^{\frac{1}{2}} = \sqrt{\frac{gh}{n+1}}$

Now we have derived the basic equations of continuity, momentum and energy; and we have also derived the basic equations of simple waves and wave propagation. Summarizing these equations and comparing them term by term, we will have the analogous terms in the two flows. These identical terms in corresponding equations may be put equal numerically, because they are already in non-dimensional forms. This was done in the following two pages.

SUMMARY OF ANALOGOUS EQUATIONS

Summarizing all the above equations, we have:

Gas Flow

1. Equation of Continuity

$$u' \frac{\partial \rho'}{\partial x'} + \rho' \frac{\partial u'}{\partial x'} + \left(\frac{l_a}{a_0 t_a} \right) \frac{\partial \rho'}{\partial t'} = 0$$

$$u' \frac{\partial h'^{n-1}}{\partial x'} + h'^{n-1} \frac{\partial u'}{\partial x'} - \left(\frac{l_w}{\sqrt{\frac{gh_o}{n-1}} t_w} \right) \frac{\partial h'^{n-1}}{\partial t'} = 0$$

2. Equation of Momentum

$$\frac{\partial u'}{\partial t'} + \left(\frac{a_0 t_a}{l_a} \right) u' \frac{\partial u'}{\partial x'} = - \left(\frac{a_0 t_a}{l_a} \right) \left(\frac{1}{k-1} \right) \frac{\partial p'}{\partial x'}^{k-1}$$

$$\frac{\partial u'}{\partial t'} + \left(\frac{\sqrt{\frac{gh_o}{n-1}} t_w}{l_w} \right) u' \frac{\partial u'}{\partial x'} = - \left(\frac{\sqrt{\frac{gh_o}{n-1}} t_w}{l_w} \right) (n-1) \frac{\partial h'}{\partial x'}$$

3. Equation of Energy

$$\frac{\partial E'}{\partial t'} + \left(\frac{a_0 t_a}{l_a} \right) u' \frac{\partial E'}{\partial x'} + (k-1) p' \frac{\partial \left(\frac{1}{\rho'} \right)}{\partial t'} \\ - (k-1) \left(\frac{a_0 t_a}{l_a} \right) p' u' \frac{\partial \left(\frac{1}{\rho'} \right)}{\partial x'} = 0$$

$$\frac{\partial h'}{\partial t'} + \left(\frac{\sqrt{\frac{gh_o}{n-1}} t_w}{l_w} \right) u' \frac{\partial h'}{\partial x'} - \left(\frac{1}{n-1} \right) h'^{n-2} \frac{\partial (h'^{n-1})}{\partial t'} \\ - \left(\frac{1}{n-1} \right) \left(\frac{\sqrt{\frac{gh_o}{n-1}} t_w}{l_w} \right) h'^{n-2} u' \frac{\partial (h'^{n-1})}{\partial x'} = 0$$

4. Equations of Standing Waves

$$\frac{\partial^2 \xi}{\partial t^2} = - \frac{1}{k} a_0^2 \frac{\partial}{\partial x} \left[\left(\frac{p}{p_0} \right) - 1 \right]$$

$$\frac{\partial^2 \xi}{\partial t^2} = - \left(\frac{n-1}{n-2} \right) \left(\frac{gh_o}{n-1} \right) \frac{\partial}{\partial x} \left[\left(\frac{h}{h_o} \right)^{n-2} - 1 \right]$$

$$\frac{\partial^2 \xi}{\partial t^2} = a_0^2 \frac{\partial^2 \xi}{\partial x^2}$$

$$\frac{\partial^2 \xi}{\partial t^2} = \left(\frac{gh_o}{n-1} \right) \frac{\partial^2 \xi}{\partial x^2}$$

$$\frac{\partial^2}{\partial t^2} \left[\left(\frac{p}{p_0} \right) - 1 \right] = a_0^2 \frac{\partial^2}{\partial x^2} \left[\left(\frac{p}{p_0} \right) - 1 \right]$$

$$\frac{\partial^2}{\partial t^2} \left[\left(\frac{h}{h_o} \right)^{n-2} - 1 \right] = \left(\frac{gh_o}{n-1} \right) \frac{\partial^2}{\partial x^2} \left[\left(\frac{h}{h_o} \right)^{n-2} - 1 \right]$$

Gas Flow

$$\frac{\partial^2}{\partial t^2} \left[\left(\frac{\rho}{\rho_0} \right) - 1 \right] = a_0^2 \frac{\partial}{\partial x^2} \left[\left(\frac{\rho}{\rho_0} \right) - 1 \right]$$

$$a = \sqrt{K \frac{p}{\rho}} = \sqrt{KRT}$$

$$a_0 = \sqrt{K \frac{p_0}{\rho_0}} = \sqrt{KRT_0}$$

Water Flow

$$\frac{\partial^2}{\partial t^2} \left[\left(\frac{h}{h_0} \right)^{nh} - 1 \right] = \left(\frac{gh_0}{n+1} \right) \frac{\partial^2}{\partial x^2} \left[\left(\frac{h}{h_0} \right)^{n+1} - 1 \right]$$

$$C = \sqrt{\frac{gA}{b}} = \sqrt{\frac{gh}{n+1}}$$

$$C_0 = \sqrt{\frac{gA_0}{b_0}} = \sqrt{\frac{gh_0}{n+1}}$$

SUMMARY OF ANALOGOUS QUANTITIES

Summarizing the analogous terms, we have:

1. Local Speed of sound

$$a = \sqrt{KRT}$$

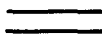


1. Local speed of wave

$$C = \sqrt{\frac{gh}{n+1}}$$

2. Local Mach number

$$M = \frac{u}{\sqrt{KRT}}$$

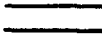


2. Local Mach number

$$M = \frac{u}{\sqrt{\frac{gh}{n+1}}}$$

3. Local density ratio

$$\left(\frac{\rho}{\rho_0}\right)$$



$$\left(\frac{h}{h_0}\right)^{n+1}$$

4. Local pressure ratio

$$\left(\frac{p}{p_0}\right)$$



4. Local water depth ratio

$$\left(\frac{h}{h_0}\right)^{n+2}$$

5. Local temperature ratio

$$\left(\frac{T}{T_0}\right)$$



$$\left(\frac{h}{h_0}\right)$$

6. Flow similarity number

$$\left(\frac{l_a}{a_0 t_a}\right)$$



6. Flow similarity number

$$\frac{l_w}{\sqrt{\frac{gh_0}{n+1}} t_w}$$

7. Function of gas specific heat ratio

$$\left(\frac{1}{k-1}\right)$$



$$(n+1)$$

7. Function of channel crosssection exponent

The last condition is the one the water channel crosssection must possess in order to represent a gas flow of desired specific heat ratio K.

DISCUSSIONS

The relationship $\left(\frac{1}{k-1}\right) = (n+1)$ shows that change of the shape of the crossection changes the values of K. For ordinary gas problems, the following values of K are interesting:

	Flows	K	n	Equation of Channel Crossection	Shape of Channel Crossection	Flows
1.	$P = c$	0	-2	$y^2z = c$	hyperbolic	isopiestic
2.	$V = c$	∞	-1	$yz = c$	hyperbolic	isometric
3.	$T = c$	1	∞	indeterminate	indeterminate	isothermal
4.	$\frac{p}{\rho k} = c$	1.4	1.5	$z = cy^{1.5}$	parabolic	isentropic
5.	$\frac{p}{\rho^{1.5}} = c$	1.5	1.0	$z = cy$	triangular	approximate isentropic
6.	$\frac{p}{\rho^2} = c$	2.0	0	$z = c$	rectangular	classical results

It is also interesting to see that if $n = 0$, the shape of the crossection is in rectangular form, and the present analogical results are exactly reduced to those given in the two dimensional steady flow case (classical results);

$$\left(\frac{p}{p_0}\right) = \left(\frac{h}{h_0}\right)^2, \quad \left(\frac{\rho}{\rho_0}\right) = \left(\frac{h}{h_0}\right), \quad \left(\frac{T}{T_0}\right) = \left(\frac{h}{h_0}\right), \quad a = \sqrt{K \frac{p}{\rho}}, \quad \left(\frac{1}{k-1}\right) = 1. \quad c = \sqrt{gh}$$

Because the velocity in a water channel can be made as small as one thousandth or less of those occurring in a gas stream, according to the analogous relationship of

$$\text{sound velocity} = \sqrt{K \frac{p}{\rho}} \quad \text{wave velocity} = \sqrt{\frac{gh}{n-1}}$$

the time scale can correspondingly be lengthened. This makes hydraulic analogue a relatively easy way for observation and study of transient effects in gas dynamics. The slow motion can even be seen by eye. This

feature is particularly useful for studies such as unsteady flow in ducts, traveling shocks and unsteady flow such as occurring in wave engines and might also be useful for study transient phenomena such as occurring during the starting of a diffuser and the stability of a diffuser during operation.

It is the purpose of this presentation to brief the "one dimensional unsteady hydraulic analogue" in addition to the classical "two dimensional steady hydraulic analogue" as possible tools for the study of gasdynamics by the "water table method".

APPENDIX A

Discussion on the Assumption that the Velocity is constant over the whole crosssection

Consider the surface s , which encloses a volume V , fixed in space. The law of conservation of energy requires that the difference in the rate of supply of energy to the volume V and the rate at which energy goes out through s must be the net rate of increase of energy in the volume V . Let U be the total energy per unit mass, then we have immediately:

$$-\int_s U \rho u_j n_j ds = \frac{\partial}{\partial t} \int_V U \rho dv$$

By Green's theorem

$$\int_s A n_j ds = \int_V \frac{\partial A}{\partial x_j} dv$$

to transform the surface integral into volume integral then

$$\int_V \left\{ -\frac{\partial}{\partial x_j} (U \rho u_j) - \frac{\partial}{\partial t} (U \rho) \right\} dv = 0$$

Since V is arbitrarily chosen the integrand itself must be zero.

Therefore,

$$\frac{\partial}{\partial x_j} (U \rho u_j) + \frac{\partial}{\partial t} (U \rho) = 0$$

Expanding and subtracting continuity equation, we have,

$$\frac{\partial}{\partial x_j} (U \rho u_j) + \frac{\partial}{\partial t} (U \rho) = \rho \left[\frac{\partial U}{\partial t} + u_j \frac{\partial U}{\partial x_j} \right] = 0$$

In the present case of one dimensional unsteady incompressible flow, this becomes

$$\frac{\partial}{\partial t} \left[\frac{\rho}{2} u^2 + p + \rho g y \right] + u \frac{\partial}{\partial x} \left[\frac{\rho}{2} u^2 + p + \rho g y \right] = 0$$

now if we assume that the vertical acceleration of the water is negligible compared with the acceleration of gravity, and the pressure at a point of the field of flow depends on the vertical distance under the free surface at that point. In other words,

$$p = \rho g (h - y)$$

Substituting this into above equation

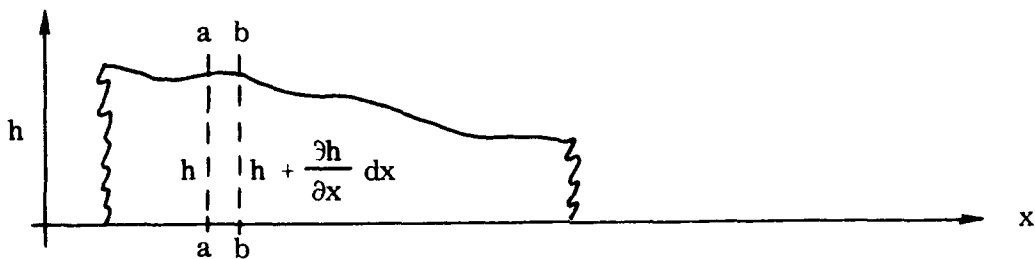
$$\frac{\partial}{\partial t} \left[\rho \frac{u^2}{2} + \rho g (h - y) + \rho gy \right] + u \frac{\partial}{\partial x} \left[\rho \frac{u^2}{2} + \rho g (h - y) + \rho gy \right] = 0$$

Therefore,

$$\frac{\partial}{\partial t} \left(\frac{u^2}{2} + gh \right) + u \frac{\partial}{\partial x} \left(\frac{u^2}{2} + gh \right) = 0$$

Since the equation does not contain the coordinate "y", therefore the velocity (the particle to be considered is arbitrary "y" distance above horizontal bottom) is constant over the entire depth of y. In other words the velocity is constant over the entire cross-section and is a function of h only.

APPENDIX B



Consider the volume between a - a and b - b which are dx apart.

In order to help the derivation of the volume integral between a - a and b - b, an enlarged sketch is drawn on the next page. Now referring to the sketch, the volume is one which is generated by moving the plane section of area A_x perpendicular to $0x$ from $x = 0$ to $x = 1$.

So

$$v = \int_0^l A_x dx$$

where A_x is a function of x . Assuming the surface change between section a - a and b - b is straight, because they are only dx apart in this treatment. Then from the sketch

$$y = \frac{h_2 - h_1}{l} x + h_1$$

$$dy = \frac{h_2 - h_1}{l} dx$$

$$\begin{aligned} v &= \int_0^l y^n dy dx \\ &= \int_0^l \frac{y^{n+1}}{n+1} dx \\ &= \int_0^l \left(\frac{y^{n+1}}{n+1} \right) \left(\frac{l}{h_2 - h_1} \right) dy \\ &= \frac{l}{(h_2 - h_1) (n+1) (n+2)} [h_1^{n+2} - h_2^{n+2}] \end{aligned}$$

Applying the result to the volume between $a - a$ and $b - b$ by using notations shown in the instantaneous flow diagram; then we have

$$h_1 = h$$

$$h_2 = h + \frac{\partial h}{\partial x} dx$$

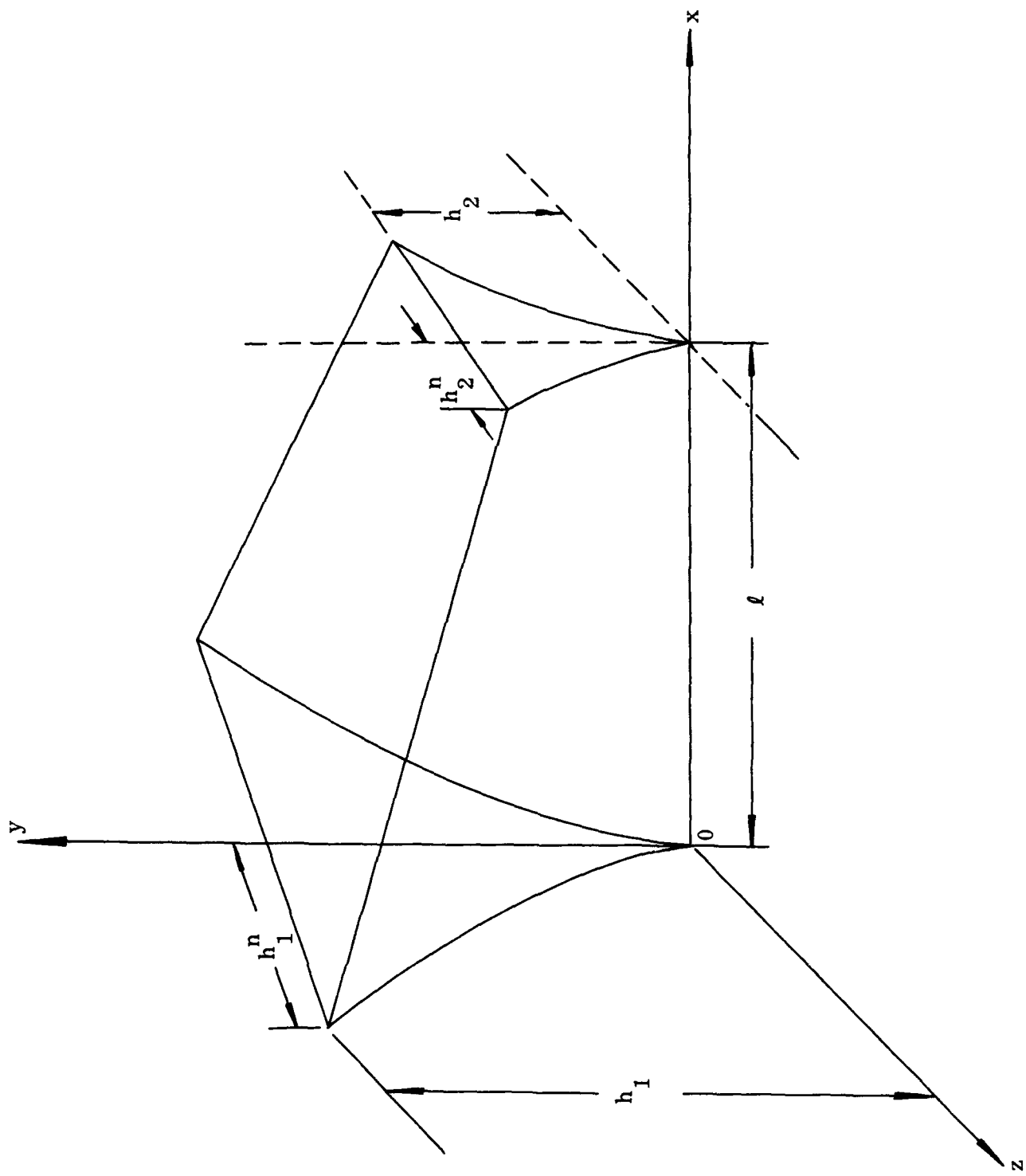
$$\ell = dx$$

$$v = \frac{dx [h^{n+2} - (h + \frac{\partial h}{\partial x} dx)^{n+2}]}{[\frac{\partial h}{\partial x} dx - h] (n+1) (n+2)}$$

$$v = \frac{[h^{n+2} - (h + \frac{\partial h}{\partial x} dx)^{n+2}]}{(\frac{\partial h}{\partial x}) (n+1) (n+2)}$$

therefore the mass between $a - a$ and $b - b$ is

$$\rho v = \rho \frac{[h^{n+2} - (h + \frac{\partial h}{\partial x} dx)^{n+2}]}{\frac{\partial h}{\partial x} (n+1) (n+2)}$$



APPENDIX C

Derivation of Equations of Standing Waves

In order to make the hydraulic analogy more clear for one dimensional unsteady flow, it is best to check further the mathematical similarities of fundamental wave equations in this appendix. The gas wave is considered to be set up in a pipe filled with gas. The water wave is considered to be set up in an open horizontal channel filled with water. In both cases, the pipe and the channel are in a constant crosssection, and the waves are set up in the fluid medium, while the fluid are considered in no motion except the small oscillations about their equilibrium positions. In the analysis, only the simple equations of wave formation produced by some simple causes are considered, since otherwise the equations would be too complicated and difficult to operate. It is believed that the analogy of waves, which exist in these simple equations will also exist in complicated wave mechanisms. From this point of view, the following simple equations were derived and compared.

1. Equation of continuity

(a) Air waves:

Consider the air in a straight pipe of uniform crosssection of area S as shown in figure.

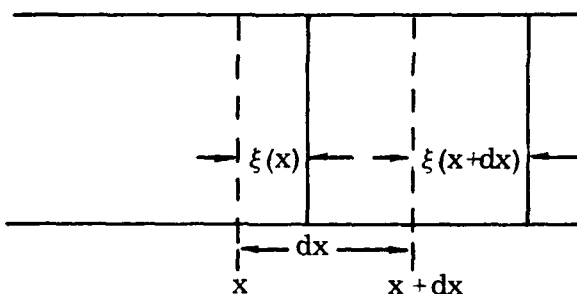


Fig (a)

When a sound wave (or any elastic wave) passes through the pipe, the planes at different points along the pipe will be displaced from their equilibrium positions back and forth along the pipe. This displacement depends on both t and x , the gas ahead of one plane will always be ahead of that plane, the gas between two planes will always be between these two planes; that means gas particles already on the same plane will remain on the same plane which the sound wave penetrates. Now refer to figure (a) and examine two planes which at equilibrium are at the distance x and $x + dx$. The gas between them has a density ρ_0 , so the mass is $\rho_0 S dx$. When the planes are displaced to the dotted position, the mass between them will not be changed, but the volume is changed due to the displacement of one plane being $\xi(x)$ and that of the other being $\xi(x + dx) = \xi(x) + \frac{\partial \xi}{\partial x} dx$, and hence the density changed to ρ in order to keep mass constant. Therefore the equation of continuity is:

$$\rho S [dx + \xi(x + dx) - \xi(x)] = \rho [S dx + S \frac{\partial \xi}{\partial x} dx] = \rho_0 S dx \quad (1)$$

let the relative change in density be $\delta(x, t)$

where

$$\delta = \frac{\rho - \rho_0}{\rho_0} \quad \rho = \rho_0 (1 + \delta) \quad (2)$$

substituting (2) into (1), one obtains

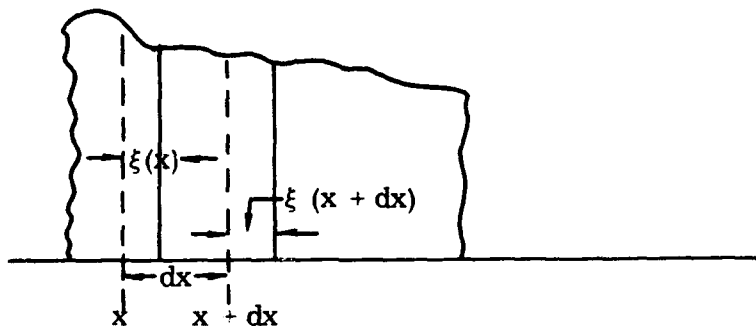
$$\begin{aligned} \rho_0 (1 + \delta) S dx (1 + \frac{\partial \xi}{\partial x}) &= S \rho_0 dx \\ (1 + \delta) (1 + \frac{\partial \xi}{\partial x}) &= 1 \end{aligned} \quad (3)$$

Since the change of density and displacement is small, the product of two small quantities $\delta \frac{\partial \xi}{\partial x}$ may be neglected.

$$1 + \delta + \frac{\partial \xi}{\partial x} = 1$$

$$\delta = -\frac{\partial \xi}{\partial x} \quad (4)$$

(b) Water waves



Consider two planes perpendicular to the length of the channel, which move with the fluid, and therefore always contain the same particles, and which before the fluid was disturbed were at a distance dx apart; at time t , their distance apart will have become

$$dx + \xi(x + dx) - \xi(x) = dx + \xi(x) + \frac{\partial \xi}{\partial x} dx - \xi(x) = dx + \frac{\partial \xi}{\partial x} dx$$

but the quantity of fluid between them will be unaltered and therefore by equation of continuity, one obtains

$$\frac{h_0^{n+1}}{n+1} dx = (dx + \frac{\partial \xi}{\partial x} dx) \frac{(h_0 + \eta)^{n+1}}{n+1}$$

here h_0 = water height at undisturbed condition

η = change of elevation due to disturbance with reference to h_0 , it is equal to $(h - h_0)$, here h is the instantaneous water height after disturbance.

$$(1 + \frac{\partial \xi}{\partial x}) (1 + \frac{\eta}{h_0})^{n+1} = 1 \quad (5)$$

Comparing (5) with (3), one obtains

$$(1 + \delta) = (1 + \frac{\eta}{h_0})^{n+1}$$

2. Equation of thermodynamics and equation of hydraulics

(a) Air waves: - equation of thermodynamics

$$\frac{dp}{p} + \frac{dv}{v} = \frac{dT}{T}$$

Now if $V = \text{constant}$ $dV = 0$ then $dp = (\frac{p}{T}) dT$

$$dQ = (\frac{\partial Q}{\partial p}) dp = (\frac{\partial Q}{\partial p}) \frac{p}{T} dT$$

$$C_v = (\frac{dQ}{dT})_v = (\frac{\partial Q}{\partial p}) \left(\frac{p}{T}\right)$$

Similarly

$$(\frac{\partial Q}{\partial p}) = C_v \left(\frac{T}{p}\right)$$

$$(\frac{\partial Q}{\partial v}) = C_p \left(\frac{T}{v}\right)$$

for adiabatic change between volume and pressure $dQ = 0$

$$dQ = (\frac{\partial Q}{\partial v}) dv + (\frac{\partial Q}{\partial p}) dp = T (C_p \frac{dv}{v} + C_v \frac{dp}{p}) = 0$$

$$C_p \frac{dv}{v} = - C_v \frac{dp}{p} \quad (6)$$

Now consider the gas in pipe contained between the planes originally at x and $x + dx$, the volume of the gas is Sdx and the change in volume is $S \frac{\partial \xi}{\partial x} dx$.

Since

$$S dx - S [dx + \xi(x) + d\xi] = S dx - S [dx + \xi(x) + \frac{\partial \xi}{\partial x} dx - \xi(x)] = -S \frac{\partial \xi}{\partial x} dx$$

the pressure is P_0 , the change in pressure is p (excess pressure over P_0). Applying the equation (6) of thermodynamics one obtains

$$\frac{C_p S \frac{\partial \xi}{\partial x} dx}{S dx} = -C_v \left(\frac{p}{P_0} \right)$$

$$p = -K P_0 \left(\frac{\partial \xi}{\partial x} \right) \quad (7)$$

substituting (4) into (7), one obtains

$$p = K P_0 \delta$$

$$\frac{\partial p}{\partial x} = K P_0 \frac{\partial \delta}{\partial x} \quad (8)$$

(b) Water waves - equation of hydraulics

$$F = \int_0^h \rho g (h - y) Z dy = \frac{\rho g h^{n+2}}{(n+1)(n+2)} = \frac{\rho g}{(n+1)(n+2)} (h_0 + \eta)^{n+2}$$

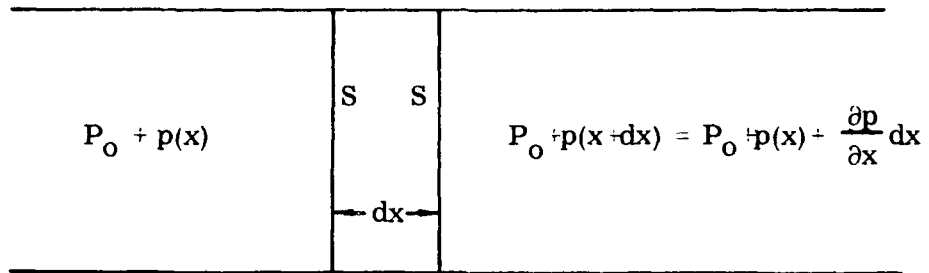
$$\frac{\partial F}{\partial x} = (n+2) \frac{\rho g}{(n+1)(n+2)} (h_0 + \eta)^{n+1} \frac{\partial \eta}{\partial x}$$

$$= \frac{\rho g}{(n+1)} (h_0 + \eta)^{n+1} \frac{\partial \eta}{\partial x} \quad (9)$$

This is the hydraulics equation of the relation between change of hydrostatic force on the volume and change of water height of the volume.

3. Equation of motion:

(a) Air waves:



The equation of motion can be written immediately

$$S[P_0 + p(x)] - S[P_0 + p(x) + \frac{\partial p}{\partial x} dx] - \rho_0 S dx \frac{\partial^2 \xi}{\partial t^2}$$

where ξ is the displacement of the plane along the pipe

$$\rho_0 \frac{\partial^2 \xi}{\partial t^2} = - \frac{\partial p}{\partial x} \quad (10a)$$

$$\frac{\partial^2 \xi}{\partial t^2} = - \frac{1}{K} a_0^2 \frac{\partial \left(\frac{p}{P_0} \right)}{\partial x}$$

putting it in non-dimensional form as before

$$\frac{\partial^2 \xi'}{\partial t'^2} = - \frac{1}{K} \left(\frac{a_0 t_a}{l_a} \right) \frac{\partial p'}{\partial x'} \quad (10)$$

(b) Water waves:

$$\rho \left(\frac{h_0}{n+1} \right)^{k+1} dx \frac{\partial^2 \xi}{\partial t^2} = - \frac{\partial F}{\partial x} dx \quad (11)$$

here $\frac{\partial^2 \xi}{\partial t^2}$ is the acceleration of the small volume between two sections dx apart in undisturbed state, and $\frac{\partial F}{\partial x} dx$ is the differential change of the hydrostatic force on the volume.

Substituting (9) into (11) one obtains

$$\frac{\partial^2 \xi}{\partial t^2} = -g \left(1 + \frac{\eta}{h_0}\right)^{n+1} \frac{\partial \eta}{\partial x} \quad (12a)$$

$$\begin{aligned} &= -\frac{gh_0}{n+2} \frac{\partial}{\partial x} \left[\left(1 + \frac{\eta}{h_0}\right)^{n+2} - 1 \right] \\ &= -\left(\frac{gh_0}{n+1}\right) \left(\frac{n+1}{n+2}\right) \frac{\partial}{\partial x} \left[\left(1 + \frac{\eta}{h_0}\right)^{n+2} - 1 \right] \end{aligned}$$

putting it into non-dimensional form as before

$$\frac{\partial^2 \xi'}{\partial t'^2} = -\left(\frac{\sqrt{\frac{gh_0}{n+1}} t_w}{\ell_w}\right) \left(\frac{n+1}{n+2}\right) \frac{\partial}{\partial x'} \left[\left(1 + \frac{\eta}{h_0}\right)^{n+2} - 1 \right] \quad (12)$$

comparing (12) with (10) one obtains immediately

$$\left(\frac{a_0 t_w}{\ell_w}\right) = \left(\frac{\sqrt{\frac{gh_0}{n+1}} t_w}{\ell_w}\right) \quad K = \frac{n+1}{n-2}$$

$$\frac{p}{P_0} = \left[\left(1 + \frac{\eta}{h_0}\right)^{n+2} - 1 \right]$$

4. Equation of waves

(a) Air waves:

Substituting (4) into (8) one obtains:

$$\frac{\partial p}{\partial x} = -K P_0 \frac{\partial^2 \xi}{\partial x^2} \quad (13)$$

Substituting (13) into (10a)

$$\frac{\partial^2 \xi}{\partial t^2} = a_0^2 \frac{\partial^2 \xi}{\partial x^2} \quad (14)$$

Similarly

$$\frac{\partial^2 p}{\partial t^2} = a_0^2 \frac{\partial^2 p}{\partial x^2} \quad (15)$$

$$\frac{\partial^2 \delta}{\partial t^2} = a_0^2 \frac{\partial^2 \delta}{\partial x^2} \quad (16)$$

Equations (14), (15) and (16) are the fundamental wave equations.

(b) Water waves:

Between (5) and (12a) either η or ξ can be eliminated out, the result in terms of ξ is simpler, so partial differentiation of (5) with respect to x gives;

$$\frac{-\frac{\partial^2 \xi}{\partial x^2}}{\left(1 + \frac{\partial \xi}{\partial x}\right)^2} = (n+1) \left(1 + \frac{\eta}{h_0}\right) \frac{1}{h_0} \frac{\partial \eta}{\partial x} \quad (17)$$

substituting (17) into (12a), one obtains

$$\frac{\partial^2 \xi}{\partial t^2} = \left(\frac{gh_0}{n+1}\right) \left(1 + \frac{\eta}{h_0}\right) \frac{\frac{\partial^2 \xi}{\partial x^2}}{\left(1 + \frac{\partial \xi}{\partial x}\right)^2}$$

substituting (5) into the above equation

$$\frac{\partial^2 \xi}{\partial t^2} = \left(\frac{gh_0}{n+1}\right) \frac{\frac{\partial^2 \xi}{\partial x^2}}{\left(1 + \frac{\partial \xi}{\partial x}\right) \frac{2n+3}{n+1}}$$

From equation (5)

$$\left(1 + \frac{\partial \xi}{\partial x}\right) = \left(1 + \frac{\eta}{h_0}\right)^{n+1}$$

Therefore

$$\frac{\partial \xi}{\partial x} \approx (n+1) \left(\frac{\eta}{h_0}\right)$$

Since $\frac{\eta}{h_0}$ is a small quantity, $\frac{\partial \xi}{\partial x}$ is also small in comparison to 1.

$$(1 + \frac{\partial \xi}{\partial x})^{\frac{2n+3}{n+1}} \approx 1$$

$$\frac{\partial^2 \xi}{\partial t^2} = (\frac{gh_0}{n+1}) \frac{\partial^2 \xi}{\partial x^2} \quad (18)$$

Similarly

$$\frac{\partial^2}{\partial t^2} [(1 + \frac{\eta}{h_0})^{n+2} - 1] = (\frac{gh_0}{n+1}) \frac{\partial^2}{\partial x^2} [(1 + \frac{\eta}{h_0})^{n+2} - 1] \quad (19)$$

$$\frac{\partial^2}{\partial t^2} [(1 + \frac{\eta}{h_0})^{n+1} - 1] = (\frac{gh_0}{n+1}) \frac{\partial^2}{\partial x^2} [(1 + \frac{\eta}{h_0})^{n+1} - 1] \quad (20)$$

Equations (19) and (20) can be proven, since the differential equations are satisfied by the functions of η found in those brackets of (19) and (20). The proof is as follows:

substituting (5) into (19) one obtains

$$\frac{\partial^2}{\partial t^2} [(1 + \frac{\partial \xi}{\partial x})^{-\frac{n+2}{n+1}} - 1] = (\frac{gh_0}{n+1}) \frac{\partial^2}{\partial x^2} [(1 + \frac{\partial \xi}{\partial x})^{-\frac{n+2}{n+1}} - 1]$$

$$\frac{\partial^2 \xi}{\partial t^2} = (\frac{gh_0}{n+1}) \frac{\partial^2 \xi}{\partial x^2}$$

The result is the same as equation (18) which has been proved already.

Since equation (18) is satisfied by ξ , equation (19) is satisfied by η .

Similarly equation (20) may be proved. Comparing equations (18), (19), and (20) with equations (14), (15) and (16) respectively after putting them into nondimensional form, one obtains again.

$$\frac{p}{P_0} = [(1 + \frac{\eta}{h_0})^{n+2} - 1]$$

$$\delta = [(1 + \frac{\eta}{h_0})^{n+1} - 1]$$

5. Equation of wave propagation velocity

(a) Air waves:

The wave propagation velocity in air is well known as the sound velocity in air which can be expressed as

$$a^2 = \frac{dp}{d\rho} = K \frac{p}{\rho}$$

so the wave propagation velocity in undisturbed stream is

$$a_0^2 = K \frac{p_0}{\rho_0}$$

(b) Water waves:

The wave propagation velocity of water in an open channel of a constant crosssection of any shape with a straight horizontal bottom was derived mathematically by J. McCowan. *

$$c^2 = \frac{gA}{b} \quad (21)$$

where A = the area of the crosssection

b = the breadth at the free surface

Applying equation (21) to the crosssection $Z = y^n$. Then

$$c^2 = \frac{g \left(\frac{h}{n+1} \right)^{n+1}}{h^n} = \left(\frac{gh}{n+1} \right)$$

so the wave propagation velocity in the undisturbed stream is

$$c_0^2 = \left(\frac{gh_0}{n+1} \right)$$

* J. McCowan: p. 258, Philosophical Magazine, Vol. 33, 1892.

In this appendix the following equations have been derived.

Equations of Gas

1. Equations of continuity:

$$(1 + \delta) \left(1 + \frac{\partial \xi}{\partial x} \right) = 1$$

2. Equation of thermodynamics:

$$\frac{\partial p}{\partial x} = K P_0 \frac{\partial \delta}{\partial x}$$

3. Equation of motion:

$$\frac{\partial^2 \xi}{\partial t'^2} = -\frac{1}{K} \left(\frac{a_0 t_a}{l_a} \right)^2 \frac{\partial p'}{\partial x'}$$

4. Equation of wave:

$$\frac{\partial^2 \xi}{\partial t^2} = a_0^2 \frac{\partial^2 \xi}{\partial x^2}$$

$$\frac{\partial^2 p}{\partial t^2} = a_0^2 \frac{\partial^2 p}{\partial x^2}$$

$$\frac{\partial^2 \delta}{\partial t^2} = a_0^2 \frac{\partial^2 \delta}{\partial x^2}$$

5. Equation of wave propagation velocity:

$$a = \sqrt{K \frac{p}{\rho}}$$

Equations of Water

1. Equation of continuity:

$$\left(1 + \frac{\eta}{h_0} \right)^{n+1} \left(1 + \frac{\partial \xi}{\partial x} \right) = 1$$

2. Equation of hydraulics:

$$\frac{\partial F}{\partial x} = \frac{\rho g}{(n+1)} (h_0 + \eta)^{n+1} \frac{\partial \eta}{\partial x}$$

3. Equation of motion:

$$\frac{\partial^2 \xi}{\partial t^2} - \left(\frac{n-1}{n+2} \right) \left(\frac{\sqrt{\frac{gh_0}{n-1}} t_w}{l_w} \right)^2 \frac{\partial}{\partial x} \left[\left(1 + \frac{\eta}{h_0} \right)^{n+2} - 1 \right]$$

4. Equation of wave:

$$\frac{\partial^2 \xi}{\partial t^2} = \left(\frac{gh_0}{n-1} \right) \frac{\partial^2 \xi}{\partial x^2}$$

$$\frac{\partial^2}{\partial t^2} \left[\left(1 + \frac{\eta}{h_0} \right)^{n+2} - 1 \right] = \left(\frac{gh_0}{n-1} \right) \frac{\partial^2}{\partial x^2} \left[\left(1 + \frac{\eta}{h_0} \right)^{n+2} - 1 \right]$$

$$\frac{\partial^2}{\partial t^2} \left[\left(1 + \frac{\eta}{h_0} \right)^{n-1} - 1 \right] = \left(\frac{gh_0}{n+1} \right) \frac{\partial^2}{\partial x^2} \left[\left(1 + \frac{\eta}{h_0} \right)^{n-1} - 1 \right]$$

5. Equation of wave propagation velocity:

$$c = \sqrt{\frac{gh}{n-1}}$$

Comparison of the corresponding equations in the two cases show that these corresponding equations have the same forms respectively. From these we may derive the conditions for the analogy that the following analogous magnitudes hold valid for the two cases:

$$\left(1 - \delta \right) \approx \left(1 + \frac{\eta}{h_0} \right)^{n-1}$$

$$\frac{a_0 t_a}{l_a} = \frac{\sqrt{\frac{gh_0}{n-1}} t_w}{l_w}$$

$$\frac{1}{k} = \frac{n-1}{n+2}$$

$$\frac{p}{P_0} = \left[\left(1 + \frac{\eta}{h_0} \right)^{n+2} - 1 \right] \quad *$$

$$\delta = \left[\left(1 + \frac{\eta}{h_0} \right)^{n+1} - 1 \right]$$

* Note here the symbol 'p' is the excess pressure.

NOMENCLATURE

A = Crossectional area of channel
a = Local velocity of sound = $\sqrt{K \frac{p}{\rho}}$
 C_p = specific heat at constant pressure
 C_v = specific heat at constant volume
C = local wave propagation velocity = $\sqrt{\frac{gh}{n+1}}$
h = local water depth of flow
k = ratio of specific heats = $\frac{C_p}{C_v}$
 l = some characteristic length in flow
n = exponent in relation $Z = y^n$, Z = width of channel, y = height of channel
P = local pressure
 t_a = some characteristic time in gas flow
 t_w = some characteristic time in water flow
t = time
T = local temperature in gas flow
u = local velocity of flow in x direction

Greek letter

ρ = local density of fluid
 δ = relative change in density = $\frac{\rho - \rho_0}{\rho_0}$
 ξ = a function of x, which represents the displacement of the plane disturbed by the wave motion
 η = change of elevation of water due to disturbance with reference to h_0

Subscripts

a = air flow
w = water flow
o = undisturbed condition or the initial equilibrium condition

TWO DIMENSIONAL STEADY FLOW

ANALOGOUS FLOWS

GAS FLOW

AN IRROTATIONAL
ISENTROPIC FLOW
OF PERFECT GAS
HAVING A RATIO OF
SPECIFIC HEATS OF

$$K = \frac{C_p}{C_v} = 2$$

WATER FLOW

AN INCOMPRESSIBLE
FRICTIONLESS FLOW
OF WATER IN AN OPEN
HORIZONTAL CHANNEL
OF A RECTANGULAR
CROSSECTION

ANALOGOUS EQUATIONS
TWO DIMENSIONAL STEADY FLOW
(BY ERNST PREISWERK UNDER DIRECTION OF J. ACKERET)

GAS FLOW

WATER FLOW

$$\text{CONTINUITY} \quad u' \frac{\partial \rho'}{\partial x} + \rho' \frac{\partial u'}{\partial x} + v' \frac{\partial \rho'}{\partial y} + v' \frac{\partial v'}{\partial y} = 0 \quad u' \frac{\partial u'}{\partial x} + v' \frac{\partial v'}{\partial x} + u' \frac{\partial u'}{\partial y} + v' \frac{\partial v'}{\partial y} = 0$$

$$\text{MOMENTUM} \quad u' \frac{\partial u'}{\partial x} + v' \frac{\partial u'}{\partial y} = - \left(\frac{1}{K-1} \right) \frac{\partial p'}{\partial x} \quad u' \frac{\partial u'}{\partial x} + v' \frac{\partial u'}{\partial y} = - \frac{x e}{y} \quad u' \frac{\partial u'}{\partial x} + v' \frac{\partial u'}{\partial y} = - \frac{x e}{y}$$

$$u' \frac{\partial v'}{\partial x} + v' \frac{\partial v'}{\partial y} = \left(\frac{1}{K-1} \right) \frac{\partial p'}{\partial y} \quad u' \frac{\partial v'}{\partial x} + v' \frac{\partial v'}{\partial y} = - \frac{y e}{x} \quad u' \frac{\partial v'}{\partial x} + v' \frac{\partial v'}{\partial y} = - \frac{y e}{x}$$

$$\text{ENERGY} \quad \frac{u'^2}{u_{\text{MAX}}^2} = 1 - \left(\frac{h_0}{h} \right)^2 \quad \frac{u'^2}{u_{\text{MAX}}^2} = 1 - \left(\frac{h_0}{h} \right)$$

$$\text{HERE} \quad u' = \frac{u}{a_0}, \quad v' = \frac{v}{a_0}, \quad \rho' = \frac{\rho}{\rho_0}, \quad p' = \frac{p}{p_0}, \quad u' = \frac{u}{\sqrt{gh_0}}, \quad v' = \frac{v}{\sqrt{gh_0}}$$

a_0 = SONIC VELOCITY $\sqrt{gh_0}$ = WAVE VELOCITY

ANALOGOUS QUANTITIES

(TWO DIMENSIONAL STEADY FLOW)

GAS FLOW

WATER FLOW

$$\begin{aligned}
 \rho' \left(\frac{\rho}{\rho_0} \right) &= h' \left(\frac{h}{h_0} \right) \\
 \rho'^{1-k} \left(\left(\frac{\rho}{\rho_0} \right)^{k-1} \right) &= h'^{1-k} \left(\frac{h}{h_0} \right) \\
 r' \left(\frac{r}{r_0} \right) &= h' \left(\frac{h}{h_0} \right) \\
 a_0 \text{ (SONIC VELOCITY)} &\sim \sqrt{gh_0} \text{ (WAVE VELOCITY)} \\
 \left(\frac{1}{k-1} \right) &= 1
 \end{aligned}$$

↑ ONLY "K=2" SATISFIES THIS CONDITION
 THEREFORE, THE LAST CONDITION SAYS THAT THE FLOW OF WATER
 IS COMPARABLE WITH THE FLOW OF A GAS HAVING A RATIO OF
 SPECIFIC HEAT K=2 ONLY.

ONE DIMENSIONAL UNSTEADY FLOW ANALOGOUS FLOW

GAS FLOW

AN ISENTROPIC FLOW OF
PERFECT GAS HAVING A
RATIO OF SPECIFIC HEATS
OF

$$K = \frac{C_p}{C_v} = \text{ANY VALUE}$$

WATER FLOW
AN INCOMPRESSIBLE FRICTION-
LESS FLOW OF WATER IN AN
OPEN HORIZONTAL CHANNEL
OF A CROSS SECTION DES-
CRIBED BY THE EQUATION

$$Z = \gamma^n \text{ and } n = \frac{2-K}{K-1}$$



EQUATION OF CONTINUITY

$$\frac{\text{GAS FLOW}}{\text{WATER FLOW}} = u' \frac{\partial \rho'}{\partial x'} + \rho' \frac{\partial u'}{\partial x'} + \left(\frac{\rho_a}{a_o t_a} \right) \frac{\partial \rho'}{\partial t'} = 0 \quad u' \frac{\partial h'^{(n+1)}}{\partial x'} + h'^{(n+1)} \left(\frac{\rho_w}{g h_a t_w} + \left(\frac{\rho_w}{g h_a t_w} t_w \right) \frac{\partial h'^{(n+1)}}{\partial t'} \right) = 0$$

ANALOGOUS QUANTITIES

$$\begin{aligned} \text{GAS FLOW} &= u' \left(= \frac{u}{\frac{a_o}{t_a}} \right) & \text{WATER FLOW} &= u' \left(= \frac{u}{\sqrt{\frac{a_o}{t_a}}} \right) \\ \rho' \left(= \frac{\rho_o}{t_o} \right) &= \rho' \left(= \frac{\rho_o}{t_o} \right) & h' \left(= \frac{h_o}{t_o} \right) &= h' \left(= \frac{h_o}{\sqrt{\frac{a_o}{t_a}} t_w} \right) \\ \left(\frac{\rho_a}{a_o t_a} \right) &= \left(\frac{\rho_a}{a_o t_a} \right) & \left(- \frac{\rho_w}{g h_a t_w} \right) &= \left(- \frac{\rho_w}{g h_a t_w} t_w \right) \end{aligned}$$

EQUATION OF CONTINUITY

GAS FLOW

WATER FLOW

$$u' \frac{\partial \rho'}{\partial x'} + \rho' \frac{\partial u'}{\partial x'} + \left(\frac{l_a}{a_0 t_a} \right) \frac{\partial \rho'}{\partial t'} = 0 \quad u' \frac{\partial h'}{\partial x'} + h^{(n+1)} \frac{\partial u'}{\partial x'} + \left(\frac{l_w}{a_0 t_w} \right) \frac{\partial h^{(n+1)}}{\partial t'} = 0$$

HERE a_0 = SPEED OF SOUND

$$u' = \frac{u}{a_0}$$

$$u' = \frac{u}{\sqrt{\frac{gh_0}{n+1}}}$$

$\sqrt{\frac{gh_0}{n+1}}$ = SPEED OF WAVE PROPAGATION

$$\begin{aligned} \rho' &= \frac{\rho}{\rho_0} & h' &= \frac{h}{h_0} \\ x' &= \frac{x}{l_a} & x' &= \frac{x}{l_w} \\ t' &= \frac{t}{t_a} & t' &= \frac{t}{t_w} \end{aligned}$$

l = SOME CHARACTERISTIC LENGTH, CONSTANT
 t = SOME CHARACTERISTIC TIME, CONSTANT
 SUBSCRIPTS

a = GAS FLOW

w = WATER FLOW

0 = UNDISTURBED FLOW

EQUATION OF MOMENTUM

GAS FLOW

$$\frac{\partial u'}{\partial t} + \left(\frac{a_{ot_a}}{a_a} \right) u' \frac{\partial u'}{\partial x'} = - \left(\frac{a_{ot_a}}{a_a} \right) \left(\frac{1}{\kappa-1} \right) \frac{\partial p'}{\partial x'} \frac{\kappa-1}{\kappa} \frac{\partial u'}{\partial t'} + \left(\sqrt{\frac{g h_o}{\kappa-1}} t_w \right) u' \frac{\partial u'}{\partial x'} - \left(\sqrt{\frac{g h_o}{\kappa-1}} t_w \right) \left(n+1 \right) \frac{\partial h}{\partial x'}$$

HERE $\kappa = \frac{C_p}{C_v}$ $n = \text{EXponent in channel cross section equation}$

WATER FLOW

ADDITIONAL ANALOGOUS QUANTITIES

GAS FLOW

$$p' \frac{\kappa-1}{\kappa} \left(= \left[\frac{p}{p_o} \right] \frac{\kappa-1}{\kappa} \right) = h' \left(= \frac{h}{h_o} \right)$$

$$\xrightarrow{\frac{1}{\kappa-1}}$$

THE LAST CONDITION IS THE ONE THE WATER CHANNEL CROSS SECTION MUST POSSESS IN ORDER TO REPRESENT A GAS FLOW OF ANY VALUE OF SPECIFIC HEAT RATIO κ

EQUATION OF ENERGY

GAS FLOW

$$\frac{\partial E'}{\partial t'} + \left(\frac{a_0 \alpha_a}{\rho_a} \right) u' \frac{\partial E'}{\partial x'} + (k-1) \rho' \left[\frac{\partial \frac{1}{\rho'}}{\partial t'} + \left(-\frac{\alpha \alpha_a}{\rho_a} \right) u' \frac{\partial \frac{1}{\rho'}}{\partial x'} \right] = 0$$

WATER FLOW

$$\frac{\partial h'}{\partial t'} + \left(\sqrt{\frac{g h_w}{n+1}} t_w \right) u' \frac{\partial h'}{\partial x'} + \left(\frac{1}{n+1} \right) h' (n+2) \left[\frac{\partial \ln \frac{1}{n+1}}{\partial t'} + \left(\sqrt{\frac{g h_w}{n+1}} t_w \right) u' \frac{\partial \ln \frac{1}{n+1}}{\partial x'} \right] = 0$$

HERE $E = \text{INTERNAL ENERGY}$ $E' = \frac{E}{E_0} = \frac{C_v T}{C_v T_0} = \frac{T}{T_0} = \text{TEMPERATURE RATIO}$

ADDITIONAL ANALOGOUS QUANTITY GAS FLOW

$$\begin{aligned} E' & \left(= \frac{T}{T_0} \right) & h' & \left(= \frac{h}{h_0} \right) \\ a_0 & \left(= \sqrt{K R T_0} \right) & \sqrt{\frac{g h_w}{n+1}} & \sqrt{\frac{g h_w}{n+1}} \\ a & \left(= \sqrt{K R T} \right) & = & = \end{aligned}$$

EQUATION OF STANDING WAVES

GAS WAVES

$$\frac{\partial^2 \xi}{\partial t^2} = -\frac{1}{K} \alpha_0^2 \frac{\partial}{\partial x} \left[\left(\frac{P}{P_0} \right) - 1 \right]$$

$$\frac{\partial^2 \xi}{\partial t^2} = \alpha_0^2 \frac{\partial^2 \xi}{\partial x^2}$$

$$\frac{\partial^2}{\partial t^2} \left[\left(\frac{P}{P_0} \right) - 1 \right] = \alpha_0^2 \frac{\partial^2}{\partial x^2} \left[\left(\frac{P}{P_0} \right) - 1 \right]$$

$$\frac{\partial^2}{\partial t^2} \left[\left(\frac{\rho}{\rho_0} \right) - 1 \right] = \alpha_0^2 \frac{\partial^2}{\partial x^2} \left[\left(\frac{\rho}{\rho_0} \right) - 1 \right]$$

EQUATION OF STANDING WAVES

WATER WAVES

$$\frac{\partial^2 \xi}{\partial t^2} = - \binom{n+1}{n+2} \binom{gh_0}{n+1} \frac{\partial}{\partial x} \left[\left(\frac{h}{h_0} \right)^{n+2} - 1 \right]$$

$$\frac{\partial^2 \xi}{\partial t^2} = \binom{gh_0}{n+1} \frac{\partial^2 \xi}{\partial x^2}$$

$$\frac{\partial^2}{\partial t^2} \left[\left(\frac{h}{h_0} \right)^{n+2} - 1 \right] = \binom{gh_0}{n+1} \frac{\partial^2}{\partial x^2} \left[\left(\frac{h}{h_0} \right)^{n+2} - 1 \right]$$

$$\frac{\partial^2}{\partial t^2} \left[\left(\frac{h}{h_0} \right)^{n+1} - 1 \right] = \binom{gh_0}{n+1} \frac{\partial^2}{\partial x^2} \left[\left(\frac{h}{h_0} \right)^{n+1} - 1 \right]$$

HERE ξ = A FUNCTION OF x , WHICH REPRESENTS THE DISPLACEMENT OF THE PLANE DISTURBED BY THE WAVE MOTION

EQUATION OF WAVE PROPAGATION

GAS

$$a = \left(\frac{dp}{dp} \right)^{\frac{1}{2}} = \sqrt{K \frac{p}{\rho}} = \sqrt{KRT}$$

WATER

$$c = \left(\frac{2A}{b} \right)^{\frac{1}{2}} = \sqrt{\frac{2h}{n+1}} = \sqrt{\frac{gh}{n+1}}$$

c = LOCAL WAVE PROPAGATION SPEED

HERE a = LOCAL SPEED OF SOUND

b = LOCAL BREADTH AT THE FREE SURFACE

THE SPEED OF SOUND
EQUATION IS KNOWN

THE WAVE PROPAGATION VELOCITY OF
WATER IN AN OPEN CHANNEL OF A
CONSTANT CROSS SECTION OF ANY
SHAPE WITH A STRAIGHT HORIZON-
TAL BOTTOM WAS DERIVED IN
P. 258, PHILOSOPHICAL MAGAZINE
VOL. 33, 1892 BY J. McCOWAN.

SUMMARY OF ANALOGOUS QUANTITIES (ONE DIMENSIONAL UNSTEADY FLOW)

GAS FLOW

1. LOCAL SPEED OF SOUND $a = \sqrt{KgRT}$

2. LOCAL MACH NUMBER $M = \frac{u}{\sqrt{KgRT}}$

3. LOCAL DENSITY RATIO $(\frac{\rho}{\rho_0})$

4. LOCAL PRESSURE RATIO $(\frac{P}{P_0})$

5. LOCAL TEMPERATURE RATIO $(\frac{T}{T_0})$

6. FLOW SIMILARITY NUMBER $(\frac{\lambda a}{a_0 t_0})$

7. GAS SPECIFIC HEAT RATIO FUNCTION $(\frac{1}{K-1})$

WATER FLOW

1. LOCAL SPEED OF WAVE $\frac{u}{\sqrt{\frac{gh}{n+1}}}$
2. LOCAL MACH NUMBER $\sqrt{\frac{u}{\frac{gh}{n+1}}}$
3. LOCAL WATER DEPTH RATIO $(\frac{h}{h_0})^{n+2}$
4. LOCAL WATER DEPTH RATIO $(\frac{h}{h_0})^{n+1}$
5. LOCAL WATER DEPTH RATIO $(\frac{h}{h_0})^{n+1}$
6. FLOW SIMILARITY NUMBER $(\frac{\lambda w}{\frac{gh_0}{n+1} t_w})$
7. CHANNEL CROSS SECTION EXPONENT $(n+1)$

THE LAST CONDITION IS THE CONDITION THE WATER CHANNEL CROSS SECTION MUST POSSESS IN ORDER TO REPRESENT A GAS FLOW OF ANY SPECIFIC HEAT RATIO K DESIRED.

BASIC RELATIONSHIP

THE RELATIONSHIP $(\frac{1}{K-1}) = (n+1)$ OR $n = \frac{2-K}{K-1}$ SHOWS THAT
CHANGE OF THE SHAPE OF THE CROSS SECTION CHANGES

THE VALUE OF $K = \frac{C_p}{C_v}$

K	n	EQUATION OF CHANNEL CROSS SECTION	SHAPE OF CHANNEL CROSS SECTION
1.4	1.5	$Z = cy^{1.5}$	PARABOLIC
1.5	1.0	$Z = cy$	TRIANGULAR
2.0	0	$Z = c$	RECTANGULAR

SPECIAL CASE

IT IS INTERESTING TO NOTE THAT IF $K=2$ THEN n BECOMES 0 AND THE SHAPE IS RECTANGULAR. THE ANALOGOUS RESULTS ARE EXACTLY REDUCED TO THOSE GIVEN IN THE TWO DIMENSIONAL STEADY CASE; THEY ARE:

PRESENT ANALOGOUS RESULTS

$n=0$

TWO DIMENSIONAL STEADY RESULTS

$$\left(\frac{\rho}{\rho_0}\right) = \left(\frac{h}{h_0}\right)^{n+1} \quad \left(\frac{\rho}{\rho_0}\right) = \left(\frac{h}{h_0}\right)$$

$$\left(\frac{P}{P_0}\right) = \left(\frac{h}{h_0}\right)^{n+2} \quad \left(\frac{P}{P_0}\right) = \left(\frac{h}{h_0}\right)^2$$

$$\left(\frac{T}{T_0}\right) = \left(\frac{h}{h_0}\right) \quad \left(\frac{T}{T_0}\right) = \left(\frac{h}{h_0}\right)$$

$$\left(\frac{u_a}{a}\right) = \left(\frac{u_w}{gh}\right) \quad \left(\frac{u_a}{a}\right) = \left(\frac{u_w}{gh}\right)$$

$$\left(\frac{u_a}{a}\right) = \left(\frac{u_w}{gh}\right)$$

$$a (= \sqrt{KRT}) \sim \sqrt{\frac{gh}{n+1}} \quad a (= \sqrt{KRT}) \sim \sqrt{gh}$$

$$a (= \sqrt{KRT}) \sim \sqrt{gh}$$

A TYPICAL PROBLEM (FOR EXPERIMENTAL MODEL)

THE DYNAMIC BEHAVIOR, (ONE DIMENSIONAL UNSTEADY MOTION) OF AIR INSIDE A STRAIGHT INDUCTION SYSTEM OF A SINGLE CYLINDER FOUR STROKE RECIPROCATING ENGINE, SET UP BY THE PERIODIC OPENING AND CLOSING OF THE INTAKE VALVE IN CONJUNCTION WITH THE PISTON MOTION, IS A TYPICAL EXAMPLE WHICH WAS STUDIED BY THE HYDRAULIC ANALOGY.

GAS FLOW THE EQUATION

$$m\ddot{x} + F_3\dot{x} + k_a x = A_V [\sigma a_0^2 \rho_0 (1 + \sin 2\omega t) - P_k \cos (K_a \omega t - \Phi_k)]$$

$$x = \frac{\sigma v_0}{A_V} [(1 + \sin 2\omega t) - \frac{P_k}{\rho_0 a_0^2 \sigma} \cos (K_a \omega t - \Phi_k)]$$

$$\frac{\dot{x}}{a_0} = \frac{\pi N_a \sigma v_0}{30 A_V a_0} \left[\cos 2\omega t - \frac{K_a P_k}{2 \rho_0 a_0^2 \sigma} \sin (K_a \omega t - \Phi_k) \right]$$

$$\frac{Q_a}{v_0} = \sigma [1 + \sin 2\omega t - \frac{P_k}{\sigma \rho_0 a_0^2} \cos (K_a \omega t - \Phi_k)]$$

$$e = \frac{Q_a}{2 \sigma v_0} = \frac{1}{2} \left[1 + \sin 2\omega t - \frac{P_k}{\sigma \rho_0 a_0^2} \cos (K_a \omega t - \Phi_k) \right]$$

WATER FLOW

THE EQUATION

$$A + \bar{A} + k_w x = A_v \left[\sigma \left(\frac{gh_o}{n+1} \right) \rho_w (1 + \sin 2\omega t) - \rho_w g H_k \cos (K_w \omega t - \Phi_k) \right]$$

$$x = \frac{\sigma v_o}{A_v} \left[(1 + \sin 2\omega t) - \frac{g H_k}{\sigma \left(\frac{gh_o}{n+1} \right)} \cos (K_w \omega t - \Phi_k) \right]$$

$$\frac{x}{\frac{gh_o}{n+1}} = \frac{\pi N_w \sigma v_o}{30 A_v \sqrt{\frac{gh_o}{n+1}}} \left[\cos \omega t - \frac{K_w H_k}{2 \sigma \left(\frac{gh_o}{n+1} \right)} \sin (K_w \omega t - \Phi_k) \right]$$

$$\frac{Q_w}{v_o} = \sigma \left[1 + \sin 2\omega t - \frac{H_k y}{\sigma \left(\frac{gh_o}{n+1} \right)} \cos (K_w \omega t - \Phi_k) \right]$$

$$e = \frac{Q_w}{2 \sigma v_o} = \frac{1}{2} \left[1 + \sin 2\omega t - \frac{H_k y}{\sigma \left(\frac{gh_o}{n+1} \right)} \cos (K_w \omega t - \Phi_k) \right]$$

ANALOGOUS QUANTITIES FOR HYDRAULIC MODEL DESIGN

$$\begin{aligned}
 \frac{A_{C\alpha}}{A_{V\alpha}} &= \frac{A_{Cw}}{A_{Vw}} & \text{WATER} \\
 \frac{P_k}{\rho_3 \alpha_3^2 C_\alpha} &= \frac{H_k}{\frac{1}{g} \left(\frac{3h_o}{n+1} \right) C_w} \\
 \frac{N_\alpha \sigma_\alpha V_{o\alpha}}{A_{V\alpha} \alpha_0} &= \frac{N_w \sigma_w V_{ow}}{A_{Vw} \cdot \frac{gh_o}{n+1}} \\
 K_\alpha &= K_w \\
 \therefore K_\alpha &\equiv q_\alpha = \ddot{\alpha} \ddot{\alpha}_o \\
 &= \frac{\sqrt{\frac{gh_o}{n+1}}}{N_w L_w} \\
 &= q_w
 \end{aligned}$$

THE HYDRAULIC RESULTS PRESSURE VARIATIONS IN THE INLET SYSTEMS (PRESSURE TAKEN NEAR THE INLET VALVE PORT)

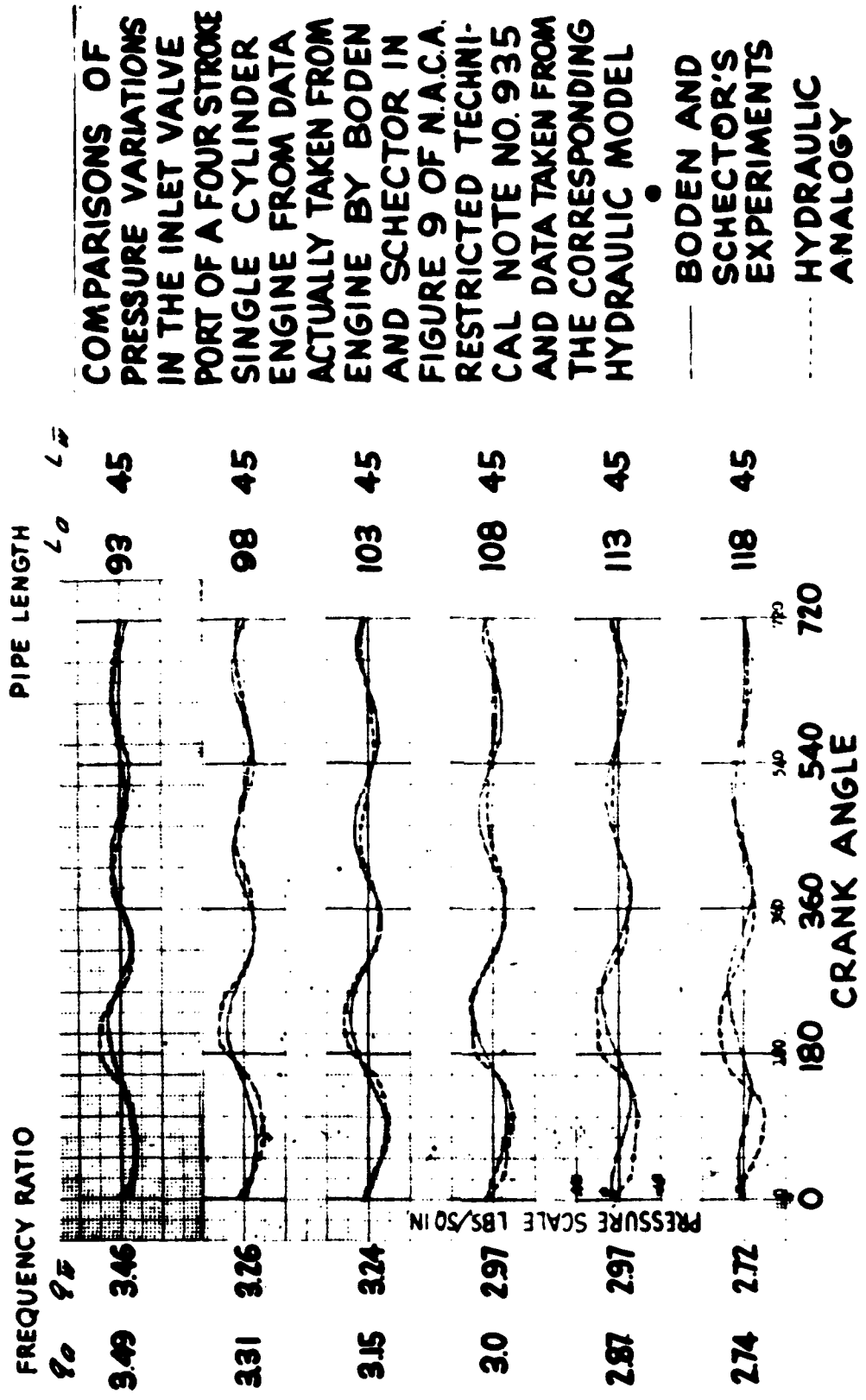
T.D.C. / T.D.C. / T.D.C.

$q_w = 5.55$
 $h_o = 7.14"$
 $T_w = 270 \text{ sec.}$
 $L_w = 90"$
 Corresponding $L_a = 45"$

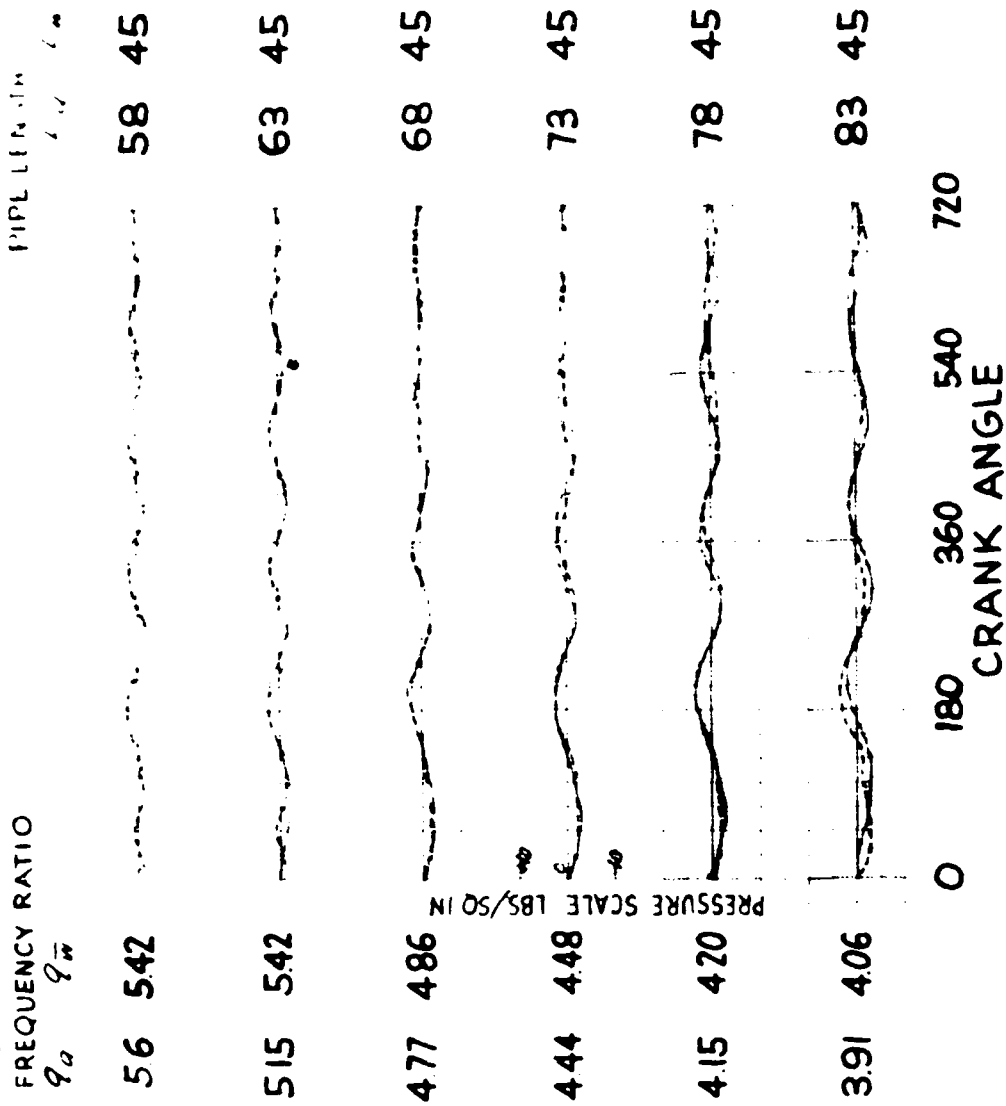
T.D.C. / T.D.C. / T.D.C.

$q_w = 5.42$
 $h_o = 7.14"$
 $T_w = 266 \text{ sec.}$
 $L_w = 90"$
 Corresponding $L_a = 45"$

HYDRAULIC RESULTS COMPARED TO GAS RESULTS

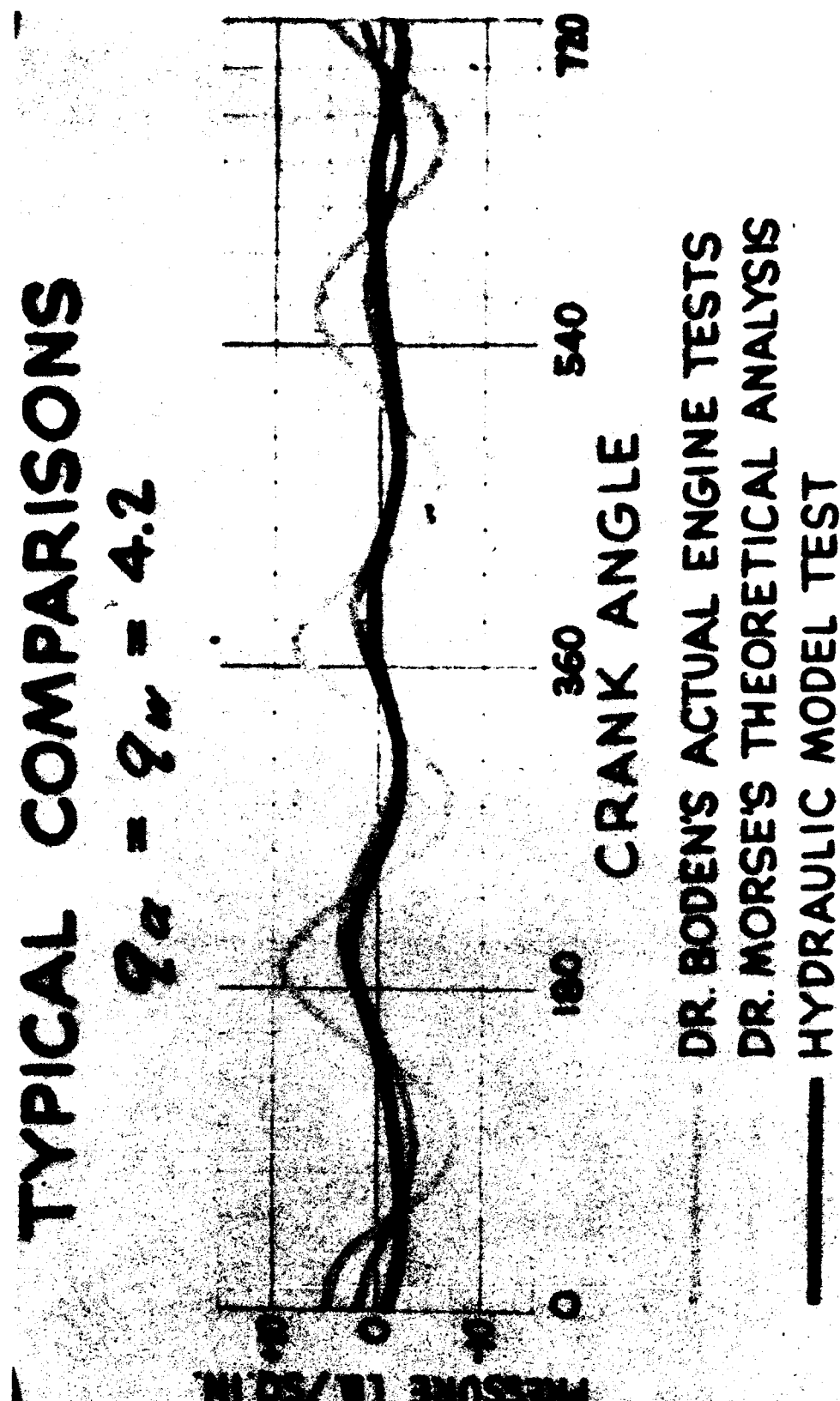


HYDRAULIC RESULTS COMPARED TO GAS RESULTS



TYPICAL COMPARISONS

$$\frac{P_a}{P_w} = \frac{P_w}{P_{in}} = 4.2$$



DR. BODEN'S ACTUAL ENGINE TESTS
DR. MORSE'S THEORETICAL ANALYSIS
— HYDRAULIC MODEL TEST

HIGH TEMPERATURE GAS DYNAMICS
PHENOMENA IN HYPERSONIC FLIGHT

W.H. Wurster and
C.E. Treanor
Cornell Aeronautical Lab.

HIGH-TEMPERATURE GAS DYNAMICS PHENOMENA IN HYPERSONIC FLIGHT

By: W. H. Wurster and C. E. Treanor

Cornell Aeronautical Laboratory

The advent of hypersonics has brought about a host of new problems relating to the nature of the medium through which high-speed aircraft fly. These problems arise not only from the direct effects of high velocities and low densities, but also from the influences of the chemical processes induced by flight at these conditions. These reactions include the dissociation of the normal molecules of the atmosphere and the formation of appreciable concentrations of new radicals and molecules. The effects of such reactions on various aerodynamic properties such as heat transfer and sound speeds are being extensively studied. I would like to emphasize still another problem, namely, the study of the interaction of electromagnetic radiation with high temperature air. Several examples can be cited where such a study is of direct value. We have already heard, and shall likely hear further at this symposium of the importance of radiative heat transfer at high-speed flight conditions. Further, in the case of the increasingly popular concept of high-speed reconnaissance not only the fidelity of visual records but the actual possibility of obtaining records with such a vehicle depend strongly on the radiative properties of the shock-heated air around the craft. A sheath of heated air can modulate the radiation from the ground to the detectors within the craft by absorption, and can further complicate data by emitting radiation of its own. In both cases it is important to know the identification of the optically active constituents of this sheath and the dependence of their radiative properties

on wave length, temperature and density.

This research was initially sponsored by the Air Force Special Weapons Center at Kirtland Air Force Base, New Mexico. The ultraviolet absorptive properties have been measured and a preliminary report of the results set forth (C.A.L. Rept. No. QM-997-A-1). I would first like to review briefly the experimental procedure and the results of that work, and then present the results of subsequent experiments.

Slide 1: The air to be studied was placed in the low pressure section of a clean but otherwise conventional closed shock tube. The processing of this air by the primary and reflected shock waves produces for about 100 microseconds a small pocket of compressed and heated air at the end of the shock tube. This air is in thermodynamic equilibrium at high temperature and density. During this interval, the continuum output of a xenon flash lamp is passed through the gas, and the resultant absorption spectrum photographed with a medium quartz spectrograph. Impurity radiation from the shock tube, which usually attends the termination of the equilibrium interval is eliminated from the record by a high speed shutter placed in front of the spectrograph slit. A photomultiplier tube mounted within the spectrograph records the exact time at which the absorption spectrum is taken, and monitors the operation of the shutter. The state of the gas is calculated using the initial conditions before the run, and the measured shock wave speed. Ion gaps serve to detect the progress of the **shock** along the tube.

Perhaps the most significant finding of this study was the strong absorption of ultraviolet radiation by shock-heated air. The next slide demonstrates this effect.

Slide 2: Here is a direct photograph of one of the spectrograph plates,

depicting the region from 2550 to 3500 Angstroms. The spectrum labelled "background" represents the unmodulated output of the xenon flash lamp, while that designated "absorption" is the same flash through the air in the shock tube which has in this case been brought to a temperature of 4400° K at four times atmospheric density. The remaining spectra were taken through filters to calibrate the photographic plate, while the superimposed iron arc spectra furnish accurate wave length references. As can be seen, at 3000 Å a structural absorption sets in, which gradually increases in strength until at 2600 Å the absorption is greater than 95%. Under these conditions a layer of air only 1 1/2 inches thick has essentially become opaque to this radiation. Experiments in pure nitrogen revealed no absorption, while similar runs in pure oxygen show a structured absorption almost identical with that in the shock-heated air. Comparison of the structure in both cases with published oxygen emission data have established unambiguously that excited molecular oxygen is by far the chief contributor to the absorption of heated air. As a result of this predominant role of oxygen in the determination of the optical properties of air, the emphasis of the research was shifted to a basic study of the absorptive properties of the oxygen molecule. This study is being sponsored by the Air Force Office of Scientific Research. Transition probabilities for several vibrational bands in oxygen have been obtained which enable their contribution to the absorption and emission of air to be calculated for any arbitrary conditions of temperature and density, including those unattainable in the laboratory.

Slide 3: It may be emphasized that this discussion relates only to transitions of the Schumann-Runge system in molecular oxygen from high (8 - 18) vibrational levels of the ground electronic state to the O₂ levels of the upper electronic state. The normal vacuum ultraviolet absorption of cold

oxygen, which takes place from the lowest vibrational level of the ground electronic state has been studied by Dichtburn and Heddle (Proc. Roy. Soc. A 226, 509, 1954).

Let us consider some of the factors involved in the measurement of transition probabilities.

Slide 4: Given a layer of gas of thickness d upon which radiation of intensity I_0 is incident, what can be said of the intensity of the transmitted beam? If we consider two energy levels of the molecules, 1, 2, between which transitions can occur, one would, in general, expect energy to be removed from the beam at the wavelength which corresponds to the energy difference of the levels involved. In an absorption spectrum, this would give rise to a line of decreased intensity at the corresponding wavelength.

The expression for the transmitted intensity is given by the usual Beer's Law, where we see it is proportional to the incident intensity I_0 and to the normal exponential attenuation factor. Here d represents the path length through the gas, N_1 the number density, particles per cm^3 , which are in the lower state 1, and d is an absorption coefficient which is related to the probability for the occurrence of an absorbing transition. It is represented as a function of λ since in general the absorption lines are of finite width. The line width and shape is, in fact, dependent on the thermodynamic state of the gas. In general, the lines broaden with an increase in temperature and density in a known manner. It should be stressed, however, that the integral of $\alpha(\lambda)d\lambda$ over a given line is a fundamental molecular constant for the particular transition. It was in fact the measurement of this quantity which constituted the research problem.

The quantity N_1 is obtained by calculating the Boltzman distribution of molecules for the energy levels involved, being given the equilibrium

conditions of the temperature and density of the gas. Two points may be mentioned here. First, it is just this factor N_1 which gives rise to the fact that oxygen at room temperature is completely transparent to ultraviolet radiation, while heated oxygen is strongly absorbing.

The transitions which correspond to these energies take place from high-lying vibrational levels of the oxygen molecule, 8-18. At 4500° K, one molecule in every hundred is in the 8th vibrational level, while at room temperatures the ratio is 1 in 10^{25} . In terms of path length, the same absorption by $1\frac{1}{2}$ inches of gas at 4500° K would require at room temperature a path length measured in light years. The overall absorption is thus very sensitive to temperature through the strong temperature dependence of N_1 .

The second point is that it is in the evaluation of N_1 that the shock tube comes into its own as a device for the thermal excitation of gases for spectroscopic work. As mentioned earlier, these transitions are of importance only in the heated gases, since only then does the population factor become large enough to make the absorption measurable. The usual arc and spark means of gaseous excitation, while producing a sufficient temperature, are not as suitable for these studies. Such sources are generally not in complete equilibrium, rendering the calculation of N_1 difficult, and also contain large temperature variations, so that an estimate of the pathlength d is poor. In the shock tube, however, the length d is accurately defined by the inside dimensions of the tube, and the gas contained therein has been uniformly brought to a high equilibrium temperature. One condition on shock tube applicability is the short duration (of about 100 microseconds) for these equilibrium conditions during which the spectrum must be recorded. The intensity of the light source

must be compatible with the optical speed of the instrumentation to produce workable density levels on the photographic plate.

The measurement of the absorption was made using the techniques described earlier in the absorption work in heated air. Several modifications were however required. Since it is the integral of the area under the absorption curve that constitutes the data, it is most important that the spectral line shape be recorded with high fidelity. It is clear, that the effective slit width or "window function" of the instrumentation which essentially scans the line must be small compared with the line width. A large Littrow quartz spectrograph with high dispersion was therefore used to photograph the spectra. And here again the shock tube proves itself useful, since the gas can be excited at high densities. The collision broadening of spectral lines increases directly with the density, and so the lines can be purposely broadened to produce a more favorable ratio of line-to-slit width.

Slide 5: is a section of the photographed spectrum and depicts a typical absorption band of the Schumann-Runge system in heated oxygen, together with the corresponding densitometer trace. This particular band consists of rotational transitions (between 3230 and 3370 Angstroms) of the 0,13 vibrational levels. As was demonstrated in the previous slide, these transitions take place from the thirteenth vibrational level of the ground electronic state, to the zeroth level of the upper state. The general nature of the band consists of the pairs of rotational lines which comprise the P and R branches of the band. At the right of the photograph is visible the head of the next (0,14) band, while at the left are the lines which comprise the tail of the 0,12 band. The small isolated lines which sometimes appear between the pairs of the 0,13 band are due to

overlapping with the preceding band.

It may be pointed out here that the envelope of the absorption maxima actually portrays the Boltzmann distribution of the population of molecules in the lower levels of each transition. This can, in principle be used to determine the rotational temperature of the gas. However, at these temperatures the shape of the envelope is not a sensitive function of the temperature, so that the intensity distribution of a single band does not readily afford an accurate thermometer for the gas.

The degree of resolution is evidenced by the separation between the pairs of lines. For $P = 47$ and $R = 51$ the separation is about one Angstrom. If the density is increased to 8 or 10 atmospheres the lines broaden to the extent that many of the line pairs coalesce. At this point the line width is about 8 times the effective slit width, which results in a good determination of the line shape.

Measurements have been made of the (0,13) and (0,14) bands of this system under varying conditions of temperature and density. The last slide presents the results.

Slide 6: Properly weighted areas under the lines were measured for various transitions of each band and plotted as a function of their energy. A more detailed description of this manner of data presentation is given in Appendix 1. In a graphical representation of this type, the points should lie on a straight line. The intercept at $E = 0$ yields a constant from which the transition probability can be extracted.

In the graph shown here, both the (0,13) and (0-14) bands are presented. The difference in the intercepts corresponds to the difference in the respective transition probabilities. The slope of the lines in this graph is $-1/RT$ and hence is specified by the gas temperature. In the present case

the scatter of the data limits the agreement with gasdynamically calculated temperatures to 10%. This scatter is due in large part to the fact that all transitions were directly included in the graph, where in fact the contribution of the higher rotational levels of an overlapping adjacent band should be subtracted from the lines affected. A reduction in the scatter would permit a separate determination of the slope.

The spread in the value of the transition probability, using the calculated temperature is about 15% and represents a precision acceptable in this field of work. The f values, a measure of the transition probabilities, are .006 for the (0,13) and .005 for the (0,14) bands. These f values are defined as the ratio of the measured absorption to the absorption calculated for a classical electron oscillator. It is these values which constitute the constants for these transitions of the oxygen molecules, and from which both the absorption and emission by oxygen can be determined for any pathlength under any thermodynamic conditions.

With the work we are doing at the present time, we hope to provide transition probabilities for some 20 bands of the Schumann-Runge system of oxygen. These bands lie between the vacuum ultraviolet limit and the visible wavelength regions, and comprise the chief absorbing system in O_2 therein. Plotted on a graph such as this the extension over many bands will yield an accurate measurement of the rotational temperature, and serve as an independent spectrographic check on the temperature obtained by shock wave calculation. And in some cases where the temperatures are not readily calculable, calibrated measurements can now be made.

In conclusion I would like to point out the further applicability of these findings in two other research fields. One is in the area of chemical kinetics, which is concerned with the dissociation and recombination times

of radicals and molecules and with the determination of reaction mechanisms. Consider for example the absorption spectrum of an oxygen reacting mixture taken in a small interval of time, the order of microseconds. The strength of the absorption is measured from the photographic plate and since the transition probability is now known, one then directly obtains the population of the various vibrational levels of the molecule. Not only can vibrational relaxation times be verified, but the role of oxygen in a flame or combustion reaction can be established.

Finally, the ability to measure quantitatively the population of the molecules in vibrational levels suggests the use of flash absorption spectroscopy for the determination of the degree of equilibrium in hypersonic flows. In shock tunnels and nozzles the flow fields and boundary layers can be probed optically and the state of the gas mapped throughout the configuration.

In the light of these considerations, it appears that the measurement of molecular transition probabilities has direct application to the problems of hypersonic aerodynamics.

APPENDIX I

The experimental quantity measured from the photo graphic plate is the product $I_1 \alpha(\nu)$ defined by the equation

$$I = I_0 e^{-N_1 \alpha(\nu) d}$$

where I_0 and I are the incident and transmitted beam intensities through a layer of gas of thickness d . N_1 is the number of particles per cubic centimeter in the lower state of the transition involved and α is an absorption coefficient. ν is the wave number in reciprocal centimeters.

Designating the rotational and vibrational quantum numbers of the lower state by K'' and v'' respectively, and those of the upper state by K' and v' , the measured integrated absorption coefficient for a single rotational line can be written

$$\int N_{K''v''} \alpha_{K''v'' \rightarrow K'v'}(\nu) d\nu.$$

The spectral lines are normally designated according to the value of v'' . The selection rules for ϵ_2 limit the values of K' to $K' = K'' - 1$ (P branch) and $K' = K'' + 1$ (R branch). Thus adding the contributions from the P and R branches for a given K'' amounts to summing over all values of K' . This summation of the integrated absorption coefficient is then proportional to the number density of molecules in the lower ($K''v''$) level of the transition and to the probability of the occurrence of an absorbing transition from the lower to the upper vibrational level. In terms of the f value for the transition the equation is

$$\sum_{K'} \int N_{K''v''} \alpha_{K''v'' \rightarrow K'v'}(\nu) d\nu = \frac{\pi e^2}{mc^2} f_{(v', v'')}^{S-R} N_0 \frac{(2K'+1)}{Q_K Q_{v'}} e^{-\frac{(E_{v''} + E_{K''})}{kT}}$$

where

$$\frac{\pi e^2}{mc^2} = 8.85 \times 10^{-13} \text{ cm}$$

N_{O_2} = number of oxygen molecules per cubic centimeter

$(2K''+1)$ = rotational degeneracy factor

Q_K, Q_v = partition functions for rotation, vibration, respectively

k = Boltzmann constant.

T = absolute temperature, $^{\circ}\text{K}$

$f_{v',v''}^{S-R}$ = f value for the Schumann-Runge transition from v'' to v' .

This transition probability is independent of K'' .

Rearranging the equation, and taking the logarithm of both sides

$$\ln \left[\frac{1}{2K''+1} \sum_{K'} \int N_{K''v''} \alpha_{K''v'' \rightarrow K'v'}^{(v)} dv \right] = \ln \left[\frac{\pi e^2}{mc^2} \frac{f_{v',v''}^{S-R} N_{O_2}}{Q_K Q_v} e^{-E_{K''}/kT} \right] - \frac{E_{K''}}{kT}$$

The usual method of handling these data is to plot the left-hand side of the equation vs $E_{K''}$. It can be seen that this should yield a straight line with slope equal to $-1/kT$ and the intercept of the line at $E_{K''} = 0$ gives the f value for the transition. In the graph of figure 6, all energies were measured relative to the $K''=0$ level of the $(0,13)$ band, so that the data from both the $(0,13)$ and $(0,14)$ bands are shown on the same graph.

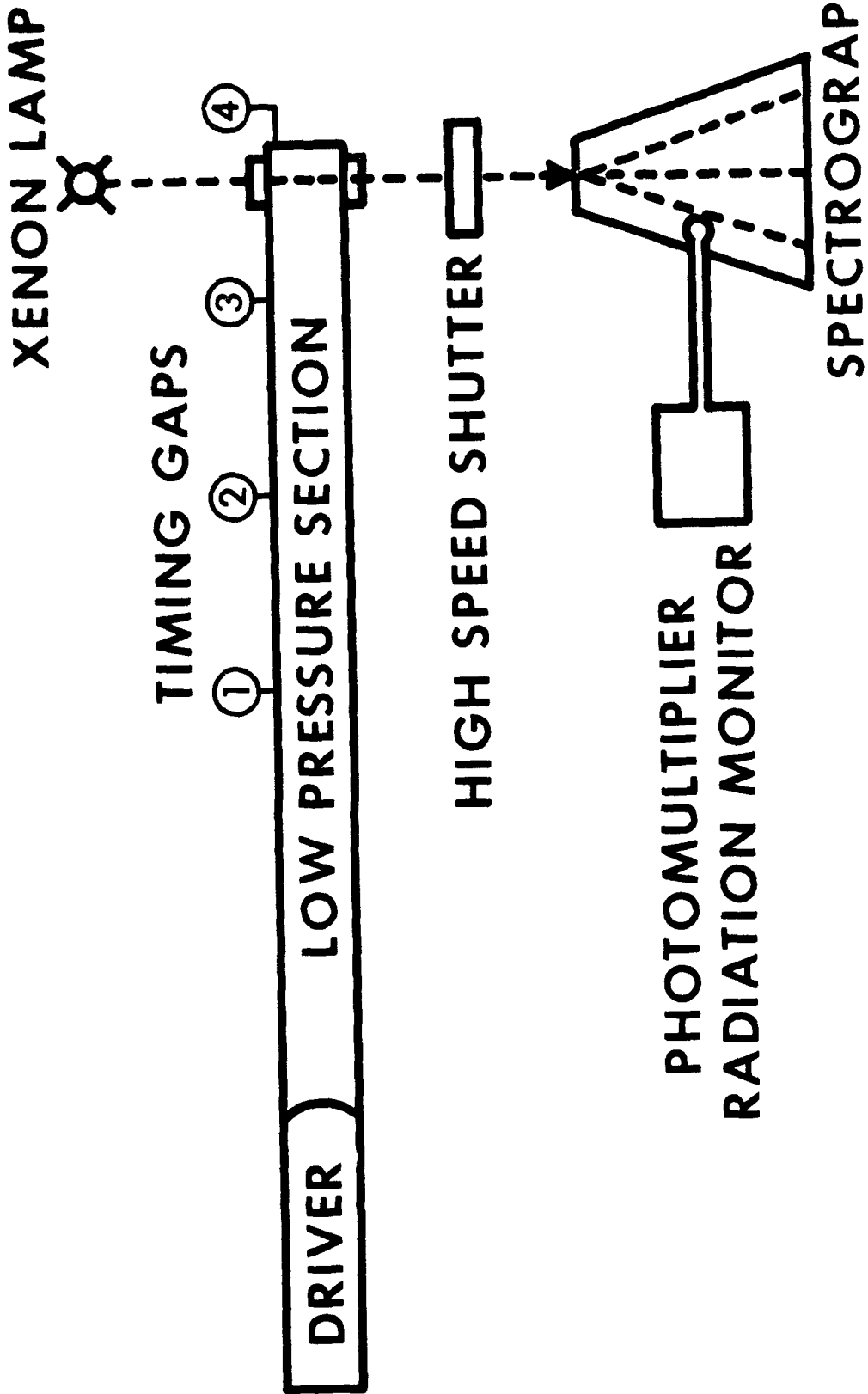


Figure #1

SCHEMATIC DIAGRAM OF THE ABSORPTION EXPERIMENT

FIGURE 1



Figure #2

AN ENLARGED PRINT OF A SPECTROGRAM SHOWING
THE EMISSION AND ABSORPTION OF AIR AT 4380 °K,
 $\rho = 4.0 \rho_0$ IN THE NEAR ULTRAVIOLET

FIGURE 2

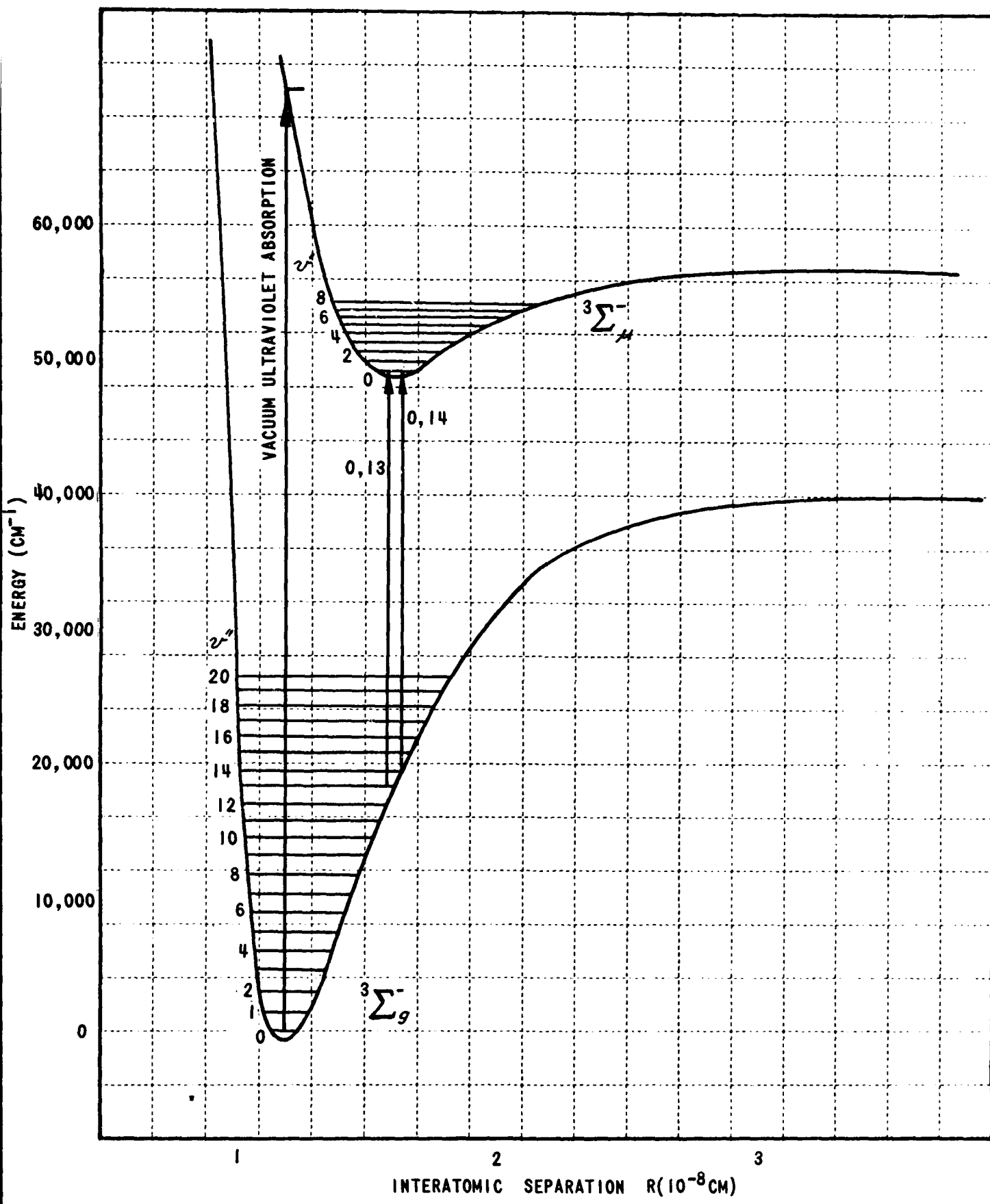
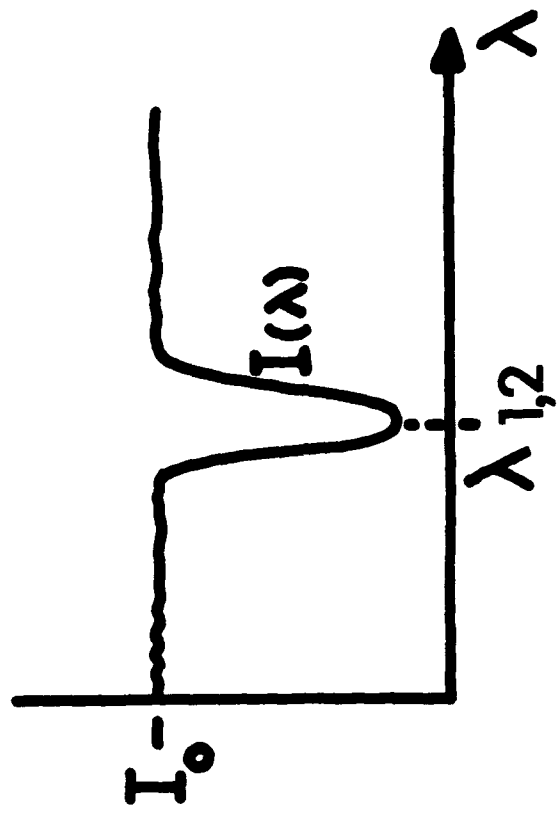
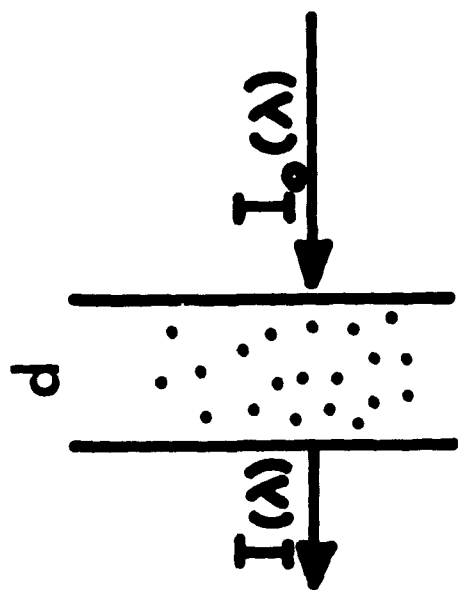
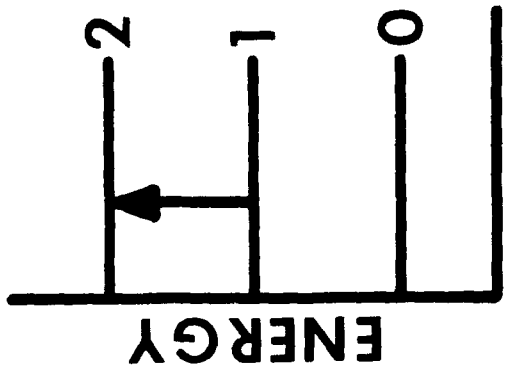


FIGURE 3 POTENTIAL CURVES OF THE OXYGEN MOLECULE

Figure #3

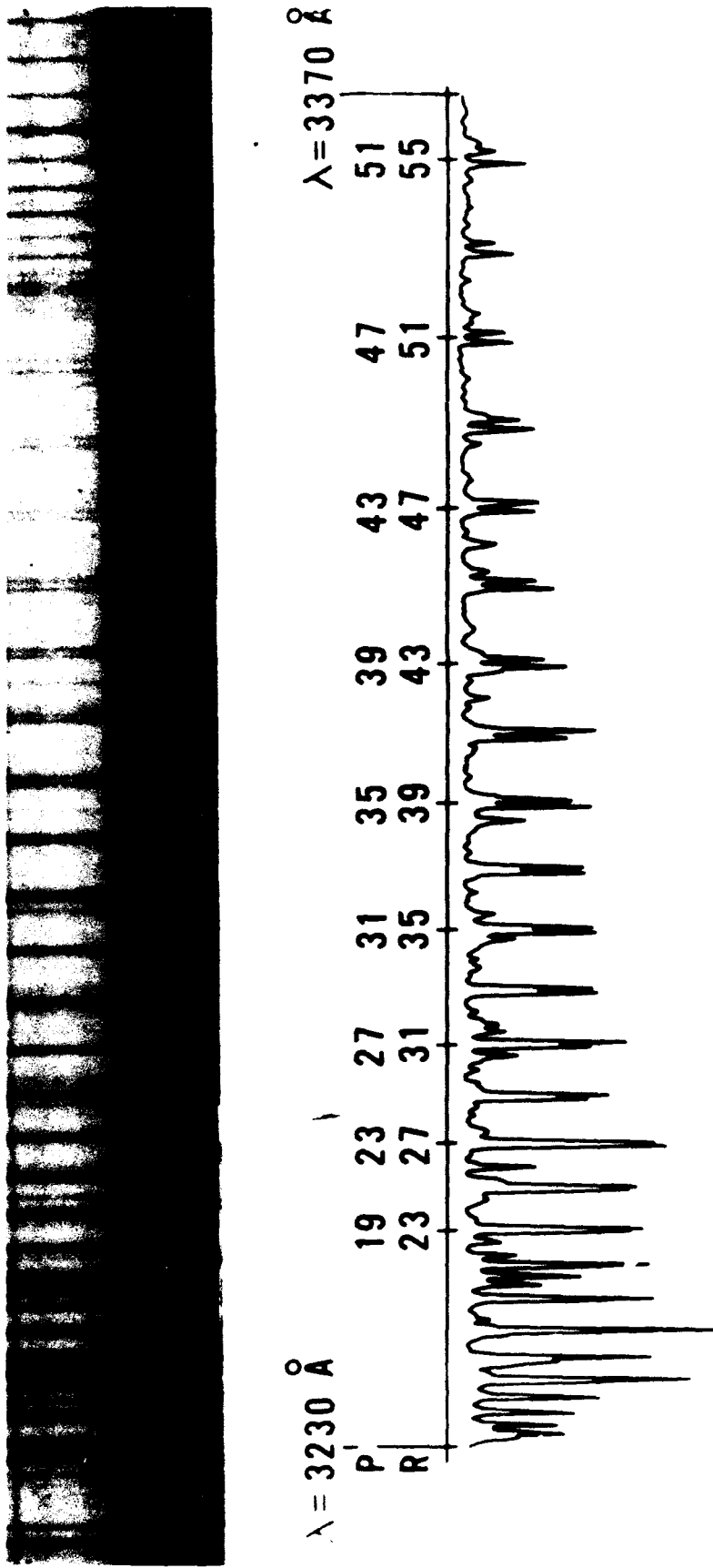


$$I(v) = I_o(v) e^{-N_1 \alpha_1(v) d}$$

$$-N_1 \alpha_1(v) d$$

Figure #4

FIGURE 4



ABSORPTION SPECTRUM OF THE 0,13 BAND
OF THE SCHUMANN-RUNGE SYSTEM OF OXYGEN
 $T = 3410 \text{ K}$, $\rho = 3.6 \rho_0$

Figure #5

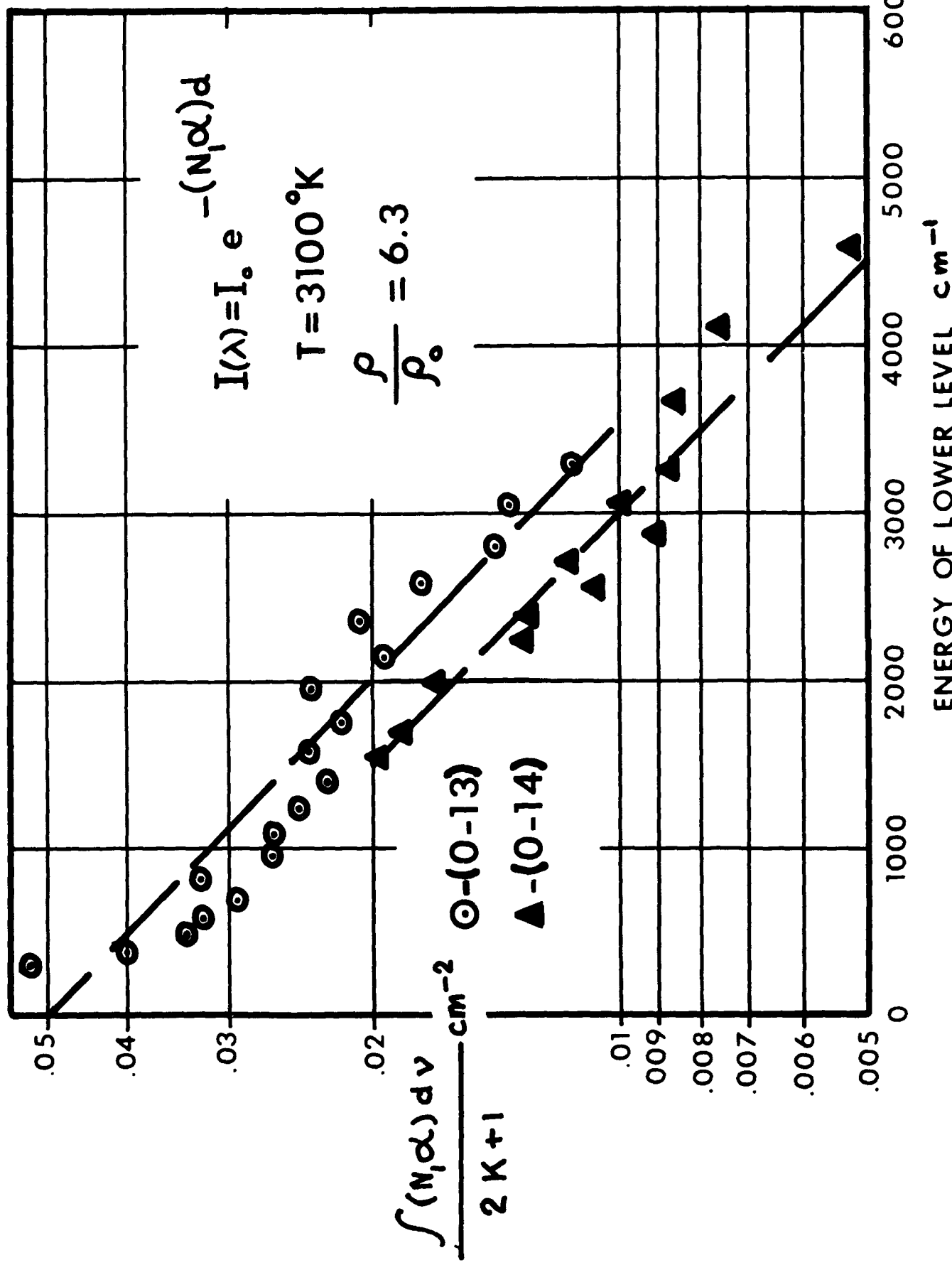


Figure #6

FIGURE 6

GENERATION OF PRESSURE WAVE FORMS THROUGH THE DETONATION OF
EXPLOSIVE CHARGES

D. C. Anderson
Armour Research Foundation of Illinois Institute of Technology

**Generation of Pressure Wave Forms
Through the Detonation of Explosive Charges**

D. C. Anderson

**CHAPTER I
INTRODUCTION**

This study investigates the general behavior of shock waves generated through the detonation of high explosive charges. The analysis in particular is concerned with one dimensional flow, that is shock waves propagating down a unit cross-sectional area channel. It is also limited to shock waves with shock front overpressures (i.e., pressures immediately behind the shock front) of ten atmospheres or below. With these limits and restrictions it is seen that this study confines itself to shock waves which may feasibly be generated in a shock tube.

The analysis is similar to that previously made for calculating total energy yields for atomic bombs.^{1,2*} However, in this case, because of the limits and restrictions placed on the study the end result is different and yields far more information. The analysis leads to shock strength-scaled distance and shock strength-scaled time decay curves, where shock strength is defined as the shock front overpressure to ambient pressure ratio. It also yields, under the assumptions made considerable insight into the behavior of the gas flow variables behind an explosive generated shock.

The laws of conservation of mass, momentum, energy governing the flow are all employed and satisfied in carrying out and completing the analysis.

With these results an approximate method is developed for generating various desired pressure pulses.

*For all numbered references see bibliography.

CHAPTER II DISCUSSION OF THE PROBLEM

A sketch of a typical distance-time curve for a shock wave propagating from a zero origin is presented in Figure 1. The figure shows the shock front distance R as a function of t , time, and also a typical particle position r_1 as a function of time. This figure will be referred to periodically throughout the analysis for a better understanding of the presentation.

The Space Density Distribution

The study begins with the assumption of a density distribution, namely

$$\rho(r) = \rho_s \left[\frac{r_1(t)}{R(t)} \right]^{q(t)} \quad (1)$$

where ρ is the gas density behind the shock at a distance r_1 from the origin, ρ_s is the gas density at the shock front distance R , and q is a function of shock front conditions to be determined by considering conservation of mass. At a fixed time, t , Eq. 1 depicts the spacial density distribution behind the shock.

Justifications for such an assumption on the density distribution are: (1) it is known that the density is some monotonically decreasing function with the distance behind the shock front, (2) the observed density distribution is closely approximated by this power law, and (3) it yields, as will be shown, results which are in agreement with experimentally gathered data. The fact this assumption requires that the density go to zero at the origin is in all probability its main error. However, in reality the density very nearly goes to zero at this point for shock front overpressures of two atmospheres or above.

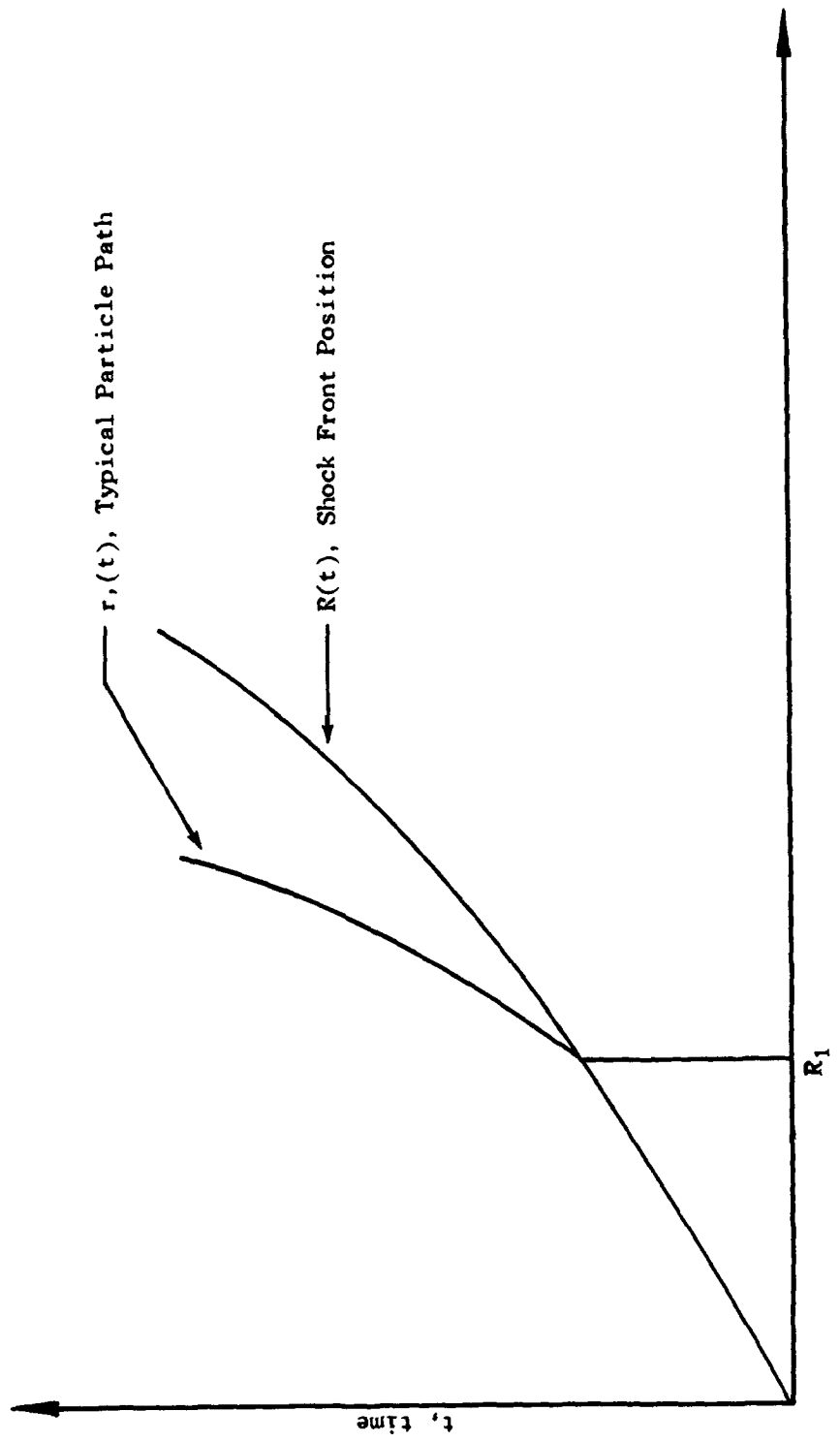


Fig. 1. Sketch of a Typical Distance Time History of a Moving Shock Wave

The difference is negligible. For weaker shocks the assumption is still good but not as accurate.

The value of q will now be determined by considering the conservation of mass law from the origin out to the shock front distance R . This states

$$\int_0^R \rho dr = \rho_0 R$$

for a constant time, where ρ_0 is the ambient gas density. Substituting the value of ρ from Eq. 1 into the above integral and integrating results in

$$\frac{\rho_s R}{q + 1} = \rho_0 R$$

Solving this equation for q gives

$$q = \frac{\rho_s}{\rho_0} - 1 = \eta_s - 1 \quad (2)$$

where η_s is the ratio of densities across the shock front.

Space Particle Velocity Distribution

Conservation of mass is again employed, but this time the mass from the origin to a particular particle path is considered (see particle path $r_1(t)$ in Figure 1). This gives the integral equation

$$\int_0^{r_1} \rho dr = \rho_0 R_1$$

where R_1 is the particle distance before the shock engulfs it. Using Eq. 1 and integrating gives

$$\frac{\rho_s \left(\frac{r}{R}\right)^q r_1}{q + 1} = \frac{\rho r_1}{q + 1} = \rho_0 R_1$$

where Eq. 1 is again used after integration.

Next the substantial derivative,

$$\frac{D}{Dt} = \frac{\partial}{\partial t} + u \frac{\partial}{\partial r}$$

where u is the particle velocity and is equal to $\frac{dr}{dt}$, of the above integration result is formed. This gives after simplification

$$\frac{D\rho}{Dt} + \frac{\rho u}{r} - \frac{\rho}{q+1} \frac{d(q+1)}{dt} = 0$$

The one dimensional conservation of mass equation

$$\frac{D\rho}{Dt} + \rho \frac{\partial u}{\partial r} = 0$$

is combined with the above equation to give

$$\frac{\partial u}{\partial r} = \frac{u}{r} - \frac{1}{q+1} \frac{d(q+1)}{dt}$$

The solution is readily obtained with the substitution $u = ry$ and integrating with respect to r at a fixed time. The solution is

$$\frac{u}{r} = - \frac{1}{q+1} \frac{d(q+1)}{dt} \ln r + A(t)$$

where $A(t)$ is the constant of integration which may be function of time. At the shock front the solution becomes

$$\frac{u_s}{R} = - \frac{1}{q+1} \frac{d(q+1)}{dt} \ln R + A(t)$$

where u_s is the particle velocity at the shock front. From this equation the value of $A(t)$ is evaluated, and the final particle velocity distribution may be expressed as

$$u = u_s \left(\frac{r}{R} \right) \left[1 - \alpha(t) \ln \left(\frac{r}{R} \right) \right] \quad (3)$$

where

$$\alpha = \frac{R}{u_s} \frac{1}{q+1} \frac{d(q+1)}{dt}$$

This value of α may be simplified considerably as follows:

$$\begin{aligned}
 \alpha &= \frac{R}{u_s} \frac{1}{q+1} \frac{d(q+1)}{dt} = \frac{R}{u_s} \frac{1}{\eta_s} \frac{d\eta_s}{dR} \frac{dR}{dt} \\
 &= \frac{U}{u_s} \frac{R}{\eta_s} \frac{d\eta_s}{dR} = \frac{\eta_s}{\eta_s - 1} \cdot \frac{R}{\eta_s} \frac{d\eta_s}{dR} \\
 &= \frac{d \ln (\eta_s - 1)}{d \ln R}
 \end{aligned}$$

where

$$U = \frac{dR}{dt} \text{ (shock propagation velocity)}$$

and

$$\frac{U}{u_s} = \frac{\eta_s}{\eta_s - 1}$$

from the Rankine-Hugoniot relation⁶ obtained from the conservation of mass across the shock front.

Space Pressure Wave Form

The conservation of momentum equation states

$$\frac{\partial P}{\partial r} = - \rho \frac{Du}{Dt}$$

where P is the absolute pressure.

The space pressure wave form may now be found by considering the following integral at a fixed time.

$$P = \int \frac{\partial P}{\partial r} dr = - \int \rho \frac{Du}{Dt} dr$$

The quantities in the integrand on the right may be found either directly or derived from Eqs. 1 and 3.

In forming the substantial derivative $\frac{Du}{Dt}$ all of the quantities appearing in the expression for particle velocity, Eq. 3, are functions of time. The derivative is thus formed and combined with the density expression to give

the above integrand. The integrand contains such expressions as $\frac{dr}{dt}$, $\frac{du_s}{dt}$, $\frac{dR}{dt}$, and $\frac{d\alpha}{dt}$ which are all rewritten as follows

$$\frac{dr}{dt} = u = u_s \left(\frac{r}{R} \right) \left[1 - \alpha \ln \left(\frac{r}{R} \right) \right]$$

$$\frac{dR}{dt} = U$$

$$\frac{du_s}{dt} = U \frac{du_s}{dR} = \frac{u_s U}{R} \frac{d \ln u_s}{d \ln R}$$

$$\frac{d\alpha}{dt} = U \frac{d\alpha}{dR} = \frac{\alpha U}{R} \frac{d \ln \alpha}{d \ln R}$$

With the integrand expressed as a function of r the integration is performed and the constant of integration is evaluated at the shock front. The resulting pressure wave is

$$\frac{P(r) - P_0}{P_s(R) - P_0} = 1 - K + \left(\frac{r}{R} \right)^{\eta_s + 1} \left[K + L \ln \left(\frac{r}{R} \right) + M \left\{ \ln \left(\frac{r}{R} \right) \right\}^2 \right] \quad (4)$$

where P_0 is the absolute ambient pressure, and P_s is the absolute pressure immediately behind the shock front. The quantities K , L , and M are parameters dependent on shock front conditions only. Their values are

$$K = \frac{1}{\eta_s + 1} \left[1 - \left(1 + \frac{\alpha}{\eta_s + 1} \right) \eta_s \beta + \frac{\alpha}{\eta_s + 1} (1 - \eta_s \phi - 2\eta_s) + \left(\frac{\eta_s - 1}{\eta_s + 1} \alpha \right)^2 \right]$$

$$L = \frac{\alpha}{\eta_s + 1} \left[\eta_s (\beta + \phi) + \frac{(\eta_s - 1)^2}{\eta_s + 1} \alpha + \eta_s - 2 \right]$$

$$M = - \frac{\eta_s - 1}{\eta_s + 1} \alpha^2$$

where

$$\beta = \frac{d \ln u_s}{d \ln R}$$

and

$$\phi = \frac{d \ln \alpha}{d \ln R}$$

The Total Shock Energy Yield

The total shock energy yield, W , manifests itself in two forms: (1) the kinetic energy, E_K , given by

$$E_K = \int_0^R (1/2) \rho u^2 dr$$

and (2) the internal energy increment, E_I , given by

$$E_I = \int_0^R \epsilon P dr - \epsilon_0 P_0 \int_0^R dr$$

For ideal gases the internal energy is known to be a function of state only, and hence the internal energy per unit volume can be written as ϵPV , where ϵ is at most a function of state, and not of process. Here V represents specific volume. For a stream tube of unit cross section, the specific volume is numerically equal to the length of the tube enclosing a unit mass of fluid. Hence, the above expression represents the change in total internal energy of the fluid from the origin to the shock front. It can be shown from thermodynamic considerations that $\epsilon = \frac{1}{\gamma - 1}$, whether or not γ , the ratio of specific heats of the fluid, is a constant.

Over the range of pressures considered in the present analysis, γ is known to be substantially constant at the value 1.4; then $\epsilon = \epsilon_0 = 5/2$.

Using the values of ρ and u given by Eqs. 1 and 3 respectively, the integral for kinetic energy may be evaluated readily. It gives

$$E_K = \frac{1}{2} \rho_s u_s^2 \frac{R}{\eta_s + 2} \left[1 + \frac{2\alpha}{\eta_s + 2} \left(1 + \frac{\alpha}{\eta_s + 2} \right) \right]$$

Likewise, employing Eq. 4 the integral for the internal energy increment is found to be

$$E_I = \frac{5}{2} (P_s - P_0) R \left[1 - K + \frac{K}{\eta_s + 2} - \frac{L}{(\eta_s + 2)} 2 + \frac{2M}{(\eta_s + 2)} 3 \right]$$

adding the two expressions and using the conservation of momentum across the shock front to simplify the equation results in

$$W = E_K + E_I = \frac{1}{2} (P_s - P_0) R \left[\frac{\eta_s - 1}{\eta_s + 2} \left\{ 1 + \frac{2\alpha}{\eta_s + 2} \left(1 + \frac{\alpha}{\eta_s + 2} \right) \right\} + 5 \left\{ 1 - K + \frac{K}{\eta_s + 2} - \frac{L}{(\eta_s + 2)} 2 + \frac{2M}{(\eta_s + 2)} 3 \right\} \right] \quad (5)$$

Equation 5, as will be shown, is a second-order differential equation. It must be revised in form in order to be solved. First the following are defined

$$\xi \text{ (shock strength)} = \frac{P_s}{P_0}$$

$$\lambda \text{ (scaled distance)} = \frac{P_0 R}{W}$$

and

$$X(\xi, R) = \frac{d \ln (\xi - 1)}{d \ln R}$$

Using the first and last definitions, and employing the Rankine-Hugoniot relations between ρ , u , and P at the shock front, it is found that

$$\alpha = \frac{d \ln (\eta_s - 1)}{d \ln R} = \frac{7X}{\xi + 6}$$

$$\beta = \frac{d \ln u_s}{d \ln R} = \frac{3\xi + 4}{6\xi + 1} X$$

and

$$\phi = \frac{d \ln \alpha}{d \ln R} = \frac{d \ln X}{d \ln (\xi - 1)} - \frac{\xi - 1}{\xi + 6} X$$

Now with the help of the Rankine-Hugoniot relations again, and the above values for α , β , and ϕ , Eq. 5 becomes

$$\frac{1}{\lambda} = \frac{5(\xi - 1)}{2(8\xi + 13)} \left[(8\xi + 6) + \frac{24\xi^2 + 169\xi + 52}{8\xi + 13} X - \frac{7(24\xi^2 - 125\xi - 46)}{(8\xi + 13)^2} X^2 \right. \\ \left. + \frac{7(6\xi + 1)}{8\xi + 13} X^2 \frac{d \ln X}{d \ln (\xi - 1)} \right]$$

which is of second order and may now be broken up into two first-order equations as follows.

$$\frac{d\lambda}{d\xi} = \frac{\lambda}{X(\xi - 1)}$$

and

$$\frac{dX}{d\xi} = \frac{\frac{1}{\lambda} \frac{2(8\xi + 13)^2}{5(\xi - 1)} - (8\xi + 6)(8\xi + 13) - (24\xi^2 + 169\xi + 52) X}{7(6\xi + 1)(\xi - 1) X} \\ + \frac{\frac{7(24\xi^2 - 125\xi - 46)}{8 + 13}}{7(6\xi + 1)(\xi - 1) X}$$

These two differential equations were integrated numerically on the IBM 650 computer using the Bell Telephone Laboratory L1 interpretive routine and the R.C.A. Laboratory routine for the solution of differential equations.^{3,4} The R.C.A. differential equation routine integrates a set of differential equations numerically using the Milne method. The initial equation must first be written as a system of first order ordinary differential equations. The system is then solved by use of the "predictor" and "corrector" equations of Milne.

The integration is initiated by computing the first three points by the Runge-Kutta-Gill method. Both of these methods yield fourth order precision, that is truncation errors of order h^5 , where h is the increment interval.

The routine provides a criterion whereby the increment size is altered until the absolute value of the difference between the "predictor" and "corrector" values of the solution do not exceed a certain pre-specified amount. In the solution obtained this amount was specified as 29×10^{-4} .

The coding process for the machine, when using the differential equation routine, involved simply coding the functions determining the differential equations. The initial conditions as well as certain constants required by this routine had to be specified. The solution was continued until $\xi - (1.01 + h)$ became less than zero. Initial conditions were taken from experimental data gathered at the Air Force's shock tube facility at Gary, Indiana, several runs were made using different initial conditions for each. Two of these runs are plotted in Fig. 2, ξ versus λ . They are represented by the broken lines; the solid line represents experimental data.⁵

The solutions given by the computer for the differential equation indicated that the problem in some way may be overdetermined. This was so indicated when the computer, regardless of starting initial conditions, tended to seek out new initial conditions which would yield a smooth solution procedure. Whether or not the problem is overdetermined is as yet unknown, but the solution obtained is considered in good agreement with experiment.

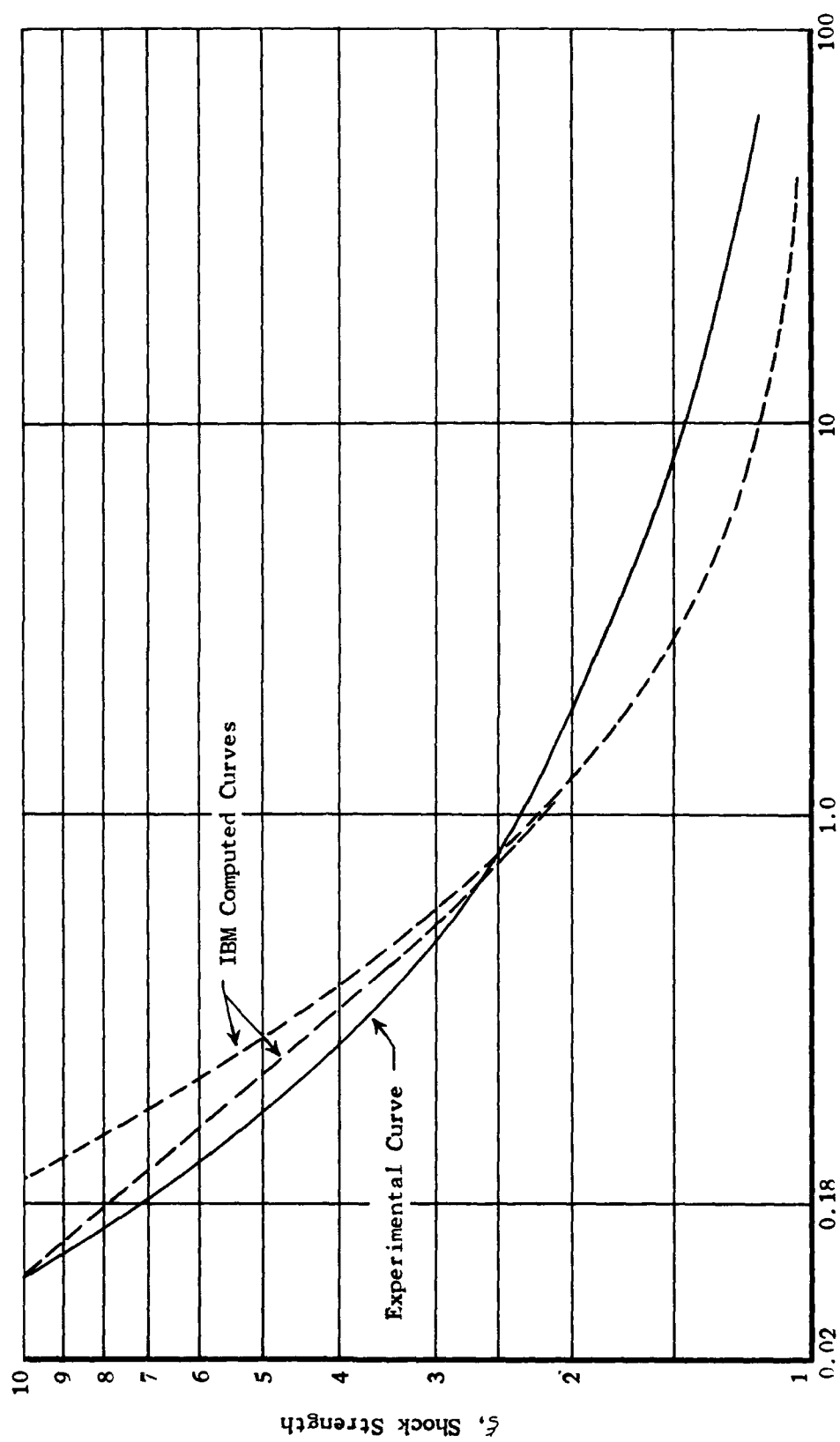


Fig. 2. Scaled Distance, λ , Versus Shock Strength, ξ

Typical Single Charge Wave Forms

In addition, the problem was set up on the computer to yield values of X and $\frac{dX}{d\xi}$ from which values of α , β , ϕ , K , L , and M are easily computed.

Table I lists these values for the range of shock strengths considered in this study.

It is now possible to plot typical density, particle velocity, and pressure wave forms using Table I and Eqs. 1, 3 and 4 respectively. Figures 3 through 8 present these wave forms for shock strengths of two and three.

Development of a Time-of-Arrival Curve

Until now the analysis has been independent of time, which has thus far appeared only as a parameter. Now, by further considerations, a shock strength-scaled time curve will be constructed.

The Rankine-Hugoniot expression for shock velocity

$$U = c \left[\frac{6\xi + 1}{7} \right]^{1/2}$$

is used to plot U/c versus ξ (see Fig. 9), where c is the sound speed in the region immediately in front of the shock. This curve is used to determine an average value of U , say \bar{U} , between two shock strengths. From the curve of λ versus ξ , Fig. 2, values of R are extracted corresponding to various ξ , for example at $\xi = 10$, $R = 0.066 \frac{W}{P_0}$. In this manner a ΔR is found between two shock strengths. This corresponds to a \bar{U} , and so yields a Δt , $\Delta t = \frac{\Delta R}{\bar{U}}$. The time corresponding to $\xi = 10$ is assumed to be $t = t_1$. $\frac{P_0 c(t - t_1)}{W}$ is now plotted versus λ , shown in Fig. 10. This curve is extrapolated back to where $\lambda = 0$ to find a value for t_1 .

With this value of t_1 , ξ versus $\frac{P_0 ct}{W}$ is plotted and is shown in Fig. 11.

The addition of this time-of-arrival curve makes it possible to find, if given values for any two of the following, ξ , R , t , or W , the remaining two.

Table 1. Single Charge Parameters

ξ	α	β	ϕ	K	L	M
1.3	- 0.854	- 0.800	0.099	0.992	0.631	- 0.066
1.5	- 0.801	- 0.729	0.120	0.976	0.496	- 0.091
1.7	- 0.762	- 0.681	0.130	0.959	0.400	- 0.107
2.0	- 0.715	- 0.624	0.168	0.937	0.275	- 0.122
2.6	- 0.648	- 0.566	0.199	0.891	0.130	- 0.133
3.0	- 0.614	- 0.540	0.218	0.865	0.064	- 0.134
4.0	- 0.540	- 0.494	0.289	0.808	- 0.052	- 0.125
5.0	- 0.477	- 0.459	0.393	0.760	- 0.131	- 0.108
7.0	- 0.358	- 0.387	0.578	0.665	- 0.266	- 0.069
10.0	- 0.437	- 0.557	- 4.243	0.442	1.431	- 0.112

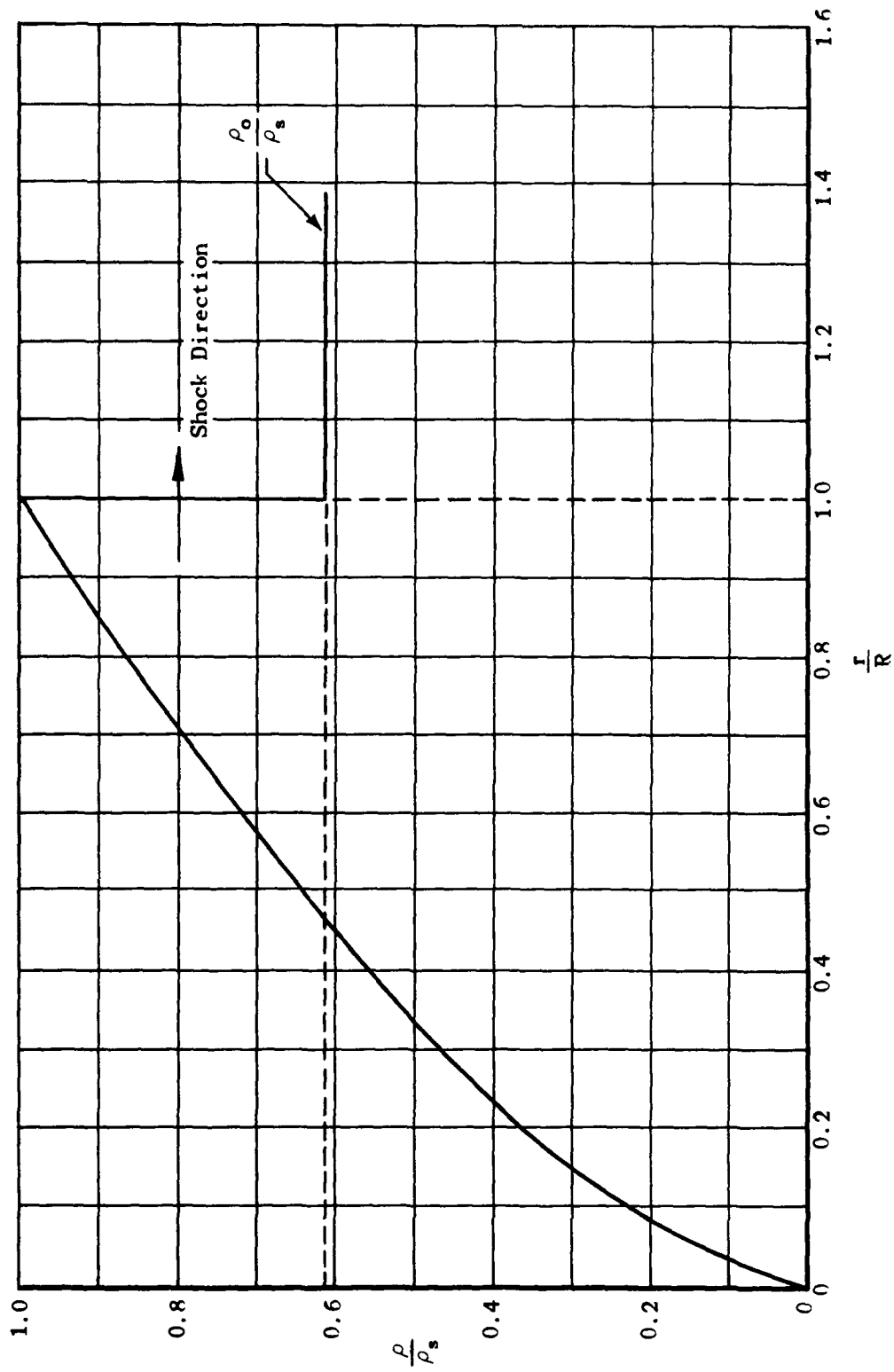


Fig. 3. Fluid Density Distribution Versus $\left(\frac{r}{R} \right)$ for $\xi = 2$

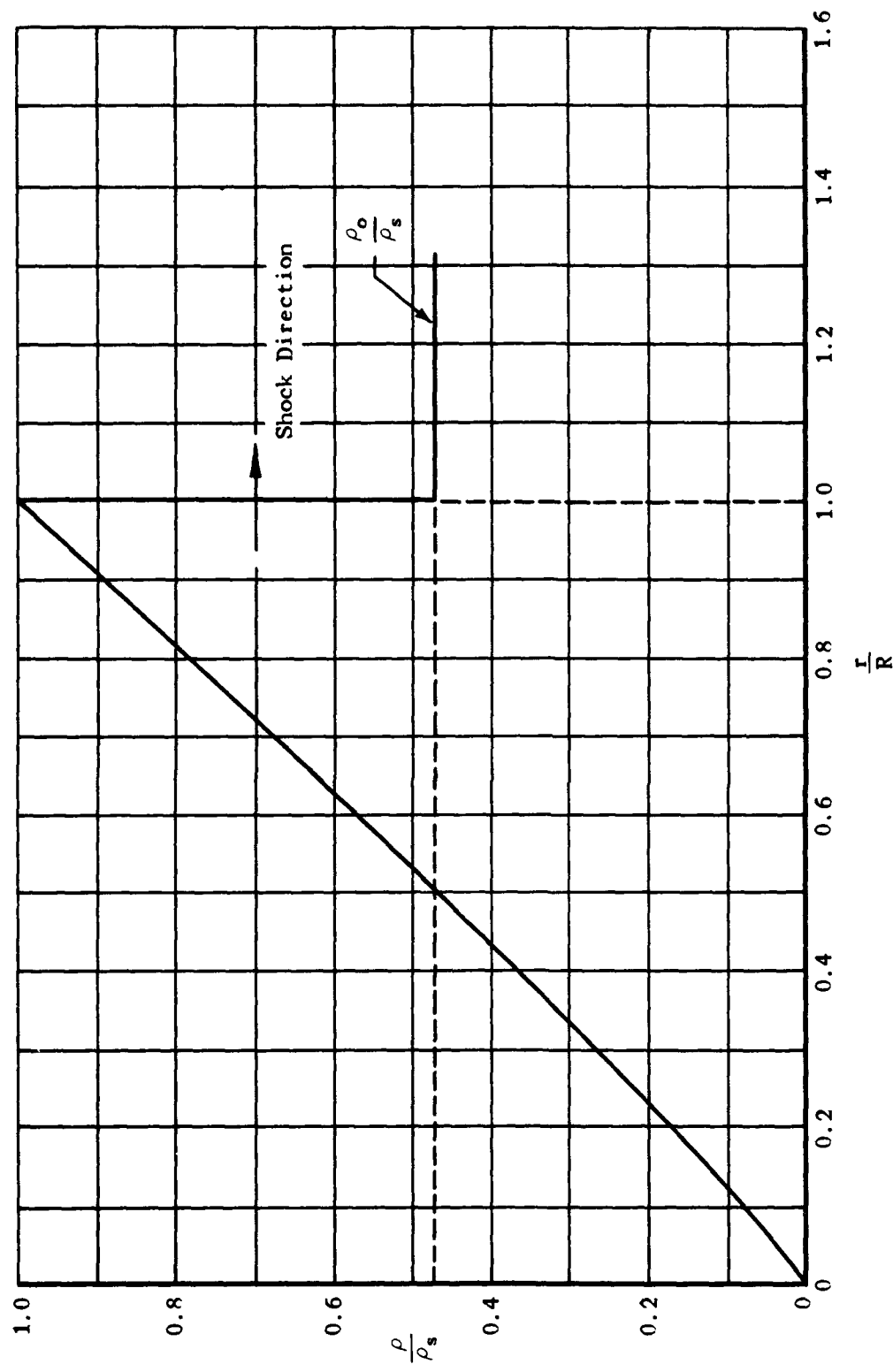


Fig. 4. Fluid Density Distribution Versus $\left(\frac{r}{R}\right)$ for $\xi = 3$

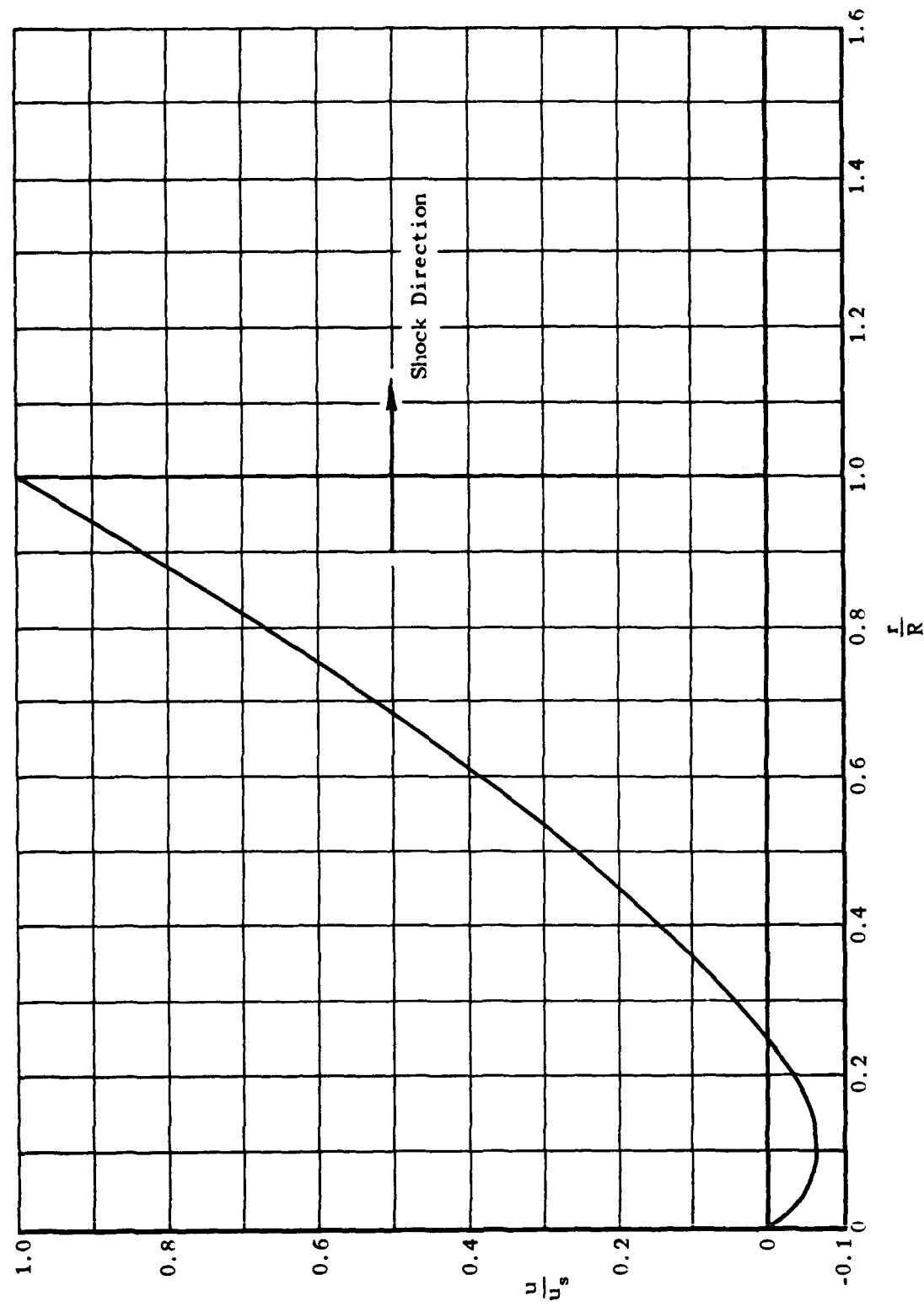


Fig. 5. Particle Velocity Distribution Versus $\left(\frac{r}{R}\right)$ for $\xi = 2$

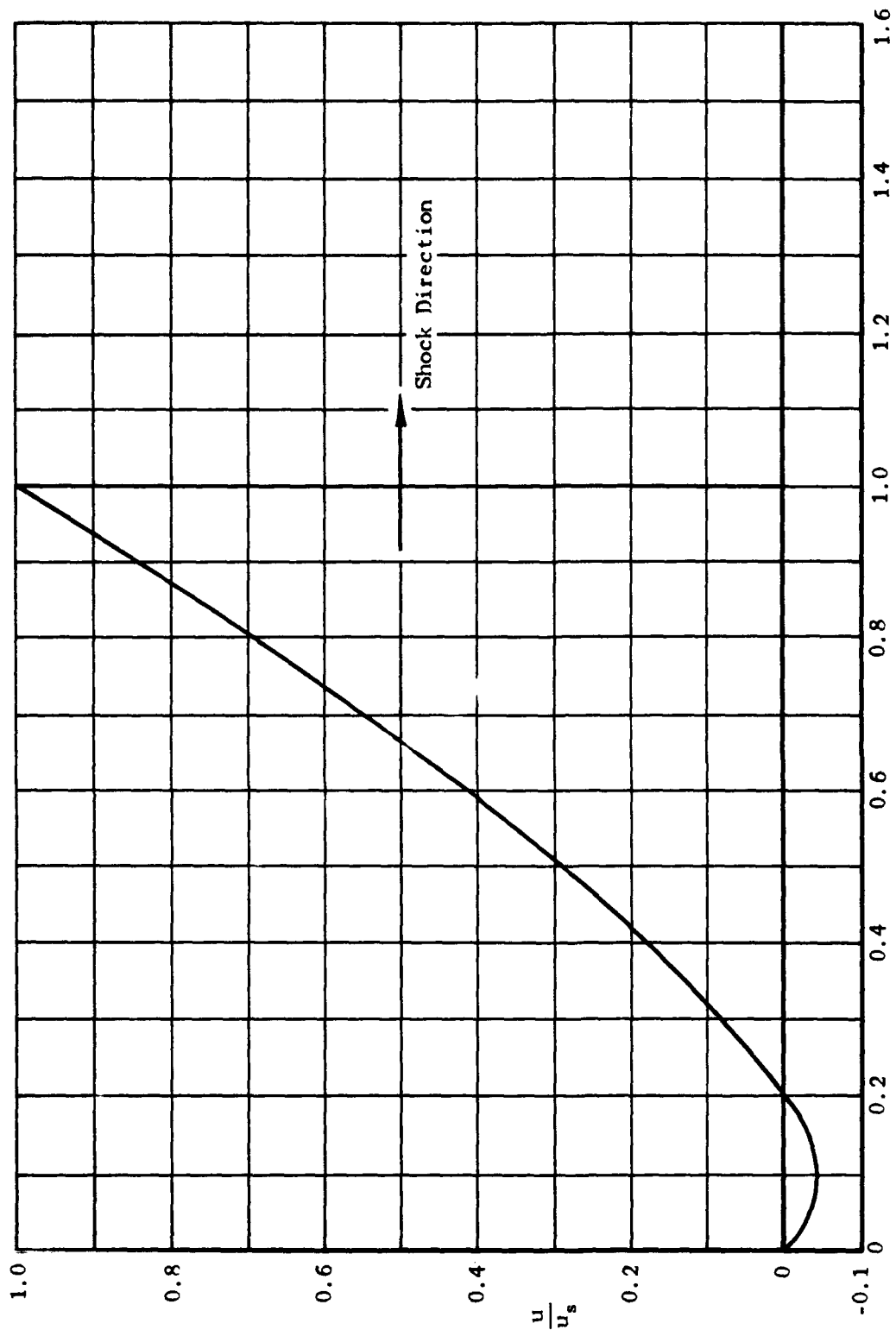


Fig. 6. Particle Velocity Distribution Versus $\left(\frac{r}{R}\right)$ for $\xi = 3$

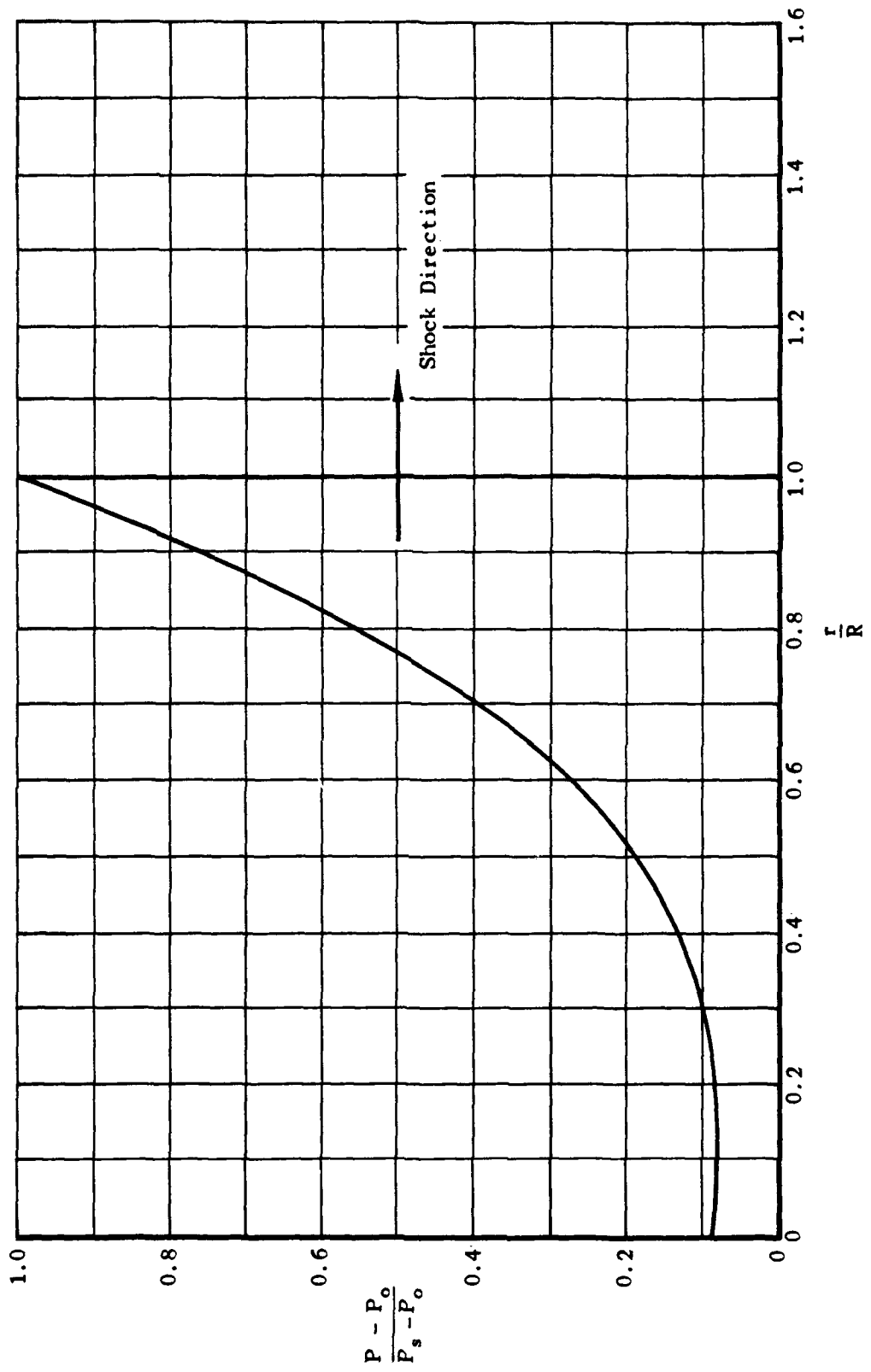


Fig. 7. Pressure Wave Form Versus $\left(\frac{r}{R}\right)$ for $\xi = 2$

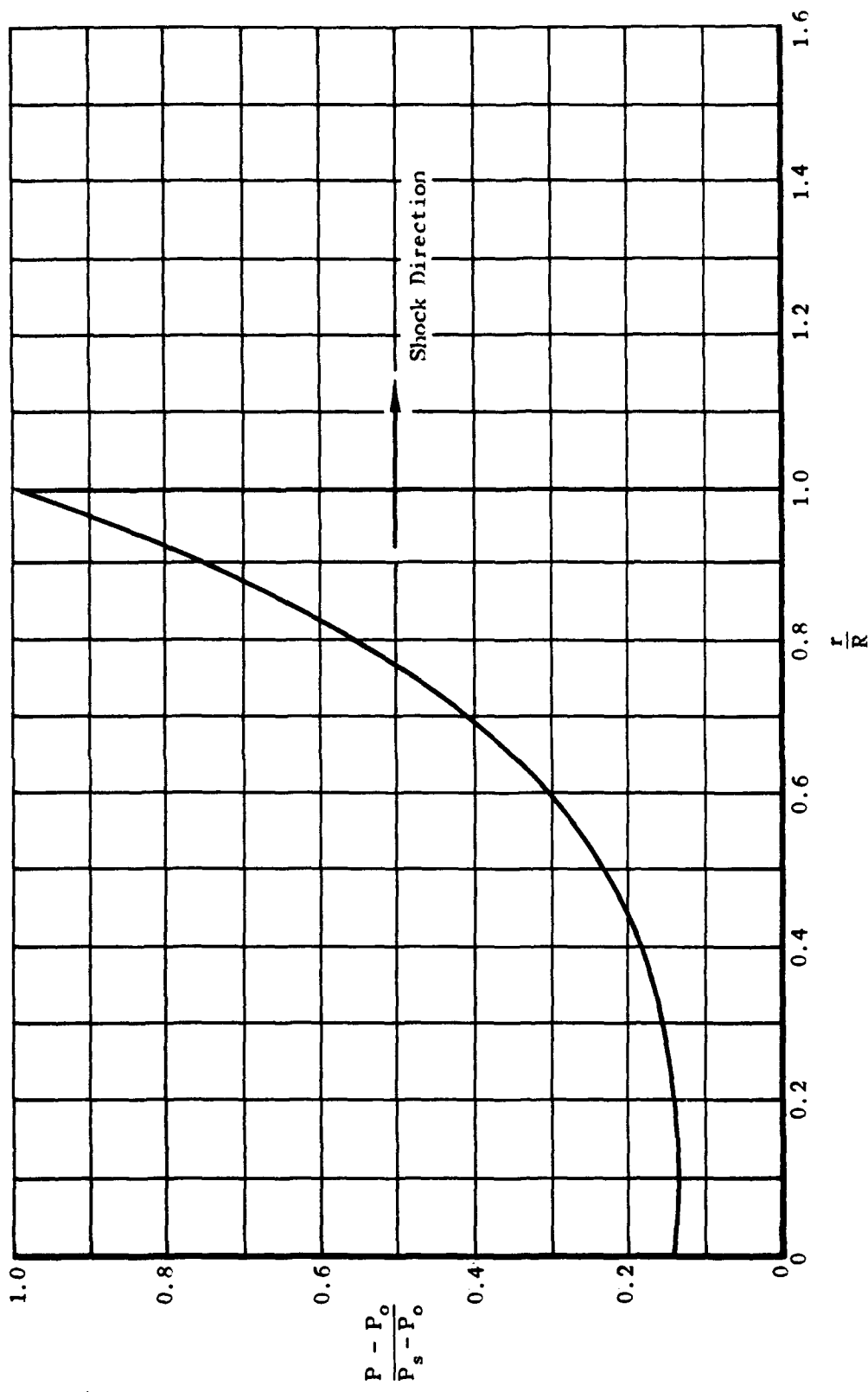


Fig. 8. Pressure Wave Form Versus $\left(\frac{r}{R}\right)$ for $\xi = 3$

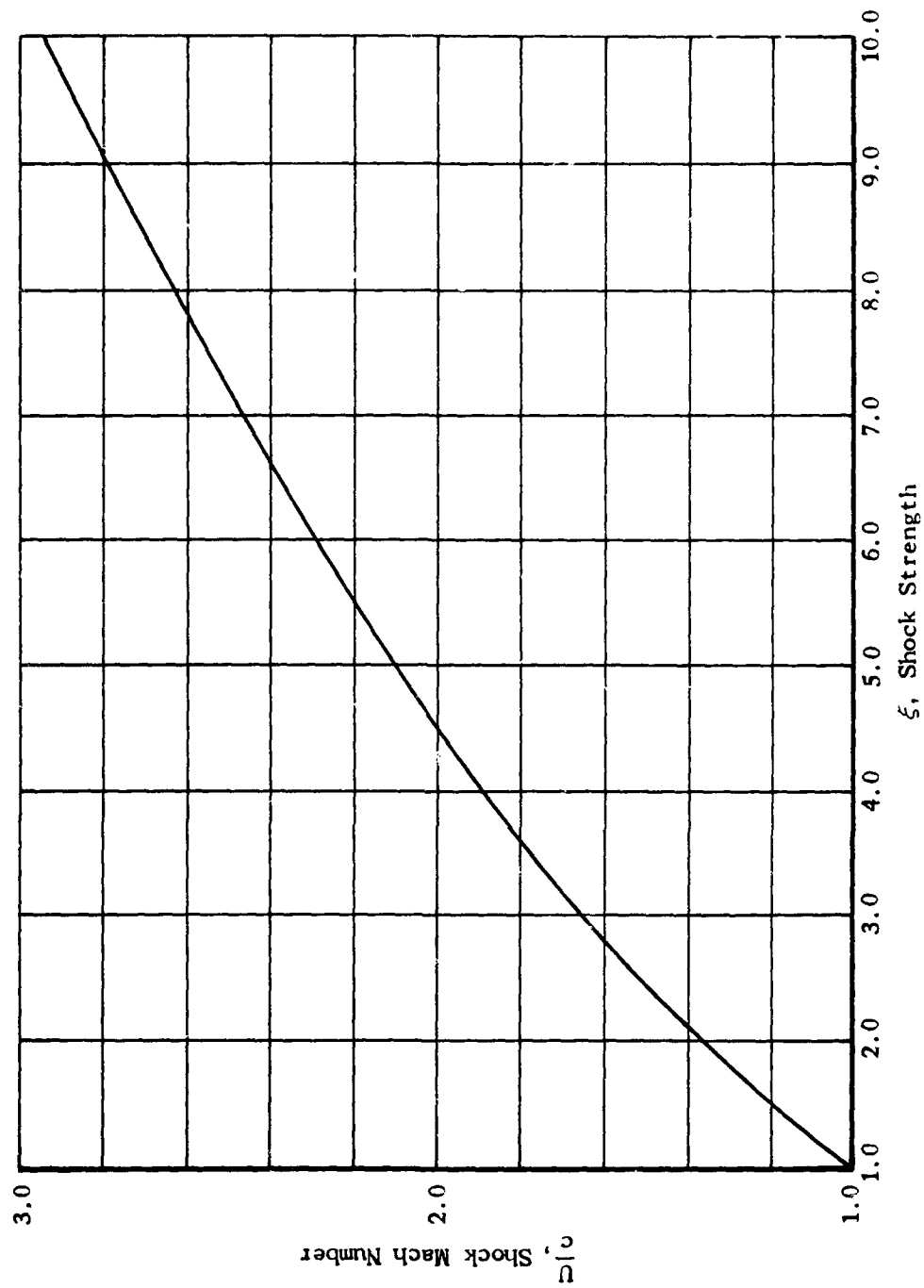


Fig. 9. Shock Mach Number Versus Shock Strength, ξ

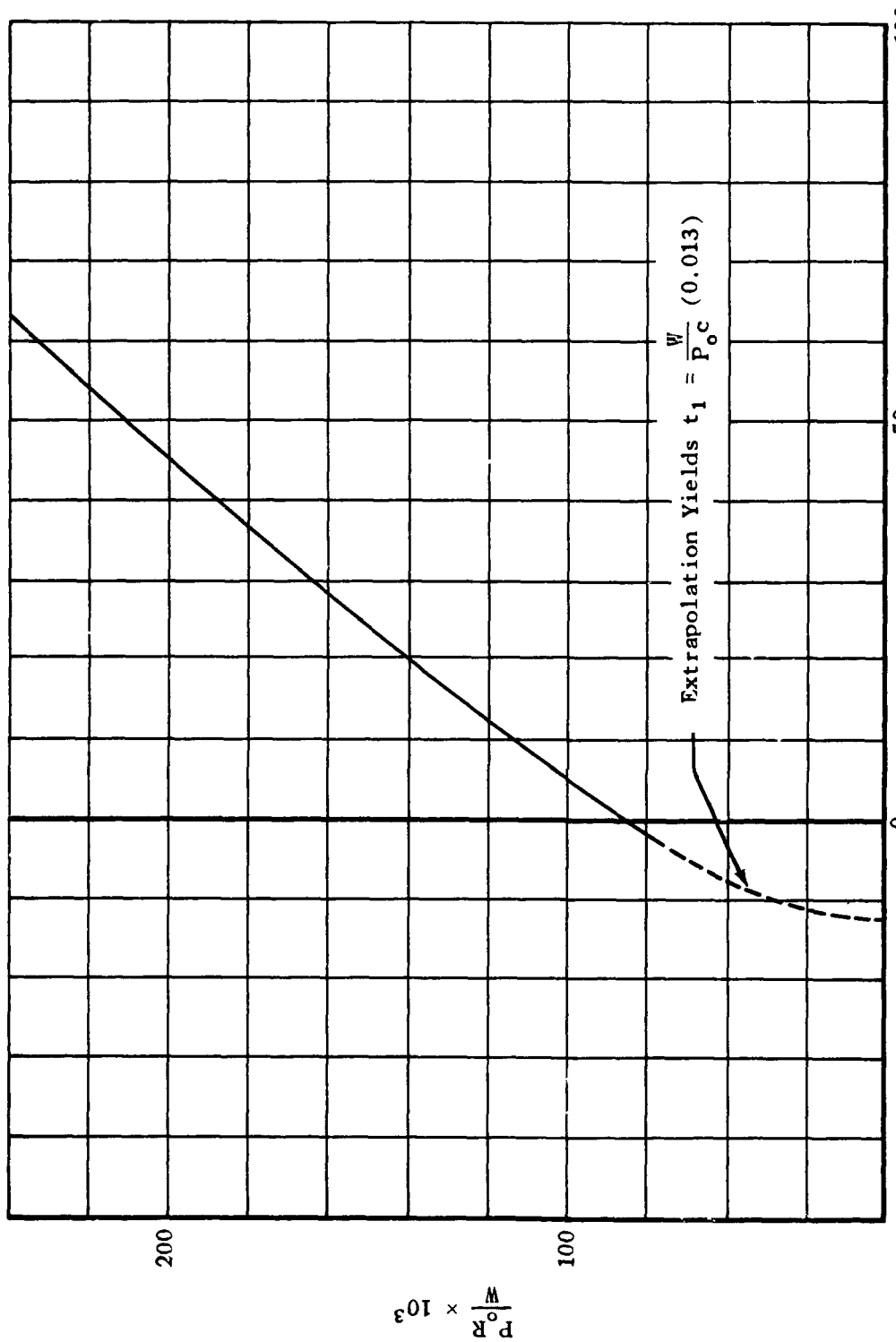


Fig. 10. Scaled Distance Versus Scaled Time $\frac{P_0 c(t - t_1)}{W} \times 10^3$

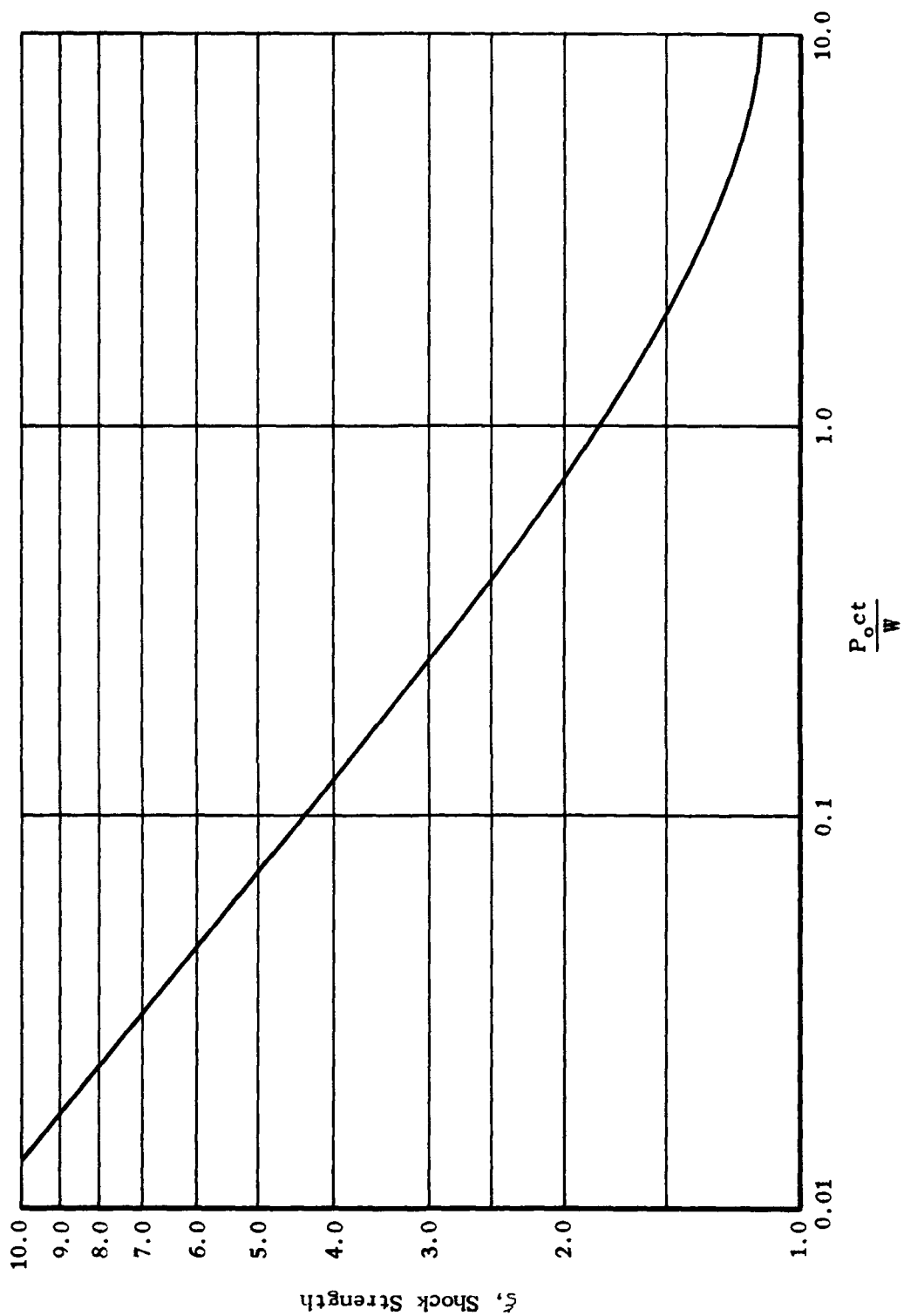


Fig. 11. Scaled Time Versus Shock Strength, ξ

CHAPTER III

SINGLE CHARGE RESULTS APPLIED TO MULTIPLE CHARGE SYSTEM FOR GENERATING DESIRED PRESSURE PULSES

In retrospect the results obtained in this study specifically are; (1) a shock strength-scaled distance decay curve, (2) a shock strength-scaled time decay curve, and (3) a complete description as to the behavior of the gas flow variables behind an explosive generated shock front, that is, under the power law density assumption.

Shock Strength-Scaled Distance Curve

The first of these results as shown in Fig. 2 is considered in good agreement with experimentally gathered data. That the theoretical and the experimental curves do tend to separate for the lower range of shock strengths is more than likely due to the fact that the assumed density distribution is less accurate for low values of shock strength. These two curves do agree quite well, however, for shock strengths above two. This result enables one to calculate the conditions necessary to generate a desired shock wave. For example, if the distance and shock strength of a desired wave are given, the size of the charge necessary to generate the wave may be easily calculated.

Shock Strength-Scaled Time Curve

This curve, as shown in Fig. 11, shows the time decay history of an explosive generated shock wave. It serves somewhat the same purpose as the shock strength-scaled distance curve. With the addition of this curve it is now possible to calculate the time of arrival of any given shock. This time decay history also makes it possible to calculate numerically the density, particle velocity, and pressure time distributions behind an explosive generated shock wave. With time distributions a direct comparison may be made with experimentally gathered data.

Behavior of the Gas Flow Variables Behind the Shock Front

Although this study makes the calculation of the various gas flow variable distributions behind the shock front possible, both space wise and time wise, it must be remembered that this is only under the density power law assumption, Eq. 1. However, the distributions, some of which are shown in Figs. 3-8, do give some indication as to the expected behavior of these gas flow variables behind the shock front. This behavior is also supported by what is experimentally observed.

Probably the most significant result this study brings forward concerning the behavior of the gas flow variables, is that concerning the existence of a positive pressure phase duration (that is, time measured from the shock front back to the point where the pressure drops below ambient). Previously the existence of such a duration has been taken for granted, the reason being that it has been clearly observed in the case of a spherical shock wave. However, in that case spherical divergence tends to emphasize the peakedness of the explosive-generated wave, and therefore explains the existence of the positive phase duration. In the one-dimensional case no such divergence exists and therefore such a duration need not exist. This is precisely what is indicated in this study. For very weak shocks, that is $\xi \sim 1$, the analysis does indicate that such a duration is present, which is to be expected as the overpressure never differs greatly from ambient pressure.

The analysis is supported by experiment in that a positive pressure phase duration is not clearly defined on pressure-time records taken in the shock tube. Records taken at the Air Force's Gary, Indiana Shock Tube Laboratory

indicate that the pressures merely approach ambient pressure asymptotically, and do not drop below.

With such experimental support it is felt that this analysis does give an insight not only as to the over-all behavior of an explosive generated shock wave, but also the behavior of the flow variables behind the shock front. It is with this foundation then that the following sections derive an approximate solution for generating various desired pressure pulses.

Approximate Method Employed for Multiple Charge Problem

In order that a solution for a second charge may be found, the conditions set up by the first charge must be considered. It is therefore assumed that the first shock sets up a new set of average ambient conditions given by the expressions

$$\bar{P} = \frac{\int_0^{R_p} dr}{\int_0^R dr},$$

and

$$\bar{u} = \frac{\int_0^{R_u} dr}{\int_0^R dr}.$$

These are easily computed using the pressure and particle velocity wave form solutions from the single charge. The results are

$$\bar{P} = \left\{ (\xi - 1) \left[1 - K + \frac{K}{\eta_s + 2} - \frac{L}{(\eta_s + 2)} 2 + \frac{2M}{(\eta_s + 2)} 3 \right] + 1 \right\} P_0$$

$$\bar{u} = \left(\frac{\alpha + 2}{4} \right) u_s.$$

A new average sound speed \bar{c} is defined by $\bar{c} = c_0 \left(\frac{P}{P_0} \right)^{1/2}$.

The two charge problems may now be solved. Suppose a ξ_1 is desired at a distance R_1 , and is to be followed by a ξ_2 at a distance R_2 ; the charge weights W_1 , W_2 and the time delay between the detonation of the two charges may be found as follows:

$$\begin{aligned} \xi_1, R_1 \text{ imply } & \left\{ \begin{array}{l} W_1 \text{ (from } \lambda \text{ versus } \xi \text{ plot, Fig. 2)} \\ t_1 \text{ (from } \frac{P_0 c t}{W} \text{ versus } \xi \text{ plot, Fig. 11)} \\ \bar{P} \text{ and } \bar{u}, \text{ (from above equations)} \end{array} \right. \\ \xi_2 \text{ implies } & \left\{ \begin{array}{l} \frac{R_c^*}{W_2} \text{ (from } \lambda \text{ versus } \xi \text{ plot)} \\ \frac{t_2}{W_2} \text{ (from } \frac{P_0 c t}{W} \text{ versus } \xi \text{ plot)} \end{array} \right. \end{aligned}$$

* some distance R corresponding to a shock of strength ξ_2 moving into a still gas, but not equal to R_2 as the gas in front of second shock is in motion.

Using the above information and noting that

$$\begin{aligned} R_2 &= R_c + \bar{u} t_2 \\ &= \left(\frac{R_c}{W_2} \right) W_2 + \bar{u} \left(\frac{t_2}{W_2} \right) W_2 \end{aligned}$$

Solving for W_2 the second charge weight gives

$$W_2 = \frac{R_2}{\left(\frac{R_c}{W_2} \right) + \bar{u} \left(\frac{t_2}{W_2} \right)} \quad (6)$$

from which

$$t_2 = W_2 \left(\frac{t_2}{W_2} \right)$$

This gives the time delay between detonations

$$\Delta t = t_1 - t_2 \quad (7)$$

These are the necessary parameters for generating the desired wave form.

It will now be shown that this method may be expanded into a solution for an arbitrary number of charges. The assumption is made as before that each successive shock sets up a new set of ambient conditions. For the n^{th} shock these conditions are:

$$\bar{P}_n = \left\{ (\xi - 1) \left[1 - K + \frac{K}{\eta_s + 2} - \frac{L}{(\eta_s + 2)^2} + \frac{2M}{(\eta_s + 2)^3} \right] + 1 \right\} \bar{P}_{n-1}, \quad (8)$$

$$\bar{u}_n = \left(\frac{\alpha + 2}{4} \right) (u_s)_n + \bar{u}_{n-1}, \quad (9)$$

and

$$\bar{c} = \left(\frac{\bar{P}_n}{P_0} \right)^{1/2} c_0. \quad (10)$$

where the parameters ξ , η_s , K , L , M , and α are all determined by the n^{th} shock.

The procedure consists of treating ξ_1 , R_1 and ξ_2 , R_2 as described above, thus obtaining the complete solution for generating waves one and two. Next wave two and wave three are considered. The procedure is the same

with the exception of the computation of \bar{P} , \bar{u} , and \bar{c} . They are computed using Eqs. 8, 9, and 10. Likewise any number of charges may be treated in this manner. In the following chapter the three desired wave forms are constructed using this procedure. The form of the solution will be more explicitly defined as these individual cases are treated.

Figures 12, 13 and 14 present \bar{P} , \bar{c} , and \bar{u} respectively as a function of shock strength. These curves eliminate many of the computations involved in the multiple charge solution procedure.

Reliability of the Approximate Solution

There are several errors introduced by the use of this approximation solution, however, each error is in itself compensating or has a corresponding compensating error. The errors are:

- (1) An average \bar{u} is used instead of its actual value at a particular point.
- (2) An average \bar{P} is used instead of its actual value at a particular point.
- (3) The above are computed by assuming the shock, which sets up the new ambient conditions, is at its desired strength and position.
 - (a) This results in a lower \bar{P} than is actually seen by the shock wave following, and thus giving the new shock wave a higher shock velocity than it actually has.
 - (b) It also results in a lower \bar{u} than is actually the case.

It is apparent that (1) and (2), being averages, are nearly self-compensating, but they are not entirely self-compensating because they are average values over the entire shock wave where as the new shock travels only a fraction of this distance.

This implies the \bar{P} and \bar{u} computed are too high, giving the new shock wave a lower computed velocity than it actually has, but the correspondingly high \bar{u} compensates. Similarly (3a) and (3b) compensate for each other. Although the errors introduced by this approximation method compensate for each other, there is no guarantee that the balance is perfect.

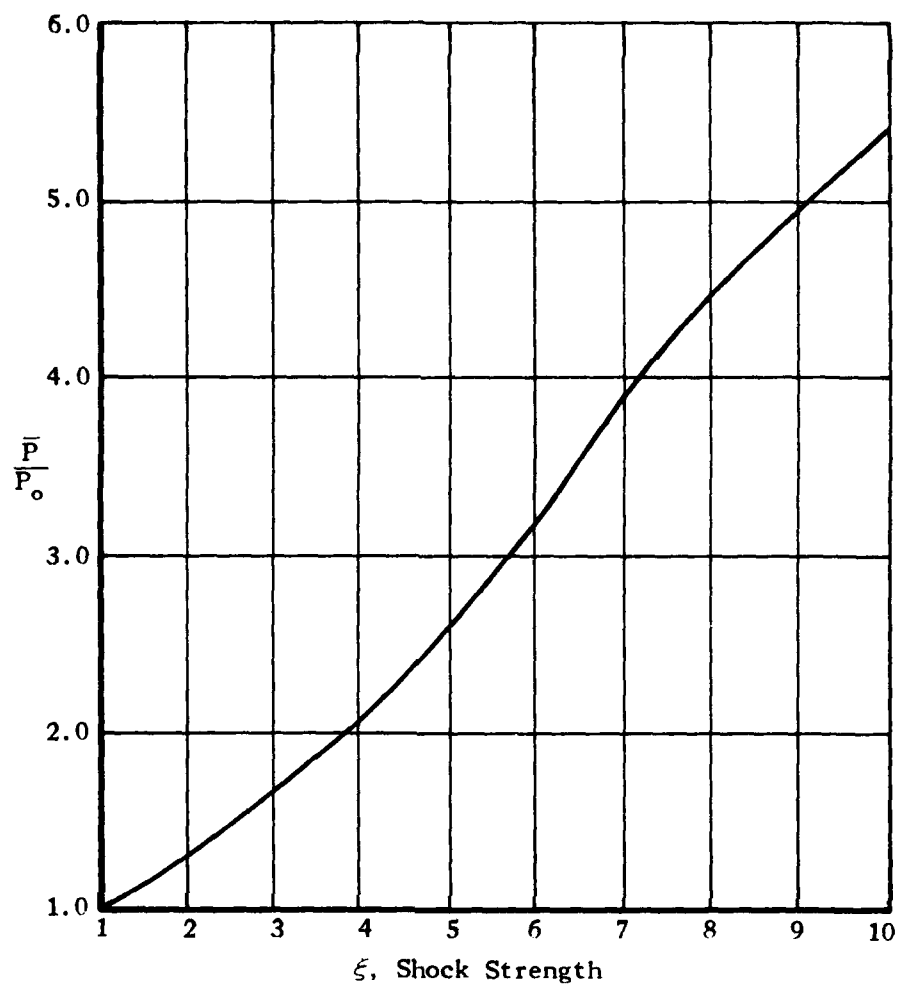


Fig. 12. Average Pressure Behind Shock Front, \bar{P} , Versus Shock Strength, ξ

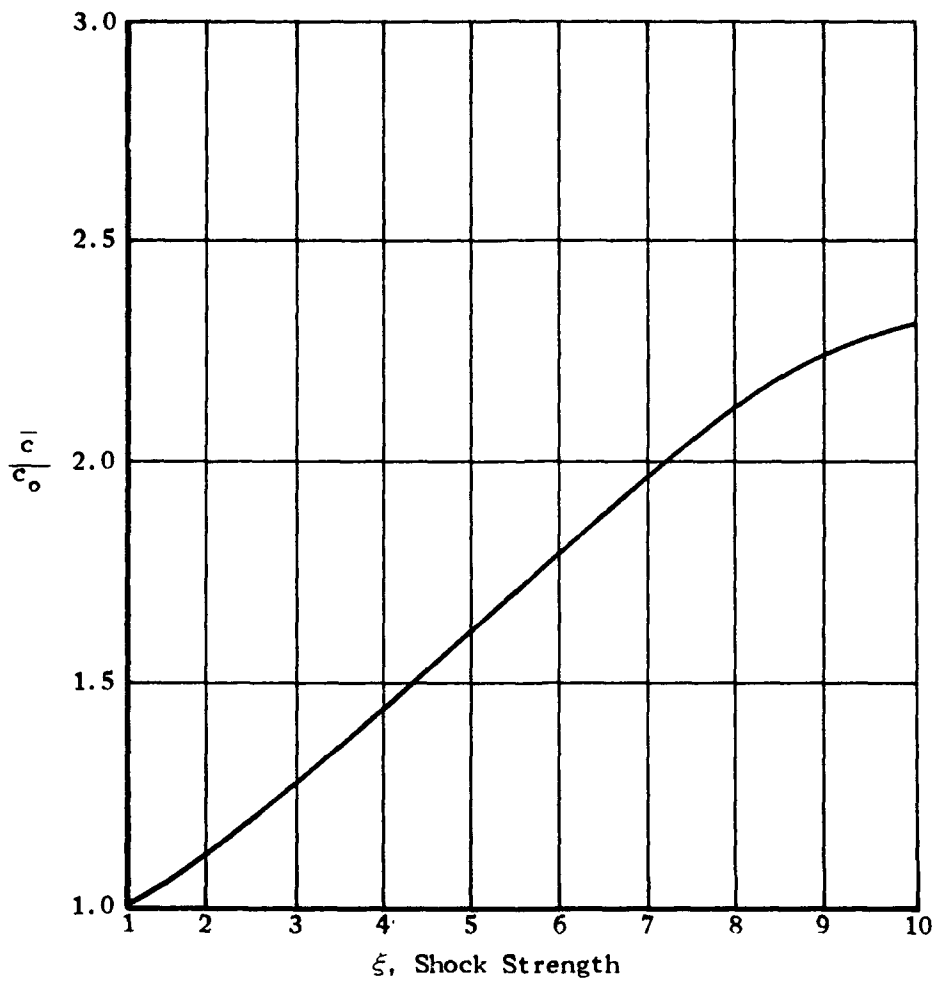


Fig. 13. Average Sound Speed Behind Shock Front, \bar{c} , Versus Shock Strength, ξ

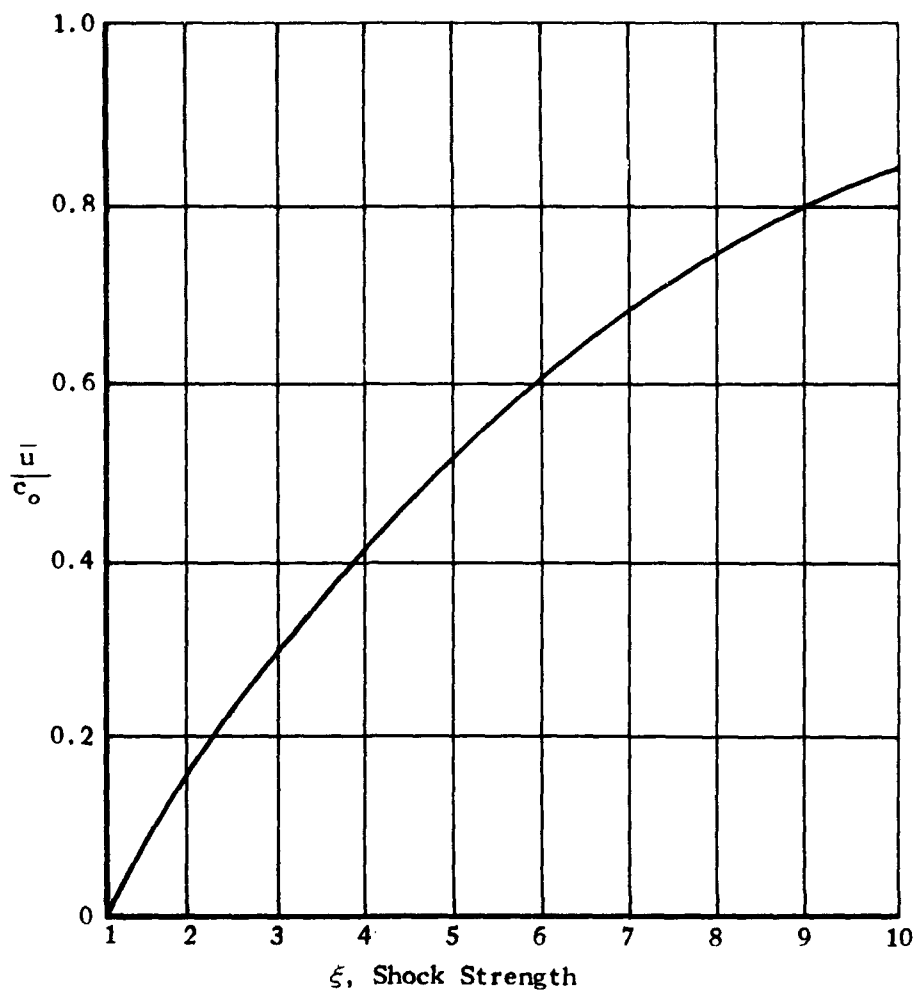


Fig. 14. Average Particle Velocity Behind Shock Front, \bar{u} , Versus Shock Strength, ξ

CHAPTER IV SOLUTIONS TO THE THREE DESIRED WAVE FORMS

It is now possible to find the charge weights and their times of detonation in order to produce a series of desired shock waves at a corresponding series of desired distances. However, in the three cases to be solved, shock strengths and time durations are given, as opposed to shock strengths and distances. This makes it necessary to determine the relationship between ξ , R , and t_0 , duration.

As shown in Figs. 7 and 8 there is no apparent duration occurring for one-dimensional shock waves; however, for very weak shocks ($\xi \approx 1$) a negative phase does occur in this theory. The theory itself is supported by actual experiment. Pressure-time records taken at the Air Force's Gary, Indiana Shock Tube Laboratory indicate that a duration, or, in other words, a positive and negative phase, does not occur. In most cases, however, the record approaches ambient pressure rapidly but asymptotically.

In the case of a spherical shock wave originating from a point source in a homogeneous atmosphere, spherical divergence tends to emphasize the peakedness of the explosive-generated wave. Decays of pressure in both space and time are thus more rapid in this "three-dimensional" case, and phases of negative pressure are clearly evident over a wide range of shock strengths. The conventional form taken for pressure-time variations in work with high explosives has been

$$P(t) - P_0 = (P_s - P_0) e^{-t/t_0} (1 - t/t_0),$$

in which t_0 is the duration of the positive pressure phase. It is seen that this wave form decays in overpressure to one-half of the peak overpressure in about one-third of the positive phase duration. The conventional "duration" for a wave propagating in a constant area channel (shock tube) is thus calculated in the present report as three times the decay time to half the peak overpressure.

Now using Eq. 4, it is possible to find a value of $(\frac{r}{R})$, say $(\frac{r}{R})^*$, which corresponds to $\frac{P - P_0}{P_s - P_0} = 0.5$, for any given shock strength. These values, $(\frac{r}{R})^*$, have been computed and are presented as a function of shock strength in Fig. 15, Values of particle velocity, where $(\frac{r}{R}) = (\frac{r}{R})^*$ are now computed from Eq. 3 for a range of shock strengths. For the same range of shock strengths the sound velocity say c^* , is computed at the half overpressure point relative to still air. With this information the following equation relates the previously defined duration to distance:

$$\left(\frac{u^* + c^*}{3}\right) t_0 = \left[1 - \left(\frac{r}{R}\right)^*\right] R$$

or solving for R gives

$$R = \frac{(u^* + c^*) t_0}{3 \left[1 - \left(\frac{r}{R}\right)^*\right]} \quad (11)$$

The ratio of the coefficient of t_0 to c , sound speed, is plotted as a function of shock strength in Fig. 16. This curve may now be used in computing a distance, given a shock strength, a duration, and the ambient conditions.

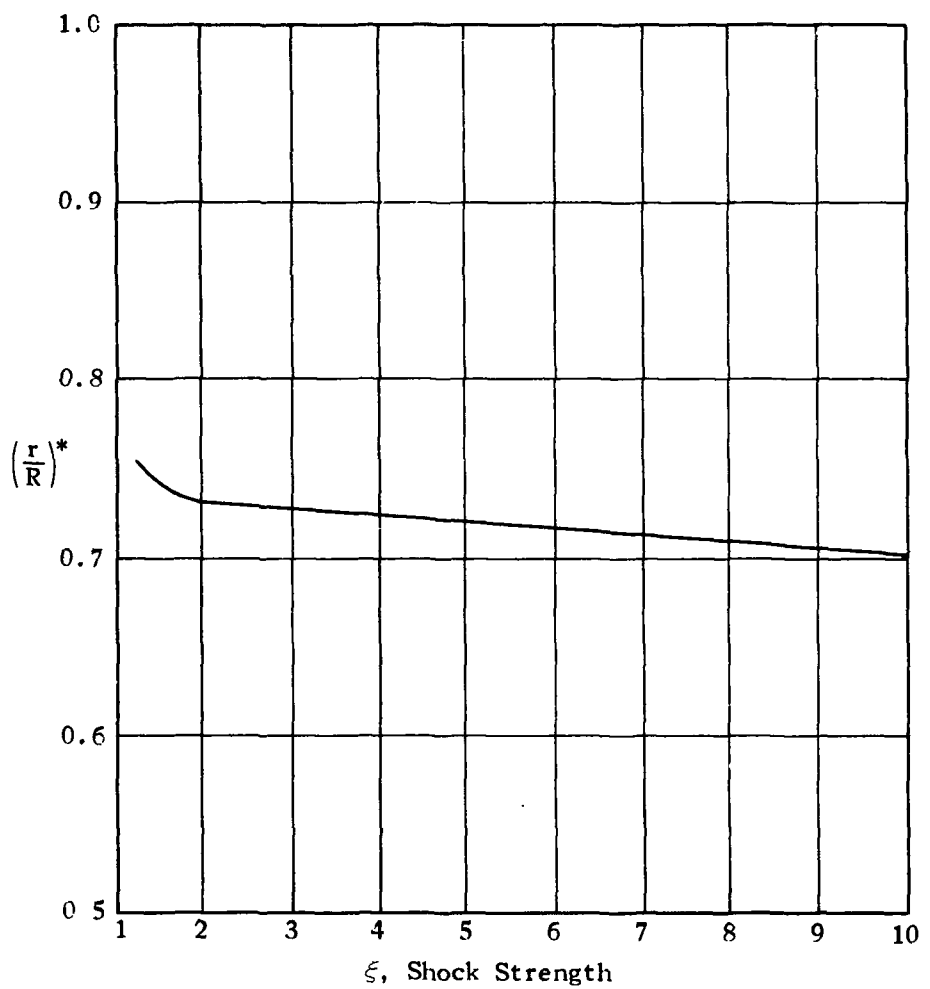


Fig. 15. $(\frac{r}{R})^*$ Versus Shock Strength, ξ

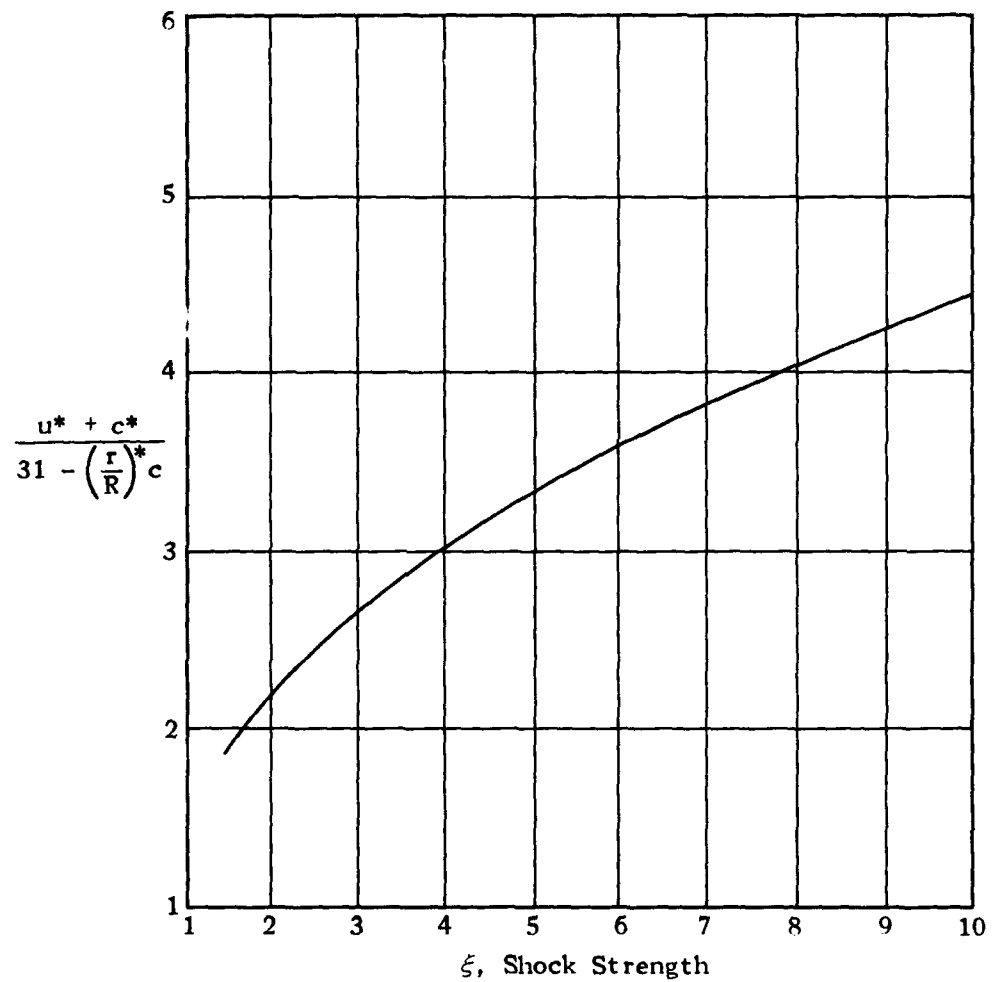


Fig. 16. $\frac{u^* + c^*}{3\left[1 - \left(\frac{r}{R}\right)^*\right]c}$ Versus Shock Strength, ξ

Solution for the Double Peaked Wave Form

The simplest of the three wave forms to be constructed is the double peaked wave form. It will therefore be treated first. The particular pressure time form desired is shown in Fig. 17.

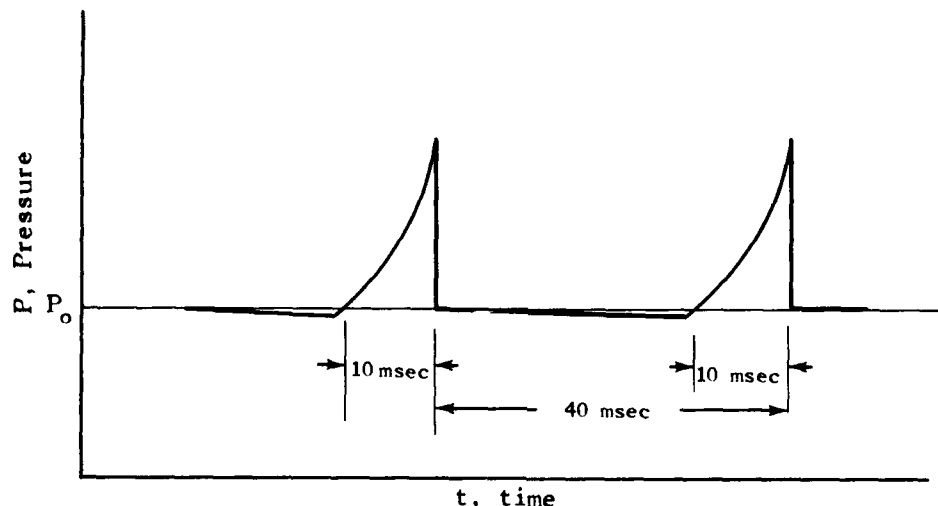


Fig. 17. Double Peaked Wave Form

Wave one is first considered. It is noted that a shock strength, ξ , of 2 with a duration of 10 milliseconds is desired. Figure 16 gives

$$\frac{u^* + c^*}{3 \left[1 - \left(\frac{r}{R} \right)^* \right]} \frac{1}{c_0} = 2.21$$

for $\xi = 2$, which gives

$$\begin{aligned} R &= 2.21 c_0 t_0 \\ &= (2.21)(1117 \text{ ft/sec})(0.01 \text{ sec}) \\ &= 25 \text{ ft} \end{aligned}$$

Figure 2, ξ versus λ , gives

$$\lambda = 1.25/\text{ft}^2$$

for $\xi = 2$, and taking the value of R from above gives

$$\frac{\lambda}{R} = \frac{P_0}{W} = 0.05/\text{ft}^3$$

$$W_1 = \frac{(14.7 \text{ lb/in.})^2 (144 \text{ in.}^2/\text{ft}^2)}{0.05/\text{ft}^3} = 42,336 \text{ ft-lbs}$$

Figure 11 gives a time of arrival for the first shock wave. For $\xi = 2$

$$\frac{P_0 c t_1}{W} = 0.7/\text{ft}^2$$

$$t_1 = \frac{0.7/\text{ft}^2}{\frac{P_0 c}{W}} = \frac{(0.7/\text{ft}^2) 10^3 \text{ msec/sec}}{(0.05/\text{ft}^3)(1117 \text{ ft/sec})} = 12.5 \text{ msec}$$

With the time of arrival known, the position of shock wave one may be found at the time the second wave is at the 25-foot distance (40 milliseconds later).

$$\frac{P_0 c (t_1 + 40)}{W_1} = 2.94/\text{ft}^2$$

which corresponds to a $\xi = 1.2$ and a distance $R = 156$.

The problem is now in the form in which the approximate method may be applied. The charge weight for the first shock has already been found, which

leaves only the second charge weight and the time differential between detonations to be found.

The values of \bar{P} , \bar{u} , and \bar{c} for $\xi = 1.2$ are, from Figs. 12, 13 and 14

$$\bar{P} = 1.05 P_0$$

$$\bar{u} = 0.04 c$$

$$\bar{c} = 1.025 c_0$$

This implies that the second wave with a $\xi_2 = 2$ relative to P_0 has for purposes of computation a $\xi = \frac{2.00}{1.05} = 1.90$. From Figs. 2 and 11, $\xi = 1.90$ implies

$$\frac{R_c}{W_2} = \frac{1.43/\text{ft}^2}{\bar{P}} = 6.43 \times 10^{-4}/\text{lb}$$

and

$$\frac{t_2}{W_2} = \frac{0.9/\text{ft}^2}{\bar{P} \bar{c}} = 3.63 \times 10^{-7} \text{ sec}/\text{ft-lb}$$

Putting these values into Eq. 6 gives

$$W_2 = 3.79 \times 10^4 \text{ ft-lbs}$$

and therefore

$$t_2 = W_2 \left(\frac{t_2}{W_2} \right) = 13.75 \text{ msec}$$

By Eq. 7

$$\Delta t = t_1 - t_2 = (12.5 + 40) - 13.75 = 38.75 \text{ msec}$$

To summarize then, the desired wave form in Fig. 17 may be generated at a distance of 25 feet using

$$W_1 = 4.23 \times 10^4 \text{ ft-lbs}$$

and

$$W_2 = 3.79 \times 10^4 \text{ ft-lbs}$$

With a time spacing of detonation equal to 38.75 milliseconds. These are the parameters for a unit cross-sectional area channel.

The 50-Millisecond Buildup, Finite Rise Time Wave Form

The next shock wave to be considered is the finite rise time wave form which builds up slowing to peak in about 50 milliseconds, and then decays to zero in another 50 milliseconds. This wave will be approximated by a series of six smaller shock waves, as shown in Fig. 18.

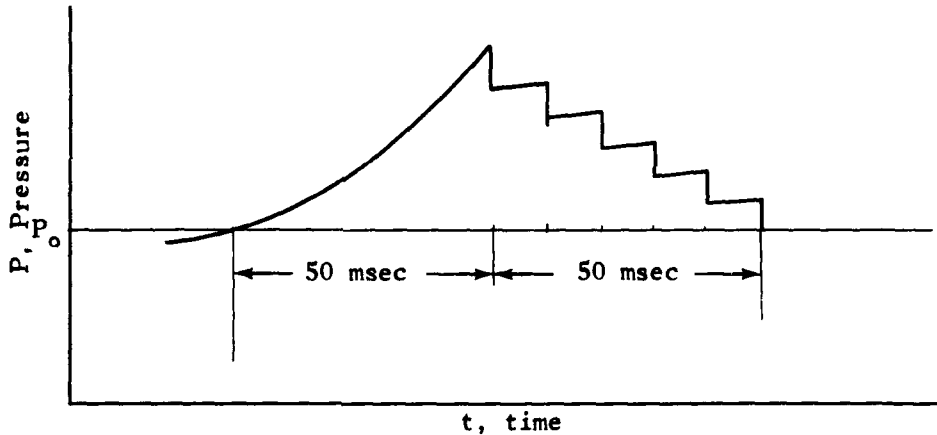


Fig. 18. The 50-Millisecond Buildup,
Finite Rise Time Wave Form

The first step in determining the parameters which will generate this finite rise time wave is to determine the distance at which a duration of 50 milliseconds occurs for a shock strength of two. Using Fig. 18

$$R = (2.205)(1117)(0.05) = 123 \text{ ft}$$

For wave one ξ_1 , = 1.167, which gives

$$\lambda_1 = 10/\text{ft}^2$$

From Fig. 1,

$$\Delta t R = 123$$

$$\frac{\lambda_1}{R} = \frac{P_0}{W_1} = 0.0813/\text{ft}^3$$

and at atmospheric conditions

$$W_1 = 2.61 \times 10^4 \text{ ft-lbs}$$

Figure 11 gives

$$\frac{P_0 c_0 t_1}{W_1} = 6.2/\text{ft}^2$$

from which

$$t_1 = 68.3 \text{ msec}$$

When wave two arrives at the 123-foot distance, wave one has traveled another ten milliseconds. It has therefore decayed to the following derived shock strength.

$$\frac{P_0 c_0 (t_1 + 10)}{W_1} = 7.11/\text{ft}^2 \text{ which implies } \xi_1 = 1.145$$

This new ξ_1 gives the new ambient conditions for the second wave.

They are, from Figs. 12, 13 and 14

$$\bar{P} = 1.04 P_0$$

$$\bar{u}_1 = 0.029 c_0$$

$$\bar{c}_1 = 1.02 c_0$$

Relative to the new ambient pressure the shock strength of wave number two is

$$\xi_2 = \frac{1.33}{1.04} = 1.28$$

Now for ξ_2 , Figs. 2 and 11 give respectively

$$\frac{\bar{P}_1 R_0}{W_2} = 5.5/\text{ft}^2$$

$$\frac{\bar{P}_1 \bar{c}_1 t_2}{W_2} = 3.7/\text{ft}^2$$

Using the values of \bar{P} and \bar{c} in the above yields

$$\frac{R_c}{W_2} = 2.5 \times 10^{-3}/\text{lb}$$

$$\frac{t_0}{W_2} = 1.48 \times 10^{-6} \text{ sec/ft-lb}$$

Equation 6 now gives

$$W_2 = 4.82 \times 10^4 \text{ ft-lbs}$$

and

$$t_2 = W_2 \left(\frac{t_0}{W_2} \right) = 70.3, \text{ xo by Eq. 7}$$

$$\Delta t_1 = (t_1 + 10) - t_2 = 8 \text{ msec}$$

Next, wave three is considered, with wave two setting up the new ambient conditions. Wave two travels for an additional 10 milliseconds before wave three is at the 123-foot distance so that it decays in shock strength. Its new shock strength is, from Fig. 11,

$$\frac{\bar{P}_1 \bar{c}_1 (t_2 + 10)}{W_2} = 4.22/\text{ft}^2$$

Which implies $\xi_2 = 1.245$. Again from Fig. 11 the new set of ambient conditions is

$$\bar{P}_2 = 1.06 \bar{P}_1 = 1.10 P_0$$

$$\bar{u}_2 = 0.048 \bar{c}_1 + \bar{u}_1 = 0.078 c_0$$

$$\bar{c}_2 = 1.048 c_0$$

Relative to the new conditions, the shock strength of wave three is

$$\xi_3 = \frac{1.50}{1.10} = 1.365$$

For ξ_3 , Figs. 2 and 11 yield

$$\frac{\bar{P}_2 R_c}{W_3} = 4.1/\text{ft}^2$$

and

$$\frac{\bar{P}_2 \bar{c}_2 t_3}{W_3} = 2.75/\text{ft}^2$$

from which

$$\frac{R_c}{W_3} = 1.76 \times 10^{-3}/\text{lb}$$

and

$$\frac{t_3}{W_3} = 1.000 \times 10^{-6} \text{ sec/ft-lb}$$

Equation 6 gives

$$W_3 = 6.66 \times 10^4 \text{ ft-lb}$$

and it follows that

$$t_3 = W_3 \left(\frac{t_3}{W_3} \right) = 66.6 \text{ msec}$$

so by Eq. 7

$$\Delta t_2 = (t_2 + 10) - t_3 = 13.7 \text{ msec}$$

By repeating this procedure, the remaining charge weights may be found, and also their times of detonation. The results are:

$$W_4 = 7.52 \times 10^4 \text{ ft-lbs} \quad \Delta t_3 = 15.8 \text{ msec}$$

$$W_5 = 8.43 \times 10^4 \text{ ft-lbs} \quad \Delta t_4 = 13.4 \text{ msec}$$

$$W_6 = 8.83 \times 10^4 \text{ ft-lbs} \quad \Delta t_5 = 14.2 \text{ msec}$$

This completes the analysis for the 50-millisecond buildup, finite rise time wave form.

The 5-Millisecond Buildup, Finite Rise Time Wave Form

The final wave considered is another finite rise time type. However, in this case the buildup time to the peak overpressure is much more rapid, 5 milliseconds to peak overpressure and then 45 milliseconds for decay to zero overpressure. The wave is generated by a series of three smaller waves as shown in Fig. 19.

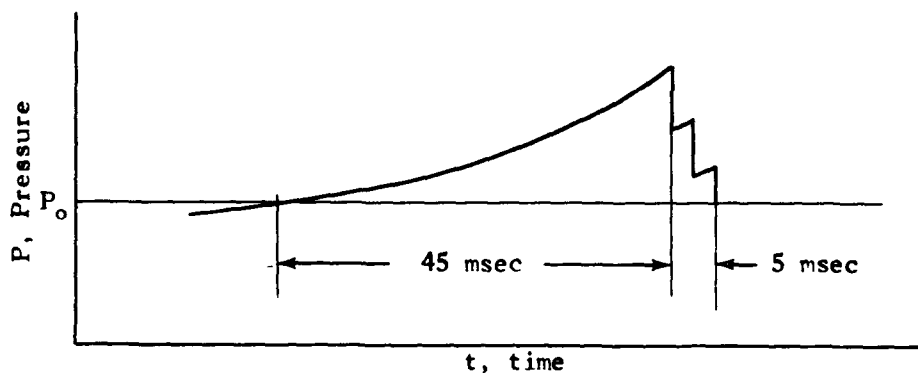


Fig. 19. The 5-Millisecond Buildup, Finite Rise Time Wave Form

The distance at which a shock strength of two has a duration of 45 milliseconds (from Fig. 17) is

$$R = (2.205)(1117)(0.045) = 110.8 \text{ ft}$$

Figures 2 and 11 give, for wave number one, $\xi_1 = 1.33$, respectively

$$\lambda_1 = 4.65/\text{ft}^2$$

$$\frac{P_0 c_0 t_1}{W_1} = 3.10/\text{ft}^2$$

At $R = 110.8$ feet

$$\frac{\lambda_1}{R} = \frac{P_0}{W_1} = 0.0420/\text{ft}^3$$

and at atmospheric conditions

$$W_1 = 5.04 \times 10^4 \text{ ft-lbs}$$

The time of arrival at $R = 110.8$ feet for wave one is

$$t = \frac{3.10/\text{ft}}{\frac{P_0}{W_1} c_0} = 66.1 \text{ msec}$$

Wave one progresses for 2.5 milliseconds farther before wave two arrives at the 110.8-foot position. Its shock strength then decays, and the new value (from Fig. 11)

$$\frac{P_0 c_0 (t_1 + 2.5)}{W} = 3.22/\text{ft}$$

is $\xi_1 = 1.32$.

This new ξ_1 gives the new ambient conditions for the second wave. They are, from Figs. 12, 13 and 14.

$$\bar{P} = 1.083 P_0$$

$$\bar{u} = 0.06 c_0$$

$$\bar{c} = 1.041 c_0$$

Relative to these ambient conditions the shock strength of wave two is

$$\xi_2 = \frac{1.67}{1.083} = 1.54$$

For ξ_2 , Figs. 2 and 11 give, respectively

$$\frac{\bar{P}_1 R_c}{W_2} = 2.63/\text{lb}$$

$$\frac{\bar{P}_1 \bar{c}_1 t_2}{W_2} = 1.68/\text{ft}$$

and knowing \bar{P}_1 and \bar{c}_1 results in

$$\frac{R_c}{W_2} = 1.147 \times 10^{-3}/\text{lb}$$

$$\frac{t_2}{W_2} = 0.628 \times 10^{-6} \text{ sec/ft-lb}$$

Equation 6 now gives

$$W_2 = 9.32 \times 10^4 \text{ ft-lbs}$$

and

$$t_2 = W_2 \left(\frac{t_2}{W_2} \right) = 58.5$$

The time differential of detonation is, from Eq. 7

$$\Delta t_1 = (t_1 + 2.5) - t_2 = 10.1 \text{ msec}$$

Next wave three is considered with wave two setting up the new ambient conditions. Wave two travels for an additional 2-1/2 milliseconds before wave three arrives at the 110.8-foot distance. Its decayed shock strength is, from Fig. 11

$$\frac{\bar{P}_1 \bar{c}_1 (t + 2.5)}{W_2} = 1.75/\text{ft}$$

which implies $\xi = 1.525$. From Figs. 12, 13 and 14 the new ambient conditions are

$$\bar{P}_2 = 1.143 \quad \bar{P}_1 = 1.24 \quad P_0$$

$$\bar{u}_2 = 0.096 \quad \bar{c}_1 + \bar{u}_1 = 0.16 \quad c_0$$

$$\bar{c}_2 = 1.114 \quad c_0$$

Relative to these conditions, wave three has a shock strength of

$$\xi_3 = \frac{2.00}{1.24} = 1.61$$

For this value of ξ , Figs. 2 and 11 give

$$\frac{\bar{P}_2 R_c}{W_3} = 2.275/\text{ft}$$

$$\frac{\bar{P}_2 \bar{c}_2 t_3}{W_3} = 1.43/\text{ft}$$

Substituting the values of \bar{P}_2 and \bar{c}_2 into the above equations give

$$\frac{R_c}{W_3} = 0.886 \times 10^{-3} \text{ lb}$$

$$\frac{t_3}{W_3} = 0.437 \times 10^{-6} \text{ sec/ft-lb}$$

Equation 6 now gives

$$W_3 = 11.73 \times 10^4 \text{ ft-lbs}$$

and

$$t_3 = W_3 \left(\frac{t_3}{W_3} \right) = 51.4 \text{ msec}$$

The t between the second and third detonations, by Eq. 6, is

$$\Delta t_2 = (t_2 + 2.5) - t_3 = 9.6 \text{ msec}$$

This completes the analysis for the third desired wave.

In the following section the results of these calculations will be summarized and tabulated.

Tabulated Results

In order that the results may be tabulated in a practical form, the charge weights are converted into feet of double-strength Primacord, the explosive used to generate blast waves in the Air Force's Shock Tube Laboratory at Gary, Indiana. Furthermore, the lengths are calculated for both a 6-foot diameter channel and a 2-foot diameter channel, which corresponds to the diameter sizes of the tubes at Gary. These parameters are indicated in Table II.

Suggestions on Experimental Set Up for Multiple Charges

The experimental procedure would involve arranging the charges, Primacord, in concentric circles. They have to be separated sufficiently to avoid sympathetic detonation, which in the case of Primacord is very rare even at distances of about one inch. The blasting caps used to detonate the Primacord might have to be shielded in some way as they are very sensitive, however, the separation of the charges is probably sufficient so that the only precaution necessary is insuring the mechanical integrity of the second charge until the time of its detonation. The time delay between charge detonations could be accomplished with instrumentation already in existence which is designed to take pulses, and at prescribed time intervals discharge pulses. These pulses then would detonate each charge at the proper time.

TABLE II
 CONDITIONS NECESSARY TO GENERATE THE
 THREE DESIRED WAVE FORMS

Wave Type*	Distance at Which Desired Wave Occurs (ft)	Charge Number	Time Detonated After Preceding Detonation (msec)	Length of Double-Strength Prima-cord (ft)	
				6-ft tube	2-ft tube
1	25	1	0	43.0	4.77
		2	38.75	38.4	4.28
2	123	1	0	26.5	2.94
		2	8.0	49.0	5.45
		3	13.7	67.5	7.52
		4	15.8	76.2	8.48
		5	13.4	84.6	9.42
		6	14.2	89.6	9.96
3	110.8	1	0	51.2	5.70
		2	10.1	94.4	10.5
		3	9.6	119.2	13.3

* 1 - double peaked wave

2 - finite rise time, slow buildup wave

3 - finite rise time, rapid buildup wave

BIBLIOGRAPHY

1. F. B. Porzel, Los Alamos Scientific Laboratory, Title Classified, LA-1664, May 1954, pp. 24-28 (Secret-Restricted Data).
2. Armour Research Foundation, "Surface Effects on Blast Loading" May 1956 (Secret-Restricted Data).
3. V. M. Wolontis, "A Complete Floating Decimal Arithmetic System for the IBM 650 Magnetic Drawn Calculator," Bell Telephone Labs., Inc., IBM Technical Newsletter No. 11, March 1956.
4. Radio Corporation of America, "An Interpretive Subroutine for the Solution of Systems of First Order Ordinary Differential Equations on the 650 Calculator."
5. Armour Research Foundation, "Memorandum Report on Calibration of Shock Tubes," Report No. 47 of Contract No. AF33(616)-2644, February 1957.
6. A. H. Shapiro, "The Dynamics and Thermodynamics of Compressible Fluid Flow," Volume 1, 1953.

ABSTRACT

This paper presents an analysis of the relationships among gas flow variables behind an explosive-generated shock front advancing in a constant area channel. A density distribution behind the shock front of the form

$$\rho = \rho_s \left(\frac{r}{R} \right)^q$$

is assumed, where ρ is the gas density at a distance, r , from the explosion source, and ρ_s is the gas density at the shock front distance R , also measured from the explosion source. The exponent, q , is determined from physical considerations. Application of the principles of conservation of mass, momentum, and energy, together with the assumed density distribution leads to a particle velocity distribution, a pressure wave form, and a shock strength, scaled distance decay curve. Values of the flow variables at the shock front are of course determined by the Rankine-Hugoniot relations.

The analogous flow variable relationships are derived by an approximate method for the case where several explosive charges are detonated successively. By employing this analysis, one may calculate the charge weights, detonation time delays, and explosion source distances required to generate pressure wave forms of various shapes. The calculations are presented for three particular wave forms, including non-peaked and multiple-peaked cases.

Substantial support was given the analysis when the results were compared with existing experimental data obtained at the Gary, Indiana 6-foot shock tube facility. This comparison was only made in the case of a single charge detonated at various distances from the test section of the shock tube. At the present time the multiple charge case has not been experimentally investigated.

Recommendations are made for the multiple charge case on instrumentation systems and techniques which may be used in conjunction with standard shock tube apparatus in the experimental application of the results.

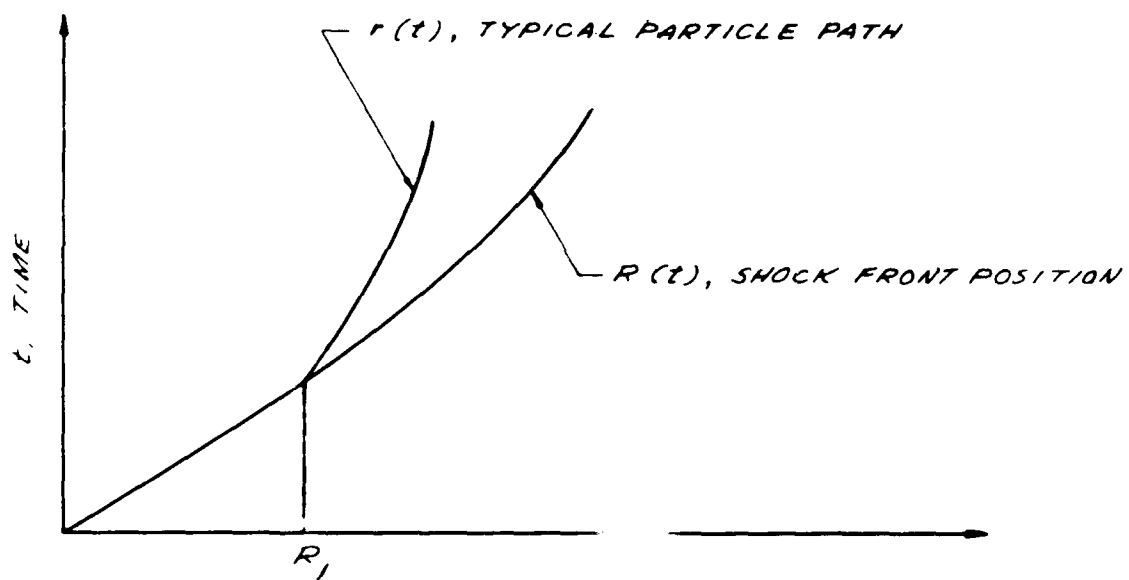
Work on this paper was conducted on Armour Research Foundation's Project No. DO82-D9 under Air Force Contract No. AF 33(616)-2534, Call 9.

LIST OF SYMBOLS

<u>Symbol</u>	<u>Definition</u>
c	Sound velocity
c_0	Sound velocity under standard atmospheric conditions
E_I	Internal energy increment in a shock wave
E_K	Kinetic energy in a shock wave
K	Parameter dependent on shock front conditions
L	Parameter dependent on shock front conditions
M	Parameter dependent on shock front conditions
P	Absolute pressure at any point behind shock wave
P_0	Absolute pressure in front of shock wave
P_s	Absolute pressure at shock front
q	Exponent in density power law assumption, dependent on shock front conditions only
r	Running distance from shock origin to shock front
R	Shock front distance
t	Time measured from explosive detonation time
t_0	Defined duration of positive pressure phase
u	Particle velocity at any point behind the shock front
u_s	Average particle velocity behind shock front at a constant time
U	Shock front velocity
W	Total energy yield
X	Logarithmic slope of shock strength minus one versus distance curve
α	Logarithmic slope of density ratio

LIST OF SYMBOLS (CONT.)

<u>Symbol</u>	<u>Definition</u>
β	Logarithmic slope of shock front particle velocity
γ	Ratio of specific heats
ϵ	$1/\gamma - 1$ = Equation of state parameters
ϵ_0	Value of ϵ under standard atmospheric conditions
$\bar{\epsilon}$	Average value of ϵ behind shock wave
η_s	Fluid density ratio across shock front
λ	Scaled shock front distance
ξ	Pressure ratio across shock front
ρ	Fluid density at any point behind shock front
ρ_0	Fluid density under normal atmospheric conditions
ρ_s	Fluid density at the shock front
ϕ	Logarithmic slope of α



SKETCH OF A TYPICAL DISTANCE TIME
HISTORY OF A MOVING SHOCK WAVE

1.

$$\rho = \rho_s \left(\frac{r}{R}\right)^{\alpha(R)}$$

2.

$$u = u_s \left(\frac{r}{R}\right) \left[1 - \alpha \ln \left(\frac{r}{R}\right) \right]$$

3.

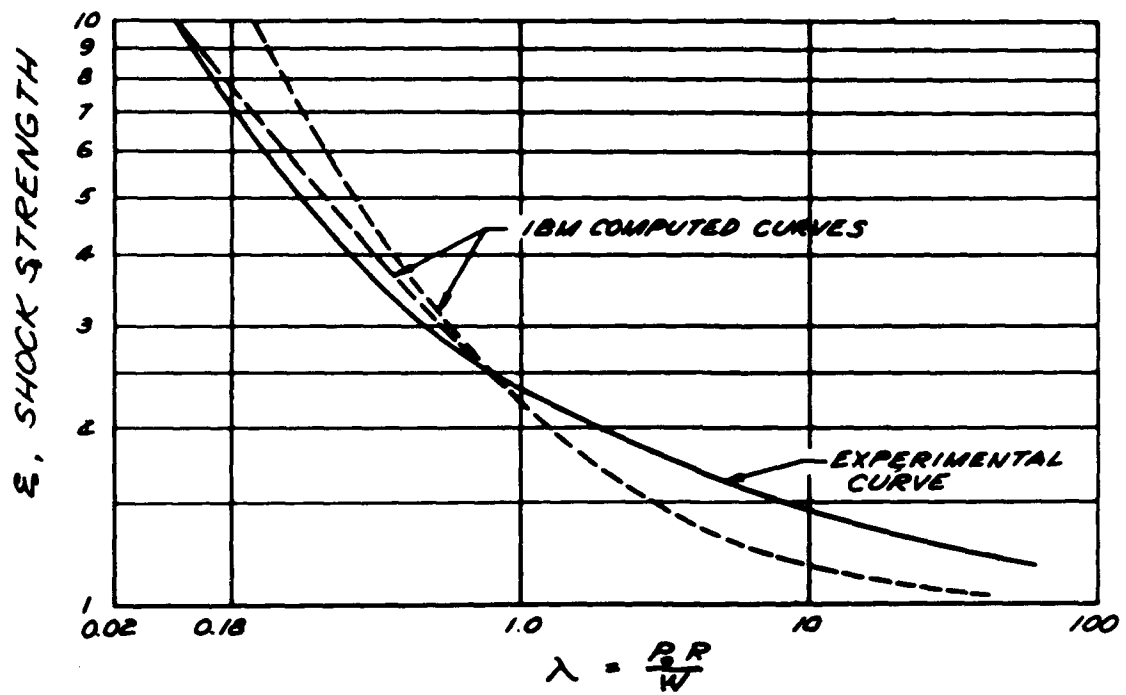
$$\frac{P - P_s}{P_s - P_o} = 1 - K + \left(\frac{r}{R}\right)^{(q+2)} \left[K + L \ln \frac{r}{R} + M \left\{ \ln \frac{r}{R} \right\}^2 \right]$$

4.

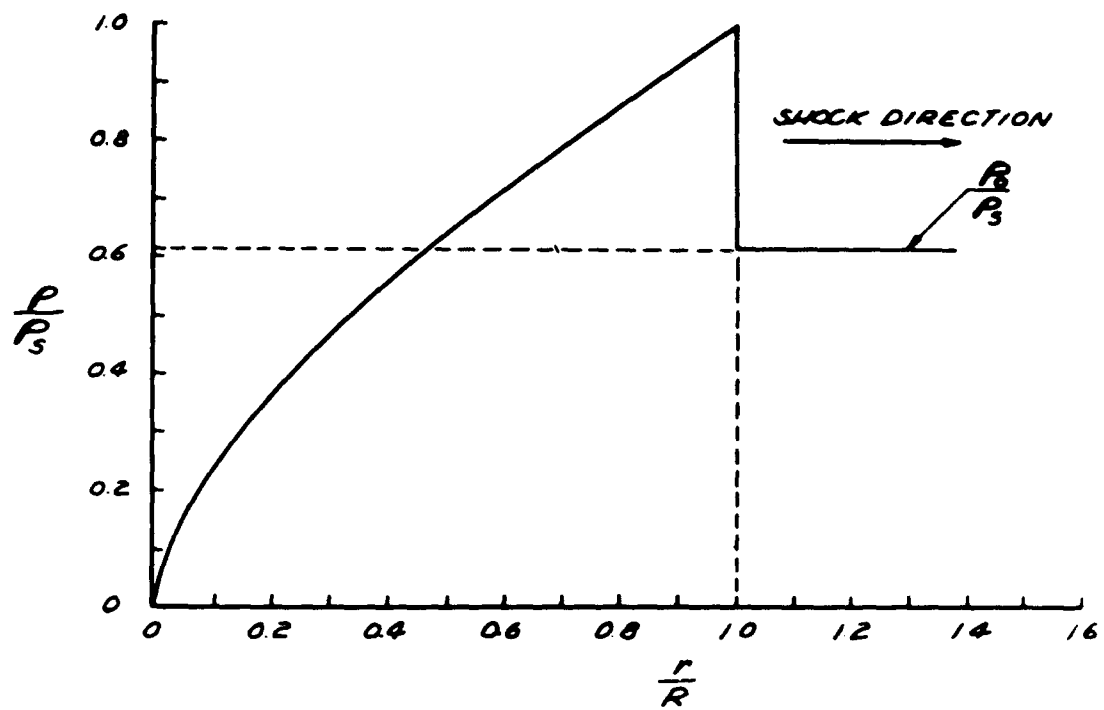
$$W = E_K + E_I$$

5.

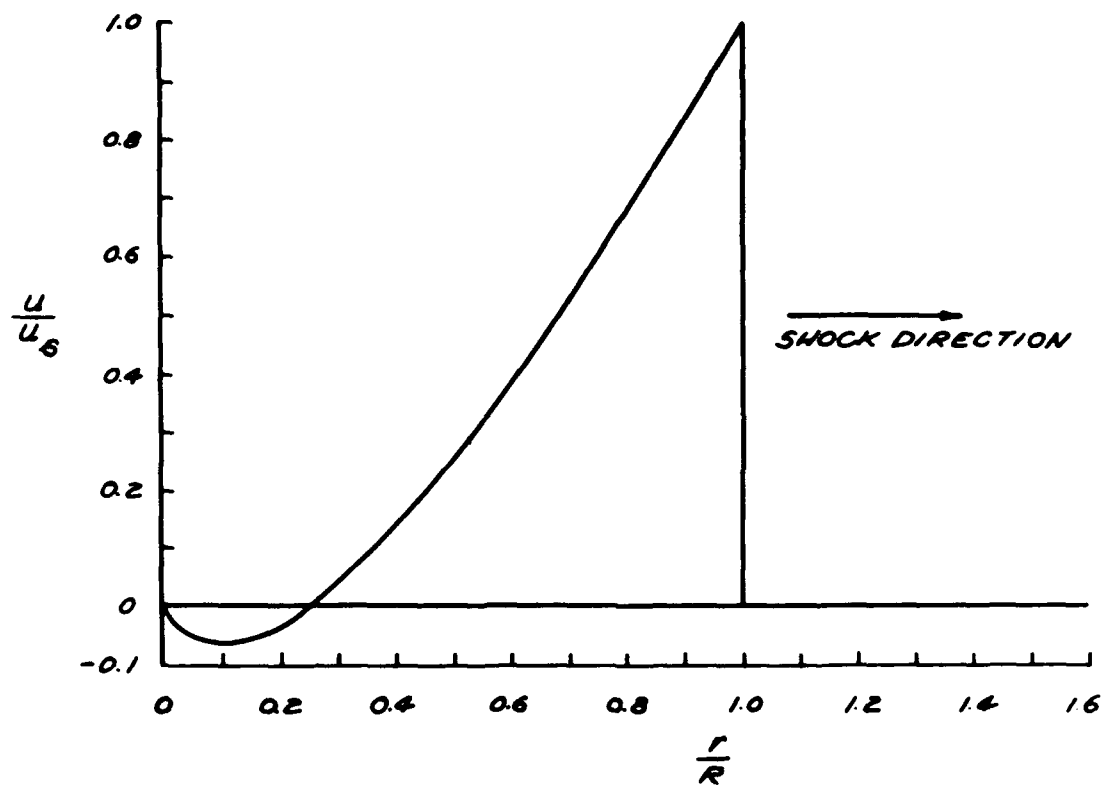
$$W = \frac{1}{2} \int_0^R \rho u^2 dr + \int_0^R \epsilon P dr - \epsilon_p R$$



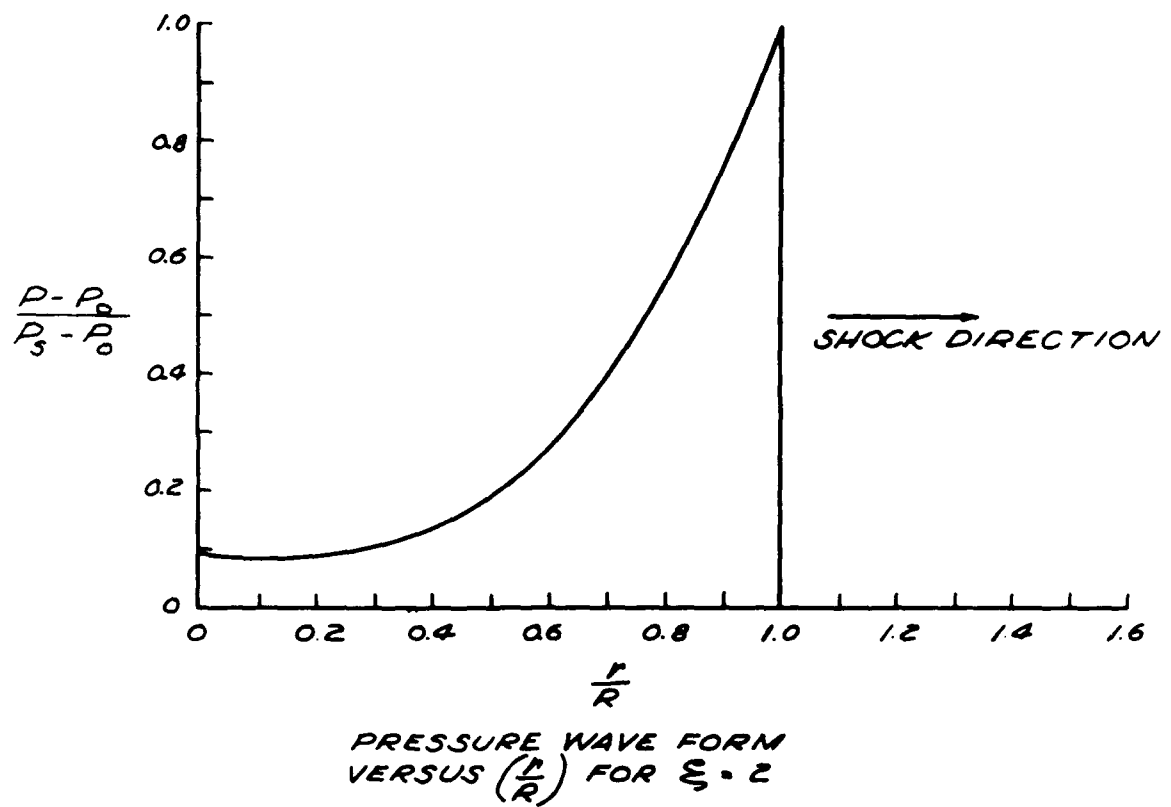
SCALED DISTANCE, λ , VERSUS SHOCK STRENGTH, E



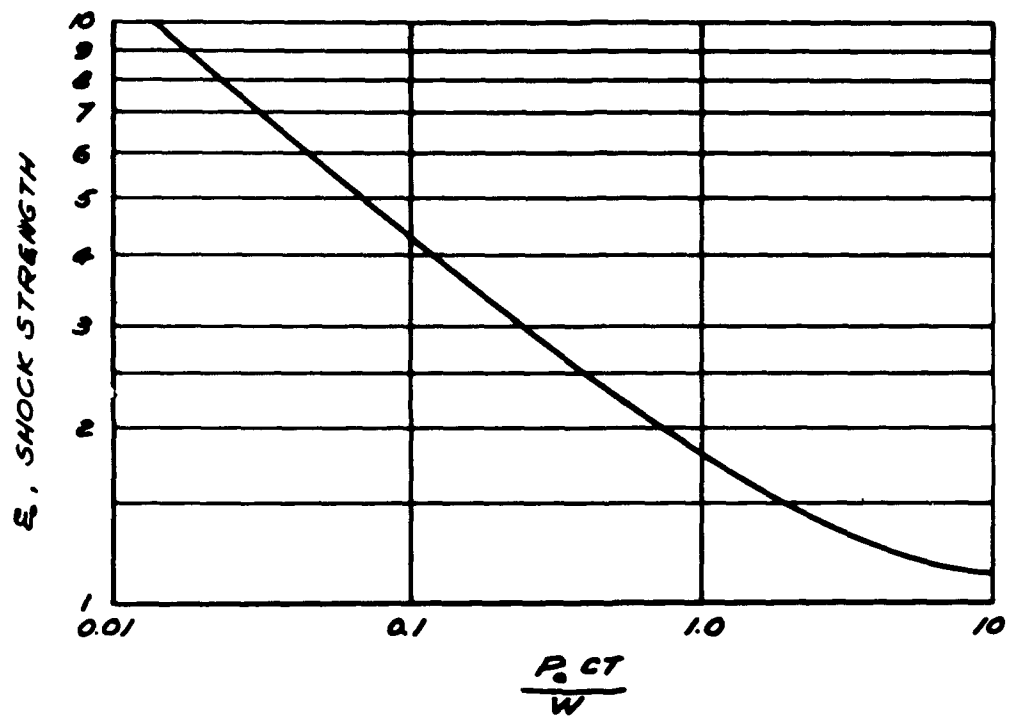
FLUID DENSITY DISTRIBUTION
VERSUS $(\frac{r}{R})$ FOR $\gamma = 2$



PARTICLE VELOCITY DISTRIBUTION
VERSUS $(\frac{r}{R})$ FOR $\gamma = 2$



Slide #6



SCALED TIME VERSUS SHOCK STRENGTH, S

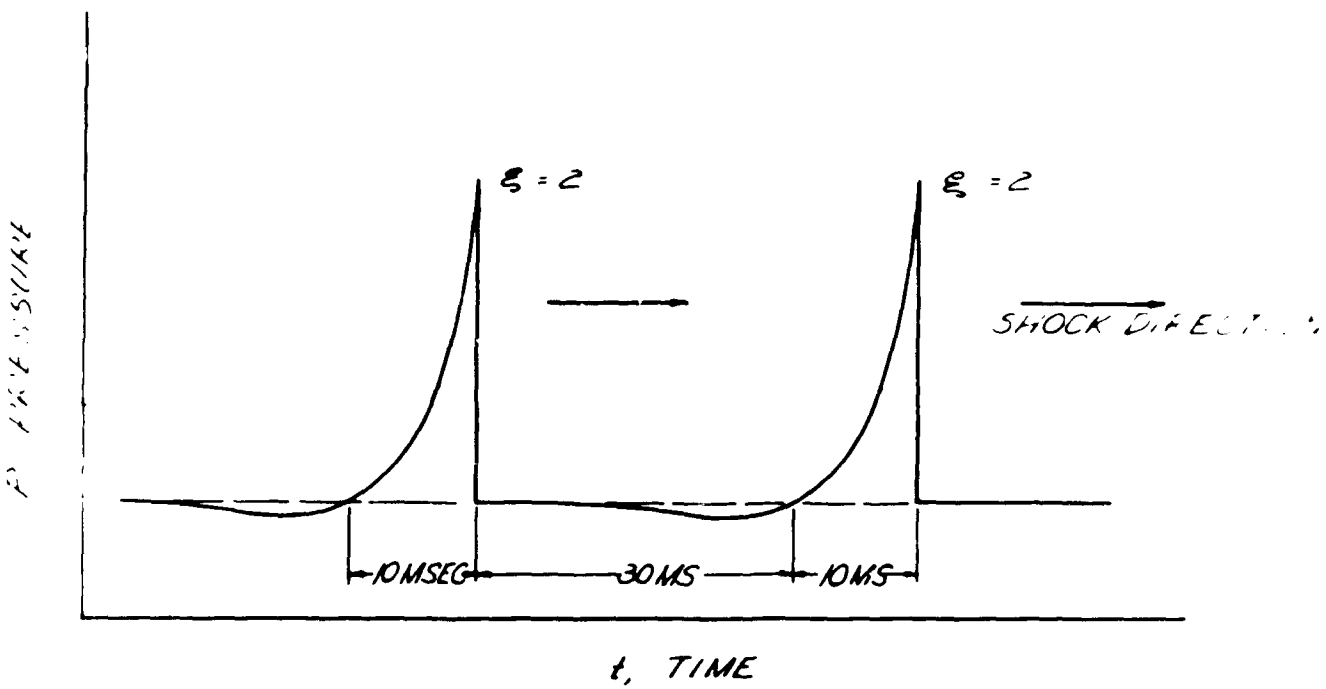
$$6. \bar{P} = \frac{\int_0^R P dr}{\int_0^R dr} = \left[(\xi - 1) \left\{ 1 - K + \frac{K}{\xi + 3} - \frac{L}{(\xi + 3)^\xi} + \frac{2M}{(\xi + 3)^3} \right\} + 1 \right] P_0$$

$$7. \bar{U} = \frac{\int_0^R u dr}{\int_0^R dr} = \frac{\alpha + 2}{4} U_s$$

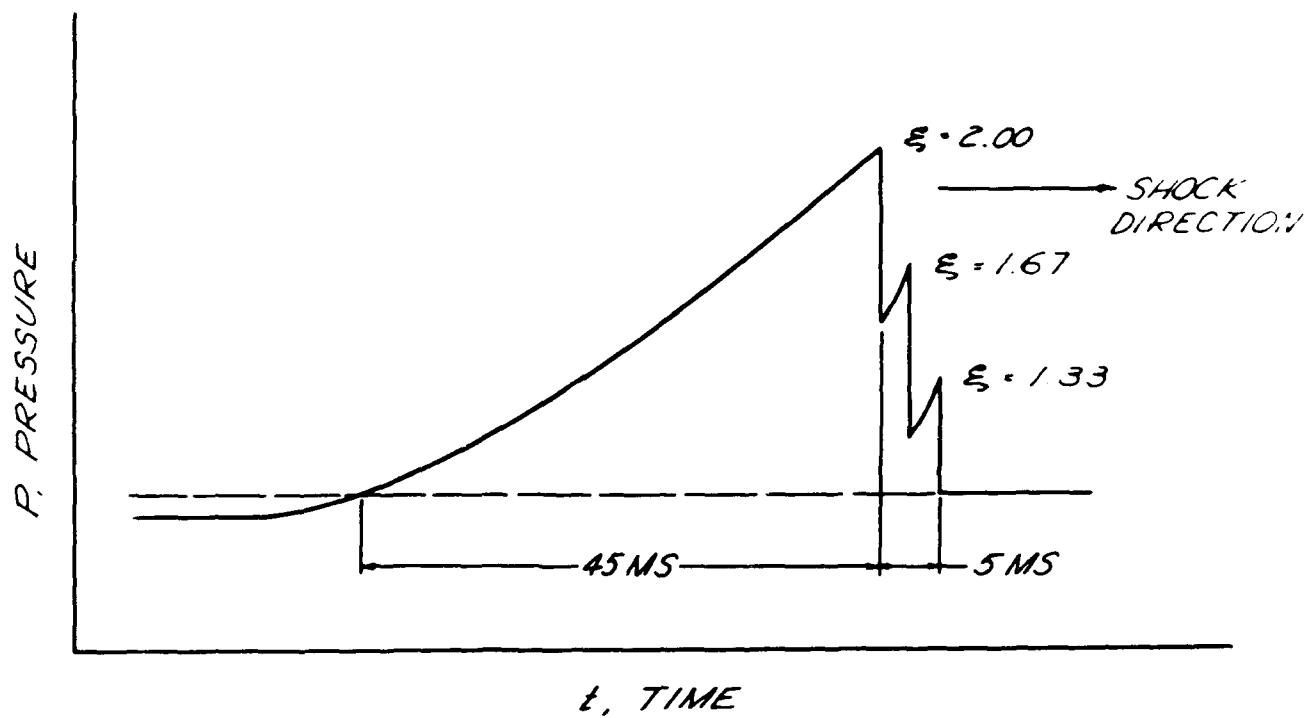
$$8. \bar{P} = P_0$$

$$9. \bar{C} = C_0 \left(\frac{P}{P_0} \right)^{1/2}$$

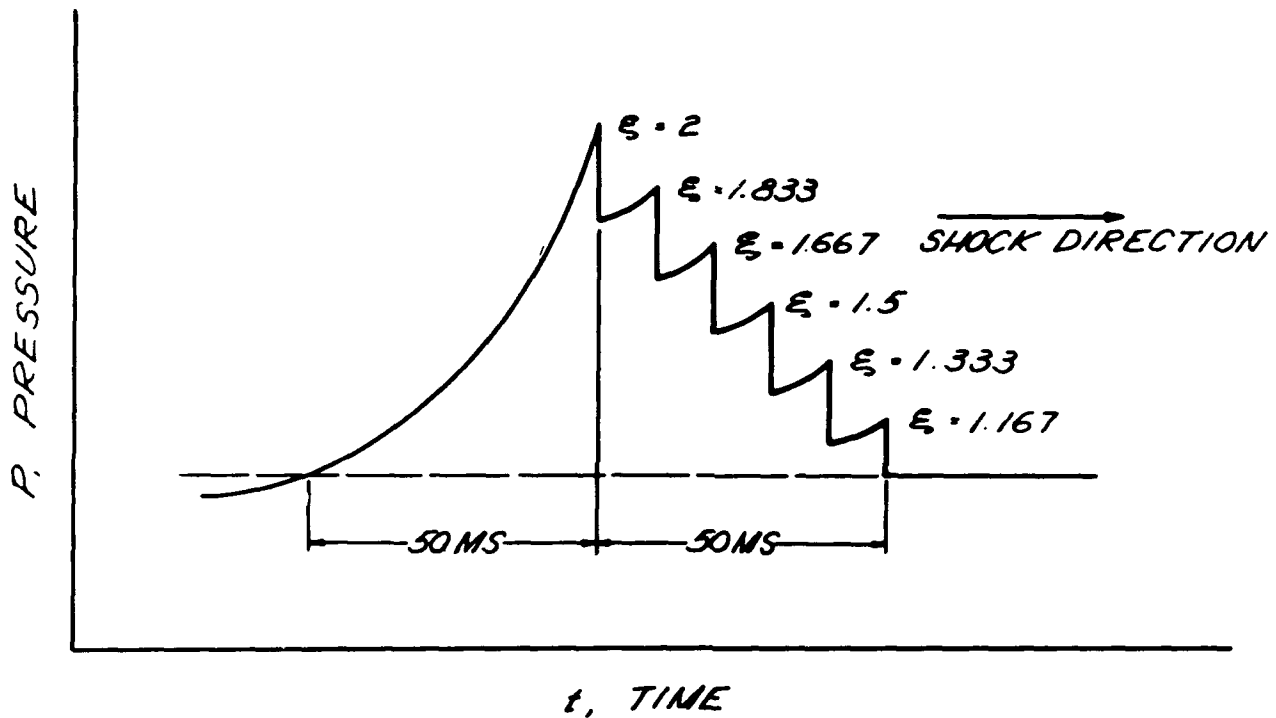
DOUBLE PEAKED WAVE FORM



FINITE RISE TIME WAVE FORM
FAST BUILDUP



FINITE RISE TIME WAVE FORM
SLOW BUILDUP



MATERIALS

CRITERIA IN THE SELECTION OF MATERIALS FOR HIGH TEMPERATURE
STRUCTURES

W. H. Steurer
Army Ballistic Missile Agcy.

CRITERIA IN THE SELECTION OF MATERIALS
FOR HIGH TEMPERATURE STRUCTURES

By

Wolfgang H. Steurer

1. Introduction

As the speeds of aircraft and missiles increase and the temperatures to which the structures are exposed rise to unprecedented degrees, considerable efforts are made on the side of structural design as well as of materials research to arrive at new solutions, entering an area in which the dividing line between materials engineering and structural design is less and less distinct. The more carefully we analyze the effect of extreme speeds on materials, the more complex problems arise, leaving us sometimes close to a state of confusion. Under such uncertain conditions, it is sometimes wise to depart from detail and take a few steps backward, in an effort to obtain a greater angle of view and to better recognize the basic lines of relation.

2. Correlation of Flight Requirements and Material Characteristics

In the first approach, we find ourselves faced with the problem of matching materials to the operational and environmental requirements of a variety of vehicles, with a wide spectrum of velocities. To appraise the potentials of materials, it appears to be necessary to analyze, in the first place, the requirements of vehicles related to the design of materials.

Table 1 gives a crude picture of the structural temperatures and times of operation for high speed aircraft and missiles.

While the speeds of bomber and fighter aircraft and, consequently, the temperatures are moderate, the number of missions and the duration of a single mission as well as the total lifetime are comparatively high. As the speeds increase, e.g., in the case of rocket aircraft, the temperatures rise considerably, while the number of missions and the time of heat exposure become smaller. Missiles, finally, encounter only a single heating cycle, of longer duration in pilotless aircraft type or glide missiles, and of very short duration, yet extremely high temperatures, in the re-entry phase of ballistic missiles.

Two predominant relationships are apparent:

- (1) As the temperatures in the structure increase, the total operation time, as well as the duration of a single mission, decrease from thousands of hours to minutes, or even seconds.
- (2) At the same time, the number of missions decreases from hundreds to a single mission of a missile.

The relation of operation, i.e., heating time to speed, is once more illustrated in Fig. 1. Even though the single points for this diagram were obtained from a variety of vehicles, whose

operational characteristics are quite different, they form, nevertheless, a continuous line and the decrease of time with climbing speed is very distinct.

If we translate speed into temperature, we find a similar relationship (Fig. 2), in that time is inversely proportional to temperature.

If we turn now to the structural materials and try to visualize their behavior at various temperatures, we observe that a number of properties of most materials, particularly of structural metals, become considerably time dependent at higher temperatures. The development and proper selection of materials for high temperature structures, therefore, relies solely on the art of matching the time-temperature characteristics of materials with the operational time-temperature relation of high speed vehicles. The following discussion on the selection of materials for high speed vehicles is, therefore, based primarily on the aspects of time and temperature.

3. Design Principles for High Temperature Structures

In the application of materials to high temperature structures, there are two basic approaches: either, we design an integral or, as often called, hot structure, in which one single material provides strength, as well as heat resistance, or we separate the two functions of the material in two structural elements and design a composite structure consisting of a stress

carrying substructure and a heat protecting superstructure. As the substructure is now protected against heat, it can be designed for mechanical properties in a conventional fashion, while the fully supported superstructures no longer requires any strength, except for resistance to the local shear forces of the airflow and can be designed for heat resistance only. This composite structure comprises the various forms of thermal protection systems which have become the most important element of structural design for high speed flight.

For the selection of the most suitable material or protection system, it is attempted in the following discussion to delineate certain time-temperature areas occupied by such systems, and to match them with operational time-temperature fields, as they are once more outlined in Fig. 3.

4. Structures Based on the Principle of Heat Protection

a. Conventional (integral) Structure

Let us first look at the time-temperature field which applies to bomber and fighter aircraft. The temperatures are comparatively moderate so that even at the long operation times of hundreds or thousands of hours, metals exhibit enough strength, to make a conventional integral structure weightwise acceptable. As the speeds and, consequently, the temperatures

increase, however, the integral structure based on conventional material properties becomes marginal weightwise. At this point, we may remember that the strength decreases at these temperatures rapidly with the time of heat exposure. By the same token, it can be expected that, at the very short times of heat exposure connected with higher speed and higher temperature, much higher properties are encountered which would permit the use of conventional structures to considerably higher temperatures.

b. Structures for Short Heating Times

In investigating this possibility, it appears appropriate to discuss the stability of the strength exhibited by metallic materials at higher temperatures, as illustrated in Fig. 4. In the annealed condition, in which all major strengthening effects are removed, no marked difference between long and short time properties will exist; the absolute strength is low, yet fully stable. In a moderately heat treated condition, as commonly used in engineering, the strength exhibits a slight decrease with time, indicating the beginning sensitivity to heating; the rate of softening is, however, so slow that even at long times useful properties are retained and the structure can, for all practical purposes, be considered as stable. If we now turn to an extreme heat treatment, the structure will be so sensitive

to heating that the strength drops almost instantly to the level of the annealed condition, in some materials to even lower values. In this condition, the structure is too unstable to produce any useful mechanical properties for even extremely short times of heat exposure. If the degree of strengthening is reduced, the loss of strength becomes more gradual and appreciably high mechanical properties will remain effective for short times. If we select for the material assumed an intermediate treatment producing an initial strengthening effect halfway between the conventional and the extreme heat treatment, the decline of strength may require one hour. From the viewpoint of conventional long time applications, the structure would still be considered as unstable. The treatment is, however, stable enough to produce superior mechanical properties at very short times.

The proper way of strengthening for short time service is, therefore, a treatment producing a metastable condition, which may be accomplished by any commonly used means of strengthening, such as heat treating, precipitation hardening or cold working.

A typical practical example for the effect of a strengthening treatment on the timewise stability of the mechanical properties is shown in Fig. 5 representing the hardness

characteristic of pure copper at short times of heat exposure to 750 °F and various degrees of cold working. While the highly strengthened condition of 80% cold reduction is very unstable, it still produces high mechanical properties for times up to 15 seconds. As the degree of cold working is decreased, the strength becomes more moderate, yet increasingly stable to longer service times.

For highest efficiency, a definite treatment has to be selected for each service condition, i.e., for the expected time of heat exposure.

In the following, a few examples for the usefulness of various strengthening treatments are presented in the familiar strength-temperature diagrams. The effect of cold working is shown once more in Fig. 6 for a low allow-high strength steel, as it was used in a ballistic missile now in service. The moderate cold working degree of the 1/4 hard condition produces at temperatures between 400 and 600 °C for an application time of 1 minute values, which are 40% higher than the conventional properties. The effect of the strengthening treatment on the short time strength is even more apparent in the example of an age hardened aluminum alloy type 2024-T3 (Fig. 7) where the 15 second values reach, at higher temperatures, almost two and one-half times the conventional strength.

AD-A286 704

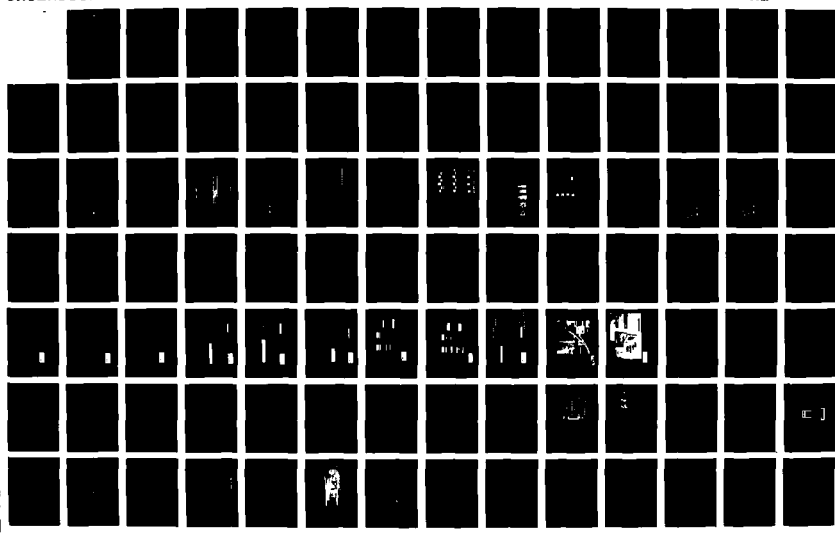
SYMPORIUM ON HIGH-SPEED AERODYNAMICS AND STRUCTURES
(3RD) HELD AT SAN DIEGO CALIFORNIA ON MARCH 25-27 1958
VOLUME 1(U) CONVAIR SCIENTIFIC RESEARCH LAB SAN DIEGO

3/5

UNCLASSIFIED

CA MAR 58 XC-ARDC

NL





Association for Information and Image Management

1100 Wayne Avenue, Suite 1100

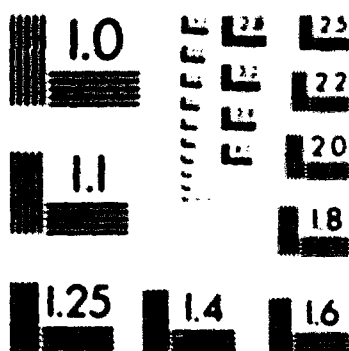
Silver Spring, Maryland 20910

301-587-6262

Centimeter



Inches



MANUFACTURED TO AIIM STANDARDS
BY APPLIED IMAGE, INC.

In other terms, the useful temperature range is extended by 100 °C or almost 50%.

The same effect was observed in other materials at much higher temperatures. In some steels, a proper treatment provided, for a time of heat exposure of 10 seconds, useful properties at temperatures up to 2200 °F, where even superalloys begin to lose their strength entirely.

As the higher strength of metals at short times permits their use to higher temperatures, their efficiency is further increased by higher amounts of heat dissipated by radiation. The integral structure may thus, in the short time region, be useful to temperatures way beyond the conventional limits and occupy in the time-temperature diagram the fields indicated in Fig. 8. The C area denotes the field of the conventional structure based on long time properties, while the extended application to higher temperatures by proper treatment is identified by the field M.

5. Structures Based on the Principle of Heat Protection (Insulation, Radiation)

This extension to higher temperatures will, as outlined, be limited to short times only. If we move toward longer service times at the same temperature level, as it is typical for highest speed aircraft, pilotless aircraft type missiles, or

certain versions of boost glide vehicles, we may attempt to apply materials of higher heat resistance, such as ceramics. This however, necessitates in most cases a composite structure, since the mechanical and technological characteristics of ceramics are inadequate for an integral, stress carrying structure. Due to their low thermal conductivity, most ceramic materials exhibit a steep thermal gradient, rendering them very efficient in protecting the stress carrying sub-structure against excessive heating. Furthermore, their high melting or sublimation points permit the use of high surface equilibrium temperatures, at which a considerable portion of the heat input may be dissipated by radiation.

The amount of the radiant heat dissipation is calculated for a number of common ceramics in Fig. 9. It appears that, even though the emissivities differ and vary considerably with temperature, the effective heat dissipation ranges within a narrow band over temperature. The usefulness of ceramics for high temperature structures is not so much due to their heat resistance and their insulating value, as to their efficiency as heat radiators.

A similar effect may be achieved by other composite designs. Fig. 10 shows, besides the ceramic structure at left, a sandwich type structure in the center, in which the high surface temperature in the shielding refractory metal, protecting

the porous insulation against the mechanical forces of airflow, is permissible, since it has no stress carrying function and can thus be used even in the plastic state.

A fully metallic radiation system is systematically sketched at the far right, consisting of a number of highly reflective layers, under the protection of a shield of high emissivity at the outside surface. The effectiveness of such metallic radiation structures may be indicated by the following test data: at a gas temperature at subsonic velocity of 1300 °C, the temperature in the shield reached 800 °C, while the inside structural wall did not surpass 125 °C under equilibrium conditions.

The suitability of metallic materials for radiation structures depends, of course, to a great extent on the timewise oxidation behavior, and its effect on the thermal surface properties.

Radiation systems permit the design of structures for longer times of operation and to temperatures close to the melting or sublimation points of the materials. They may, thus, occupy the time-temperature field indicated in Fig. 11. Here we apply in structural design for the first time the principle of heat absorption, in which so much of the heat flux into the surface is absorbed, that the resulting wall temperatures remain within

permissible limit.

6. Structures Based on the Principle of Heat Absorption

As we proceed to temperatures beyond the melting and sublimation points of our materials, we will rely solely on the principle of heat absorption. The most obvious way is the use of a coolant in the form of a liquid film or transpiration system. The designer will, however, avoid such functional means with regard to the weight of coolants, containers and distributing hardware, as well as for the sake of reliability, as long as the extremely short operation times of vehicles involved permit the use of the skin material itself for heat absorption.

a. Heat Sink

Such heat absorption may be provided by the thermal capacity of a material in the solid state. In the heat sink principle, a wall of high thermal capacity is dimensioned so that the temperatures stay within permissible limits during the heating cycle. The time limitations are primarily dictated by weight considerations, while the temperatures are limited by the melting temperature of the material. Since this leads to comparatively high wall thicknesses with considerable load carrying ability, it may permit return to the integral structure.

The amounts of heat which may be absorbed by a number of metallic materials are compared in Table 2, which lists in the

second column the heat content in the solid state from room to melting temperature. While some metals, as iron, molybdenum or magnesium, have a capacity in the neighborhood of 160 cal/gr, beryllium appears to be much superior with about 600 cal/gr. The chart lists further in the last 3 columns the heat which may be absorbed if it were possible to include the heat of fusion, the liquid state, and finally the heat of vaporization where heat capacities in terms of thousands of cal/gr may be obtained. As illustrated in the third column, which represents the percentage of the heat content of the solid state as compared with the total heat up to and including vaporization, only 4 - 9 percent can be absorbed in the solid state. This indicates the desirability of utilizing the heats of fusion and even vaporization in skin materials for extreme temperatures. This is feasible in view of the short times and single mission of the missiles involved at highest temperatures, permitting to adopt the principle of expendability.

b. Ablation

Since melting and vaporizing commonly mean destruction, a way has to be found where these processes can be controlled in an orderly fashion. In the ablation process, the melting is confined to a surface layer and the material removed by the

airflow as soon as its heat capacity is exhausted, to make room for a new layer, thus leading to a gradually progressing, continuous process. The elements of heat absorption may be represented by the expression

$$Q_{\text{tot.}} = Q_{\text{sol.}} + Q_{\text{melt.}} + Q_{\text{liq.}} + Q_{\text{vap.}}$$

The total heat of ablation may consist only of the combined heat absorbed in the solid state and by fusion, or may include the heat in the liquid state $Q_{\text{liq.}}$ and even the heat of vaporization $Q_{\text{vap.}}$. If we introduce the rate of ablation a in cm/sec, we can express the heat flux absorbed in ablation by

$$q_{\text{abl.}} = a \cdot \rho (c_{\text{psol.}} \cdot T + H_f + c_{\text{pliq.}} \cdot T + H_v) \quad [\text{cal/cm}^2 \text{ sec}]$$

Due to the high surface temperatures involved, considerable additional heat absorption is provided by radiation, identified by the familiar expression:

$$q_{\text{rad.}} = \epsilon \cdot \sigma \cdot T_{\text{max}}^4 \quad [\text{cal/cm}^2 \text{ sec}]$$

Finally, the material may undergo endothermic reactions in the solid or liquid state, such as chemical reactions or phase changes in metals, which can also be tied to the ablation rate with the relation

$$q_{\text{ER}} = a \cdot \rho \cdot \epsilon Q_{\text{ER}} \quad [\text{cal/cm}^2 \text{ sec}]$$

The total heat flux absorbed during ablation consists of

$$q_{\text{tot.}} = q_{\text{abl.}} + q_{\text{rad.}} + q_{\text{ER.}}$$

For the development and design of materials for ablation, the following requirements evolve out of the foregoing considerations:

- 1) High thermal capacity
- 2) Confinement of the process to a surface layer
- 3) Retention at the surface until the heat capacity is fully utilized, i.e., correct timing of removal
- 4) Uniformity (retention of shape).

The first requirement of high thermal capacity has been discussed sufficiently. The second requirement of confinement of the process to a minute surface layer can be best accomplished by a steep thermal gradient, as shown in Fig. 12, for a material A of low thermal conductivity. The majority of materials of high thermal capacity, however, exhibit a high thermal conductivity. This is particularly dangerous in view of the fact that most metallic materials assume a viscous behavior before reaching the melting point, as indicated by the semi-solid range (SS). If a material of the conductivity and thermal gradient B reaches the melting point, as required in the ablation

process, the removal may extend deep into the interior due to the poor shear resistance of the viscous material, which, most likely, will lead to destruction of the body. Even materials which do not exhibit this viscous range may ablate unevenly so that some parts may be lost before their heat capacity has been fully utilized.

These considerations demonstrate clearly the unsuitability of homogenous materials for the ablation process and the absolute necessity of heterogeneous or composite materials. In combining two dissimilar constituents, we may create an artificial combination of properties, not found in homogenous materials, which may meet all requirements of the ablation process. If we, e.g., choose a heterogeneous mixture of ceramic metal particles, the ceramic material may provide

- 1) an overall low thermal conductivity, insuring confinement of the process to a minute surface layer;
- 2) a heat resisting, solid skeleton, in which the heat absorbing metal particles are embedded and held in place to fusion or even vaporization;
- 3) a built-in stopping device, which prevents progressing of the melting process beyond the size of a particle. This, in turn, insures uniformity.

The full and well controlled utilization of the thermal capacity of the metal phase of a heterogenous metal-ceramic mixture is further illustrated in Fig. 11, showing the time-temperature characteristic of the surface layer. By selecting a ceramic component whose melting or sublimation temperature is somewhat higher than the vaporization temperature of the metal, the metal will be held in place to full vaporization. In the subsequent fast rise of the temperature due to the absence of cooling, the ceramic skeleton collapses and makes place for the next layer, which in the meantime has reached the temperature of fusion.

In some designs (as in the case of a metal of high melting point), it may be desirable to go only to fusion, producing a liquid ablation system, which usually provides better surface uniformity (Fig. 11). Vaporization may start while the liquid material is moving downstream: we have a semi-gaseous system. And finally, in the fully gaseous system, the metal will vaporize out of the surface pockets provided by the heterogeneous structure.

In order to appraise the potential amount of heat absorption in heterogenous materials, we will have to modify the formerly established relationships by introducing the properties

of the two components and their volumetric ratio r , which determines the predominant phase. It can be deduced by simple geometry that either component becomes predominant and denotes the overall conductivity as soon as it occupies more than two-thirds of the volume. If we designate the metallic component by the suffix M, and the ceramic by the suffix C, the total heat flux absorbed by ablation may be represented by

$$q_{\text{tot}} = a \left[r \cdot \rho_M \left(\eta_{\text{ablin}} + \eta_{\text{BERM}} \right) + (1-r) \rho_C \left(\eta_{\text{SolC}} + \eta_{\text{BERC}} \right) \right]$$

(gaseous system) $\rightarrow \sigma T_{\text{vapM}} \left[r \cdot \epsilon_M + (1-r) \epsilon_C \right]$

or
(Liquid system) $\rightarrow \sigma \epsilon_M T_{\text{meltM}}$ $\left[\text{cal/cm}^2 \text{sec} \right]$

To judge the efficiency of various heterogeneous mixtures, the heat flux values, which may be absorbed by the ablation part only, have been calculated for various metal-ceramic combinations (Table 1). It appears that particularly Boron and Copper in ZrO_2 are promising. If we compare the flux absorbed of 593-863 cal/cm sec at an ablation rate of 1 mm/sec with the heat fluxes expected during the entry of ballistic missiles, which may be somewhere between

20 - 50 cal/cm sec for short range missiles

50 - 250 for intermediate range missiles

200 - 500 cal/cm sec for intercontinental missiles

These figures depend, of course, on the specific trajectory and may, therefore, only serve as a guide. In Fig. 15, the efficiency of heterogenous metal-ceramic systems is once more illustrated and, by means of background shading, related to ranges of heat flux of ballistic missiles. This picture shows, for comparison, the amounts achievable with a metal-carbon system, even though it does not meet the requirement of a steep thermal gradient and may encounter a number of difficulties in practical performance. Heterogenous systems, in which both components exhibit high thermal conductivity, may only be feasible at extreme heat flux rates.

On the other hand, heterogeneous systems in which both components are of low conductivity may be highly desirable, as long as sufficiently high thermal capacity can be provided. There the particle character is no longer necessary since the very steep thermal gradient provides sufficient assurance against an uncontrolled and disuniform progress of the ablation into the interior. A typical example of this kind are the resin-glassfiber combinations, which have proven highly effective in flight applications. As already outlined in detail in the paper presented by H. Connell, highest heat absorption and uniformity is obtained by normal orientation of the fibers to the surface.

Figure 16 gives a qualitative picture of the various processes contributing to the overall heat absorption.

In the initial phase of the heat exposure, the resin will burn or pyrolyze and form a carbon skeleton, which holds the glass fibers firmly in place through the process of melting. Simultaneously, with the progressing heat into the bulk material, endothermic processes may occur in the resin in the form of decomposition or other chemical reactions. While the molten glass is moving downstream under the mechanical forces of the airflow, it may start to vaporize, and at the same time radiate at its vaporization temperature.

The amount of heat dissipated by the radiation of the various surfaces depends, however, on the transparency or absorptivity of the adjacent material components and the potential re-radiation from the boundary layer gases or the ablation products.

Of particular interest is the early vaporization of the flux type constituents in some glasses, which increases the viscosity of the remaining material until it reaches its melting or sublimation temperature. The process is illustrated in Fig. 17. For simplicity, two groups of components are assumed, one with a boiling point T_A and another with a boiling point T_B . As soon as the surface arrives at the temperature T_A , the constituents "A" vaporize while the remainder consists now only

of the constituents "B", which are of high viscosity and act as a mechanical shield for the almost liquid layer underneath, yet soft enough to permit the escape of the vapors. As soon as the constituents "B" reach their melting temperature, ablation starts and the thermal characteristic attained at this point moves gradually into the interior. This effect of fractional distillation of constituents may even lend itself to the design of a homogeneous ablation material.

It is realized that there are many other effects and processes which may contribute to the overall heat exchange in heterogeneous or homogenous systems at extreme speeds, such as the overheating of the ablation vapors, endothermic or exothermic chemical processes in the bulk material, decomposition, chemical or physical interaction between the material surfaces and the ablation products, as well as the boundary layer gases. The appraisal of these effects has to await intensive fundamental studies.

As for today, we cannot predict yet to what extreme temperatures and heat flux rates the ablation process will be feasible. On the basis of the present state of the art we can, however, safely delineate another field in the time-temperature diagram, which includes the majority of our ballistic missiles (Fig. 18).

c. Transpiration

As the material is expended at a high rate, the ablation process will always be limited to comparatively short times. If we have to design for a longer duration of extreme heat exposure, we may no longer be able to use the skin material itself for heat absorption, and may have to turn to a liquid film or a transpiration cooling system. While in the transpiration system the major amount of heat is absorbed by vaporization of a liquid, the primary effect in the liquid or gaseous film cooling system is the reduction of the heat transfer into the skin material. Related to this is the proposed formation of gas blankets, where a gas may either be supplied from containers, or precipitate out of a suitable vaporizing material upstream.

If we introduce these means, even though not yet proven in flight tests, in our time-temperature diagram in a tentative manner, we have finally covered all potential time and temperature combinations (Fig. 19).

7. The Time-Temperature Characteristic as Criterium for the Selection of Materials

In looking over the discussed spectrum of structural high temperature materials and thermal protection systems, we find well-defined limitations of temperature and time. The limitations

are in the first place determined by the predominant elements of heat resistance or heat absorption as they are listed once more in Table 4. As strength becomes distinctly time-dependent at higher temperatures, the integral (or "hot") structure can serve only for short times of operation. The structures based on radiant heat dissipation may serve indefinitely under steady state conditions, as long as the emissivity of the surface is not changed by secondary effects. Likewise, long operation times may be achieved in protection systems based on a (not necessarily limited) supply of absorptive matter, such as a liquid in transpiration cooling, or a gas in film cooling or in the formation of gas blankets. As soon as the absorption is provided by the material itself, in form of the thermal capacity in the solid state in the heat sink system, or of the heat of fusion or vaporization in the ablation process, the service time will be limited to short operation times and single missions.

The so-obtained time and temperature limitations (Fig. 20) do not claim to be exact. We cannot even expect to ever arrive at quantitatively clear defined limits in view of the many secondary influences involved. Nevertheless, even the qualitative time-temperature definition may well serve as a key to match design principles and vehicle requirements and at the same time provide the designer as well as the materials engineer

with a common language of mutual understanding.

It is, however, to be hoped that the extensive efforts made today towards establishing data and knowledge of the exchange between skin material and environment, will, in due time, enable the materials engineer to replace the present empirical approach by systematic developments and provide him with the tool to design materials for high speed flight.

TABLE 1
MAXIMUM OPERATIONAL DATA OF HIGH SPEED VEHICLES

	MACH NO. MAX	SKIN TEMP OF MAX	TOTAL HEAT- ING TIME MAX	DURATION EA. MISSION MAX	NO. OF MISSIONS MAX	RATE OF HEATING °F/SEC MAX
BOMBER	1.5	200	1000 hrs	10 hrs	500	1
FIGHTER	3	700	100 hrs	1 hr	100	5
PILOTL. AIRCR. MISSILE	?	1000	10 hrs	10 hrs	1	
ROCKET AIRCR. I	4.5	1000	10 hrs	30 min	30	10
ROCKET AIRCR. II	7	1000	2 hrs	5 min	15	20
BOOST. GLIDE MISSILE	10	3500	10 min	10 min	1	15
SHORT RANGE B. MISSILE	7	2000	40 sec	40 sec	1	200
INTERMED. R. B. MISSILE	16	6000	15 sec	15 sec	1	700
INTERCONT. B. MISSILE	24	10,000	15 sec	15 sec	1	1000
INSTRUMENTED SATELLITE RE-ENTRY	30	15,000	10 sec	10 sec	1	2000

TABLE 2
 HEAT CONTENTS OF SEVERAL METALS AT VARIOUS STATES
 (Reference Temperature 25 °C)

Metal	To Melting Point cal/gr	Heat Absorbed in Solid State* %	To Include Heat of Fusion cal/gr	To Boiling Point cal/gr	To Include Heat of Vaporization cal/gr
Aluminum	139.0	4.4	234.0	597.0	3177.0
Beryllium	606.0	9.5	866.0	1966.0	6404.0
Copper	98.0	6.6	149.0	328.0	1474.0
Iron	165.0	8.5	230.0	457.0	1913.0
Magnesium	155.0	9.0	244.0	397.0	1713.0
Molybdenum	160.0	7.9	230.0	394.0	2019.0
Silver	50.0	6.2	75.0	160.0	809.0
Titanium	215.0	8.5	315.0	506.0	2521.0
Tungsten	111.0	7.8	155.0	247.0	1430.0
Zirconium	126.0	7.7	179.0	263.0	1633.0

* In per cent of total heat content including vaporization

TABLE 3

HEAT ABSORPTION OF HETEROGENOUS
MATERIALS AT AN ABLATION
RATE OF 1 mm/sec
cal/cm² sec

	Cu	B	Ag	Al	Mg
ZrO ₂	593	863	413	408	165
ZrSiO ₄		812	367	365	141
BeO			500	489	208
B ₄ C			441	434	181
SiC			403	399	160
La ₂ O ₃			287	291	102

Refractory Sublimes

CaO		825	379	377	148
Al ₂ O ₃				413	167
Spinel				426	175
B ₄ C				370	144
Mullite					153

TABLE 4
HEAT ABSORPTION IN VARIOUS
HIGH TEMPERATURE SKIN DESIGNS

PRINCIPLE	MAJOR ABSORPTION	MINOR ABSORPTION
CONVENTIONAL		(RADIATION)
METASTABLE METALS		RADIATION
INSULATION	RADIATION	
RADIATION	RADIATION	THERMAL CAPACITY
HEAT SINK	THERMAL CAPACITY	RADIATION, E. R.
ABLATION	TH. CAPACITY TO INCLUDE VAPORIZATION OR FUSION	RADIATION, E. R. REDUCTION OF HT
TRANSPIRATION	HEAT OF VAPORIZATION & SUPER HEATING	REDUCTION OF HT
FILM COOLING	MASS COOLING	HEAT OF VAPORIZATION REDUCTION OF HT
FORMATION OF GAS BLANKETS	REDUCTION OF HEAT TRANSFER	MASS COOLING

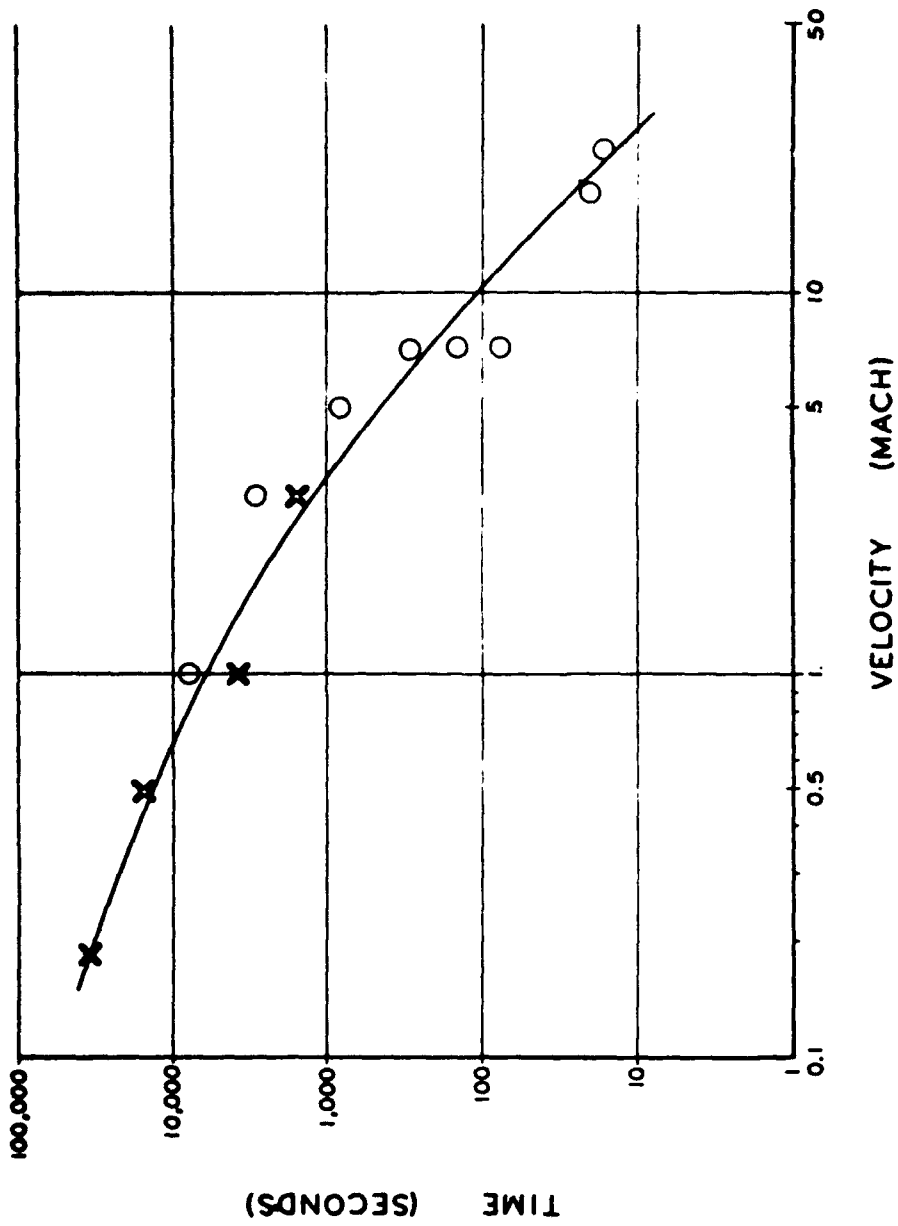
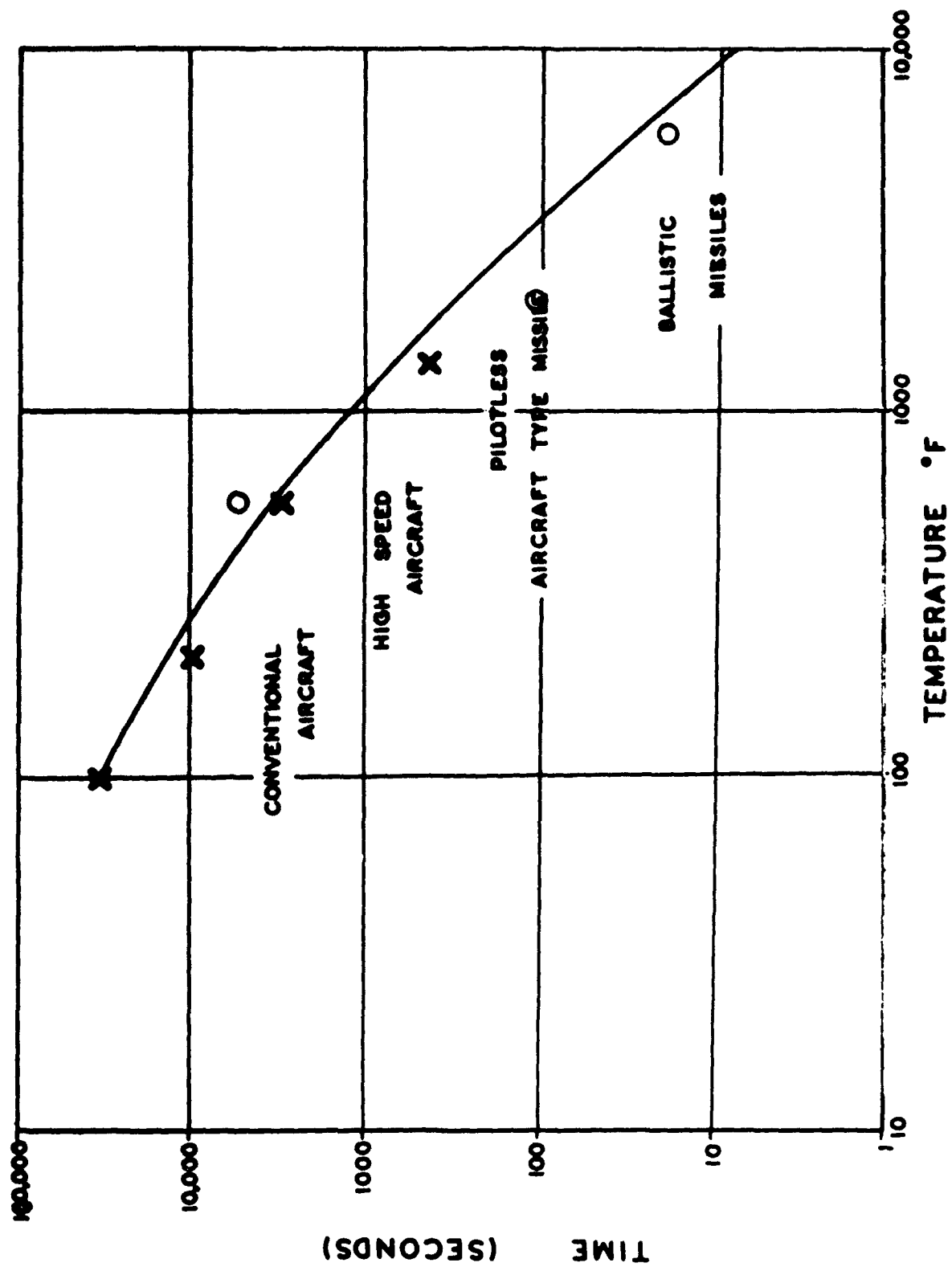


FIG. 1 - SPEED - TIME RELATIONSHIP
FOR HIGH SPEED VEHICLES



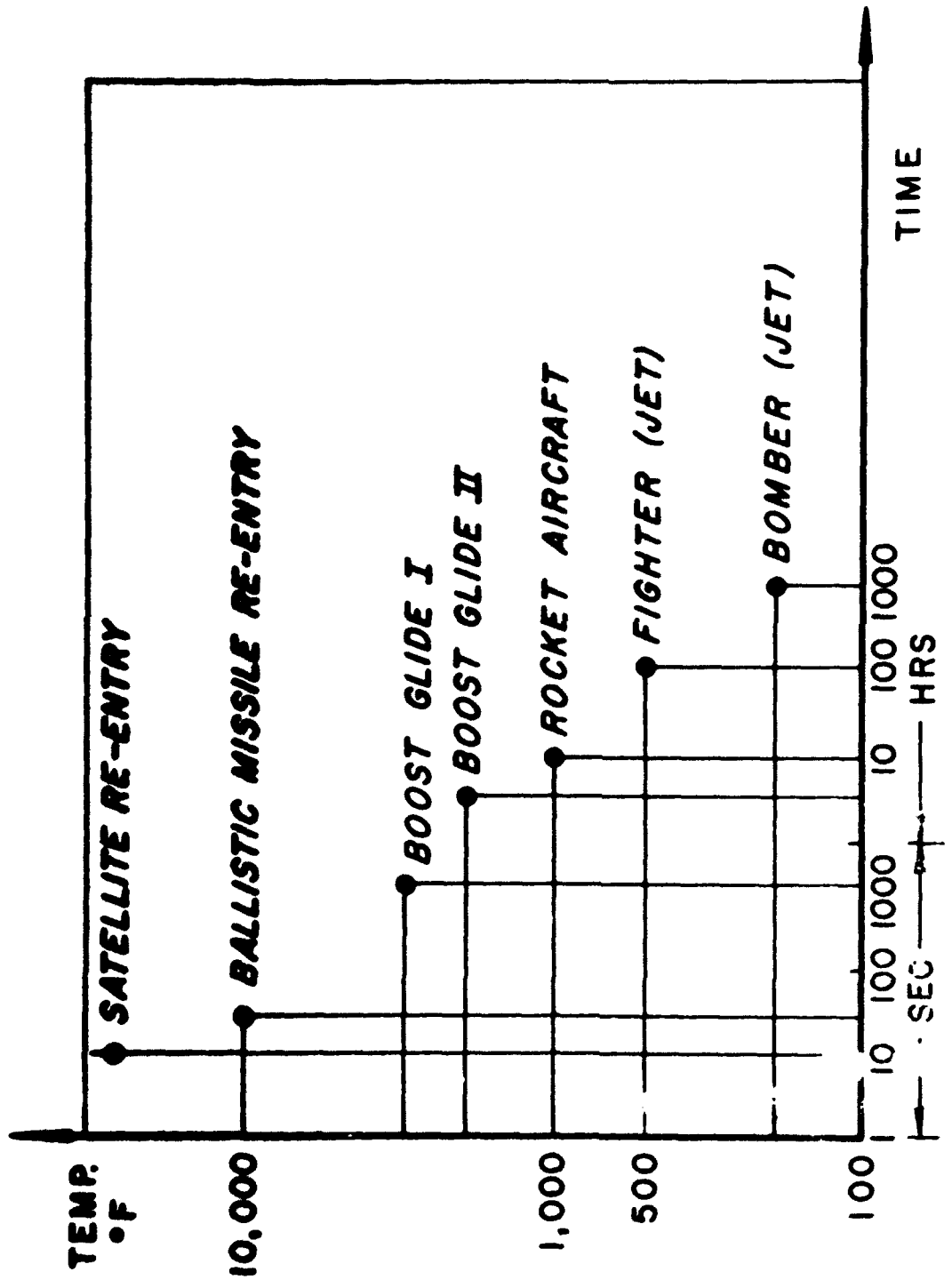


FIG. 3 - OPERATIONAL CHARACTERISTICS OF HIGH SPEED VEHICLES IN TERMS OF TIME AND TEMPERATURE

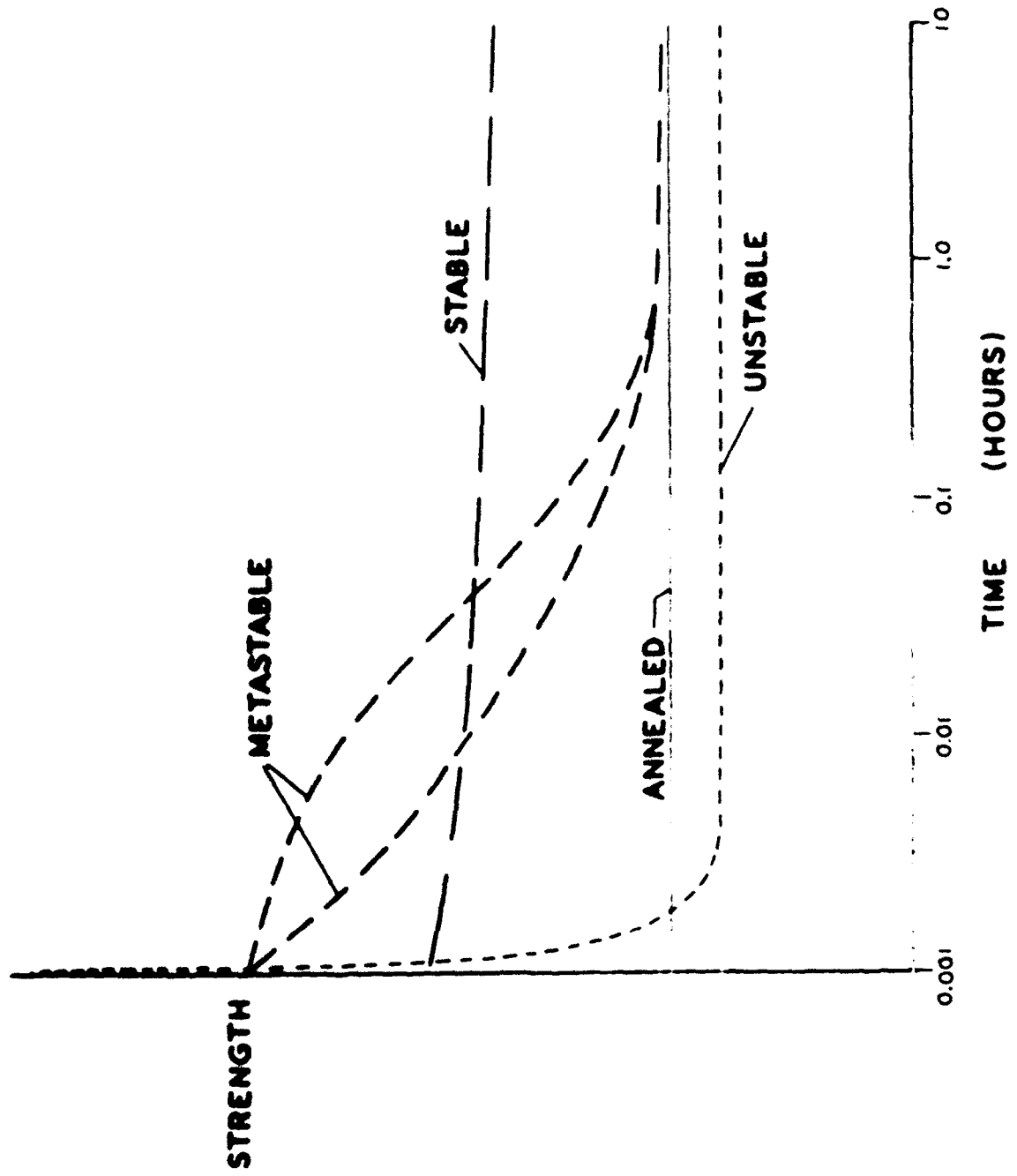


FIG. 4 - METALS AT SHORT TIMES OF HEAT EXPOSURE. EFFECT OF VARIOUS STRENGTHENING TREATMENTS ON THE TIMEWISE STABILITY

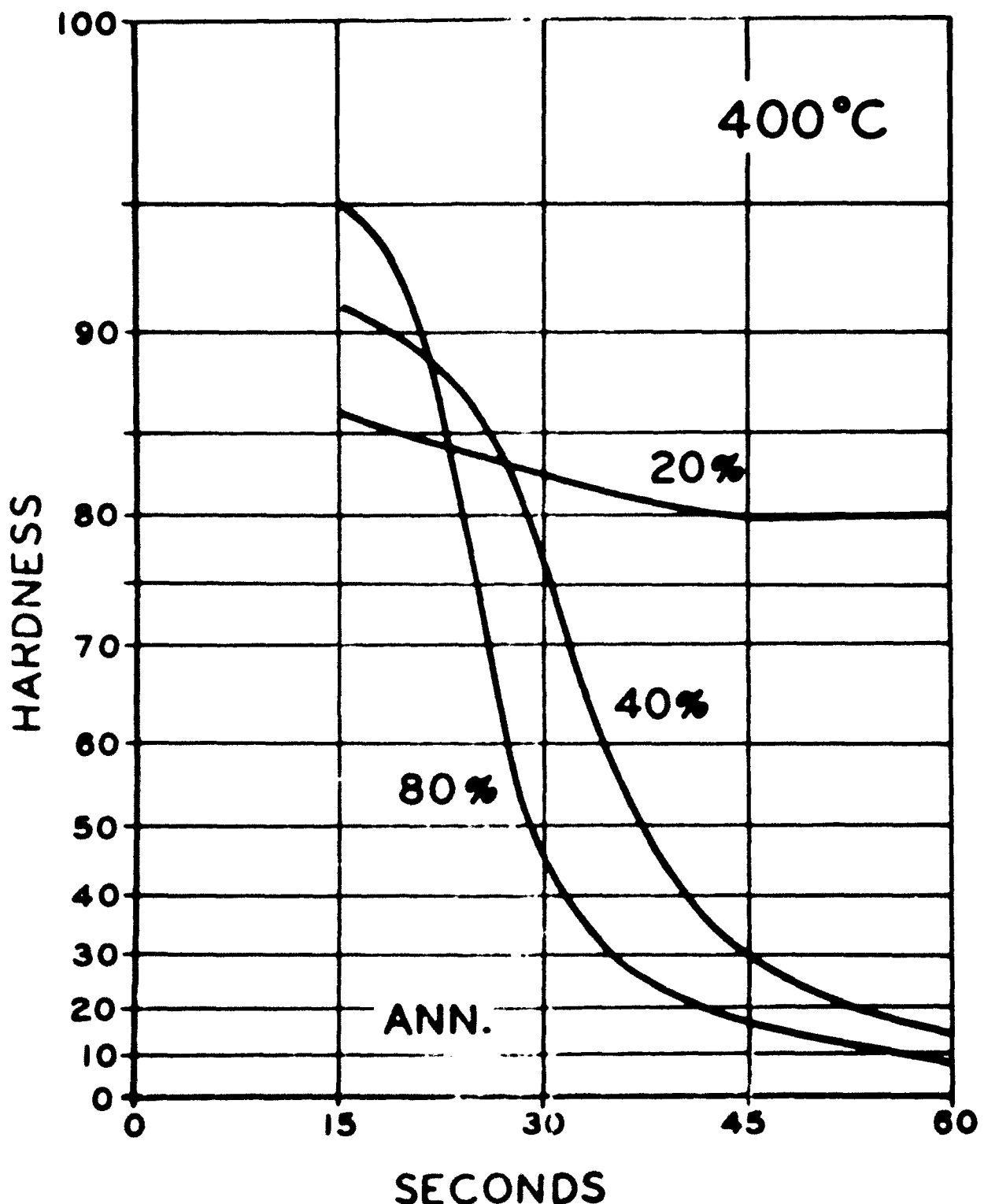
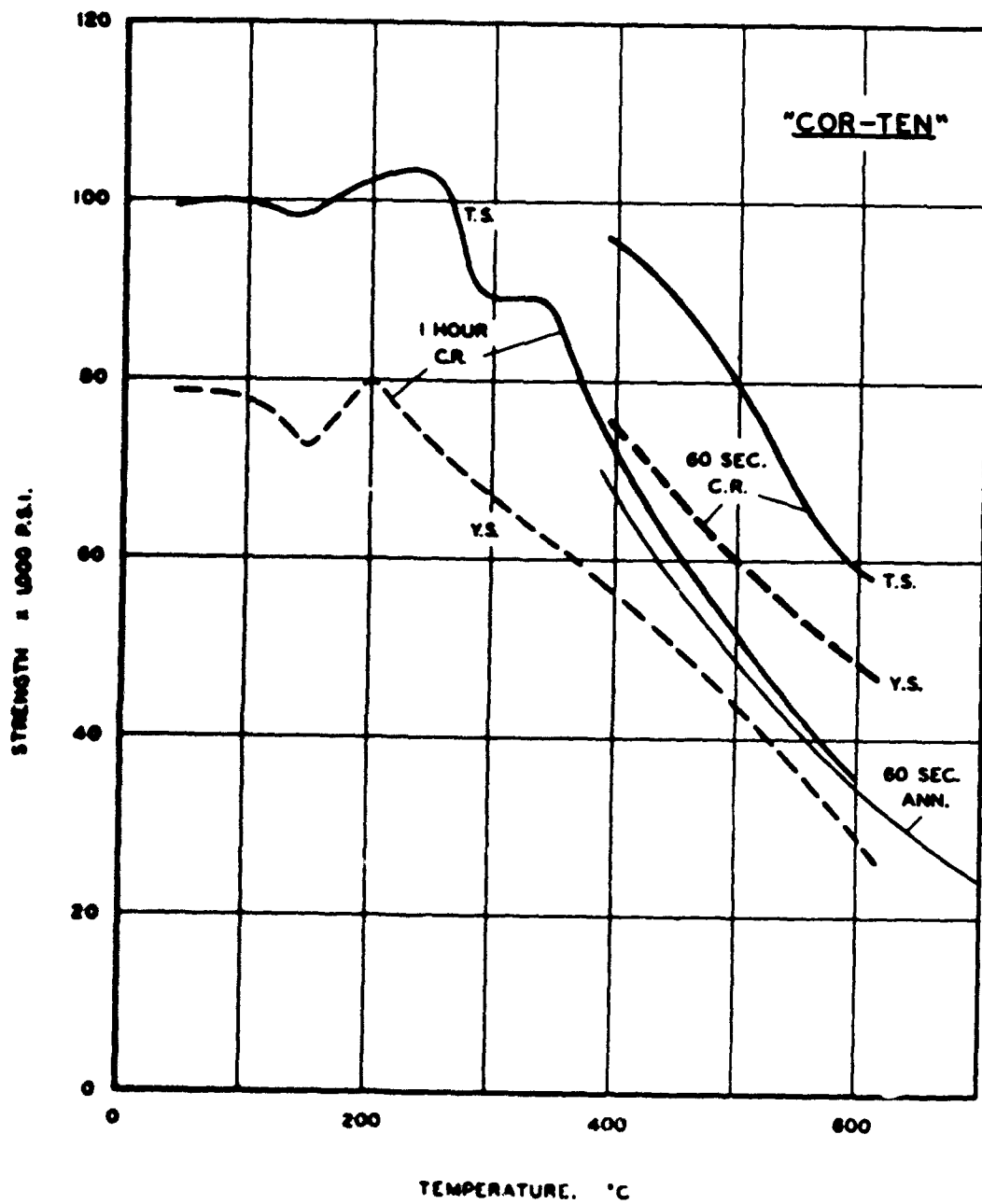


FIG. 5 - STABILITY CHARACTERISTICS (HARDNESS) OF COPPER
AT 400°C FOR VARIOUS DEGREES OF COLD WORKING



**FIG. 6 - STRENGTH - TEMPERATURE DIAGRAM FOR A
LOW ALLOY STEEL ("COR-TEN") FOR 60
SECONDS AND 1 HOUR OF HEAT EXPOSURE**

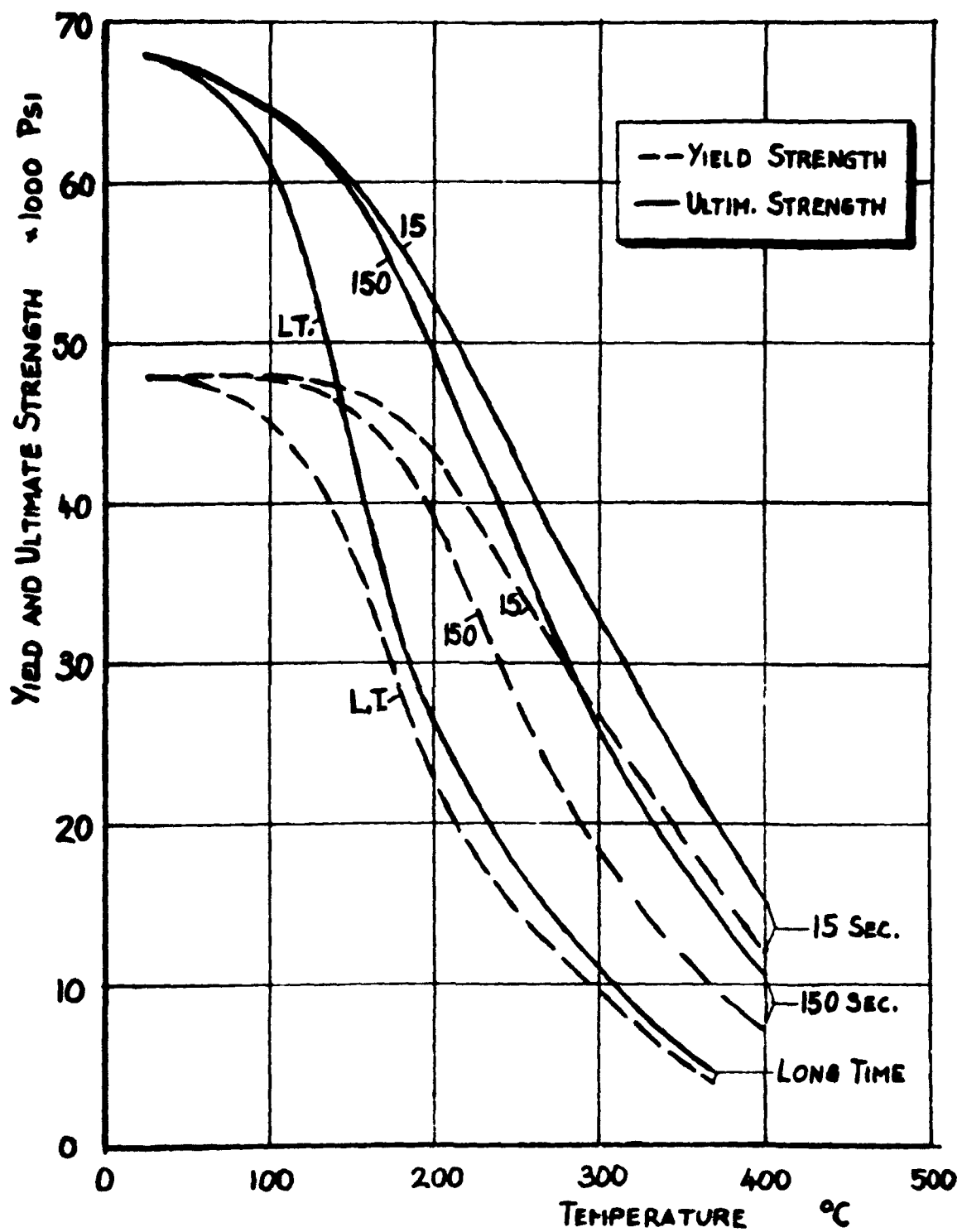


FIG. 7 - STRENGTH - TEMPERATURE DIAGRAM OF A
PRECIPITATION HARDENED AL-CU-MG ALLOY

(2024-T3) AT VARIOUS TIMES OF HEAT

EXPOSURE

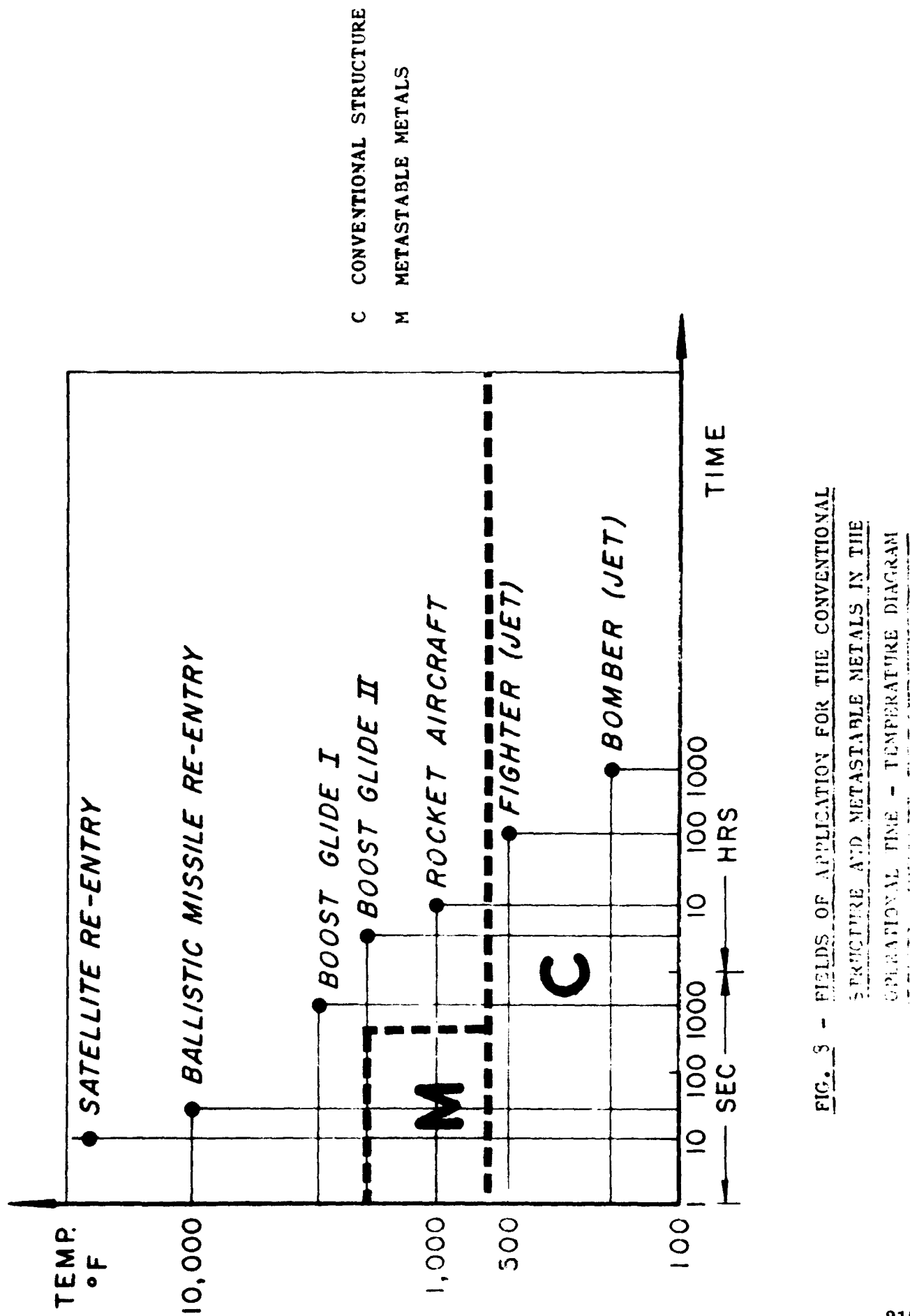


FIG. 5 - FIELDS OF APPLICATION FOR THE CONVENTIONAL STRUCTURE AND METASTABLE METALS IN THE OPERATIONAL TIME - TEMPERATURE DIAGRAM

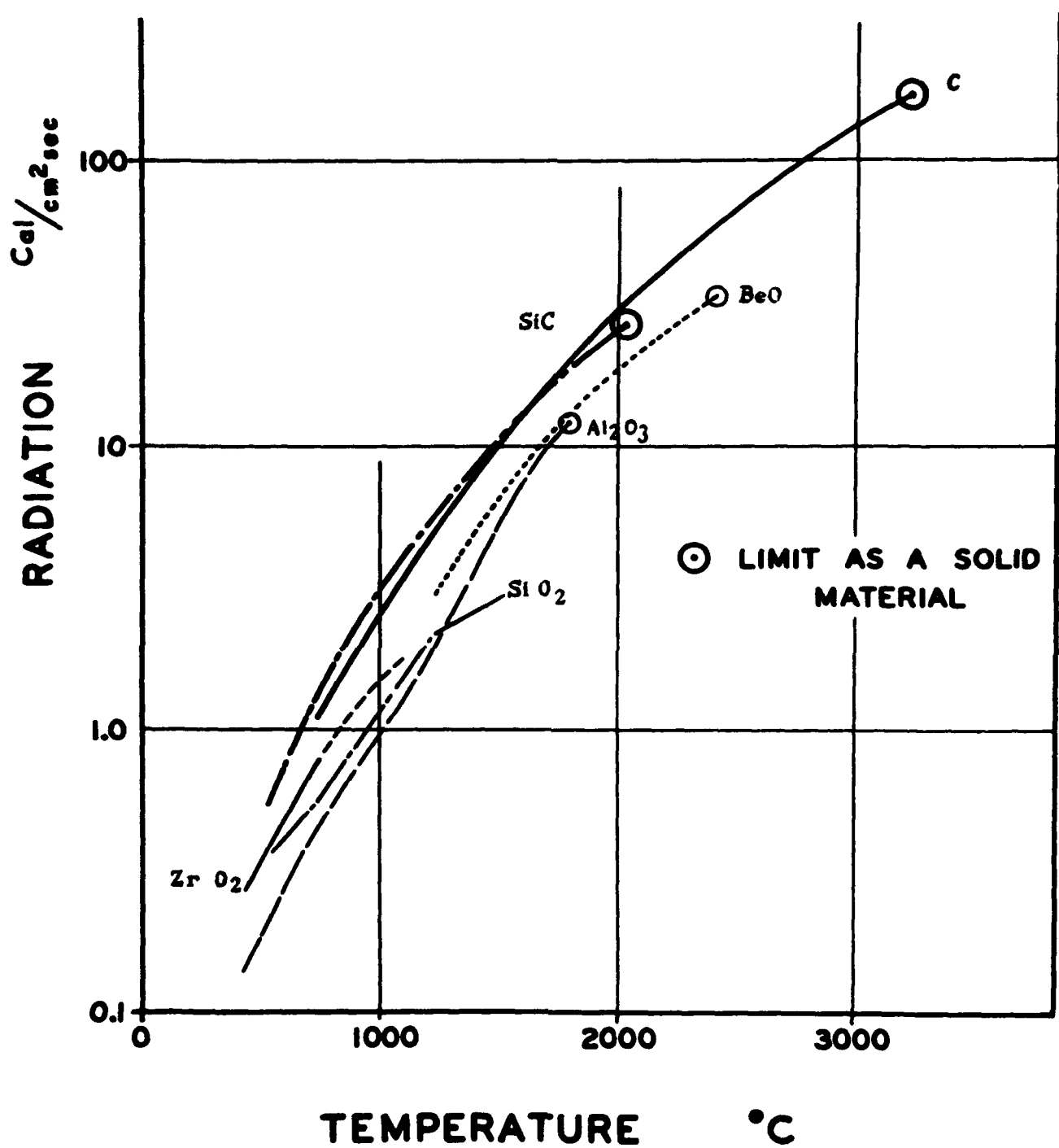
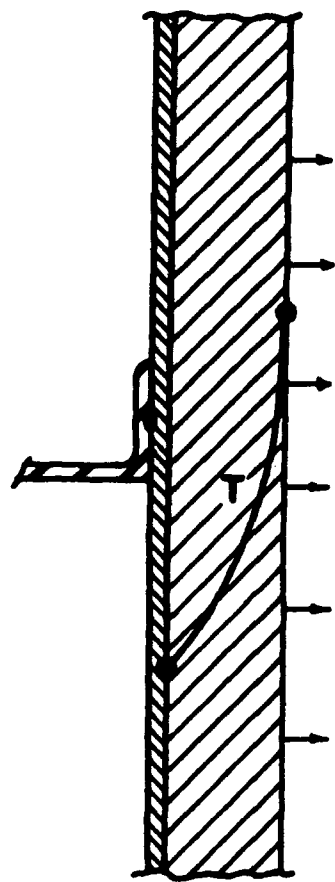
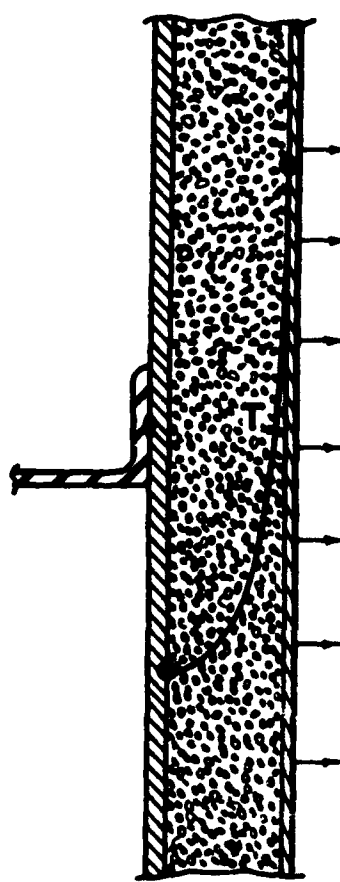


FIG. 9 - HEAT DISSIPATED BY RADIATION FOR SEVERAL CERAMICS AT HIGH SURFACE TEMPERATURES

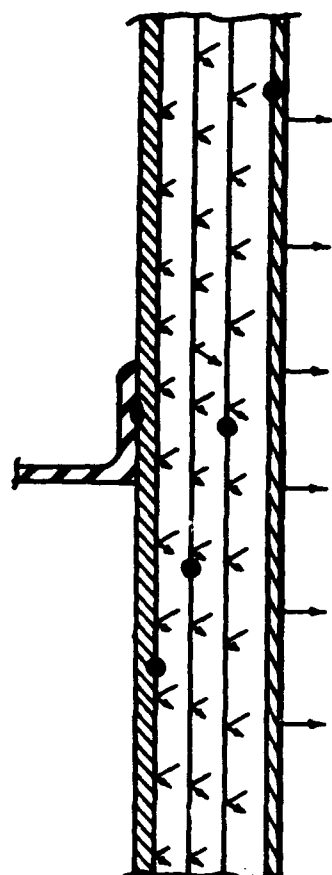
RADIATION SYSTEMS



(a) CERAMIC



(b) INSULATION



(c) REFLECTION

FIG. 10 - TYPICAL COMPOSITE STRUCTURES BASED ON
THE PRINCIPLE OF HEAT PROTECTION

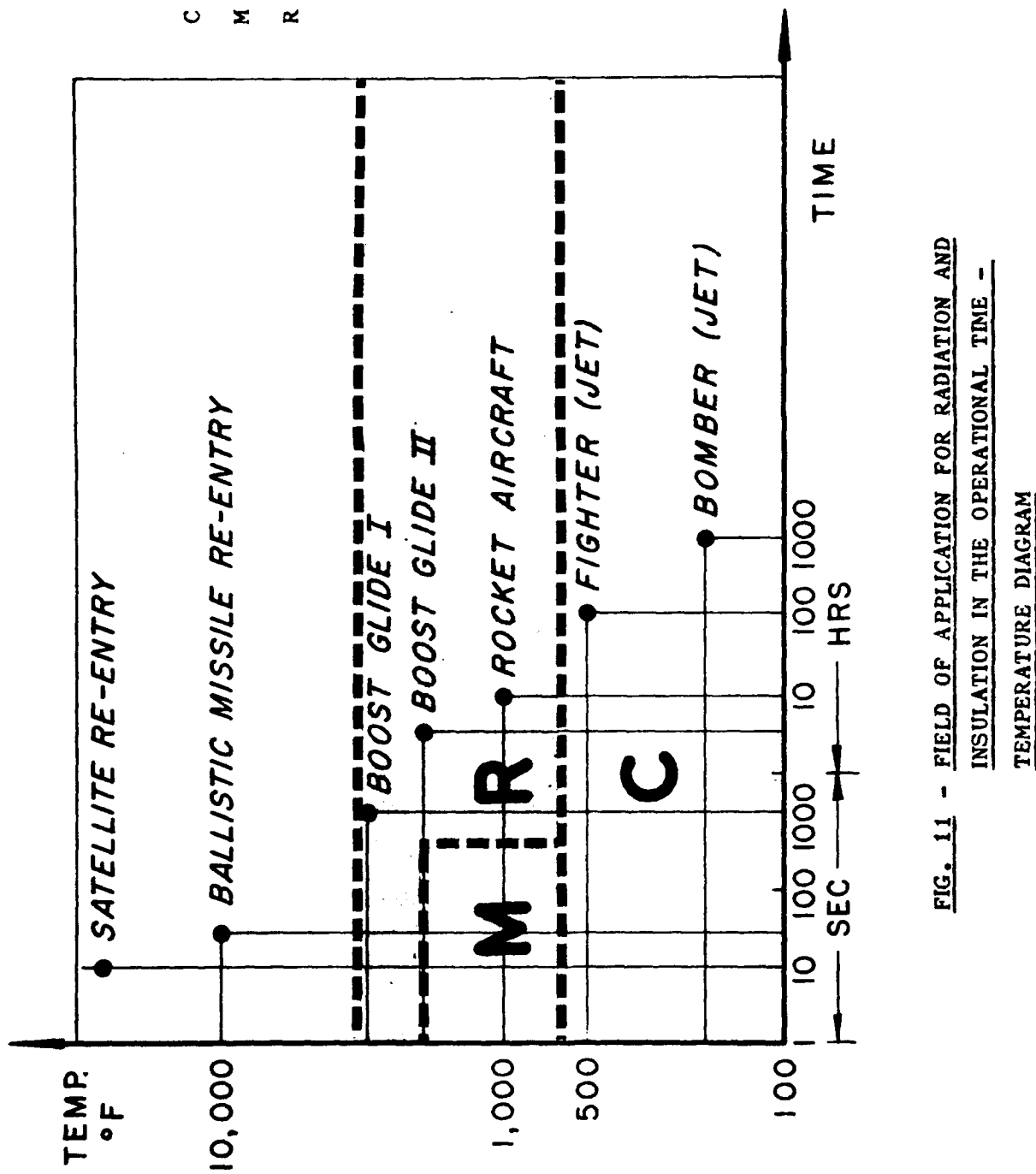


FIG. 11 - FIELD OF APPLICATION FOR RADIATION AND INSULATION IN THE OPERATIONAL TIME - TEMPERATURE DIAGRAM

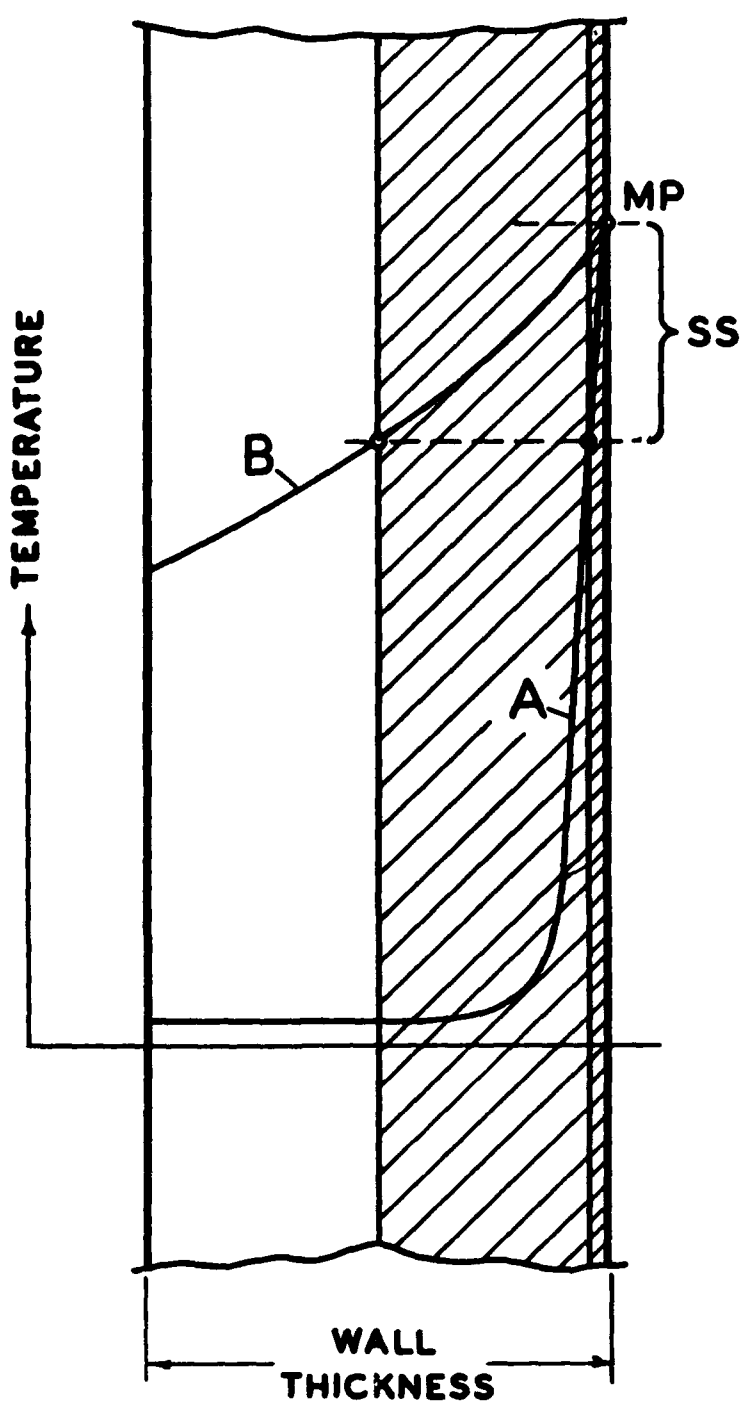


FIG. 12 - POTENTIAL DEPTH OF INITIAL ABLATION
FOR DIFFERENT THERMAL GRADIENTS

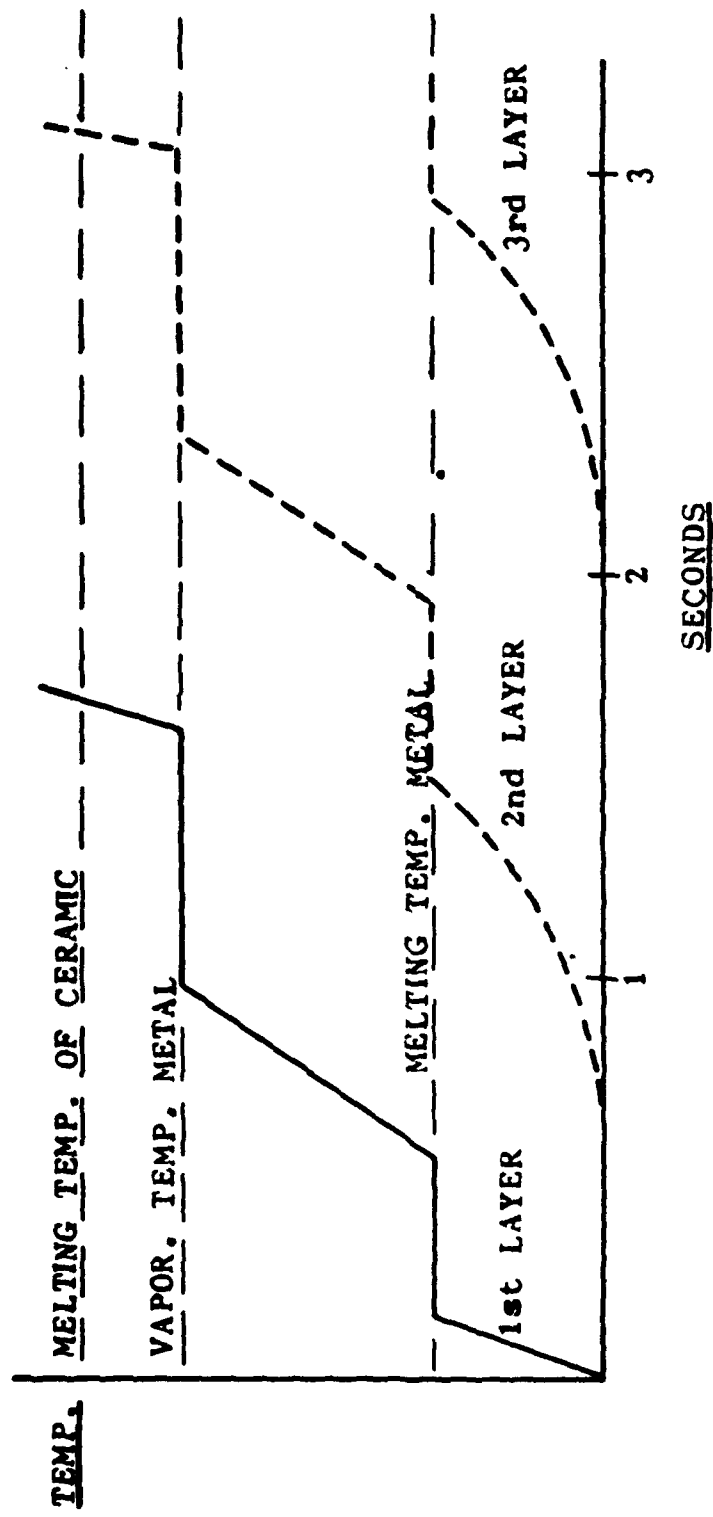
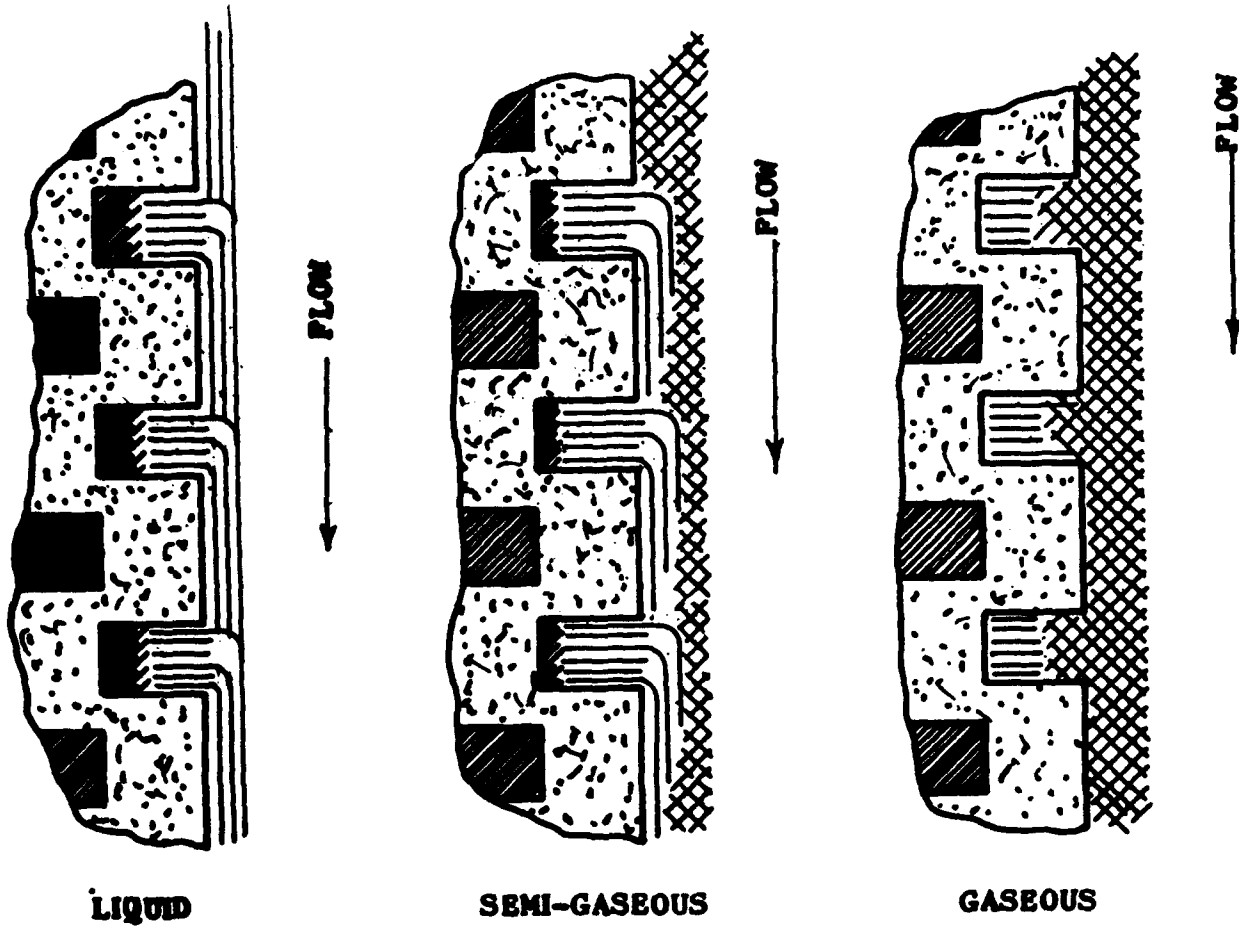


FIG. 13 - SYSTEMATIC REPRESENTATION OF THE ABLATION PROCESS
 FOR A HETEROGENEOUS MATERIAL: TIME - TEMPERATURE
 CHARACTERISTIC OF THE SURFACE LAYER



SURFACE

TEMPERATURE: T_p

18

T_V

FIG. 14. - PRINCIPAL TYPES OF ABLATION

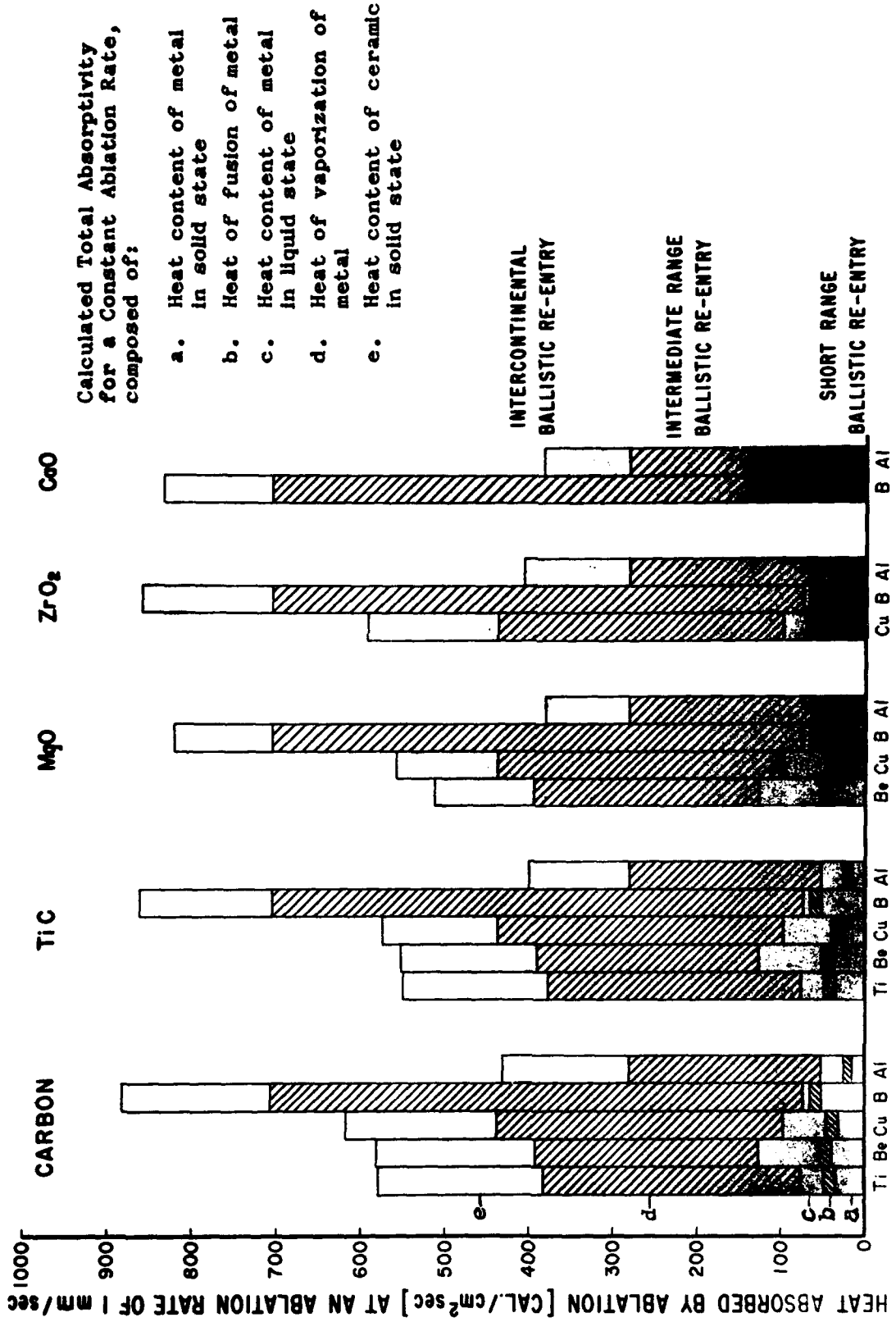


FIG. 15 - EFFICIENCY OF VARIOUS HETEROGENOUS
METAL - CERAMIC SYSTEMS IN ABLATION

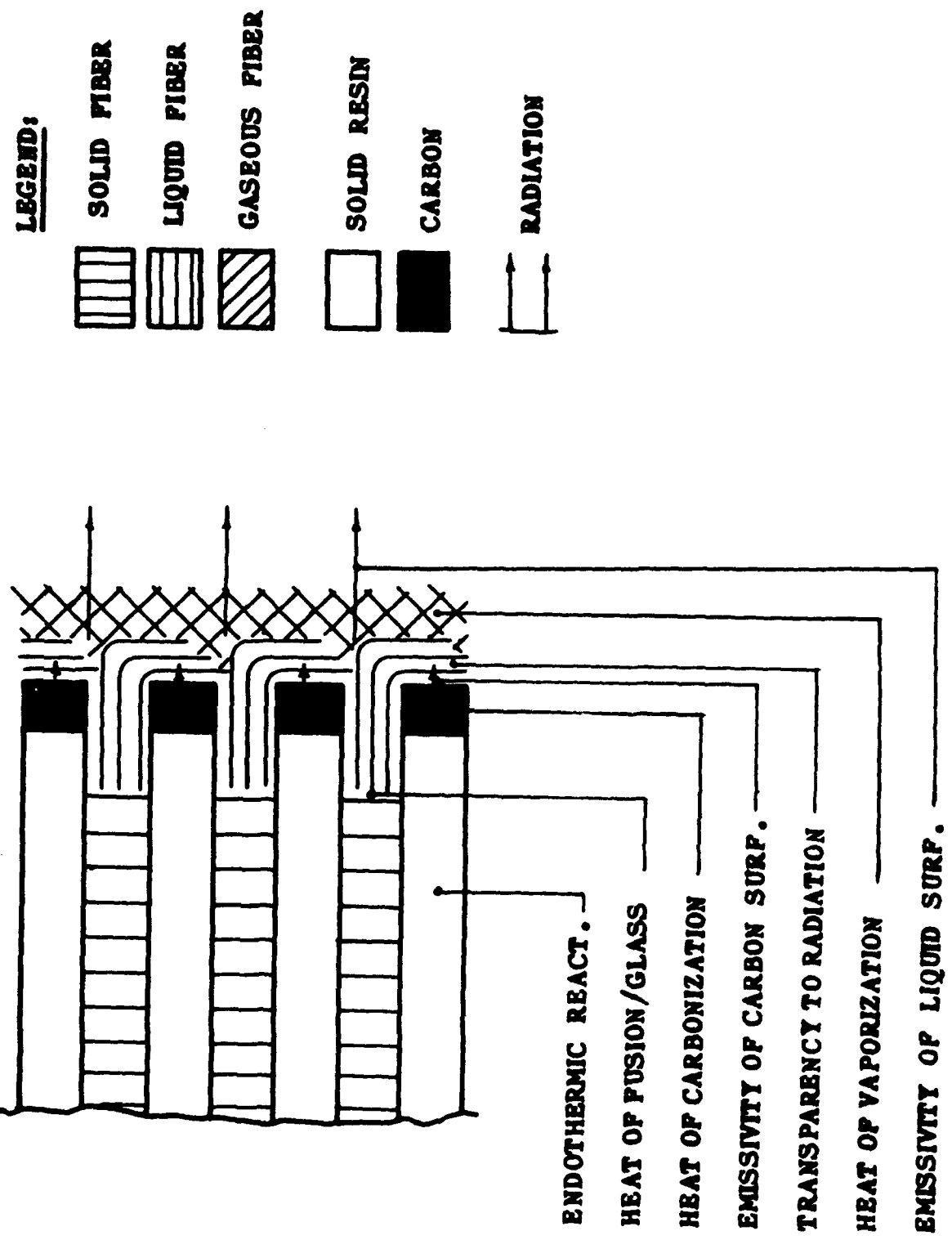


FIG. 16 - ELEMENTS OF HEAT ABSORPTION IN A RESIN - FIBER SYSTEM DURING ABLATION

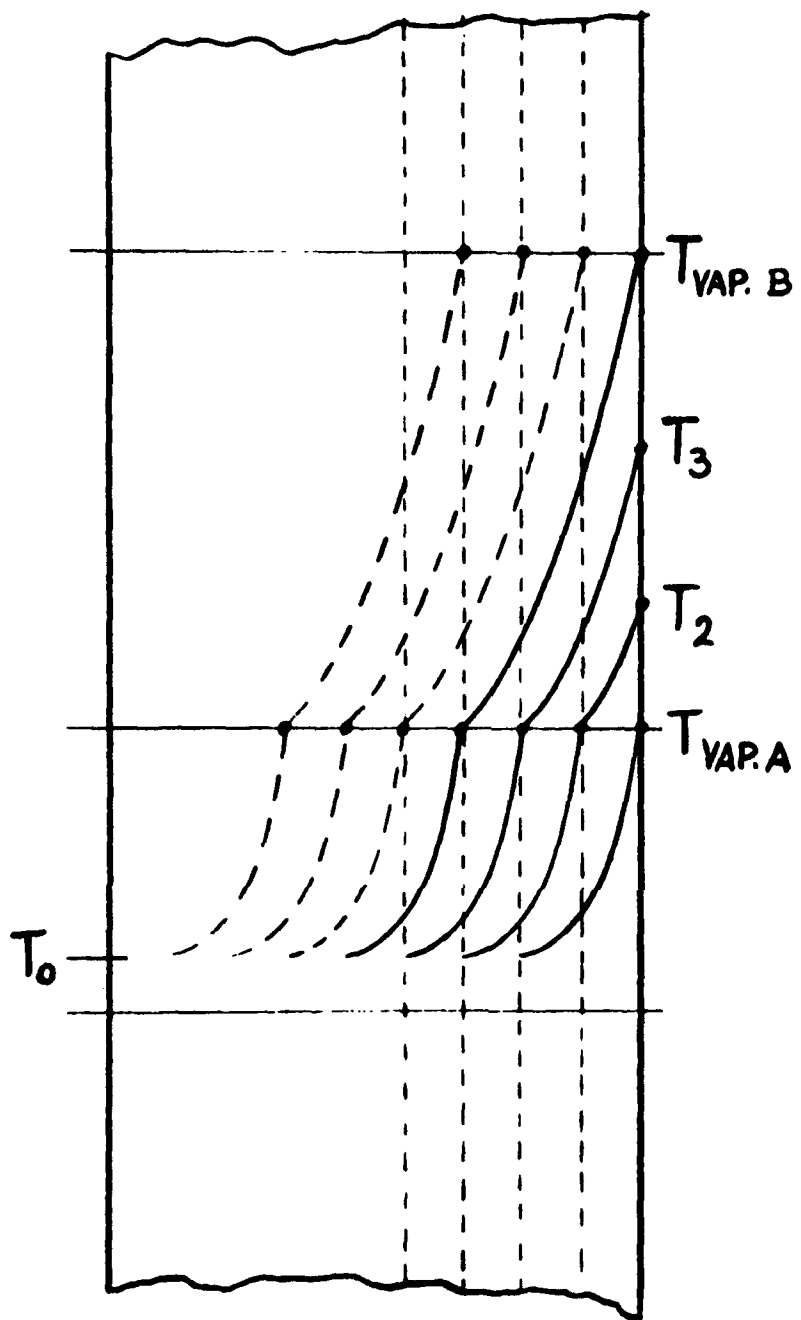


FIG. 17 - ABLATION OF A MATERIAL WITH
CHANGING VISCOSITY DUE TO
FRACTIONAL DISTILLATION

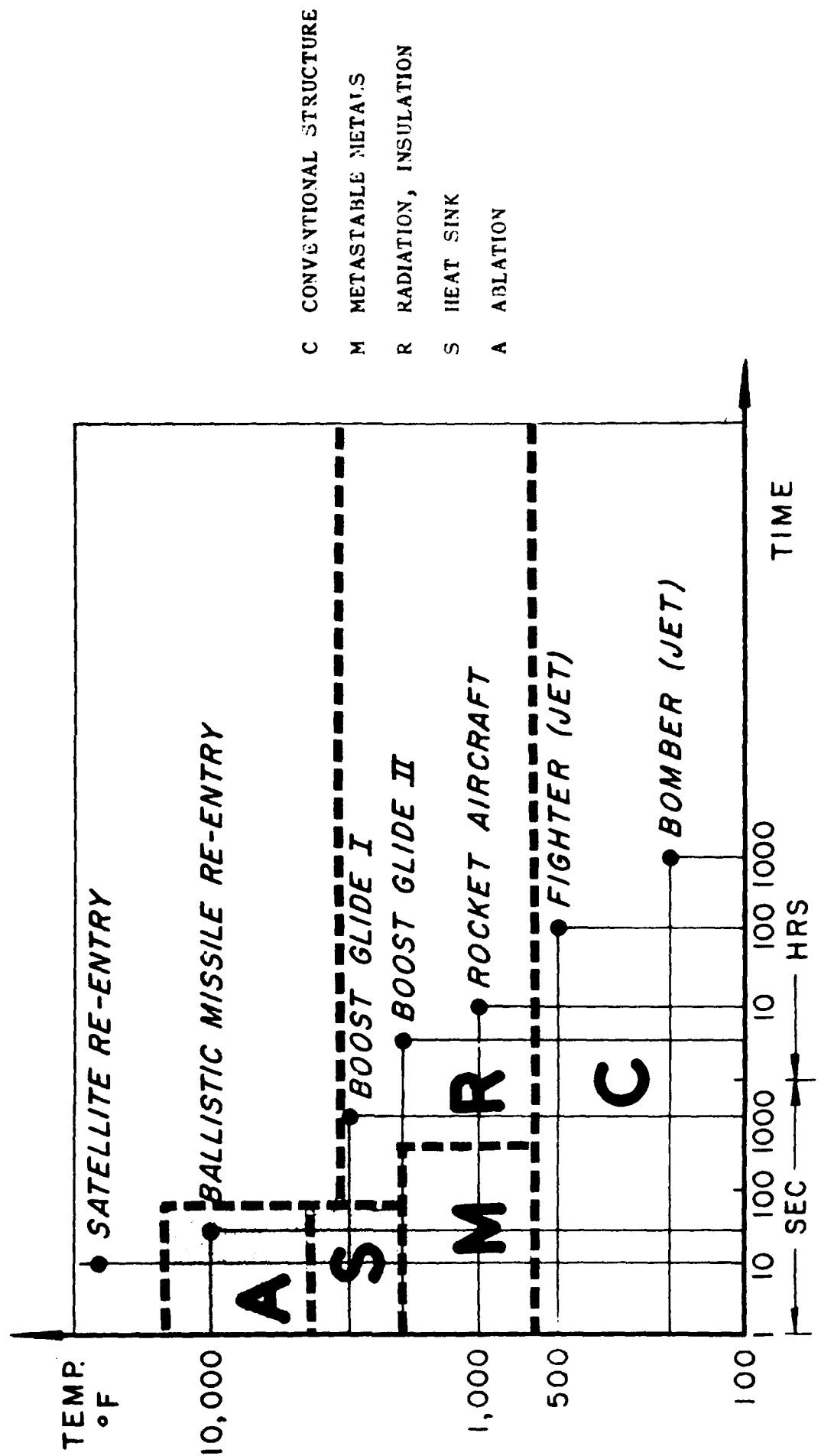
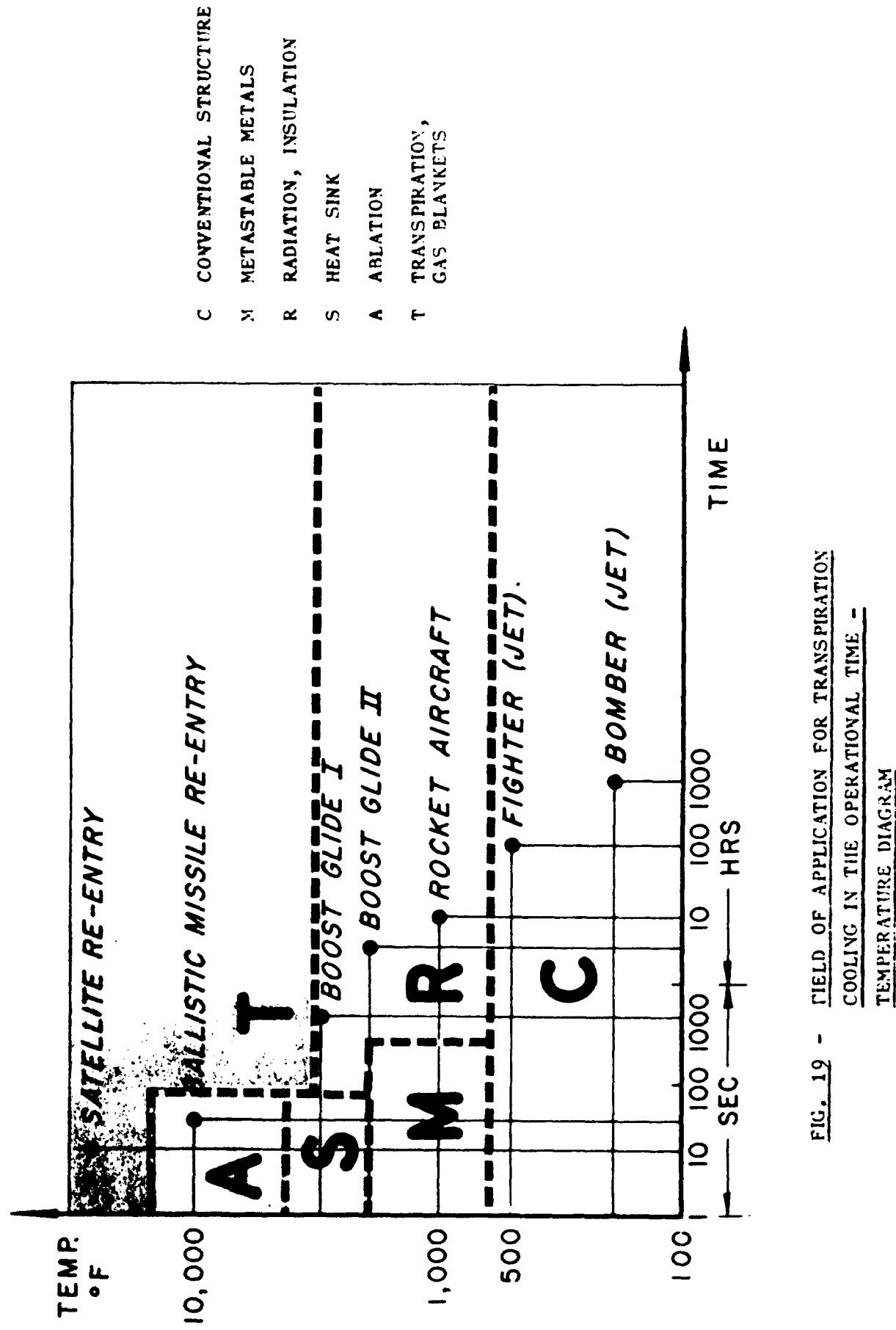


FIG. 18 - FIELDS OF APPLICATION FOR HEAT SINK

AND ABLATION IN THE OPERATIONAL



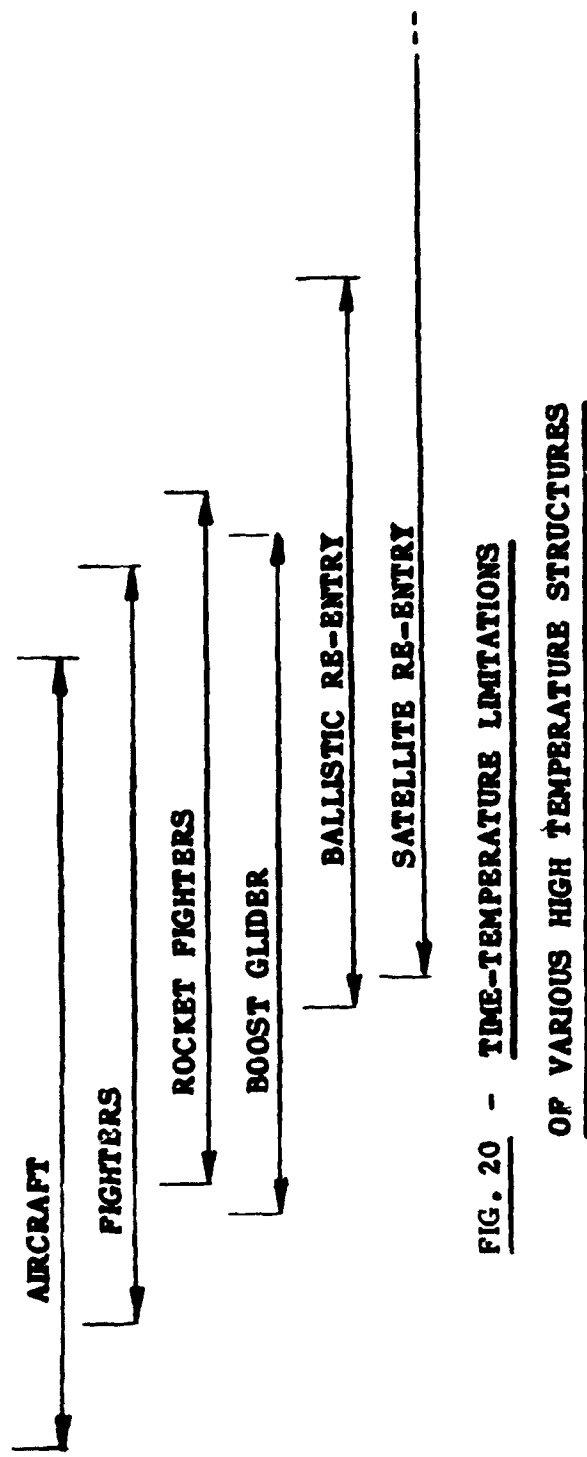
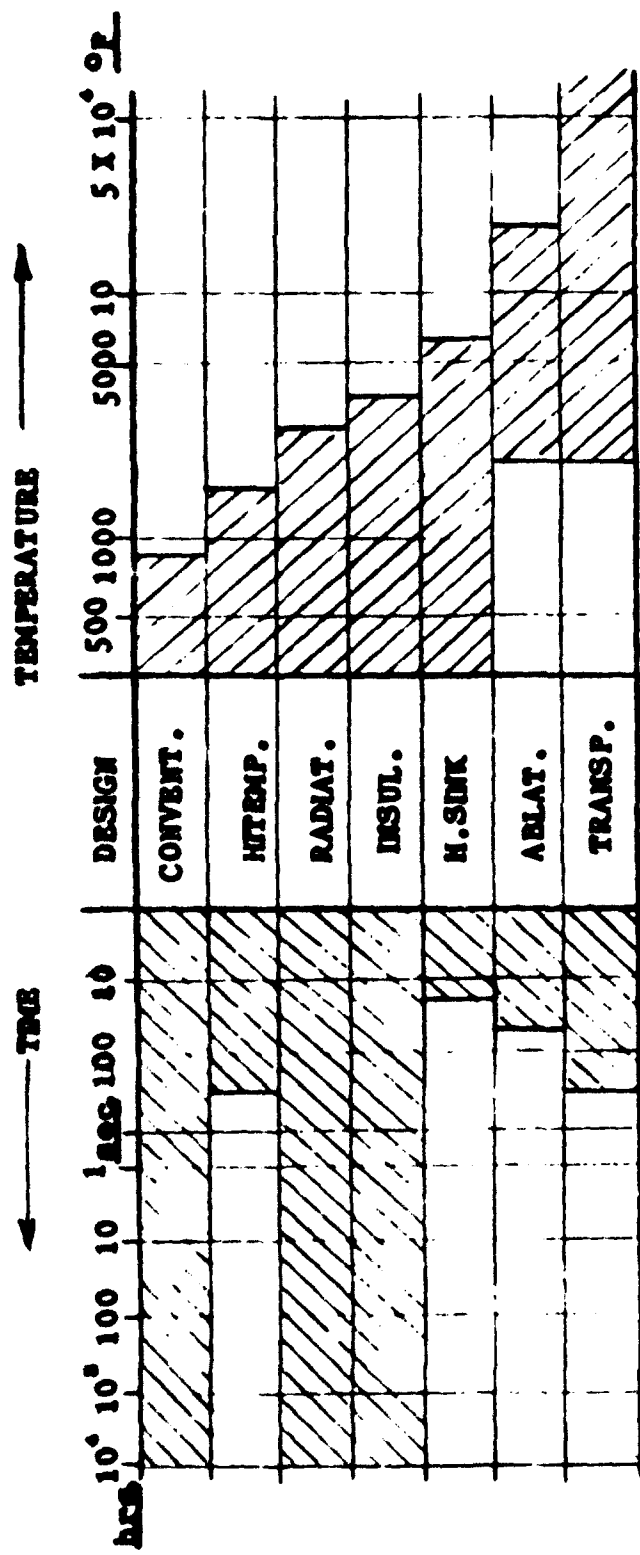


FIG. 20 - TIME-TEMPERATURE LIMITATIONS

OF VARIOUS HIGH TEMPERATURE STRUCTURES

CERAMIC MATERIALS FOR USE IN HYPERSONIC AIRCRAFT

John M. Nowak
Bell Aircraft Corporation

March 24, 1958

CERAMIC MATERIALS FOR USE IN HYPERSONIC AIRCRAFT

John M. Nowak
Bell Aircraft Corporation
Buffalo 5, New York

Introduction

The attendance at this session is an excellent indication of interest in the problems of using high temperature stable materials in aircraft and missiles. Until very recently, with the relatively slower vehicles, metals have adequately fulfilled the structural requirements. However, as the speeds in our new aircraft and missiles continue to Mach 10, Mach 15, and beyond, use of conventional designs radically limits the use of present metals. Metal alloys useful to temperatures of about 1350 F to 1600 F are commercially available. Some of the high temperature alloys, as an example a high cobalt type, have reported stress rupture strengths in wrought form of about 7200 psi at 1800 F after 100 hour exposure at 1800 F. The short time tensile strength of this alloy is reported to be about 22,700 psi at 1800 F. However, as operating temperatures increase to 1800 F and above, more and more of our technical people are looking to ceramics to solve their material problems.

Ceramics is one of the oldest of arts. Yet it is only relatively recently that modern technology has been extensively applied to the study of ceramics. The term ceramics means many things to many people. It means pottery to some; brick to some; abrasives to some; glass and refractories to others. Conventional ceramic materials are prepared by mixing certain amounts of plastic, filler and flux. The ceramic material processed and prepared for the forming operation had ingredients which functioned in these three ways. It has to be plastic so that it could be formed into any shape; it had to have a low drying shrinkage so that cracks would not develop with resultant failure of the ware; and it had to have low enough fusibility to be fired into a strong product at temperatures economically practical. The minerals which contribute the property of plasticity are called plastics in the ceramic field of technology. They are not the same materials to which the term

March 21, 1959

plastic has now been generally associated. The minerals which contribute to the low degree of fusibility are called fluxes. The minerals which contribute the property of elongation and age control are called fillers. However - many of today's ceramic materials, such as pure Al_2O_3 , are not compounded in the conventional manner. High purity bodies may be formed by hydrostatic pressure at high temperatures. Bodies may be fired at very high temperatures. Some of the recently developed commercial bodies such as dense silicon carbide do not use a flux but are self bonded.

Brittleness is the major drawback in using ceramic materials as structural hardware. Although the materials are usually poor in tensile strength at room temperature, their compressive strength is generally excellent. Many ceramic materials however, have better tensile strengths than metals at temperatures of 1800 F and above. James Gangler and associates (NACA TN 1911) reported a short time tensile of about 22,500 psi at 1800 F for a boron carbide body. Designs using a ceramic material should take this into account. Studies are now underway by Dr. Joseph Pask and associates at the University of California and probably others, to improve the ductility of ceramics. It may be many years, however, before ductile ceramics are developed. In the meantime, studies are underway to utilize in flight vehicles the better heat resistant properties of ceramics. Some ceramic materials have what appears to be definite strength advantages over metals at elevated temperatures. We have compiled Table I showing the strength to weight ratio of an Al_2O_3 body compared to molybdenum at various elevated temperatures. It can be seen that Al_2O_3 may be considered competitive in the temperature range of about 2000 F, based on ultimate strength-density ratio. Metals for use at temperatures of 2000 F and higher, possessing high mechanical strength, are subject to oxidation. Reviewing data now shown, there are, of course, many other factors which must be considered including: effect of brittleness of the alumina on design application, the creep rupture strength, the effect of oxidation on molybdenum, effect of oxidants on the strength of molybdenum, etc. This data is presented to bring to your attention the possibilities that do exist for ceramics as structural materials in hypersonic air vehicles even at the relatively low temperature of 2000 F.

March 24, 1958

The use of ceramic materials as high temperature, low density insulants has been accepted by industry for many years. However, the effect of vibration of these materials at high temperatures has not been investigated to our knowledge. Ceramic materials have been used as coatings for metals for applications such as enamels for household appliances, enamels for outdoor service on steel and aluminum. We hope that our presentation this afternoon will add to the sum of knowledge on the possible application of ceramics to high speed flight vehicles. One cannot overlook any of the materials available. Our studies were directed toward use of ceramics in applications at elevated temperatures for periods of one to 100 hours.

March 24, 1958

RESULTS

About five years ago our laboratories undertook the investigation of materials for application to proposed hypersonic aircraft. Reviewing the material problems which we could anticipate at that time and based on the best information available from designs made by our Structures Engineers, we decided to direct our preliminary efforts into several functional channels. We divided our studies into the following: (1) refractory materials for "hot spot" areas, (2) thermal insulants, and (3) protective coatings to prevent oxidation of metals. In a proposed vehicle, the refractories were considered for the wing leading edges and the nose. The insulants were for application between the outer skins or walls and the interior structure. The protective coatings were considered for application to metal skins fabricated from super alloys in foil thickness and to other metallic and non-metallic components subject to elevated temperatures. With the exception of a few of the coatings, all the materials evaluated are ceramic.

Refractory Materials for Hot Spot Areas

Tests were conducted on a number of selected high temperature materials which may be useful as refractories for hot spot areas where temperatures in excess of 2500 F and approaching 4000 F may be anticipated. Most of the high melting point materials have mechanical, thermal, or chemical properties which make them unsuitable for some of these applications. Although no material to our knowledge is presently available which will meet all the target requirements for all hot spot areas, test data establishing useful life temperatures for available materials is imperative. A number of refractory carbide and graphite materials were selected on the basis of their theoretical properties and were screened for rate of oxidation at 2800 F under a controlled oxygen flow of one liter per minute. This temperature was selected as a plateau representing the lower temperature limits of proposed applications.

Oxides as a class appear to have lower useful operating temperatures than do the carbides. The oxides tend to have lower strength at the high temperatures. Some are

March 24, 1958

subject to thermal shock. The carbides, however, generally have higher melting points, higher strengths at the elevated temperatures and are not subject to the degree of thermal shock that is common to some oxides. At sufficiently elevated temperatures the carbides will oxidize. Purpose of our studies on the carbides and graphite was to ascertain the degree of oxidation which we could expect.

In addition, preliminary temperature tests to 3700 F were conducted on a magnesia-zirconia body, on a dense silicon carbide body and on a zirconium carbide body. Modulus of rupture tests were conducted at temperatures to 2700 F on an experimental, aluminum modified, dense silicon carbide body, and at temperatures to 1500 F on a number of zirconia bodies. The aluminum modified silicon carbide was fabricated in an attempt to obtain a commercially producible silicon carbide possessing a modulus of rupture approaching the best hot pressed variety known to us. A hot pressed, high strength SiC body with a reported modulus of rupture of 70,000 psi at 2500 F was prepared by Alfred University on a laboratory scale.

Of the bodies tested only SiC-B₄C, recrystallized SiC, and AGR graphite coated with about .005" SiC were capable of withstanding exposure to oxygen at 2800 F for three hours without excessive deterioration. The ZrC oxidized to a powder. The TaC and the TaC-ZrC bodies oxidized excessively. Based on the change in weight and the amount of CO₂ collected per square centimeter of surface area, the SiC-B₄C body showed the greatest resistance to oxidation under those test conditions. Examination of the SiC coated graphite showed pronounced voids under the coating. These voids were concentrated at the edges. This would indicate that it may be difficult in getting an adequate coating on the edges. Detailed oxidation resistance test data for the bodies evaluated is given in Table III. The weight of CO₂ collected per square centimeter of exposed area against exposure time for all samples tested is plotted in Figures 1, 2 and 3.

March 24, 1958

To determine resistance to higher temperatures, preliminary qualitative tests consisting of exposing test samples in an oxy-acetylene furnace up to 3700 F were conducted on a 75% magnesia-25% zirconia body, a dense silicon carbide body, and a zirconium carbide body. The magnesia-zirconia body has been used as a funnel for transferring molten stainless steel. Visual examination of the test specimens showed little evidence of attack on the dense silicon carbide exposed for 10 minutes at 3700 F. Exposure for about 85 minutes resulted in severe oxidation of the body. Table IV lists more complete visual data taken on the dense SiC specimens exposed. A substantial weight loss was noted after exposure of the MgO-ZrO₂ body for one hour at about 3450 F. A white coating was formed over the ZrC test specimens after 2 to 6 minutes exposure at temperatures from 3275 F to 3450 F. The coating was observed to have poor adhesion to the body.

Modulus of rupture tests at temperatures to 2700 F on the aluminum modified, experimental, dense silicon carbide body showed a considerable spread within each test point. Test data for the 60 minute exposure at temperature is plotted in Figure 5. Table V compiles the test data collected for the body. Considerably lower modulus of rupture values were obtained for the ZrO₂ as shown in Table VI.

Thermal Insulants

Vibration tests at temperatures of 1800 to 2000 F and water absorption tests were conducted on a number of low density, silica and alumina-silica fibrous insulants.

1. Vibration at Elevated Temperature

Alumina-silica and silica fibrous insulants with a nominal density of 3 to 4 lb/ft³ were vibrated at elevated temperature in three mutually perpendicular planes for 48 hours according to a predetermined schedule, at frequencies of 5 to 2000 cps with .05" double amplitude. These conditions are normal for missile applications. Temperatures of about 1800 F to 2000 F for most of the test were recorded on the hot side facing the heat source. No attempt was made to cool the other side of the insulant where temperatures in the range of 800 F to 1000 F were recorded. Figure 6 illustrates the test equipment used in our

March 24, 1958

vibration studies. Figure 7 shows the position of the insulant test specimens in the fixture.

After the 48 hour test it was observed that alumina-silica fibrous insulant, our number HD-2-AS-3, had the least physical deterioration. Alumina-silica fibrous insulant, our number HD-1-AS, exhibited the least shrinkage but was badly pitted by its impurities. Additional test specimens of the materials tested for 48 hours vibration at elevated temperature were vibration tested at elevated temperature at an increased amplitude. An amplitude of 0.4 inch double amplitude was used. Such amplitude is greater than that expected for a useable structure. Due to the possible adverse effect of this amplitude on the test unit, the test was restricted to 1/2 hour in each plane, for a total of 1-1/2 hours. All the specimens remained dimensionally unchanged based on approximate measurement, except a high silica fibrous insulant. The 3 lb/ft³ alumina-silica insulant HD-2-AS-3 showed the least change in density. A 12 hour vibration test at elevated temperatures was conducted in several alumina-silica fibrous insulants having densities from 4 lb/ft³ to 12 lb/ft³. Vibration tests were conducted on the higher density materials primarily to correlate vibration resistance with density. With the exception of some powdering, the materials appeared to withstand the vibration satisfactorily.

2. Water Absorption

A water immersion test was conducted on all the insulant specimens evaluated. All the insulant test specimens absorbed water in the "as received" condition. The amount of water absorbed by the specimens having low "as received" water absorption values increased after vibration testing. None of the specimens retained water after oven drying. There was no evidence of hydrolysis or chemical reaction of water on any of the specimens.

Protective Coatings

Five ceramic coatings and three diffusion type coatings were evaluated for oxidation resistance protection, thermal shock, adherence, and flexibility. The coatings were applied to Inconel X foil (.005"). Coatings are being considered not only for the oxidation protection they may afford the metal, but also as a high emissivity source on the metal surface. Heat transfer from the hot metal to the atmosphere may thus be increased. Uncoated Inconel X foil (.005") has a room temperature tensile strength of about 29,000 psi after 24 hours exposure in air at 2000 F, and a room temperature tensile strength of about 109,000 psi after 24 hours at 2000 F in an argon atmosphere. Table II illustrates the effect on the room temperature tensile strength of 0.005" Inconel X after exposure to 2000 F. Inconel X was selected as the metal for our coating studies because it is representative of the high nickel class of high temperature alloys; it showed a large decrease in room temperature strength when exposed to oxidizing atmospheres and therefore, should reflect coating effectiveness; and it was available in foil thicknesses. The metal undergoes phase changes at elevated temperatures which are not appreciably influenced by coatings. It is, therefore, necessary to test the metal at the elevated temperatures to establish properties at those temperatures. Such tests are now scheduled in our laboratories.

Diffusion type coatings were the most promising evaluated. They provided excellent protection against intergranular oxidation. No oxidation of Inconel X was evident after exposure periods of 1 hour, 100 hours, and 150 hours at 2000 F. Photomicrographs of uncoated Inconel X and Inconel X coated with a diffusion type coating, our number JPC-8, exposed to 2000 F are shown in Figure 4. With exception of coating, our number JPC-5, the ceramic coatings evaluated did not meet the basic oxidation resistance protection requirement and the flexibility and adherence requirements established as screening tests. The JPC-5 appeared to provide good oxidation resistance protection.

Enlarged photographs of etched JPM-8 specimen cross sections indicate that the original composition and the interfacial constituents have been altered by exposure to 1650 F, 2000 F, and 2200 F. The nature of these changes and effect on mechanical properties will be investigated. Preliminary testing conducted in our laboratories showed that it is possible to spotweld Inconel X specimens through the JPM-8 coating. Effects of oxidation on the weld will have to be investigated.

There appears to be no theoretical limitations to the size or shape of structural elements that might be coated by the JPM-8 process. The process consists essentially of packing the component to be coated in a patented chromium compound, adding inert and energizer materials, and heating to 1650 F to 2000 F.

It is planned that emissivity measurements will be conducted on the coatings that may be selected. Additional studies now underway will establish the strength at elevated temperature of coated Inconel X specimens. It is entirely possible that the primary advantage of coatings on heavy metals may be the emissivity it imparts to the surface. Due to phase changes some refractory metals may have limited elevated temperature strength even without the adverse effect of an oxidizing atmosphere.

March 24, 1958

Graphite and

Refractory Materials for Hot Spot Areas

1. Of the carbide materials tested the best oxidation resistance at 2800 F was exhibited by the refractory body consisting of 90% silicon carbide and 10% boron carbide ($\text{SiC-B}_2\text{C}$).
2. At about 1700 F the standard dense silicon carbide body showed 15% volume deterioration after 10 minutes exposure in an oxy-acetylene furnace. Specimens subjected to 85 minutes exposure at these temperatures deteriorated quite badly resulting in loss of about 1/4 of the original volume of the specimen.
3. An attempt to obtain by the addition of aluminum a commercially producible silicon carbide possessing a modulus of rupture approaching that of a hot pressed laboratory body was not successful.
4. The graphite coated with SiC shows promise for applications at temperatures of at least 2800 F and possibly 3000 F for short periods. Oxidation tests would have to be conducted at 3000 F on the coated graphite. Coated graphite has substantial weight advantage over SiC. The density of graphite is about 1.8. The density of commercial varieties of silicon carbide vary from about 2.8 to 3.1.

Thermal Insulants

1. Based on the tests conducted it appears that an alumina-silica fibrous insulant, our code RU-2-1S-3, having a nominal density of 3 lb/ft³ shows the most promise as an insulant for our application. Selection of an insulant will be based on tests conducted in this and previous studies and on the thermal conductivity of the insulants before and after environmental exposures.
2. The labor absorption tests designed in the laboratory were used to compare the insulants for screening purposes only. It appears that the use of protective seals to prevent labor absorption by different insulants may be necessary.

March 24, 1958

Protective Coatings

1. On the basis of the preliminary screening tests, diffusion coating JPM-8 appears to be the most promising coating for Inconel X. This coating affords excellent oxidation protection; possesses good thermal shock resistance; and shows good flexibility and adherence. The JPM-8 coated specimens exposed to 2200 F for various time periods experienced a degree of warpage not encountered in the specimens exposed to 2000 F.

Most of the work presented in this report was sponsored by the U.S. Air Force. Their assistance is gratefully acknowledged.

TEMPERATURE °F	ULTIMATE TENSILE STRENGTH (psi $\times 10^{-3}$) / DENSITY (lb./in. ³)	
	ALUMINUM OXIDE (Al ₂ O ₃)	MOLYBDENUM (0.5% Ti-Mo)
70	264,000	-
570	250,000	-
1470	236,000	250,000
1920	229,000	200,000
2070	215,000	170,000

TABLE I MECHANICAL PROPERTIES OF ALUMINUM OXIDE AND
MOLYBDENUM



Table I

EXPOSURE TEMP. °F	24 HOURS EXPOSURE IN AIR ATMOSPHERE		24 HOURS EXPOSURE IN ARGON ATMOSPHERE	
	TENSILE STRENGTH	YIELD STRENGTH	TENSILE STRENGTH	YIELD STRENGTH
Room	158,000	120,000	-	-
1500	-	-	-	-
1600	-	-	-	-
1700	-	-	-	-
1800	73,370	59,300	117,900	59,000
2000	29,360	-	109,600	54,600
2100	16,700	-	-	-

TABLE II ROOM TEMPERATURE STRENGTH PROPERTIES (PSI)
OF UNCOATED .005" INCONEL X



Table II

TABLE VI MODULUS OF RUPTURE TEST DATA ON ZIRCONIUM OXIDE BODIES

BODY	TIME	TEMPERATURE °F	AVERAGE MODULUS OF RUPTURE (psi)
W1129	-	80	3730
W1127	-	80	3710
W1128	-	80	1930
W1129	3 min.	1500	Below 100 psi
W1127	-	1500	3200
W1128	-	1500	2150



Table VI

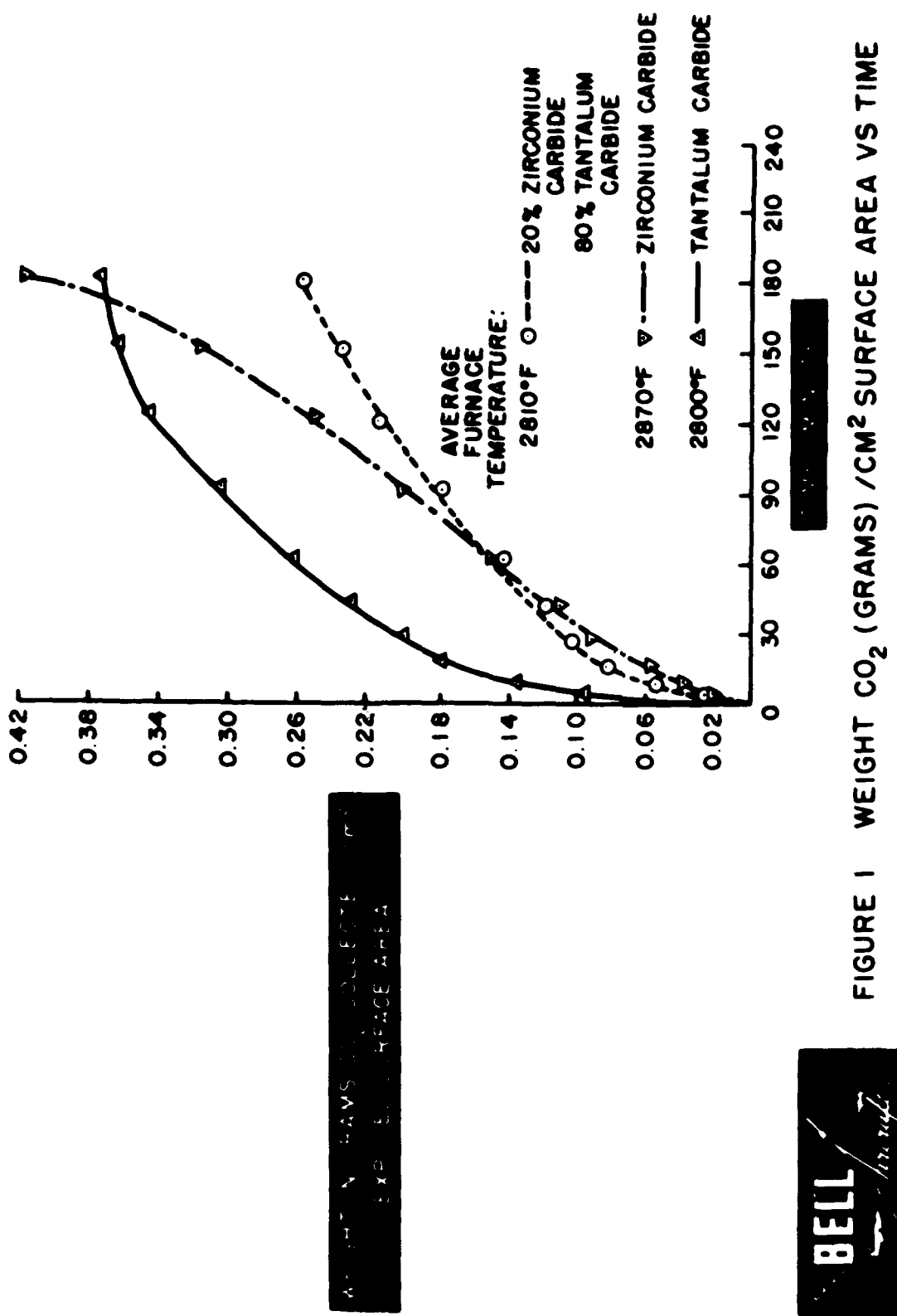


Figure #1

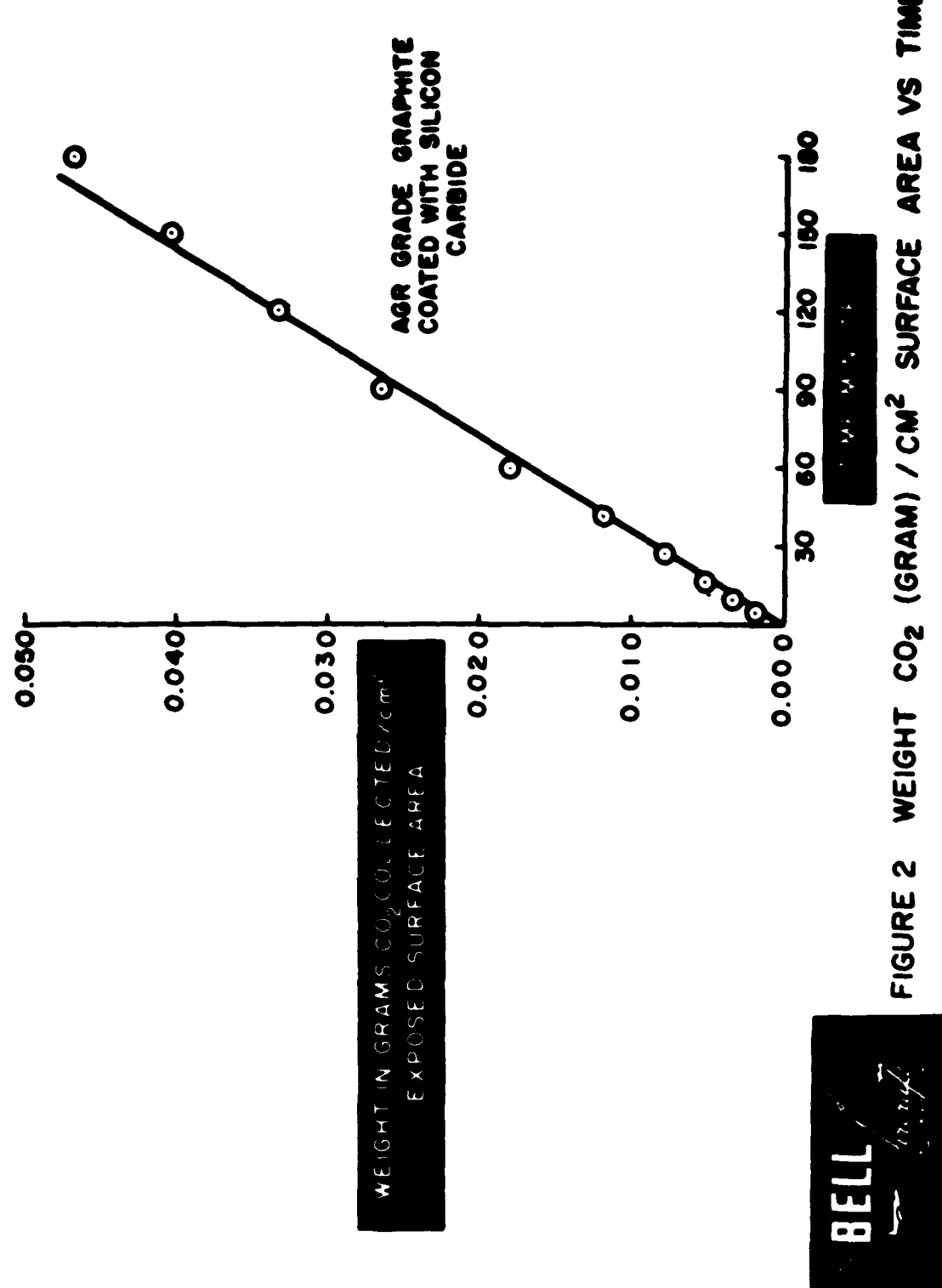


Figure #2

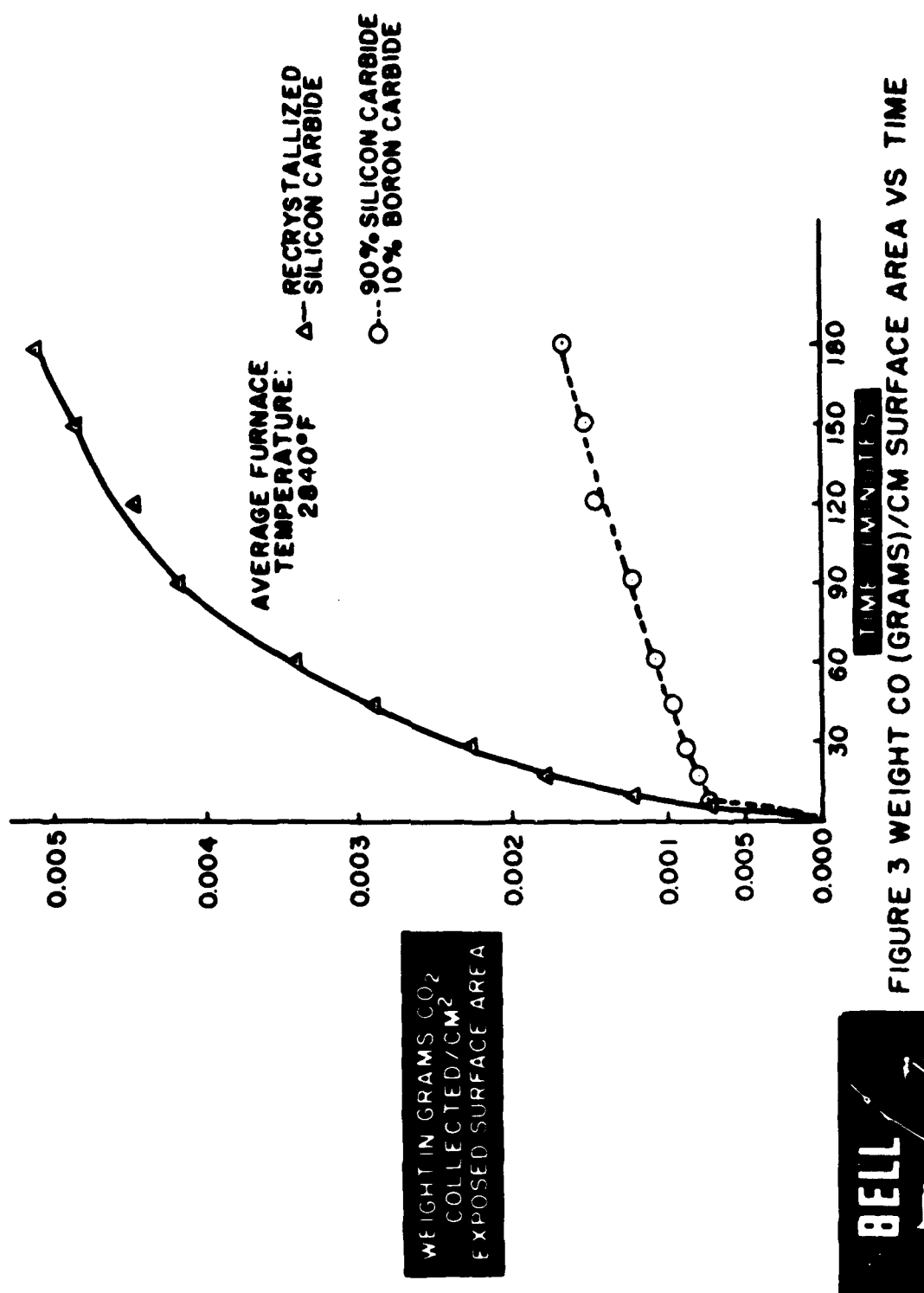


Figure #3

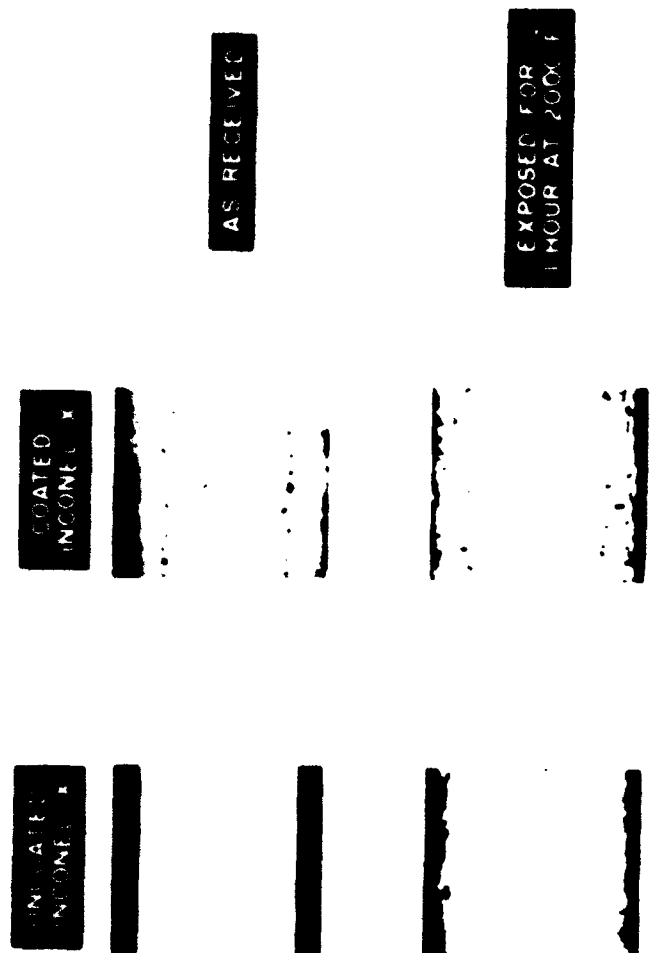


FIGURE 4A PHOTOMICROGRAPHS (250X) OF UNCOATED AND JPM-8 COATED INCONEL X AFTER EXPOSURE IN AIR AT HIGH TEMPERATURES



Figure #4-A

FIGURE 4B PHOTOMICROGRAPHS (250X) OF UNCOATED AND JPM-8
COATED INCONEL X AFTER EXPOSURE IN AIR AT HIGH TEMPERATURES



Figure #4-B

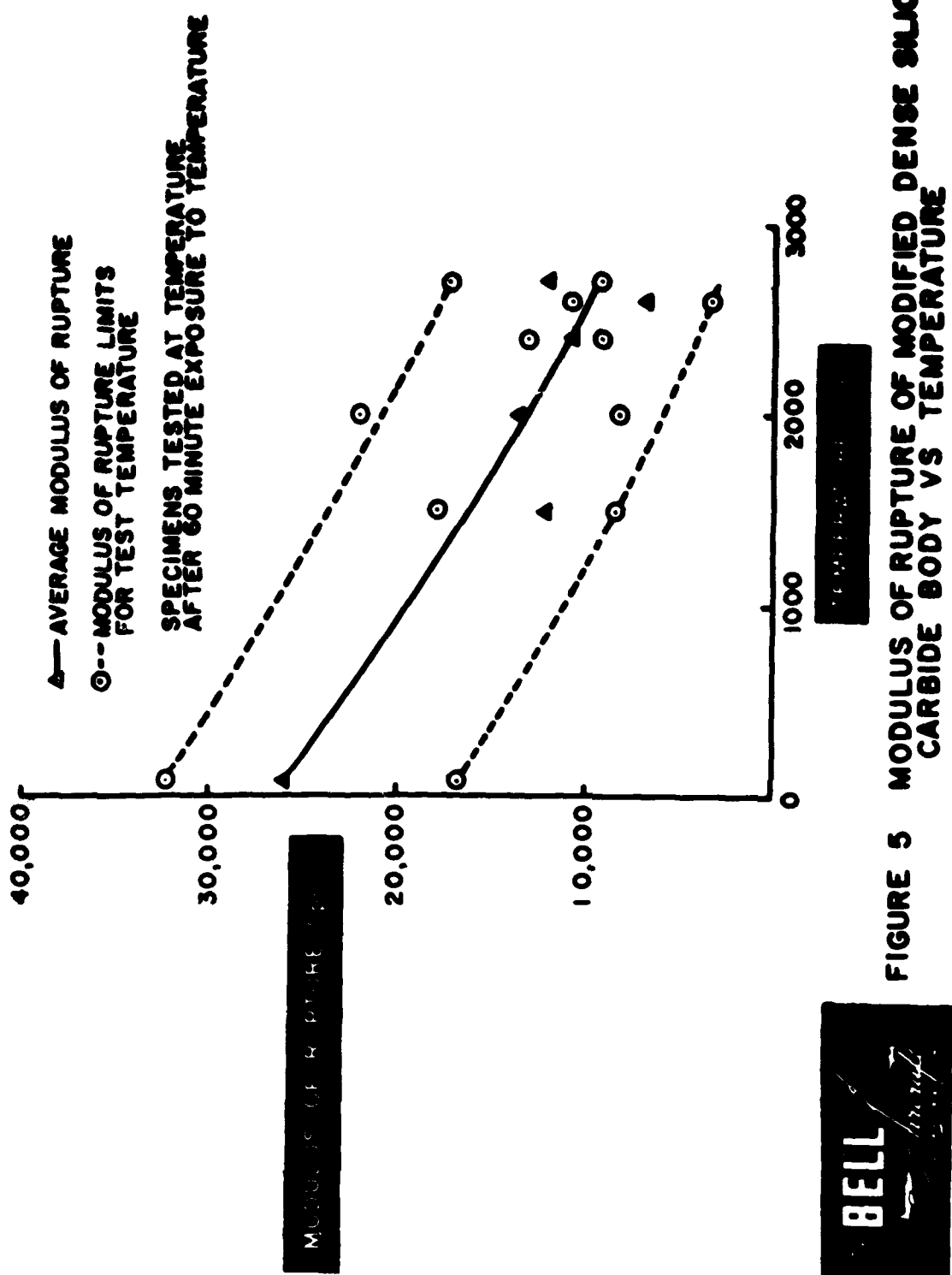


FIGURE 5 MODULUS OF RUPTURE OF MODIFIED DENSE SILICON CARBIDE BODY VS TEMPERATURE

Figure #5

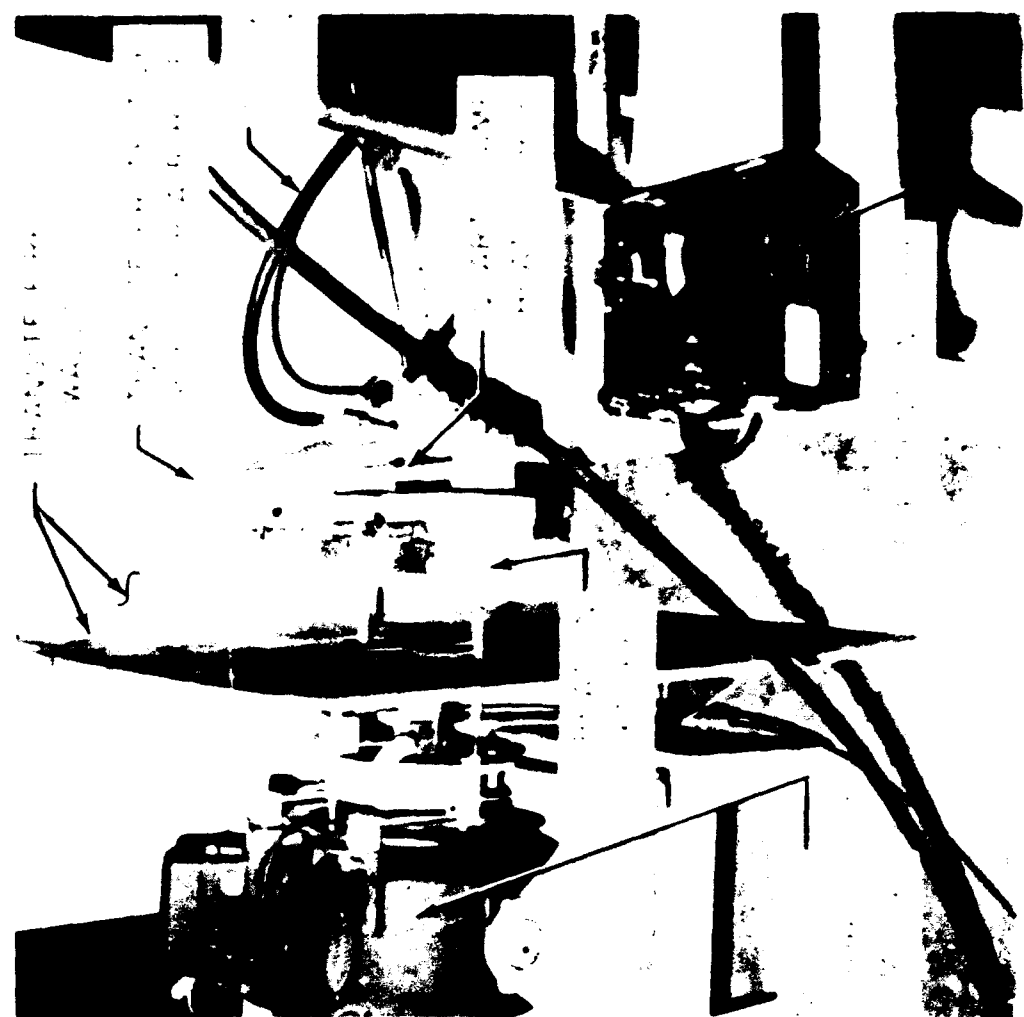


Figure #6

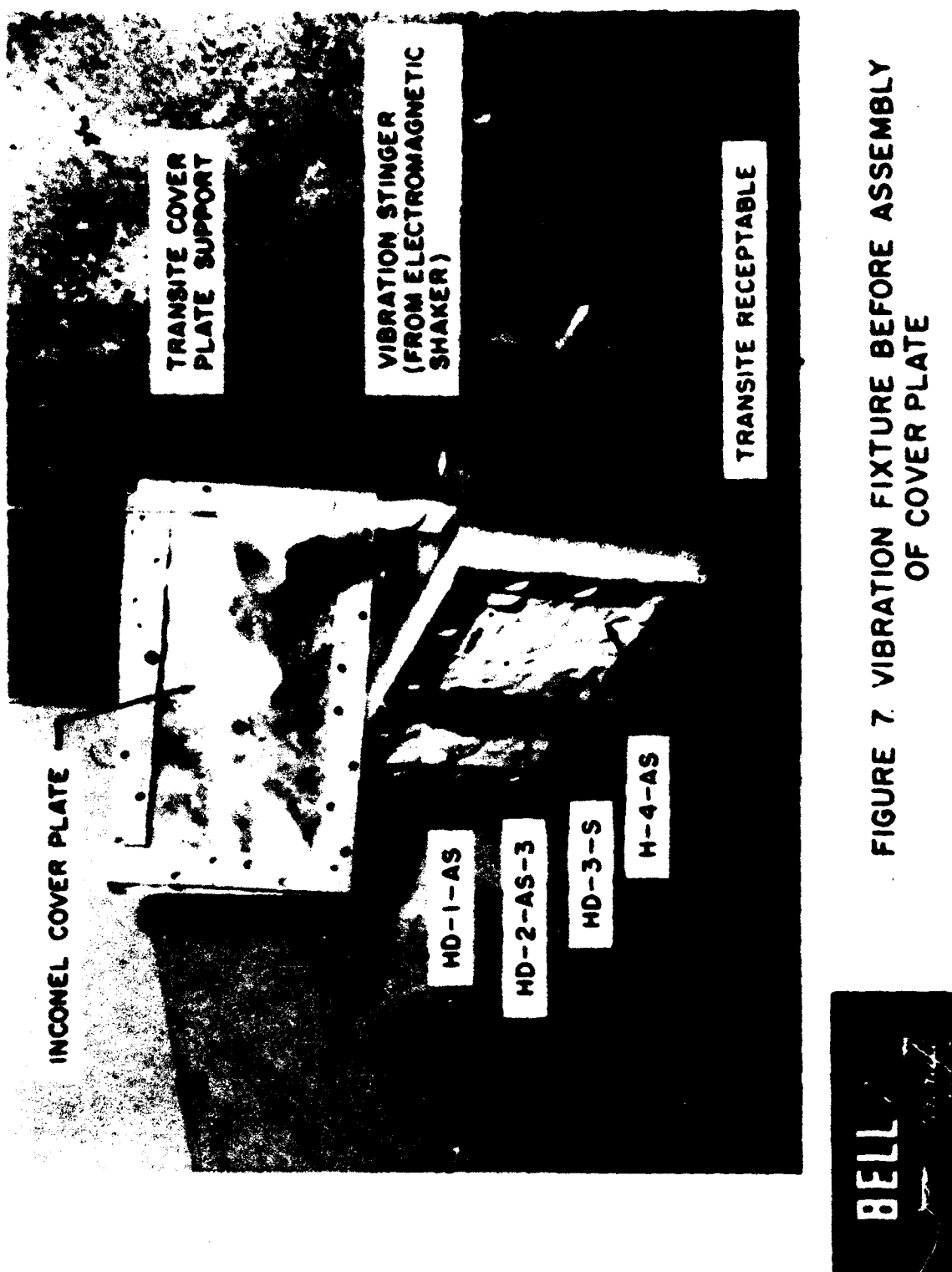


FIGURE 7 VIBRATION FIXTURE BEFORE ASSEMBLY
OF COVER PLATE

Figure #7

THERMAL PROPERTIES OF NOSE
CONE MATERIALS

I.V. Fieldhouse
J.I. Lang
A.N. Takata
T.E. Waterman
Armour Research Foundation

THERMAL PROPERTIES OF NOSE CONE MATERIALS

I. B. Fieldhouse, J. I. Lang, A. N. Takata and T. E. Waterman

I. INTRODUCTION

The thermal properties of materials at high temperatures are of considerable practical and theoretical interest to the engineer and scientist. The practical value is well demonstrated by the demand for thermal property data above 1500°F which is lacking in the literature and required for computations to determine the optimum material and design of the nose cone of ballistic missiles.

In early 1955, a program to measure the thermal conductivity, specific heat and linear thermal expansion of five materials was initiated at Armour Research Foundation under contract No. AF 33(616)-2093. The materials covered in this contract were copper, molybdenum, nickel, type GBE graphite and type 3474D graphite. This information was presented at the First Technical Symposium on Ballistic Missiles held in Los Angeles in June 1956. Since then, more information has been obtained and will be presented here along with a brief description of the experimental methods.

II. THERMAL CONDUCTIVITY OF SOLIDS

A. Experimental Method and Apparatus

The method used for determining thermal conductivity is one of unidirectional heat flow through a disk of the sample material. The apparatus used is shown in Fig. 1. The heating system consists of a main heater, guard heater, and superheater. The heating elements for the main and guard heaters consist of molybdenum wire 0.09 inch in diameter wound in a coil 3/8 inch in diameter. The coils are supported alundum refractory shapes and the unit insulated with bubbled alumina.

The purpose of the superheater is to prevent condensation of the evaporating liquid from occurring before the vapor reaches the condenser. The temperature of the superheater is regulated so that it is always about 10°F above the boiling point of the liquid.

As shown in Fig. 1, the calorimeter assembly consists of a test section, guard section, two condensers, superheater, and a two-way valve. It is held about 1/8 of an inch above the sample. As heat is transferred from the sample to the calorimeter, the liquid in the calorimeter will begin to boil. The vapor formed in the 3 inch diameter test section will rise in the tube separating the test section from the guard section, pass through the heated inclined tube and then flow into the condenser where it can either be collected and weighed, or allowed to drain back into the calorimeter. The vapor from the guard section is condensed in a separate condenser and then drained back into the calorimeter.

With the exception of tantalum, the test sample is a disk 6-3/4 inches in diameter and 1-1/2 inches thick. As present methods of fabrication are not capable of producing high density sintered tantalum in sheets thicker than about 1/4 inch, the sample (6-3/4 inch in diameter and 1-1/2 inch thick) was made by stacking varying lengths of 1/4 inch by 1-1/2 inch strips to form the sample disk as shown in Fig. 2. This provided a sample which was continuous from surface to surface in the direction of heat flow, which eliminates problems concerning contact resistance. The sample with platinum - platinum 10% rhodium thermocouples in place is lowered into the furnace and supported 1/4 inch above the main heater by alumina posts. The thermocouples are lead out through small tubes in the sides of the furnace and are connected to the measuring instrument (type K-3 Leeds & Northrup potentiometer with ice bath reference junction). The guard thermocouples are placed within the refractory supporting guard heater and on the same horizontal plane as the cold surface of the sample.

B. Test Results

Preliminary tests at temperatures of 1000 to 1600°F were made using an Armco iron sample in order to verify the accuracy of the test equipment. The results were compared with values reported by Armstrong and Dauphinee¹, Powell² and Jakob³. The maximum disagreement was found to be 3 per cent at 1600°F between ARF and Powell.

The experimental results obtained on the materials tested are shown graphically in Figs. 3 and 4. In the cases of Hastelloy B and C, and the graphites, the results given are those obtained during the first run of each sample in the furnace. Subsequent runs give higher numbers. To obtain an approximation of this increase in conductivity, one sample of Hastelloy B was left in the furnace at 1400°F for 24 hours after the completion of a run. The results obtained after this period ranged from 30 to 35 per cent higher than the original.

A metallographic examination of this sample of Hastelloy B was made before and after testing. Small pieces were cut from the edge of the disc, mounted in Bakelite, polished and etched with ferric chloride. The piece in the "as received" condition had a grain structure of equiax twinned grains characteristic of this alloy after being worked and annealed. The heat treatment occurring during the test produced a microstructure which consisted of three phases, an alpha nickel solid solution matrix, a beta nickel-molybdenum ($Ni_4 Mo$) phase precipitated as small particles in the grain boundaries and within the grains, and a gamma phase present as larger particles appearing within the grains.

1. Armstrong, L. D. and Dauphinee, T. M. "Canadian Journal of Research." Section F, Vol. 25, pp 221-225, 1947.
2. Powell, R. W. "Proceedings of the Physical Society." London, Vol. 46, pp 659-674, 1934.
3. Jakob, Max. "Heat Transfer." Vol. 1, John Wiley and Sons, Inc., pp 146-166, 1949.

In measuring the graphite samples, a definite odor of coal gas was noticed in the purge helium leaving the furnace. Also, carbon deposits were found on the calorimeter. These phenomena suggest that either the structure of the graphite was changing, or that impurities were being driven from the sample. That some change in the nature of the graphite samples had occurred was verified in the earlier ~~work~~ testing a sample of 3474D graphite. A definite increase in thermal conductivity was noted, with the greatest difference occurring at 1000°F (the lowest temperature at which measurements were made).

C. Estimated Accuracy

An article by Somers and Cyphers⁴ indicates that the maximum error due to sample thickness and ratio of test section area to guard area on distorting perpendicular heat flow lines is 2 per cent. The article consists of steady state heat transfer calculations by means of the solution of particular differential equations for heat flow in homogeneous materials of cylindrical cross section and various thicknesses. One face of the sample is assumed to be at a given temperature and the other face at a temperature greater than the first. The side of the sample is assumed to be at the same temperature as one face, which is a more drastic condition than that which takes place in the actual case. The authors report the ratio of true thermal conductivity to that measured experimentally for various test sections, guard sections, and sample thickness dimensions.

Since careful consideration was given to the instrumentation, errors due to measurements alone should be less than one per cent. However, errors produced by slight misalignment of the heaters, variations in the resistance of the heater wires, small inaccuracies in machining and thermocouple locations, and other random errors account for the spread in data.

With these points in mind, it is believed that the curves drawn through the experimental data are accurate within 5 per cent.

4. Somers, E. V. and Cyphers, J. A. "Analysis of Errors in Measuring Thermal Conductivity of Insulating Material." *Review of Scientific Instruments*, Vol. 22, No. 8, pp 583-586, August, 1951.

III. THERMAL CONDUCTIVITY OF LIQUID COPPER

A comparative method was used to determine the thermal conductivity of the liquid sample. Heat was passed downward from an electric heater, through the sample, through a disk of molybdenum whose thermal conductivity as a function of temperature is known, to a heat sink. This was necessitated due to the convection currents which are set up if the sample is heated from below.

A. Experimental Method and Apparatus

The apparatus used is shown in Figs. 5 and 6. As downward heat flow was required, the calorimeter used for solid samples was not suitable. Therefore, a solid (molybdenum) whose thermal conductivity was known was placed below the liquid, and the heat flow determined by the temperature drop through the known material.

The copper used for these measurements was electrolytic tough pitch copper having a density of 551.4 lb/ft³. The results of the thermal conductivity measurements are shown in Fig. 7 along with those for the solid.

Based on known theoretical considerations, the thermal conductivity of liquid copper should have been equal to 0.5 of that of solid copper, or approximately $92 \text{ B hr}^{-1} \text{ ft}^{-1} \text{ F}^{-1}$. The experimental results obtained during this investigation yield results which indicate that this ratio should be 0.36 instead of 0.5. However, from a further examination of the liquid metal literature, it appears that a very definite need exists on both experimental and theoretical grounds for further work in this field before the relationship between the solid and liquid thermal conductivities is known.

It is believed that the experimental data are accurate to within ± 5 per cent.

IV. SPECIFIC HEAT

A. Introduction

The values of specific heat were derived from enthalpy data obtained by dropping heated samples into a modified Parr Adiabatic Calorimeter.

B. Apparatus

A diagram of the apparatus used is shown in Fig. 8. The furnace is a vertical tube type purchased from the Harper Electric Company. The interior of the furnace contains an alundum tube, 1-1/2 inches inside diameter, 44 inches in length. The tube length and diameter was specified to assure a uniform temperature region surrounding the sample.

The furnace was heated electrically by a globar tube, exterior to and concentric with the alundum tube. Power input to the globar element was controlled by a 3-step 6-position transformer. An inert atmosphere in the furnace interior was assured by constant purging with helium. Sealing at the top of the tube was attained by a pipe flange; bottom sealing was provided by a gate valve.

The temperature of the furnace at the point where the sample was suspended was measured by two platinum platinum 10 per cent rhodium thermocouples contained in protection tubes and suspended from the furnace top. An axial temperature survey at the in-furnace sample position indicated a temperature gradient of less than $1^{\circ}\text{F}/\text{inch}$, at a mean furnace temperature of 2500°F .

As indicated in Fig. 8, the furnace tube is connected to the calorimeter by means of a 1-1/2 inch stainless steel pipe. Immediately above the calorimeter the 1-1/2 inch pipe was reduced by a convergent section to a one inch pipe. The one inch pipe was inserted into the receiver for a length of one inch. The receiver, though modified several times, is based on a design described by D. C. Ginnings⁵.

5. Ginnings, D. C. and Corruccini, R. J. *Journal of Research NBS* 38, 1947, Research Paper 1797.

Heat content of the sample was measured by a Parr Adiabatic calorimeter. The calorimeter cover was modified to provide entrance to the receiver, inert gas tubes and gate shaft.

The temperatures in the calorimeter and in the calorimeter jacket were measured with calibrated thermometers.

C. Calculation of Specific Heat

Specific heat at constant pressure is defined by the equation:

$$C_p = \left[\frac{\partial(\Delta H)}{\partial T} \right]_p \quad (1)$$

ΔH = enthalpy change relative to a specified datum

T = temperature

P subscript indicates the partial derivative at constant pressure.

The experimental method described here yields measurements of enthalpy change and corresponding temperature level. The relation between specific heat and the measured quantities is given by integration of equation (1) with respect to temperature.

$$\int C_p dT = \int \left[\frac{\partial(\Delta H)}{\partial T} \right]_p dT \quad (2)$$

Enthalpy change may be expressed in terms of a temperature function:

$$\Delta H = \phi(T) \quad (3)$$

Simple differentiation of $\phi(T)$ then gives C_p . The expression $\phi(T)$ used here was a quadratic of the form:

$$\Delta H = a + bT + cT^2 \quad (4)$$

So:

$$C_p = b + 2cT \quad (5)$$

The enthalpy equation $\phi(T)$ was obtained from the experimental data by a least squares method. The specific heat function was determined as indicated above. Figures 9 and 10 present specific heat values in the temperature range investigated.

D. Accuracy of Measurements

The accuracy of the results is limited only by the accuracy of in-furnace sample temperature measurements. The magnitude of error from the calorimeter is probably no more than one per cent. This conclusion is difficult to check experimentally because it was not possible to maintain furnace temperatures constant to less than 5°F. Furnace temperature variation was caused by fluctuation in voltage input to the furnace transformers.

Measurement of in-furnace sample temperature was accomplished by two platinum platinum 10 per cent rhodium thermocouples inserted in protection tubes. The protection tubes were necessary to prevent contamination of the thermocouples, and also to allow diffusion of oxygen down the interior of the protection tube. The validity of this measurement method was checked in the following manner. A graphite sample was axially bored to accommodate an insulated platinum platinum 10 per cent rhodium thermocouple. The sample was placed in the normal in-furnace position, and the temperatures sensed by the thermocouples enclosed in protection tubes were compared with the thermocouple enclosed in the sample. The results of this test indicated that the temperature sensed by the sample thermocouples agreed with the arithmetic average of the temperatures sensed by protected thermocouples to 4°F. The error introduced from this source is probably about one per cent.

The combined accuracy of the enthalpy measurements is, then, about two per cent.

V. SPECIFIC HEAT OF LIQUID COPPER

The apparatus for determining the specific heat of liquid copper was the same as that used for the solids. The only additional requirement was that the sample be held in a containing cylinder. The containing cylinder used was a molybdenum capsule 4-3/4 inches in length by 5/8 inch OD with a 1/16 inch wall. The bottom of the container was welded to the sides and a plug was fitted to the top to provide a seal against loss of liquid. The contribution of the molybdenum capsule to the total heat content was evaluated

from the data measured earlier. The specific heat values obtained are shown in Fig. 11 along with those obtained for the solid.

VI. LINEAR THERMAL EXPANSION

The linear thermal expansion was determined by measuring the distance between two recrystallized alumina pins mounted in a rod of material to be evaluated.

A. Apparatus

A schematic diagram of the apparatus is shown in Fig. 12. The furnace is heated by three banks of globar elements at the front, middle and rear of the furnace. Each bank of globar elements may be heated independently so as to insure a uniform temperature along the middle of the furnace. Preliminary tests indicated that the variation of temperature of the specimens along their length was within 5°F. The furnace temperature was measured by platinum platinum 10 per cent rhodium thermocouples located one inch from either end of the sample and the sample temperature was measured by a thermocouple located in one end of the specimen.

The specimen is mounted in a ceramic tube in the center of the furnace, with the ceramic pins pointing upward. In this position the line-up is such that the pins may be seen from outside the furnace and the distance between them measured directly with the telemicroscopes. During the lower temperature portions of each run, the pins are silhouetted against a lighted white background behind the furnace. Once the interior of the furnace begins to get cherry red, the lights are turned off and the red pins are easily seen against the now dark background. A slow stream of helium is maintained into the ceramic tube supporting the sample to protect the sample from oxidation.

The telemicroscopes are mounted on an invar bar which has a very low coefficient of thermal expansion and the displacements of the pins read by means of a micrometer to an accuracy of 0.0001 inch. The complete assembly is shock mounted to minimize vibrations.

B. Results

The thermal expansion of each material was measured from 80°F to slightly below its melting point or to 3000°F, as shown in Fig. 13. ΔL is the fractional increase in sample length and L is the sample length at 80°F.

C. Discussion of Experimental Errors

The measurement of thermal expansion is an absolute measurement and hence all errors are inherent in the apparatus and observer (such as incorrect temperature measurements or variations in the optical system). These sources of error are considered to be relatively small and of a random nature.

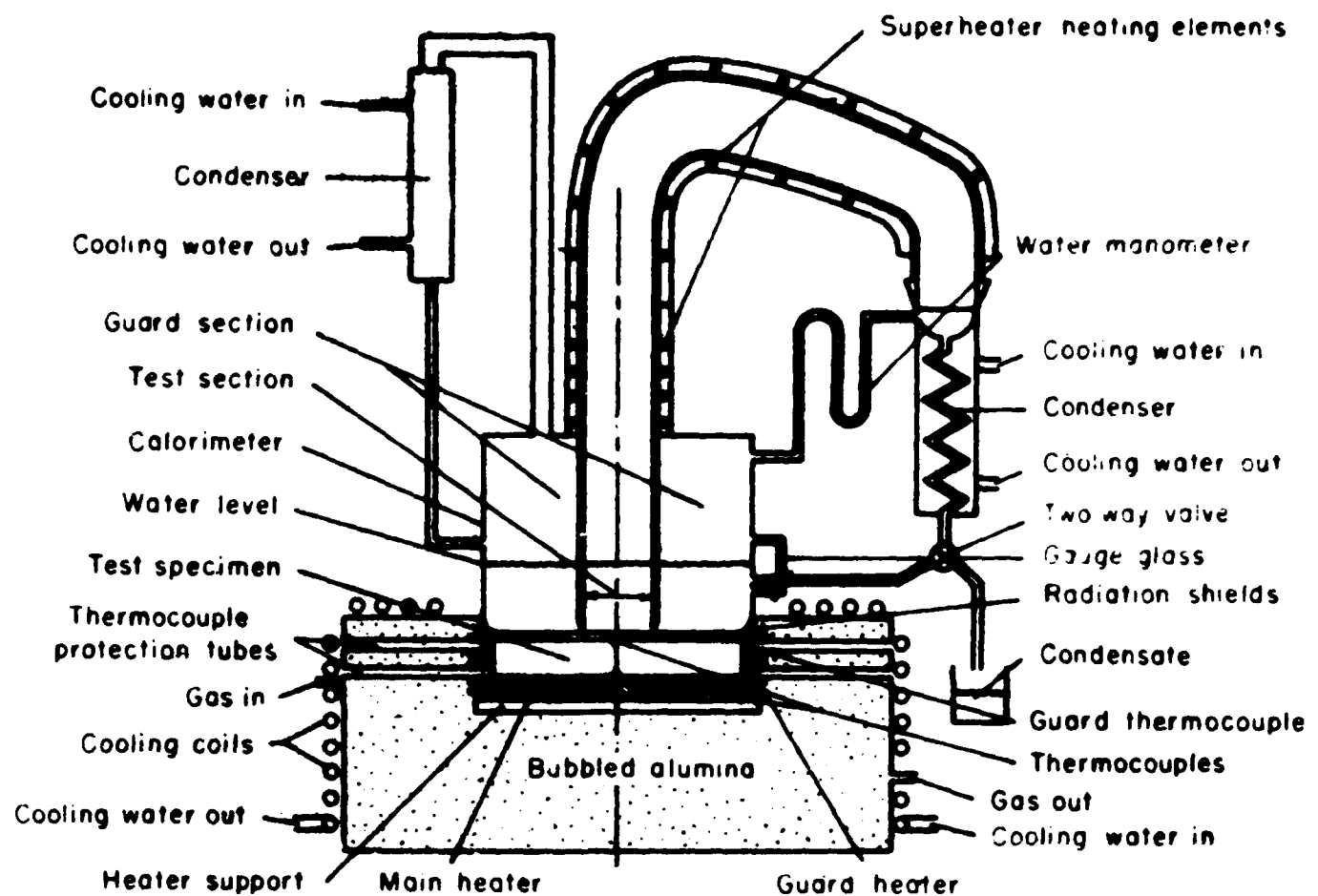


FIG. 1 SCHEMATIC DIAGRAM OF APPARATUS FOR
MEASURING THERMAL CONDUCTIVITY

Figure #1

Fig. 2 TANTALUM TEST SAMPLE

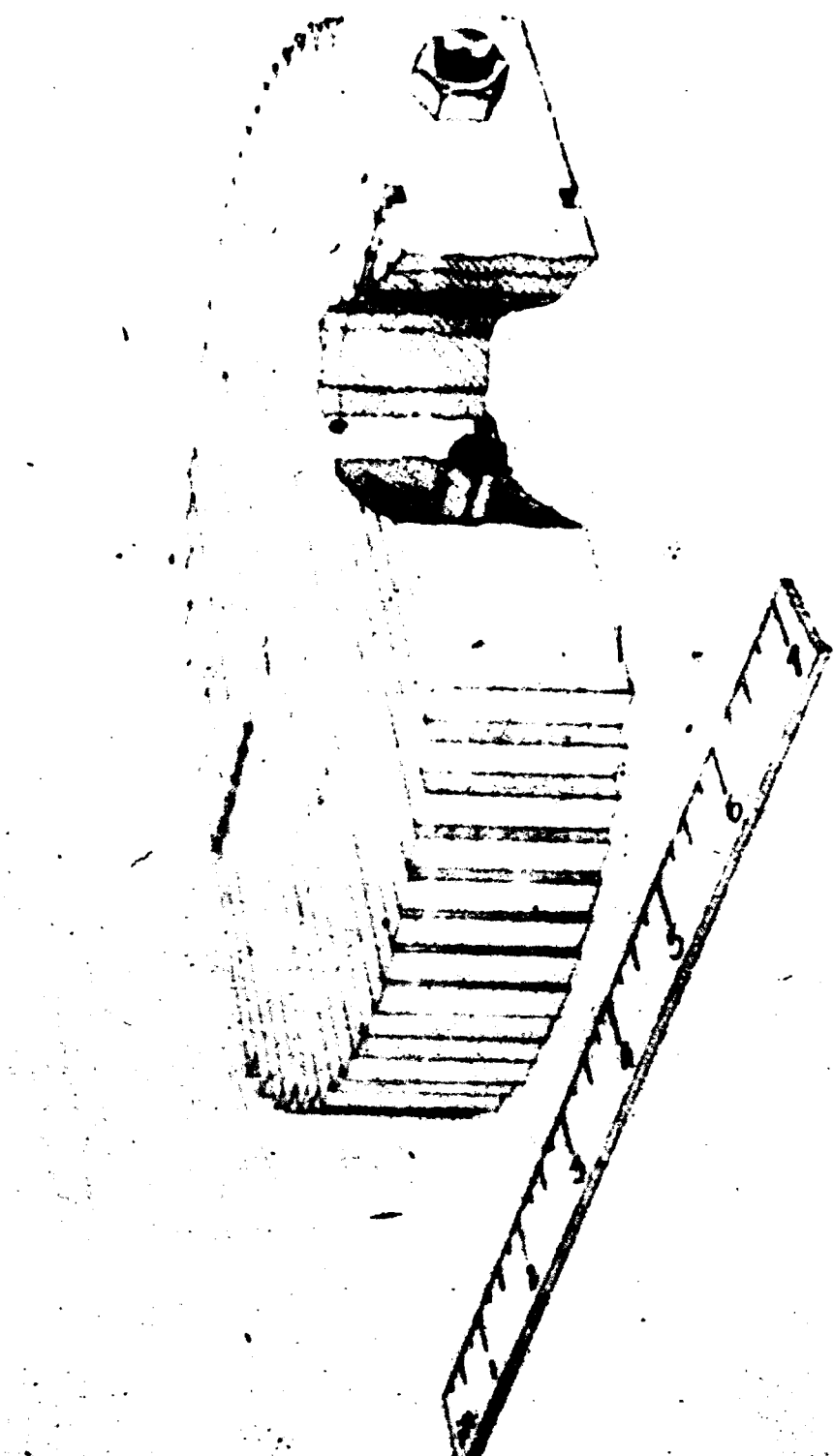


Figure #2

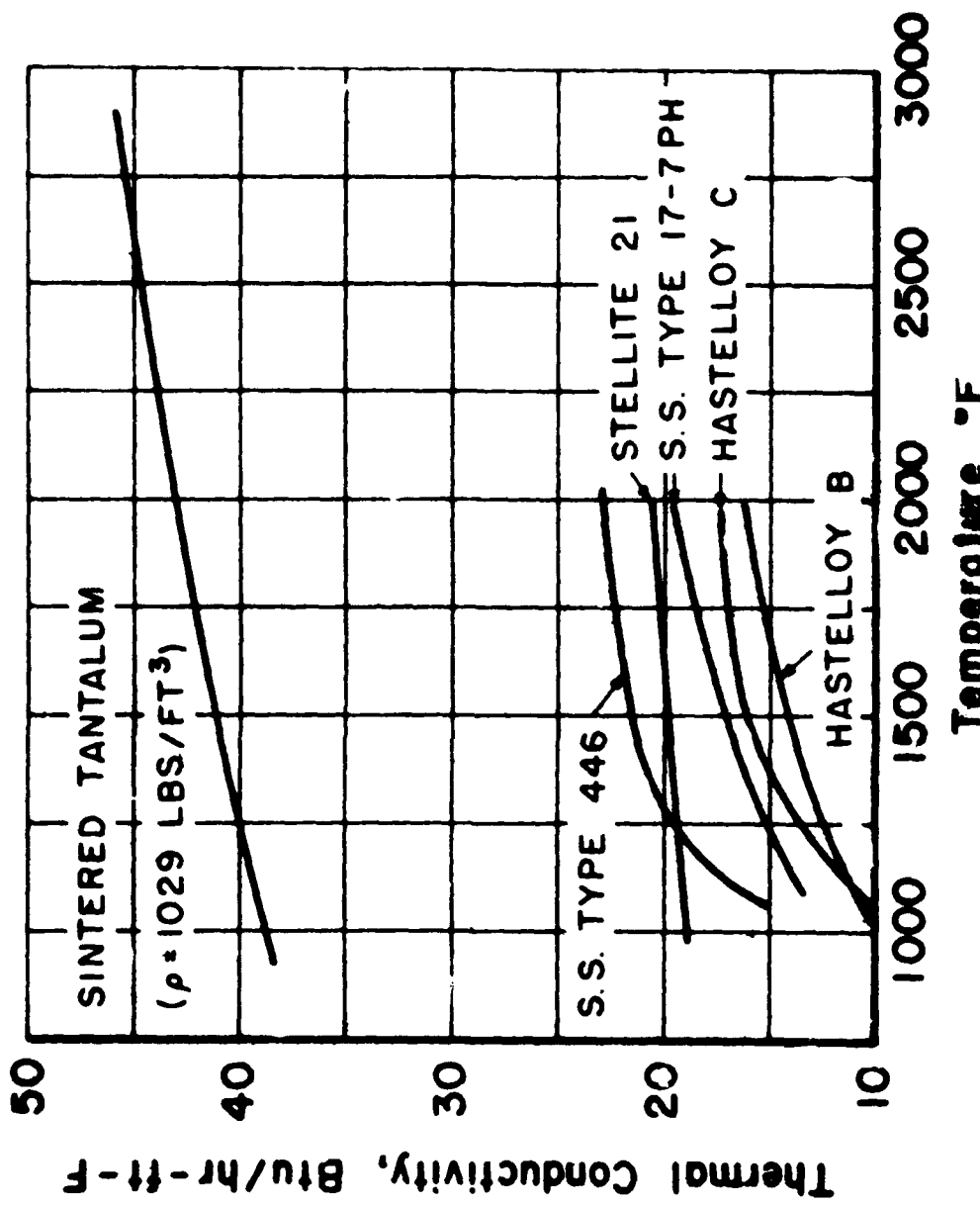


Fig. 3 THERMAL CONDUCTIVITY OF METALS

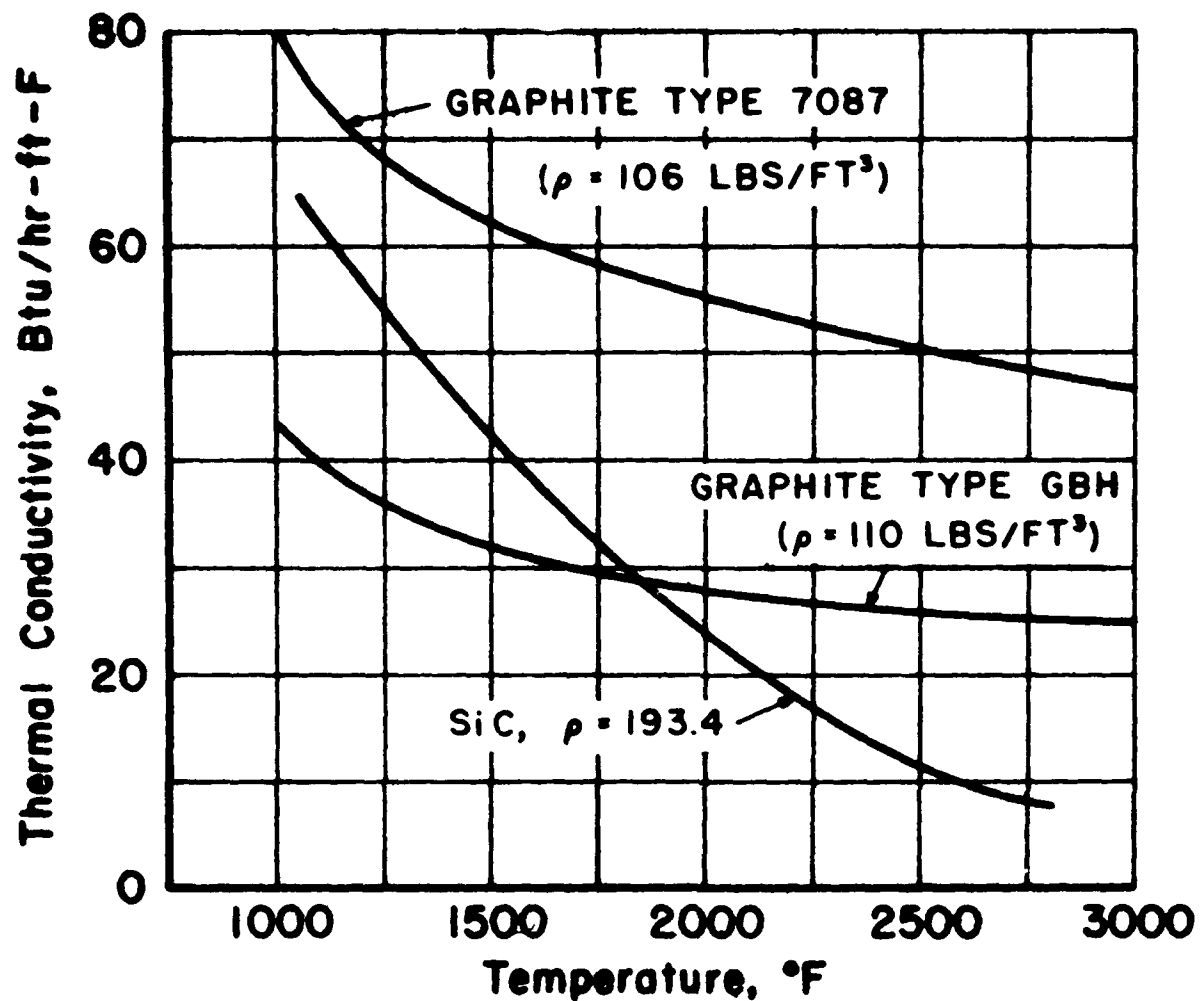


Fig. 4 THERMAL CONDUCTIVITY OF NON-METALS

Figure #4

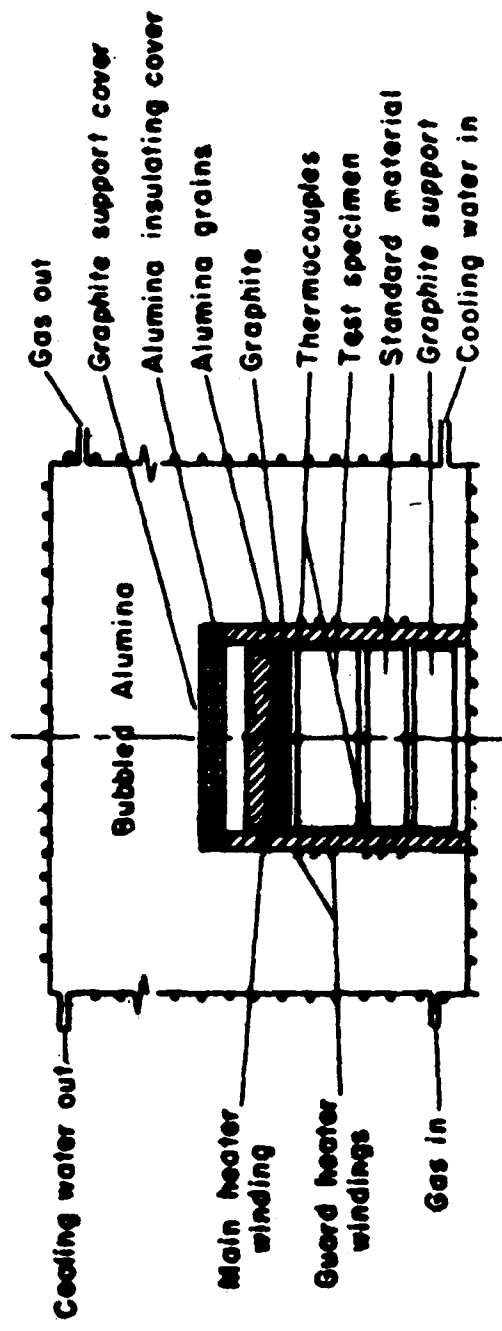


Fig.5 SCHEMATIC DIAGRAM OF THERMAL CONDUCTIVITY FOR LIQUID COPPER

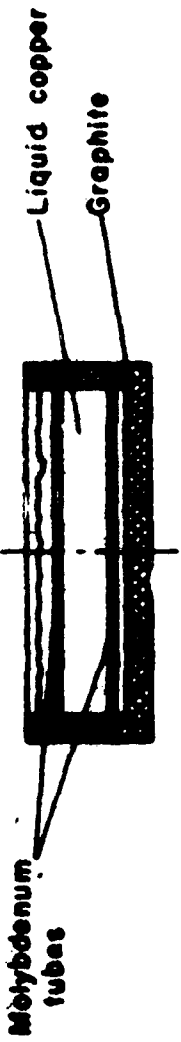


Fig.6 SCHEMATIC DIAGRAM OF LIQUID COPPER TEST SPECIMEN

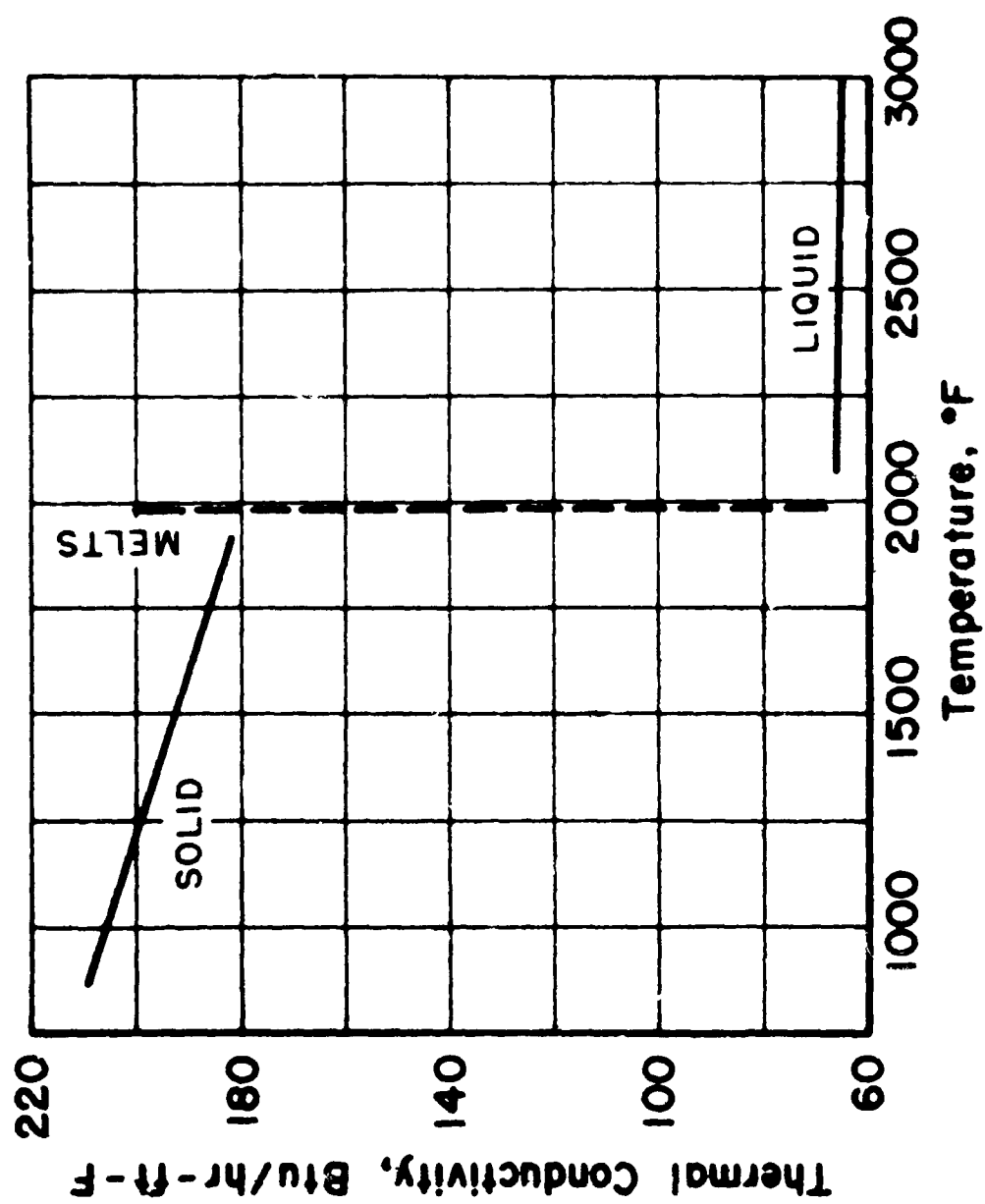


Fig. 7 THERMAL CONDUCTIVITY OF COPPER

Figure #7

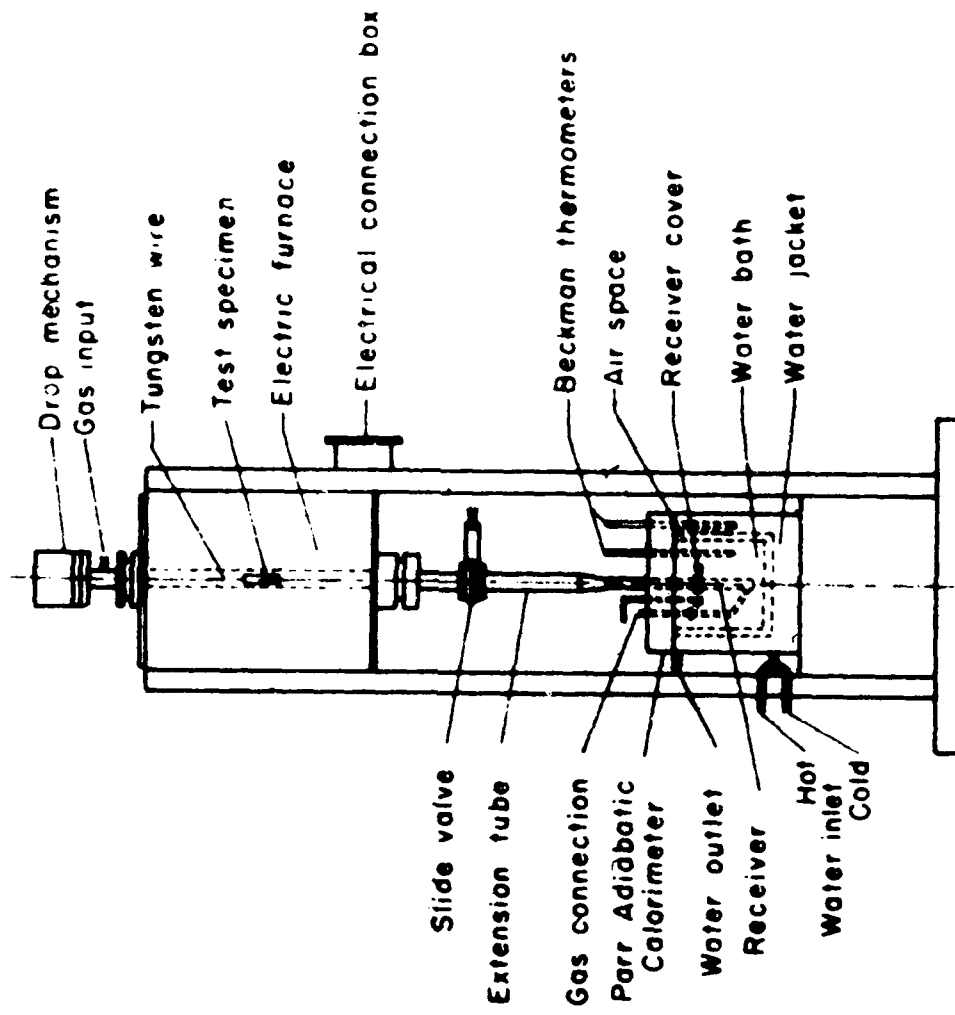


Fig 8 SCHEMATIC OF SPECIFIC HEAT APPARATUS

Figure #8

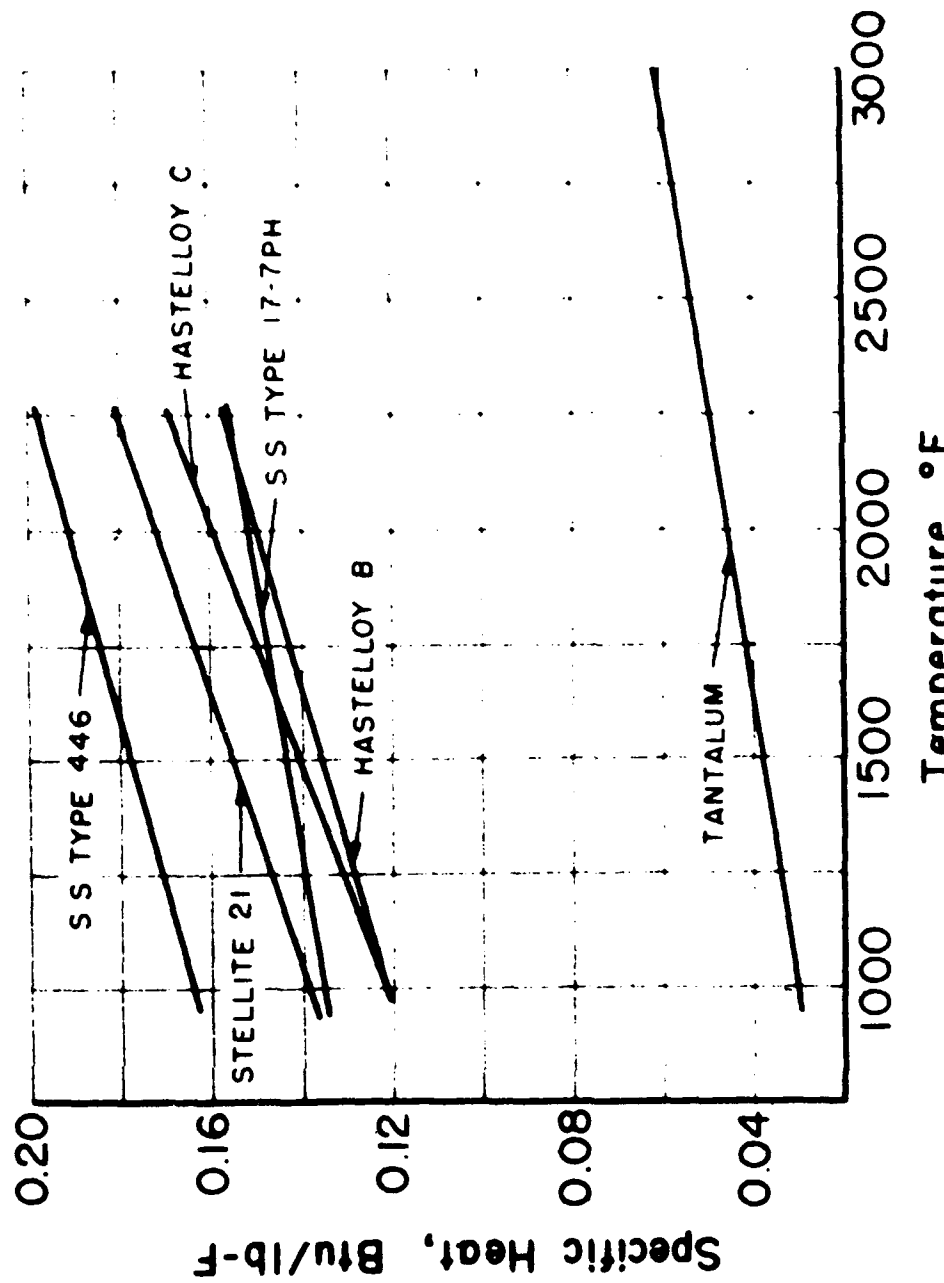


Fig. 9 SPECIFIC HEAT OF METALS

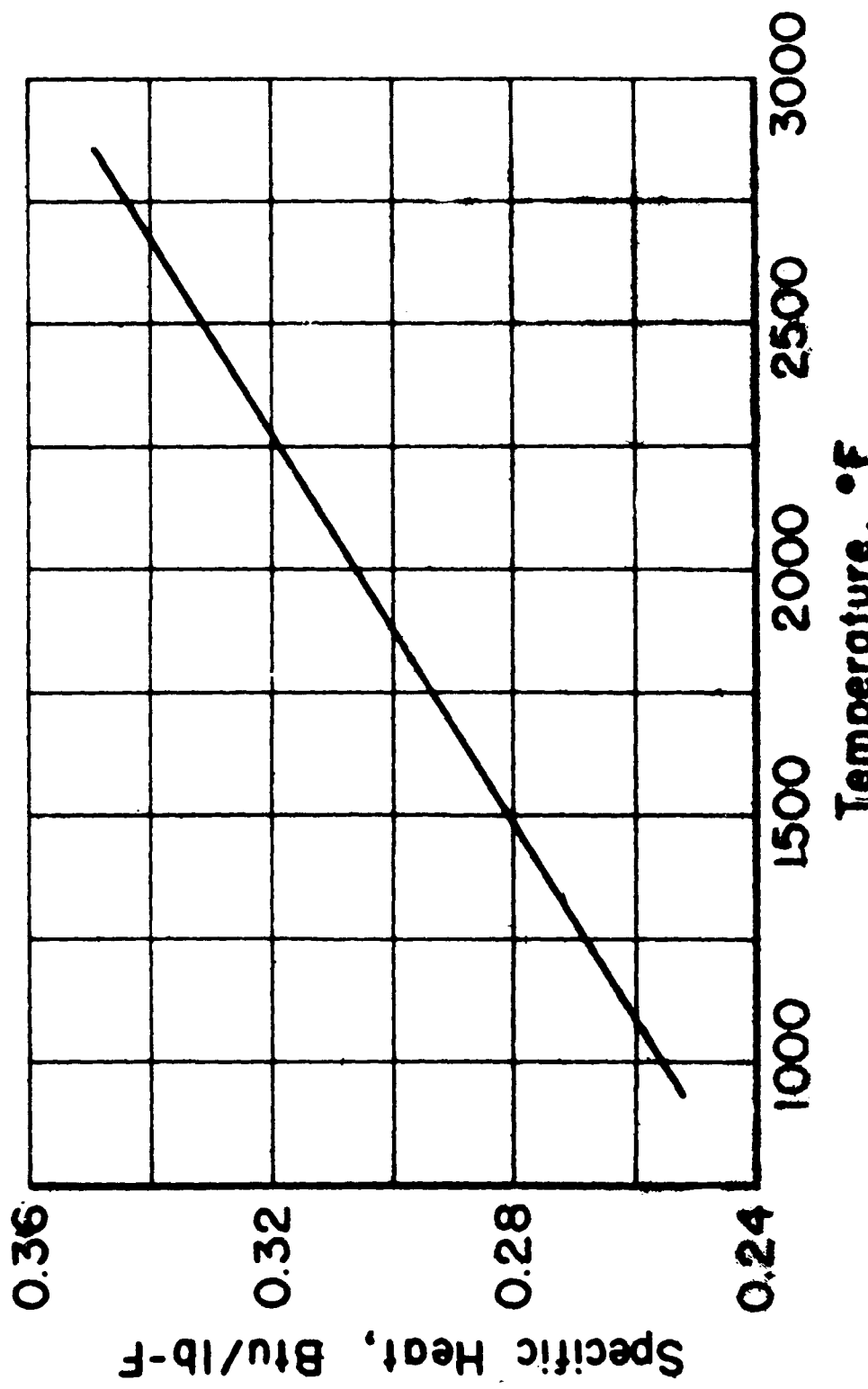


Fig. 10 SPECIFIC HEAT OF SILICON CARBIDE

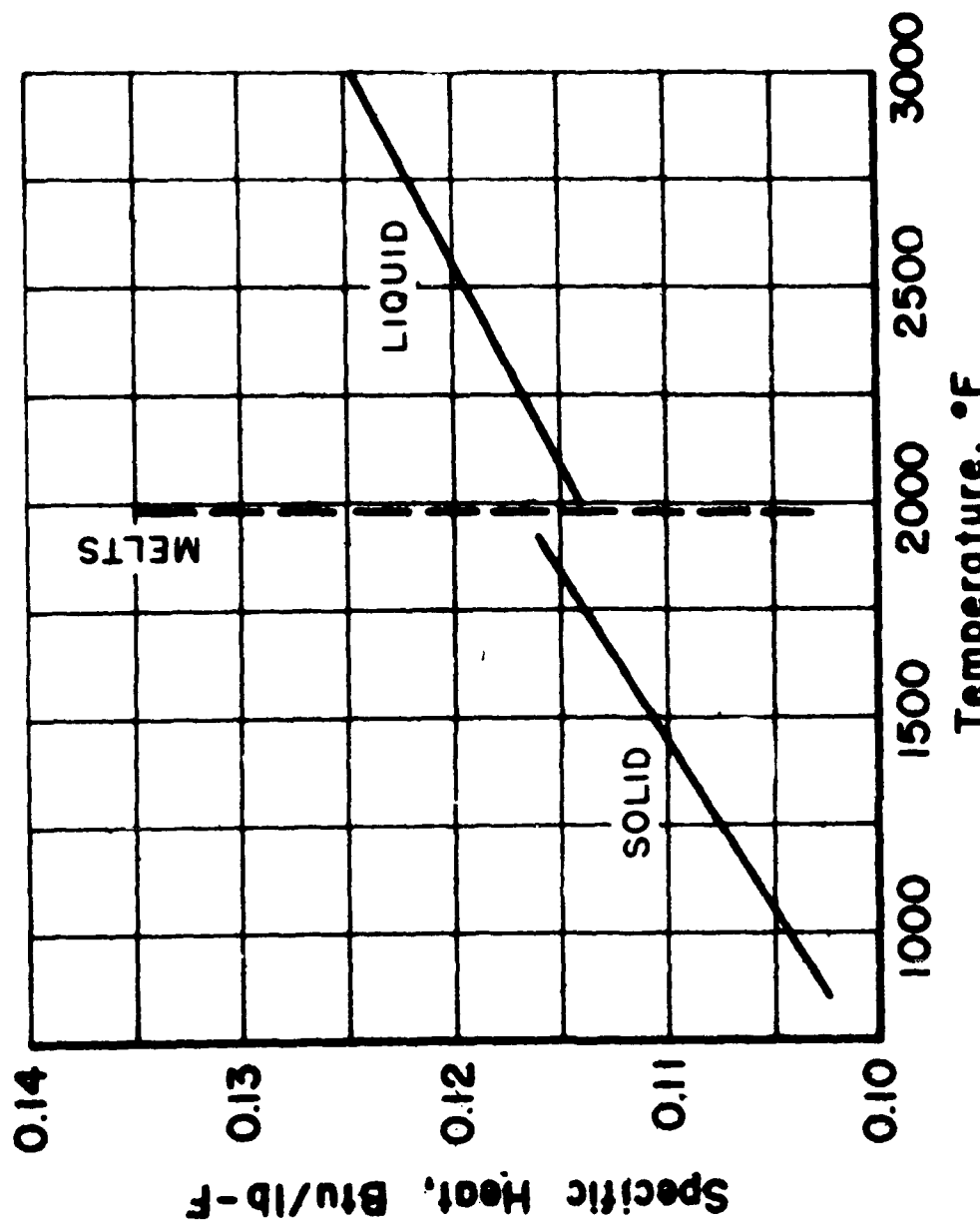


Fig. 11 SPECIFIC HEAT OF COPPER

Figure #11

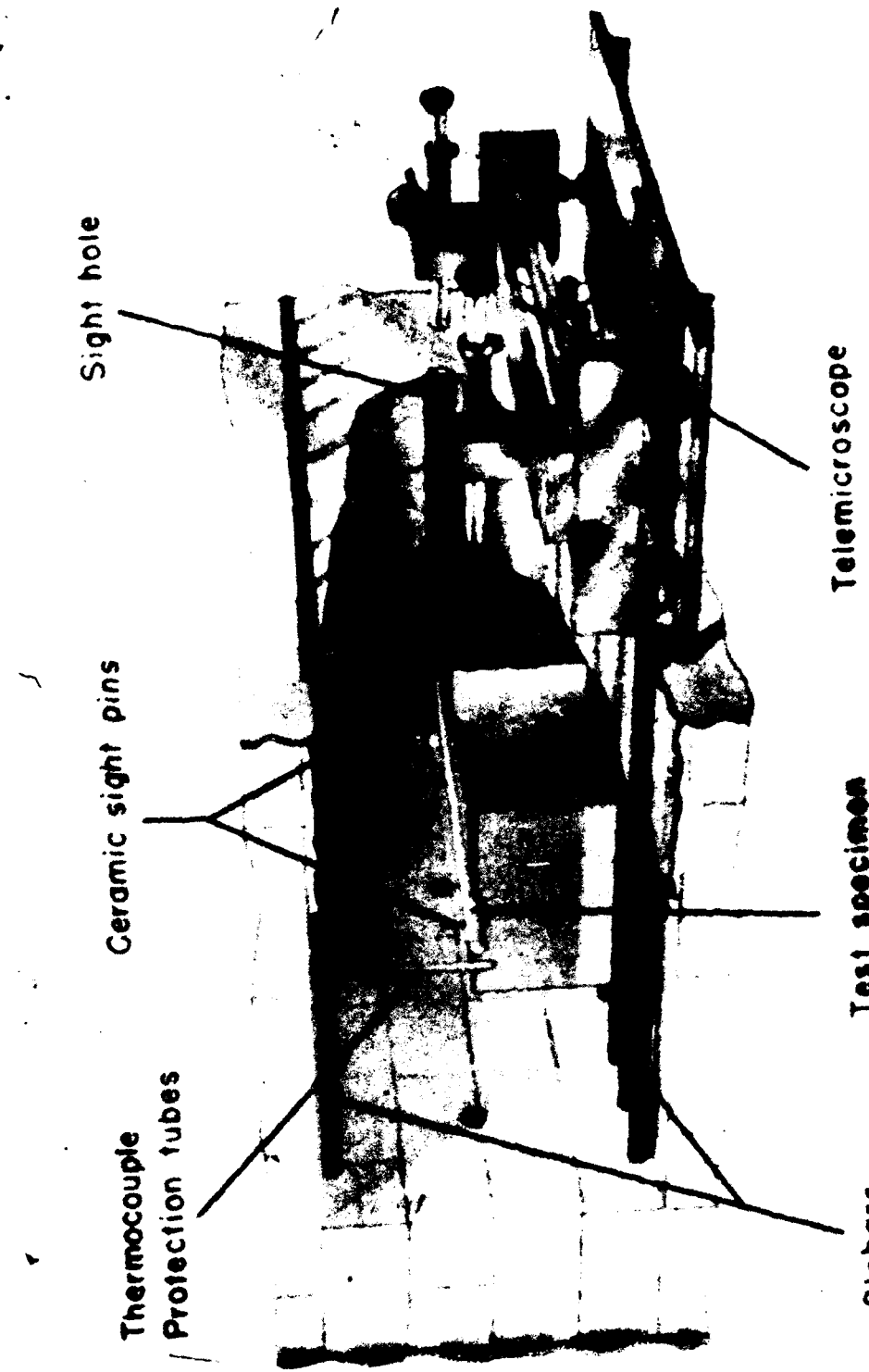


Figure #12

Fig. 12 APPARATUS FOR MEASURING LINEAR THERMAL EXPANSION

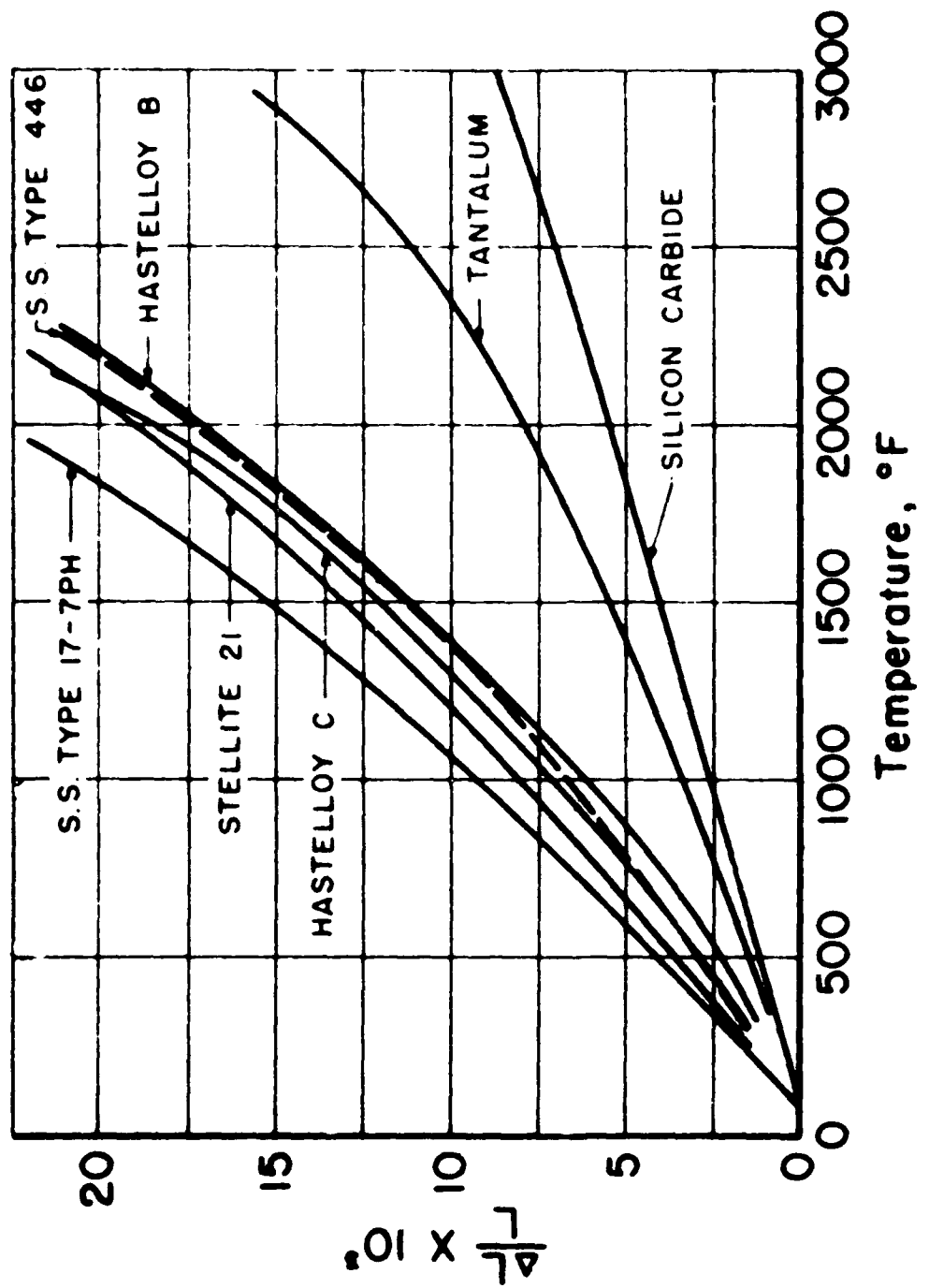


Fig. 13 LINEAR THERMAL EXPANSION

Figure #13

HEAT TRANSFER

THE APPROACH TO THERMAL EQUILIBRIUM
IN A LAMINAR HYPERSONIC BOUNDARY
LAYER

D. E. Knapp

THE APPROACH TO THERMAL EQUILIBRIUM IN A LAMINAR
HYPersonic BOUNDARY LAYER

D. E. Knapp

SUMMARY

Availability of relaxation time measurements makes it possible to examine the approach to thermal equilibrium in hypersonic flow. Non-equilibrium conditions may occur in both ballistic and glide re-entry trajectories. In this paper the second case is considered where wing leading edges are assumed to have sufficient sweep so that inactive degrees of freedom are not excited by the initial shock front. Under this condition molecular vibration and dissociation do not come into play until viscous heating in the boundary layer raises the air temperature above about 4500°R . This case is thus quite different from a ballistic vehicle where the boundary layer flow passes first through a strong bow shock wave.

In air flowing over a hypersonic glide vehicle dissociation of oxygen and vibration of nitrogen absorb most of the energy stored in inactive degrees of freedom. Approximate relaxation lengths are computed for these two processes followed by a more exact numerical integration of the temperature history of a particle passing through the boundary layer.

The following results are obtained from this analysis:

- (1) The boundary layer temperature distribution is significantly different from the equilibrium case.
- (2) The calculated temperature distribution remains consistent with the customary boundary layer similarity assumption.
- (3) The maximum temperature is 9500°R compared to 6000°R for an equilibrium boundary layer.

These results should be of interest in two problems which arise in connection with hypersonic glide vehicle design: first, the evaluation of boundary layer ion concentration and second, the detailed treatment of boundary layer heat transfer.

INTRODUCTION:

At the high temperatures which occur in hypersonic flow both active and inactive degrees of freedom share in molecular kinetic energy. In air, translational and rotational motion are called active degrees of freedom since only a few collisions between molecules are required to reach an equilibrium distribution of energy. Molecular vibration, dissociation, and at extreme temperatures ionization are called inactive degrees of freedom because a very large number of collisions are required before an equilibrium distribution of energy among these processes is achieved.

The time lag for energy absorption by inactive degrees of freedom may cause thermal disequilibrium whenever a large amount of thermal energy is rapidly added to a fluid. This situation exists both in a strong shock wave and in a hypersonic boundary layer. The approach to thermal equilibrium behind shock waves was examined by Bethe and Teller⁽¹⁾ at a period when little experimental information was available. Based on theoretical estimates of the number of collisions required to reach equilibrium among the active and inactive degrees of freedom, they predicted rather large relaxation lengths behind strong shock waves in air. However, they considered their most important result to be that the velocity, pressure, temperature, and density asymptotically approach equilibrium values which are independent of the intervening physical processes.

The problem of interest in this paper is the approach to equilibrium in a hypersonic boundary layer over a dart shaped wing at small angle of attack. This geometry has an element of simplicity similar to that of a planar shock, but at the same time it is of practical interest in the design of a boost glide vehicle. For a dart shaped wing with suitably blunted leading edges, the shock front will be wrapped

closely over the compression surface of the wing. In addition, the strength of the detached shock ahead of the swept leading edge is about the same as the strength of the shock ahead of the flat lower wing surface. These shock strengths are of course much below that of the nose shock. Now most of the boundary layer flow over the compression wing surface passes through the weak shock at the swept leading edge rather than the strong shock at the nose. In this way, energy to excite inactive degrees of freedom is supplied almost entirely by viscous forces in the boundary layer. This creates an element of simplicity for the present problem in contrast to a symmetric ballistic vehicle where nearly all of the boundary layer flow passes first through a strong nose shock.

AVAILABLE EXPERIMENTAL RESULTS:

With the extensive activity in shock tube experiments, direct measurements of relaxation time or the time required for inactive degrees of freedom to reach equilibrium are now available. Measurements of relaxation time for vibration in oxygen and nitrogen have been made by Blackman.⁽²⁾ Relaxation times for both vibration and dissociation of oxygen have been measured by Glick and Wurster.⁽³⁾ In both experiments the relaxation time was obtained by observing the change in density behind a shock by means of spark interferometer photographs. In Figure 1, the product of relaxation time and pressure is shown plotted against $T_{av}^{-1/3}$. Here the average temperature is the arithmetic mean between the equilibrium temperature and the temperature when no energy is distributed to the inactive degrees of freedom. Although Blackman has found a small change in relaxation times in mixtures of oxygen and nitrogen, we will use the relaxation times for pure nitrogen or oxygen in the following analysis.

EVALUATION OF RELAXATION PROCESSES IN A HYPERSONIC BOUNDARY LAYER:

A boundary layer structure must now be established within which the relaxation time results may be applied. For this purpose a series of boundary layer enthalpy profiles calculated by Royce and Chase⁽⁴⁾ for the boundary layer over a flat plate will be used. Using the best available real gas properties, they integrated the compressible flow boundary layer equations with the following assumptions:

- (1) Surface cooled only by radiation
- (2) Local thermal equilibrium throughout the boundary layer
- (3) Similarity of velocity and enthalpy profiles in the direction of flow.

The enthalpy-velocity relationships computed in reference⁽⁴⁾ are assumed to be unchanged as the non-equilibrium boundary layer approaches thermal equilibrium. This assumption implies that non-equilibrium processes represent a small perturbation on the energy balance in the boundary layer. This view of the energy balance in the boundary layer is in a sense supported by the work of Lees⁽⁵⁾, Bromberg⁽⁶⁾, and others where for Lewis number = 1 the boundary layer heat transfer is shown to be independent of the exact nature of the physical processes in the boundary layer. As in the case of any perturbation analysis it will be necessary to examine the results with respect to the enthalpy similarity assumption.

Figure 2 shows two boundary layer temperature profiles. These were obtained from the equilibrium boundary layer enthalpy profile in the following way. The upper curve represents the temperature when no energy is absorbed by inactive degrees of freedom. Since the boundary layer is assumed to be a constant pressure process, this curve is geometrically similar to the enthalpy profile. The lower curve represents the temperature which results when an equilibrium distribution of energy among the active and inactive

degrees of freedom has been achieved. The temperature profile shown here represents a glide vehicle near maximum altitude and velocity. As altitude and velocity decrease the non-equilibrium temperature profile drops steadily while the equilibrium temperature curve changes very slowly. It is clear that the difference in temperature is not a small perturbation in the usual sense of the word.

The principal energy sinks among the inactive degrees of freedom in air in this example are dissociation of oxygen and vibration of nitrogen. A simple approximation to relaxation lengths in the boundary layer flow field may be obtained by forming the product of local velocity and relaxation time obtained from Figure 1. Results of this calculation are shown in Figure 3. The first case represents about the maximum altitude and velocity short of orbiting velocity at which a glider could maintain lift. The second corresponds approximately to a peak heating condition. The temperature difference shown, ΔT_{max} , is the maximum difference between equilibrium and non-equilibrium flow in the boundary layer. From these results two important conclusions can be drawn. First, before flow enters the boundary layer, that is for $u/u_1=1$, equilibrium is not reached within the length of a conceivable glide vehicle. Second, for glide flight conditions which are associated with a significantly large ΔT_{max} , the dissociation of oxygen is the more rapid process.

With this background the temperature histories of three particles passing through the boundary layer shown in the first part of Figure 3 will be investigated in detail. A particle in the present use of the word really means an ensemble of molecules of oxygen and nitrogen moving through the boundary layer as a group. Also, diffusion of atoms and molecules will be neglected to simplify the analysis. This approximation is good as a particle first enters the boundary layer and becomes progressively worse as concentration differences

tions the temperature histories of individual particles in the boundary layer can be obtained by stepwise integration.

In Figure 4, the results of this calculation are shown for three particles at successively greater distances from the flat plate. The dashed lines represent the temperature limits corresponding to equilibrium or non-equilibrium flow. The solid line between these limits shows the progress of energy distribution among the inactive degrees of freedom in terms of the local temperature. The temperatures in each case retain an approximate similarity structure. The maximum temperatures are the same in each case because they are governed by the extreme temperature dependence of the dissociation reaction rate. The temperatures at the maximum enthalpy position for each particle are also nearly the same because dissociation of oxygen is complete and vibration of nitrogen is still only slightly activated. From these results the maximum temperature in the boundary layer obtained is 9500°R compared to 6000°R for an equilibrium boundary layer. The temperature determined here falls gradually to about 8000°R at a point corresponding to the maximum temperature in an equilibrium boundary layer.

Beyond this point recombination of oxygen should begin while energy continues to be absorbed by vibration of nitrogen. Because of the lack of experimental data on recombination rates, the integration is not continued in this region. However, at the density considered here the gas phase recombination is expected to be a very slow process, and a region of over dissociation should exist as the flow is further decelerated in the boundary layer.

These results are collected in Figure 5 which shows a logarithmic plot of the boundary layer cross-section. The particle paths whose temperature histories were determined by integration are shown here by long dashed lines.

The principal structural features of the boundary layer which have been determined are the regions of maximum temperature and of complete dissociation of oxygen. This structure is consistent with the customary similarity assumption in boundary layer theory.

REFERENCES

- (1) Bethe, H. A. and Teller, E., "Deviations from Thermal Equilibrium in Shock Waves", Aberdeen Proving Ground, B.R.L. Report No. X-117 (1945).
- (2) Blackman, V., "Vibrational Relaxation in Oxygen and Nitrogen", Journal of Fluid Mechanics, 1 61 (1956).
- (3) Glick, H. S. and Wurster, W. H., "Shock Tube Study of Dissociation Relaxation in Oxygen", Journal of Chemical Physics, 27 1149 (1957).
- (4) Royce, W. W. and Chase, R. A., "Laminar Boundary Layer Equilibrium Temperatures of Flat Plates in Compressible Supersonic Flow Using Real Gas Properties", D.A.C. Report No. LB-25269.
- (5) Lees, L., "Laminar Heat Transfer Over Blunt-Nosed Bodies at Hypersonic Flight Speeds", Jet Prop., 26 259 (1956).
- (6) Bromberg, R., "A Note on the Effects of Gas Dissociation on Boundary Layer Heat Transfer", J.A.S. 23 976 (1956).

RELAXATION MEASUREMENTS IN OXYGEN AND NITROGEN

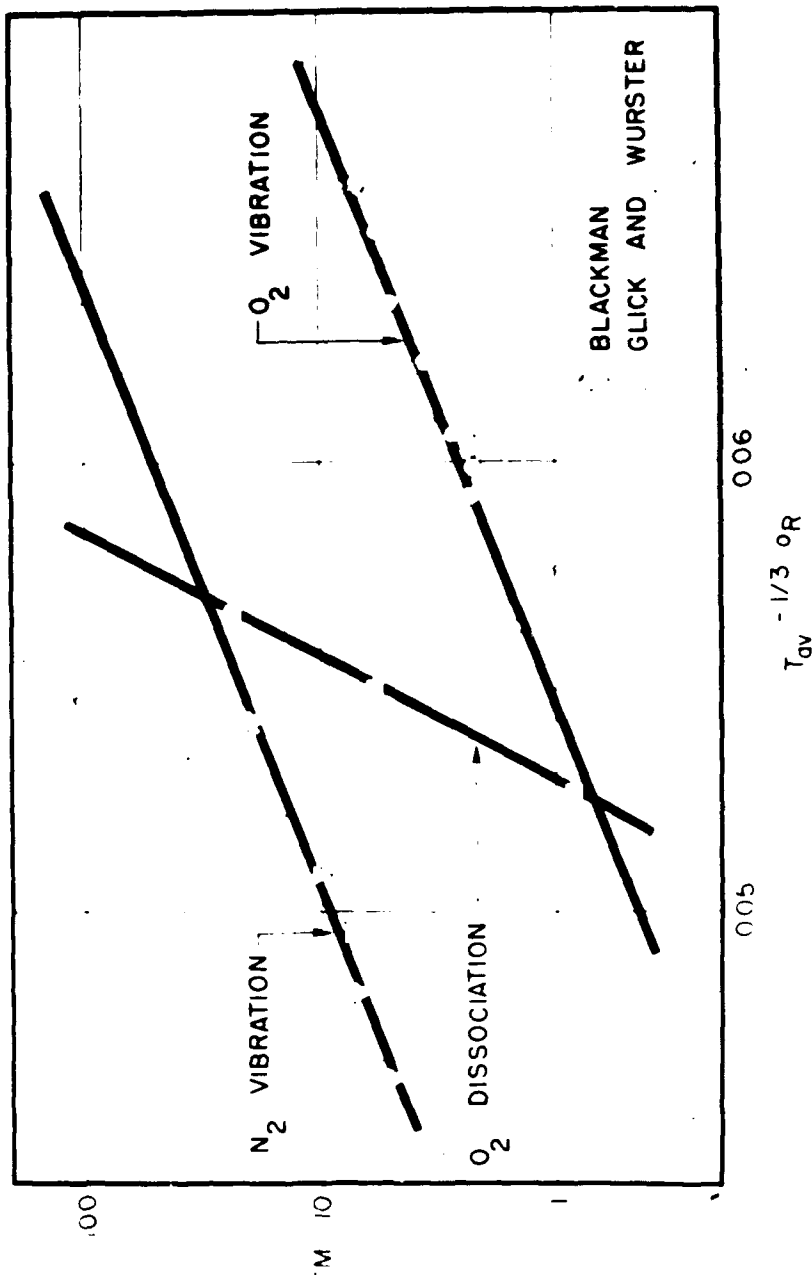


Figure #1

HPI461

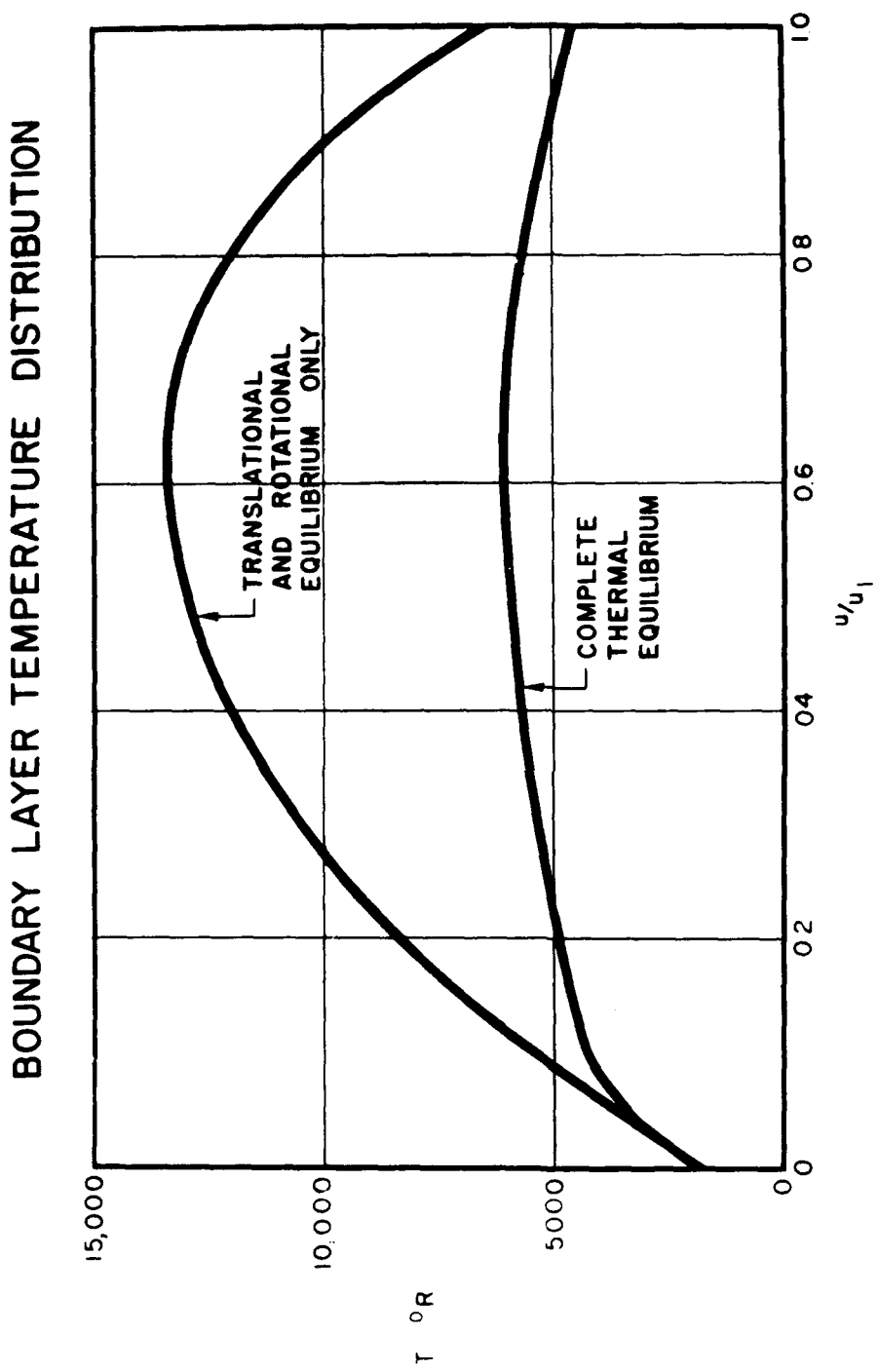
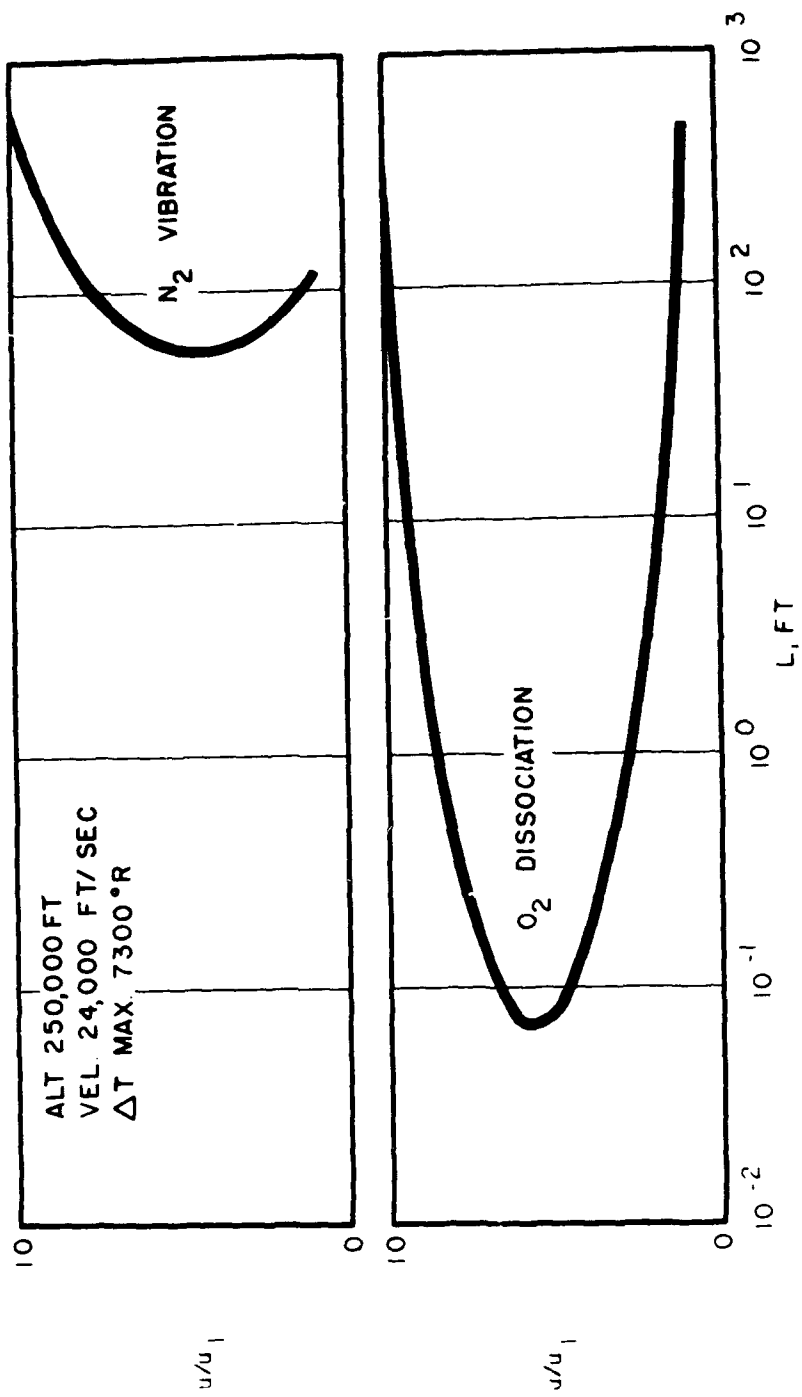


Figure #2

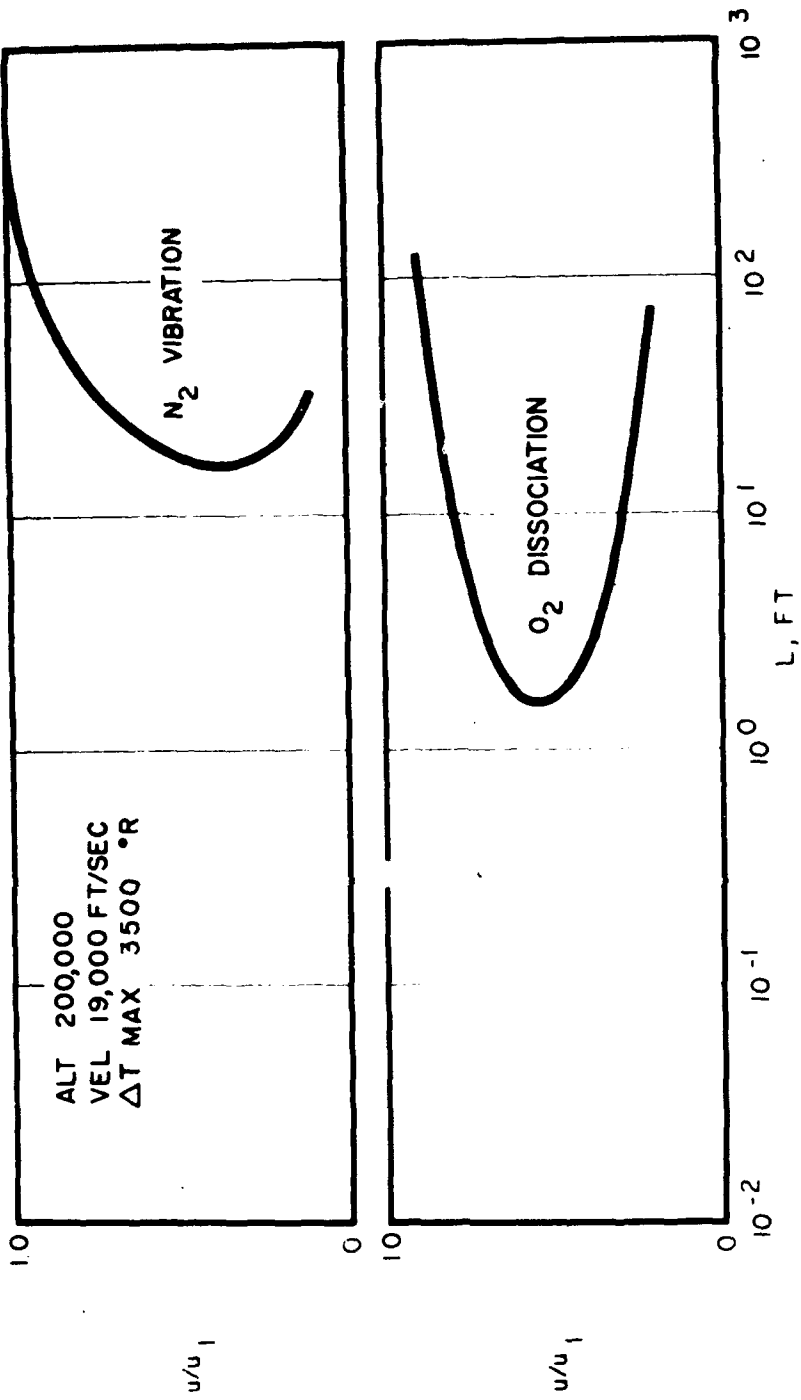
ESTIMATED BOUNDARY LAYER RELAXATION LENGTHS



8P146-3

Figure #3

ESTIMATED BOUNDARY LAYER RELAXATION LENGTHS



8P146-4

Figure #4

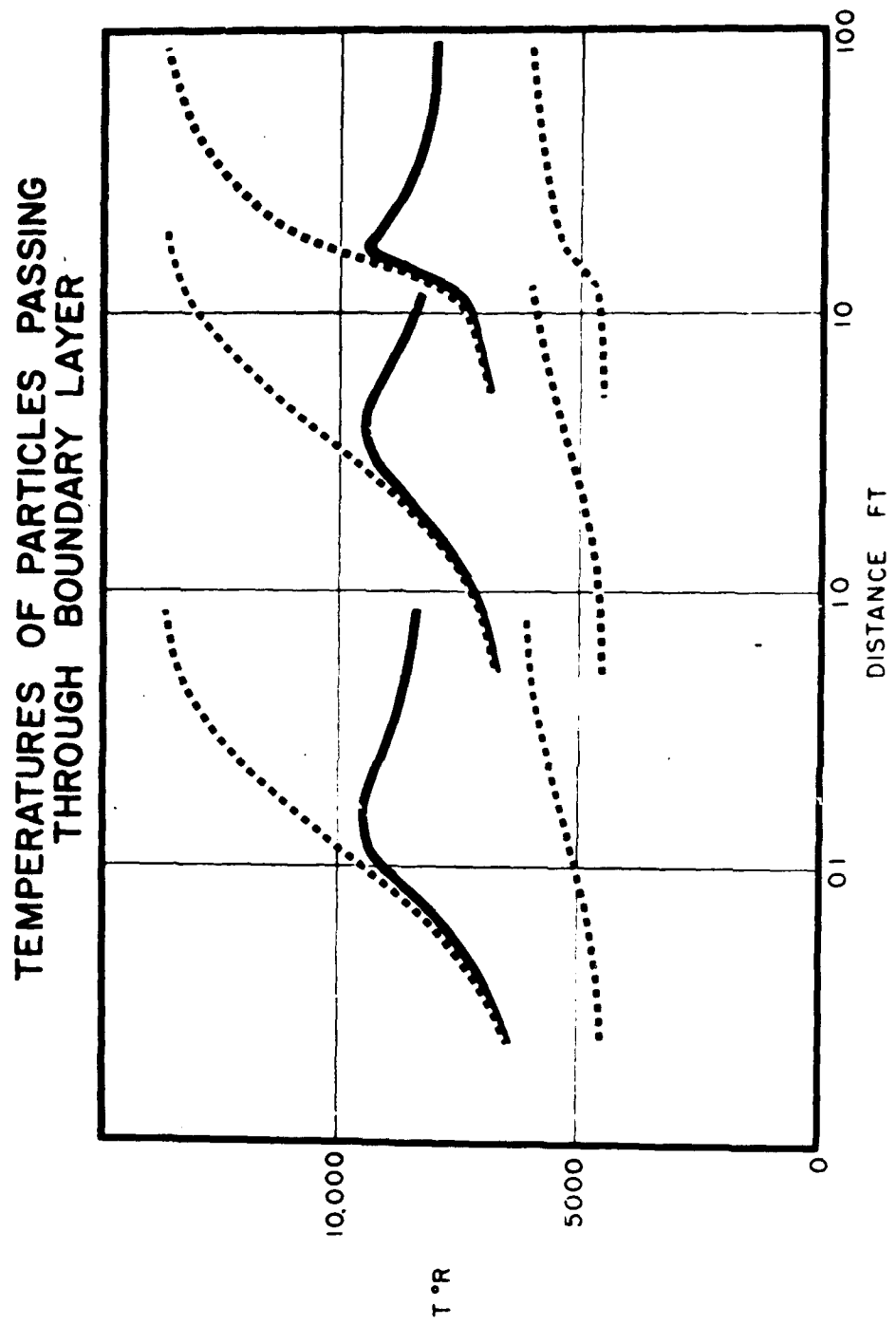
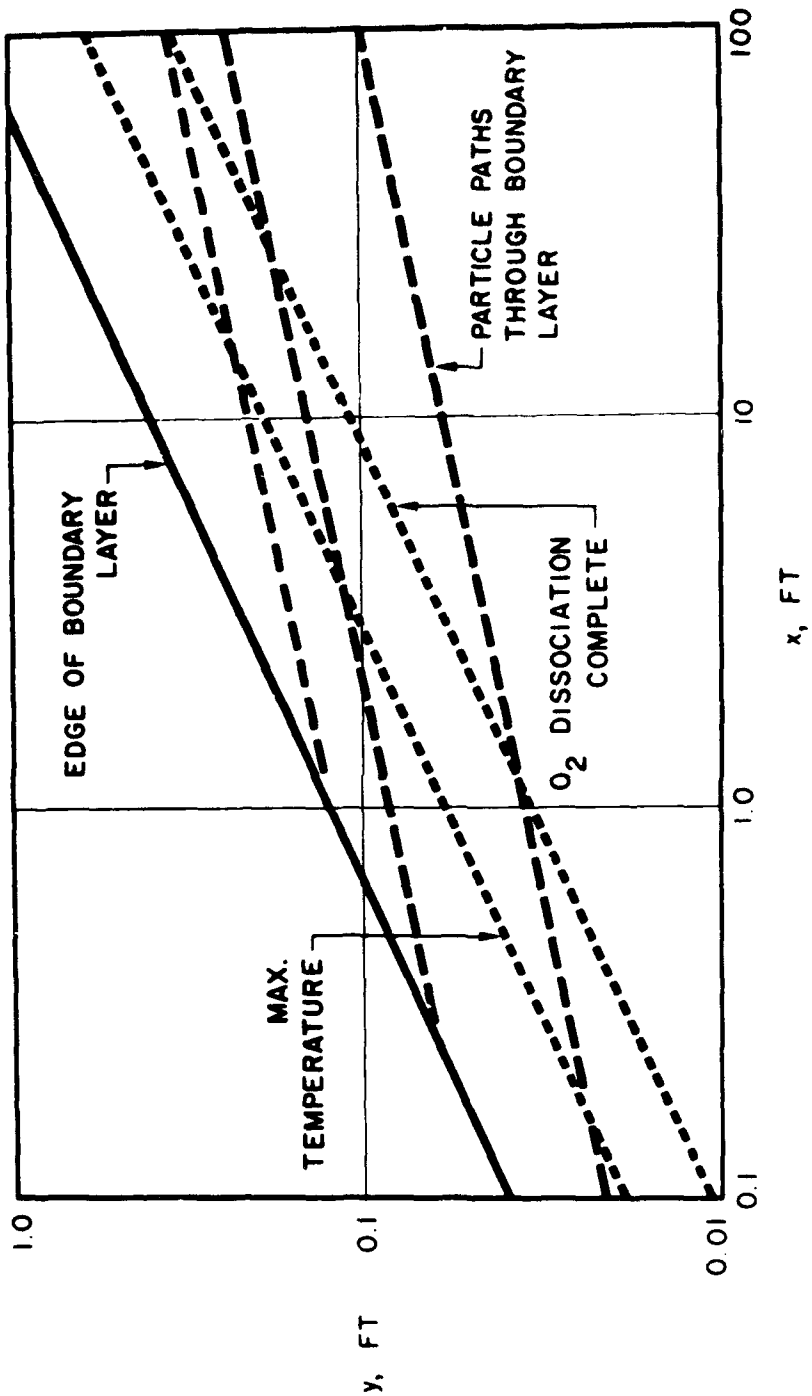


Figure #5

8P146-5

HYPersonic BOUNDARY LAYER STRUCTURE



8P146-6

Figure #6

GENERAL CHARACTERISTICS OF BINARY BOUNDARY LAYERS WITH
APPLICATIONS TO SUBLIMATION COOLING

C. Gazley, Jr.
D. J. Masson
J. F. Gross

The RAND Corporation

CONTENTS

	Page No.
SYMBOLS	298
Section:	
I. INTRODUCTION.....	301
II. BINARY LAMINAR BOUNDARY LAYER THEORY.....	304
III. DISCUSSION AND DERIVATION OF GENERALIZED EXPRESSIONS	311
IV. STABILITY OF THE BINARY LAMINAR BOUNDARY LAYER ..	316
V. TURBULENT BOUNDARY LAYER	319
VI. SUBLIMATION COOLING.....	321
VII. ABLATION COOLING	329
REFERENCES	330
FIGURES	332

SYMBOLS

a speed of sound

$$C = \frac{\mu}{\mu_2} \frac{T_2}{T}$$

$$c_f \text{ friction coefficient } \frac{2\tau_w}{\rho u_e^2}$$

$$c_H \text{ Stanton number } \frac{q_w}{\rho_e u_e c_p \frac{(T_w - T_{aw})}{e}}$$

$$c'_H = c_H / \sqrt{C_w}$$

c_i mass concentration of i^{th} component

c_{p_i} specific heat of i^{th} component

D_{ij} mass diffusion coefficient

E internal energy

$$f_w = -2 \left[(\rho v)_w / (\rho u)_e \right] \sqrt{Re_x}$$

$$f'_w = f_w / \sqrt{c_w}$$

g_c gravitational constant

h_f condensation coefficient

h_i partial enthalpy of i^{th} component

k thermal conductivity

L characteristic length

$M_e = u_e / a_e$ Mach number

m average molecular weight of mixture

$$\bar{m} = m_1 / m_2$$

m_i molecular weight of i^{th} component

n_i number of molecules of i^{th} component

\bar{P}	pressure tensor
p	pressure
p_i	partial pressure of i^{th} component
Pr	$c_p \mu / k$
\vec{q}	heat flux vector
R	universal gas constant
Re_x	$\rho u L / \mu$
\vec{r}	position vector
Sc	$\mu / \rho D_{12}$
T	temperature
u	x-directed velocity component
v	y-directed velocity component
\vec{v}	center-of-mass velocity
\vec{v}_i	diffusion velocity
$\nabla^* \vec{v}$	is transpose of $\nabla \vec{v}$

α	thermal diffusion coefficient
$\tilde{\alpha}$	disturbance wave length
γ	c_p / c_v
ΔH_s	heat of sublimation
δ_{ij}	Kronecker delta
ϵ	emissivity
λ	$\frac{1}{C} \frac{\rho \mu}{\rho_e \mu_e}$
μ	shear viscosity
ρ	density
σ	Stefan-Boltzmann constant
τ	viscous shear stress

Subscripts

- 1 foreign material
- 2 air
- w wall
- aw adiabatic wall
- e edge of boundary layer
- x based on x-direction

GENERAL CHARACTERISTICS OF BINARY BOUNDARY
LAYERS WITH APPLICATIONS TO
SUBLIMATION COOLING

Carl Gazley, Jr.
David J. Masson
Joseph F. Gross

I. INTRODUCTION

Recently, the alleviation of the high heating rates at the surface of hypersonic vehicles has been recognized as an important problem. One of the cooling methods that appears to have great ultimate promise is mass-transfer cooling - i. e., the injection of a foreign material from the surface into the boundary layer. This has a two-fold advantage in alleviation of the heat-transfer problem. The foreign material may absorb heat from the boundary layer through a phase change (sublimation) and/or by acting as a dispersed heat sink. It will be advantageous therefore to employ surfaces with high heats of sublimation as well as injectants with high thermal heat capacities. In addition, it has been shown that the introduction of a material (with its normal velocity component) at the surface acts to decelerate the flow and consequently to reduce the skin friction. This also implies a reduction in heat transfer at the wall.

The usual compressible boundary-layer equations are complicated by the appearance of (1) an equation defining the conservation of the species at any point in the boundary layer, and (2) transport terms which result from thermodynamic coupling coefficients such as thermal diffusion coefficient, etc. Although there are several ways of effecting the injection of a foreign material into the boundary layer, only three will be considered here, namely:

1. Transpiration cooling
2. Film cooling
3. Sublimation or ablation cooling

Although these three methods all involve the same mechanism in the gaseous phase of the boundary layer, there is a fundamental difference in the boundary conditions at the wall which distinguish the three methods from a thermodynamic as well as a mechanical viewpoint. Transpiration cooling is limited by the separation point of the boundary layer and the maximum rate at which the foreign material can be pumped through the surface. The rate of fluid injection at the surface is arbitrarily adjusted by purely mechanical means and the temperature at the surface may be regulated depending upon the injection rate of the material. It should be noted that a transpiration-cooling system requires pumps, storage tanks, pressure regulators, and accessory plumbing.

A film-cooling system involves pumping a liquid or gas onto the surface through some sort of slot configuration so that a thin film of the material covers the surface. This acts as an insulating coating and absorbs heat in its vaporization. These systems are usually limited by such characteristics as the stability of the liquid film or the pumping power available. Film-cooling systems require essentially all the plumbing and control equipment of a transpiration-cooled operation.

A sublimation-cooling system is self-controlled through the relation between the vapor pressure and surface temperature of a solid (the Clausius-Clapron equation):

$$\ln p_i = \frac{-\Delta H_s}{RT} + B \quad (26)$$

where

p_i = vapor pressure of subliming material

R = universal gas constant

ΔH_s = heat of sublimation

B = constant of integration

Heat is absorbed by the material as it sublimes. Thus, the heat transfer is reduced in two ways: (1) direct absorption in the form of heat of sublimation, and (2) reduction of heat transfer because of the mass transfer of the sublimed material. The mass release at the surface depends upon the heat of sublimation and the temperature of the surface. Furthermore, the surface temperature can no longer be arbitrarily controlled and, in fact, will always find 'its own level' depending upon the heat load, heat of sublimation, and the particular flow system in which we are interested.

Ablation cooling is a similar but much more complex process. Depending upon the surface material and the flight conditions, it is possible to have such complicating effects as fusion of the surface material, mechanical erosion, dissociation of both air and surface material, ionization, and chemical reactions between the components in the boundary layer. Sublimation cooling is only a specialized case of ablation. The obvious complications involved in an analysis of ablating systems has prevented any really accurate description of the mechanism.

There is another method of classifying these systems which may be helpful conceptually - by specifying the method of controlling the rate of injection. In the case of transpiration cooling, as we have seen, the rate is arbitrarily controlled depending upon certain mechanical requirements such as the porous surface and pumping power available. This may be considered an arbitrarily-controlled system. For a subliming or ablating surface, however, the rate of injection is determined by the heat of sublimation and the surface temperature. For a set of flight conditions and a surface material, the steady-state injection is fixed thermodynamically. We may call this a self-controlled system. Film cooling may be considered transitional. The rate of mass transfer into the boundary layer is self-controlled but the flow rate of liquid or gas over the surface remains arbitrary.

II. BINARY LAMINAR BOUNDARY-LAYER THEORY

Baron, ⁽¹⁾ Eckert, et al., ⁽²⁾ and Sziklas and Banas ⁽³⁾ have investigated theoretically the problem of mass-transfer cooling in the laminar boundary layer. The introduction of a species conservation equation as well as the appearance of thermodynamic coupling terms in both the species and energy equations complicates the mathematical analysis of the boundary layer. The equations may be derived as follows:

Let us assume:

1. Two dimensional flow
2. No dissociation, ionization, or chemical reactions in the boundary layer
3. No external forces
4. Transport phenomena are linearly dependent upon property gradients.
5. Fluid medium is locally homogeneous and isotropic

The species conservation equation may be written:

$$\frac{\partial n_1}{\partial t} + \nabla \cdot n_1 (\vec{V} + \vec{V}_1) = 0 \quad (1)$$

$$\vec{V}_1 = - \frac{D_{12}}{c_1} \left\{ V c_1 - \frac{m_1 - m_2}{m} c_1 c_2 \nabla \ln p + \alpha c_1 \nabla \ln T \right\} \quad (2)$$

where

n_i = number of molecules of species *i*

\vec{V} = center of mass velocity

\vec{V}_i = diffusion velocity

α = thermal diffusion coefficient

p = pressure

c_i = mass concentration of i^{th} component

()₂ = air

()₁ = foreign material

D_{ij} = diffusion coefficient

m_i = molecular weight of i^{th} component

The momentum equation is:

$$\nabla \cdot \bar{P} = -\rho \frac{D\vec{V}}{Dt} = \nabla \cdot \left\{ \left[p - \frac{2}{3} \mu V \cdot \vec{V} \right] \delta - \mu \left[\nabla \vec{V} + \nabla^* \vec{V} \right] \right\} \quad (3)$$

where

\bar{P} = stress tensor

δ = kronecker delta

$\nabla^* \vec{V}$ = transpose of $\nabla \vec{V}$

μ = viscosity

The energy equation is:

$$\frac{D(nE)}{Dt} + nE(\nabla \cdot \vec{V}) + \nabla \cdot \vec{q} = -\bar{P} : \nabla \vec{V} \quad (4)$$

where

E = internal energy of system

In order to obtain a relationship between the pressure and heat flux tensors and the dynamics of the molecular encounters in the system, it will be necessary to apply the Boltzmann equation as well as the principles of irreversible thermodynamics. The following approximate relationships are obtained:

$$-\bar{P} = - \left[p + \frac{2}{3} \mu \nabla \cdot \vec{V} \right] \delta_{ij} + \mu \left[\nabla \cdot \vec{V} + \nabla^* \cdot \vec{V} \right] \quad (5)$$

$$\bar{q} = -k \nabla T + (n_1 \bar{h}_1 \vec{V}_1 + n_2 \bar{h}_2 \vec{V}_2) + \frac{\alpha R T c_1 c_2 m^2 n}{m_1 m_2} (\vec{V}_1 - \vec{V}_2) \quad (6)$$

where

k = thermal conductivity

\bar{q} = heat flux vector

\bar{h}_i = partial enthalpy of i^{th} component (per molecule)

m = average M. W. of gas

α = thermal diffusion coefficient

The thermal flux is made up of three parts. The first is the usual conduction term arising as a result of the temperature inequalities in the gas. The second is due to a transfer of energy resulting from a diffusion flux relative to the mass velocity. The last term represents the heat flux occurring as a result of the concentration and pressure gradients in the boundary layer.

These equations may be modified to include the usual boundary-layer assumptions (1) steady-state, (2) boundary layer thickness small in comparison to a characteristic length along the surface, (3) small injection velocities at the surface, and (4) no pressure gradient along the surface. Now the equations are:

$$\frac{\partial(\rho u)}{\partial x} + \frac{\partial(\rho v)}{\partial y} = 0 \quad (7)$$

$$\rho u \frac{\partial u}{\partial x} + \rho v \frac{\partial u}{\partial y} = \frac{\partial}{\partial y} (\mu \frac{\partial u}{\partial y}) \quad (7a)$$

$$\rho u \frac{\partial c_1}{\partial x} + \rho v \frac{\partial c_1}{\partial y} = - \frac{\partial j_1}{\partial y} \quad (7b)$$

$$\rho c_p (u \frac{\partial T}{\partial x} + v \frac{\partial T}{\partial y}) = \frac{\partial}{\partial y} (k \frac{\partial T}{\partial y}) + \mu \left(\frac{\partial u}{\partial y} \right)^2 - \frac{RT\alpha m}{m_1 m_2} \frac{\partial j_1}{\partial y} - \frac{\partial}{\partial y} (h_1 - h_2 + \frac{RT\alpha m}{m_1 m_2}) j_1$$

$$(7c)$$

where

$$j_1 = - \rho D_{12} \left[\frac{\partial c_1}{\partial y} + \alpha c_1 c_2 \frac{\partial \ln T}{\partial y} \right] \quad (7d)$$

The boundary conditions for the system of equations indicated above are given as follows from simple physical considerations:

$$\left. \begin{array}{l} u = 0 \\ T = T_w \\ c_1 = c_{1w} \end{array} \right\} \quad y = 0 \quad (8)$$

$$\left. \begin{array}{l} u = u_e \\ T = T_e \\ c_1 = 0 \end{array} \right\} \quad y \approx y_e \quad (9)$$

A transformation of coordinates ⁽¹⁾ is now possible which will enable us to represent all the variable unknowns as functions of a new set of coordinates s and η .

$$\begin{aligned} s &= \int_0^x C u_e \mu_e \rho_e dx \\ \eta &= \frac{\rho_e u_e}{(2s)^{1/2}} \int_0^y \frac{\rho}{\rho_e} dy \end{aligned} \quad (10)$$

The stream function has the form:

$$\Psi = (2s)^{1/2} f(\eta) \quad (11)$$

The equations now appear as:

$$(\lambda f'')' + ff'' = 0 \quad (12)$$

$$\left(\frac{\lambda c_1'}{Sc_1} \right)' + fc_1' = 0 \quad (12a)$$

$$\left(\frac{\lambda c_p}{Pr} T'\right)' + \left(\frac{\lambda c' p}{Sc} + c_p f\right) T' = -\left(\frac{\gamma_e - 1}{4}\right) M_e^2 \lambda f'^2 \quad (12b)$$

with

$$\lambda = \frac{1}{C} \frac{\rho \mu}{\rho_e \mu_e} \quad M_e = \frac{u_e}{a} \quad \text{Mach number}$$

$$C = \frac{\mu}{\mu_2} \cdot \frac{T_2}{T} \quad \gamma_e = \frac{c_p}{c_v}$$

It is assumed that the thermal diffusion coefficient $\alpha = 0$. Since we are concerned with a seventh-order system of equations, another boundary condition must be specified. It has been shown that this condition may be obtained by assuming the mass velocity of the air molecules negligible in comparison to that of the foreign material at the surface. This leads to the relationship that:

$$(\rho v)_w = -\frac{\rho}{c_2} D_{12} \left(\frac{\partial c_1}{\partial y}\right) \quad (13)$$

Transforming all the boundary conditions to the new coordinates gives:

$$\begin{aligned} f' &= 2 \\ c_1 &= 0 & \eta \rightarrow \eta_e \\ T &= 1 \end{aligned} \quad (14)$$

$$\begin{aligned} f' &= 0 \\ c_1 &= c_{1w} & \eta = 0 \end{aligned} \quad (15)$$

$$f_w = \frac{\bar{\rho}_w}{Sc(1 - c_{1w})} \left(\frac{\partial c_1}{\partial \eta}\right)_w$$

It should be noted that the rate of diffusion or normal injection velocity will satisfy the similarity and boundary conditions provided that a constant surface temperature is specified. The amount of foreign material diffusing away from the surface is

given by Eq. (13). When this is translated into the similarity coordinates, the last equation in (15) is obtained. Now, for a constant wall temperature, examination of the equation shows f_w to be a constant. Furthermore, since $f_w \sim (pv)_w \sqrt{Re_x}$, the normal velocity will vary as $1/\sqrt{x}$ just as it must to satisfy similarity conditions. It will not matter whether we consider sublimation, evaporation, etc., because this will only add a constraint to our solution selection; it will not change Eq. (15).

If a sublimation or evaporation system is under consideration, then it will be necessary to impose a further condition, namely, between the wall temperature and concentration. In effect, this means that the number of possible solutions will be limited. The nature of this boundary condition and the effect of imposing it on the system of equations will be discussed in Section VI.

The system of equations shown above has been transformed into ordinary non-linear equations and may be solved by numerical methods. However, it is clear that for $Pr = Sc = \lambda = 1$ the momentum equation can be solved independently and solutions of the form:

$$\begin{aligned} T &= T(u) \\ c &= c(u) \end{aligned} \tag{16}$$

may be obtained. Although studies show that the momentum, temperature, and concentration boundary-layer thicknesses are of the same order of magnitude, the previous assumption is poor because of the severe fluctuation in magnitude of Pr and λ for mixtures. Nevertheless, a simple method for obtaining the directional effects of mass transfer could be obtained by permitting λ to vary in an iterative scheme. This would lead to:

$$\begin{aligned} T &= T(u, \lambda) \\ c &= c(u, \lambda) \end{aligned} \tag{17}$$

It has been shown that the assumption of $\mu \sim T$ for air flow leads to a Blasius momentum equation and skin-friction results independent of Mach number. A constant wall temperature also results in temperature and velocity functions dependent upon a single variable. Baron has shown that the equations above give similar solutions even when λ , Pr and Sc vary both with temperature and concentration. By using the transformation coordinates, it has been demonstrated that the system of partial differential equations may be changed into a new system of inter-dependent ordinary differential equations.

The numerical solutions indicate^(1, 2, 3) that the Stanton number and skin-friction coefficient are functions of a blowing parameter defined as $f_w = -\frac{2(\rho v)w}{\rho_e u_e \sqrt{Re_x}}$ as well as Mach number and the ratio of wall- to free-stream temperatures. Plots of $c_f \sqrt{Re_x}$ and $c_H \sqrt{Re_x}$ against the blowing parameter show a definite decrease with increasing ($-f_w$). The amount of the decrease depends upon the properties of the material which is diffusing through the boundary layer.

III. DISCUSSION AND DERIVATION OF GENERALIZED EXPRESSIONS

These equations have been solved numerically for air, water, helium and hydrogen injection and the cases of an insulated and cooled wall. Before comparing solutions, it should be noted that the η used by Eckert, et al.⁽²⁾ and Sziklas and Banas⁽³⁾ can be obtained from Eq. (10) by letting $C = 1$ and $\bar{\rho} = 1$.

Figure 1 shows the effect of hydrogen injection on the velocity profile. For an isothermal boundary layer, a moderate hydrogen injection ($c_{1w} = 0.2$) causes some increase in the boundary-layer thickness. The compressible cases show much more pronounced thickening at the same injection rate, particularly for the case of an insulated wall. One might expect the cooled wall to have more decelerating effect on the boundary layer than in the case of the insulated wall. The decrease in the boundary-layer thickness, however, negates this effect. Thus, the overall effect of the flow deceleration is evident from the comparison of the velocity profiles.

A similar comparison may be made for the temperature profiles. Figure 2 shows temperature profiles for $M_e = 0$ and $M_e = 12$ at a wall to free-stream temperature ratio of 6. In the former case the wall is, of course, being heated by the boundary layer and in the latter case the opposite effect occurs. Injecting hydrogen into the boundary layer reduces the temperature gradient and the heat transfer in both cases. It should be noted that, in general, the temperature, concentration, and velocity thicknesses are about the same size.

From the appearance of the 'warped' profiles, then, it will certainly be expected that reduced friction and heat-transfer coefficients will occur as a result of the mass transfer. This is, in fact, true and a typical variation of the heat-transfer parameter is shown in Fig. 3. Figure 3 presents the results of Sziklas and Banas⁽³⁾ for a Mach number of three, and the reduction in heat transfer even

at moderate values of the injection parameter, is seen to be significant. The cases of the insulated wall and a wall cooled to free-stream temperature are indicated. Note the linear relationship between the heat-transfer parameter and f_w , as well as the fact that the effect of the heat transfer at the wall on the Stanton number seems to be independent of the blowing parameter. Figure 4 shows the effect of increasing Mach number on the heat transfer for an insulated wall. Again it appears that Mach number effect is unaffected by the blowing parameter. In Fig. 5, both effects are indicated and, in addition, the results of Baron for an insulated plate are compared with those of Sziklas.

The effect of different diffusing materials on the heat transfer is shown in Fig. 8. Results for hydrogen, helium, water vapor and air are shown. The light-weight, high heat-capacity hydrogen gives the most significant decrease because (1) high thermal capacity makes for a very efficient dispersed heat sink and (2) light weight of gas results in a large thickening of the boundary layer and hence decrease in the heat transfer. These curves suggest that the introduction of materials with molecular weights higher than air will continue the trend toward less efficient heat-transfer reduction.

The effects of blowing parameter, wall- to free-stream temperature ratio, Mach number, and molecular weight of injected material on the heat transfer has been shown. For design purposes and for interpretation of experimental work, it would be desirable to have a unified relationship. What is required may be expressed as: $c_H \sqrt{Re_x} = c_H \sqrt{Re_x} (M_e, T_w/T_e, f_w, m_1/m_2)$. The purpose would be to obtain a relationship which is as simple as possible - analytically and graphically.

A first attempt at generalization, suggested by Baron's parameters, involves modification of the heat-transfer parameter by the square root of the Chapman-Rubesin constant, C. This brings together the Mach-number effects as shown in Fig. 6. A similar modification in the blowing parameter corrects for the wall temperature as shown in Fig. 7. Here, the calculations of Sziklas and Banas⁽³⁾ for

different Mach numbers and wall cooling conditions have been approximated by the curve shown. Baron's theory has been plotted to show the comparison. There is close correspondence at low blowing parameters. The slight discrepancy at the higher f_w 's is caused by differences in property evaluation, particularly in the viscosity of the mixtures. Such correlations can be made for each injection material and the variation of the different substances is shown in Fig. 8. The addition of a foreign diffusing material thickens the boundary layer and, in fact, it has been shown that the amount of this thickening will depend upon the substance used. The density and velocity of the diffusing medium will determine just how much the boundary-layer thickness is increased. A lighter material will diffuse further out into the free stream creating a thick concentration boundary layer. A previous analysis⁽⁵⁾ has shown that the boundary-layer thickness should depend upon the molecular-weight at moderate blowing parameters and the diffusion coefficient at very low blowing rates. On this basis, it is possible to bring together the effects of injecting different materials by means of a molecular weight parameter. This is indicated in Fig. 9. The computed heat-transfer results of Sziklas and Banas⁽³⁾ are shown for comparison and the agreement is seen to be within 5 per cent. The resulting generalization may be expressed as:

$$c_H' \sqrt{Re_x'} = 0.4 \frac{f_w'}{\bar{m}^{1/3}} + 0.407 \quad (18)$$

where $\bar{m} = \frac{m_1}{m_2}$, the ratio of molecular weight of foreign material and air. The friction factor is included in the same figure by the use of a modified Reynolds analogy. For a Prandtl number of unity, it can be shown that, for both laminar Couette flow and laminar boundary-layer flow, the usual Reynolds analogy

$$c_H' = \frac{c_f}{2} \quad (19)$$

holds also for the mass-transfer case provided c_H' is based on an enthalpy difference - rather than the customary temperature difference. The use of the customary Stanton number in Fig. 9 undoubtedly accounts, in part, for the modified analogy. For Prandtl numbers different from unity, Eq. (19) does not hold. Furthermore,

the large variation in the Pr number through the boundary layer makes the usual assumption of constant Pr quite unjustified. Skin friction results using carbon dioxide and iodine vapor as injectants⁽⁵⁾ check the generalization of Eq. (18) to within the 5 per cent indicated for the other computed values.

In his analysis of chemically reacting boundary layers, Lees⁽⁶⁾ introduces an effective heat of sublimation' which may be thought of as the actual heat of sublimation plus the bonus reduction in heat transfer due to the blocking action of the diffusing sublimed material. Examination of Fig. 10 indicates that this parameter may be considerably greater than the actual heat of sublimation, even at moderate blowing rates. The abscissa, which has been modified to account for the different injection materials, may be calculated by noting that it is equivalent to the ratio $\Delta H_{\text{eff}}/\Delta H_S$, where $q_w = \rho_e u_e c_H \Delta H_{\text{eff}}$. The quantity H_{eff} , which has been called an 'effective enthalpy potential', is:

$$\Delta H_{\text{eff}} = \sum c_{ie} (h_{ie} - h_{iw}) + \frac{u_e^2}{2} - \frac{\epsilon \sigma T_w^2}{\rho_e u_e c_H} \quad (20)$$

Equation (20) is a special case of a general formulation by Lees which includes chemical reactions and radiative heat transfer from the gases to the surface. Therefore, it would be possible to extend these arguments to a chemical reaction and radiation system on the basis of Lees equations (if $\frac{D_{12} \rho_c p}{k} = 1$). Note that for the case where the convective and radiative heat transfer are negligible in comparison to $u_e^2/2$, we can say that the effective heat of sublimation becomes larger as the velocity of the free stream increases. There is a practical limit to this, namely, when transition occurs. The calculated results of Cohen and Reshotko for air injection at the stagnation point have also been plotted on Fig. 10. The deviation here is about 10 per cent so that no large error would be incurred by using the same values for stagnation or flat-plate calculations.

The temperature recovery factor for helium and air injection is shown in Fig. 11. The experimental results for helium and air are those of Sziklas and Banas⁽³⁾ for $M_e = 2.6$ on an insulated wall. The air data agree well with the calculations of Low.⁽⁷⁾ The experimental helium results are not in agreement with the

theory and, while the deviation is not excessive, the effect of blowing in the experimental results appears opposite to what one might expect. Baron's results for variable λ and λ_w are shown. The deviation due to variation of property values is of the order of 10 per cent. Sziklas' results, for which $C_w = 1$, compares essentially with the λ_w values of Baron. A generalization similar to that for the Stanton number was tried (see Fig. 12). Here we note that the agreement is not as good as for the heat transfer parameter and the curve is no longer linear at low blowing parameters. This curve can be expressed as:

$$r = 0.031 \frac{f_w}{(m)^{-4/3}} + 0.885 \quad (21)$$

These considerations represent an attempt to generalize the theoretical computations of laminar binary boundary-layer characteristics. The results indicate that the effects of different foreign materials are primarily dependent on the relative molecular weight. The advantages of the use of an injected material having a low molecular weight are apparent. Equations (18) and (21) can be used to predict, for example, the performance of various sublimation systems (see Section VI).

IV. STABILITY OF THE BINARY LAMINAR BOUNDARY LAYER

The stability of the Laminar binary boundary layer was first investigated using the Lin⁽⁸⁾ approximation:

$$Re_{\min_{cr_{\delta^*}}} = \frac{25(du/dy)_w}{\frac{4}{u_i}} \quad (22)$$

where

$$0.58 = \pi \left(\frac{du}{dy} \right)_w \left[\frac{2(du/dy)_w y_i}{u(y_i)} - 3 \right] \frac{u(y_i) \frac{d^2 u(y_i)}{dy^2}}{\left[\frac{du(y_i)}{dy} \right]^3} \quad (23)$$

to calculate the minimum critical Reynolds numbers.⁽⁵⁾ This is the Reynolds number below which all disturbances are damped and therefore the flow will always be stable. It would be noted that Eq. (22) applies to an incompressible single-component flow. The values of the velocity profiles used in Eq. (22) were 'incompressible' in the sense that they were functions of concentration dependent coordinates. The boundary layer itself was assumed isothermal. It was assumed that Eq. (22) remained valid for small injection rates, i. e., the disturbance equations were for velocity and temperature independent of the concentration equation. In this way, minimum critical Reynolds number relationships with blowing parameter and molecular weight were obtained (see Fig. 13).

E. E. Covert⁽⁹⁾ has treated this problem by using the Tollmien-Schlichting perturbation analysis, i. e., he lets:

$$Z = Z_1(\vec{r}) + \Phi(\vec{r})e^{i(\bar{\alpha}x - \bar{\alpha}ct)} \quad (24)$$

where Z is any property of the flow such as velocity, temperature, etc.,

r = the position vector

α = disturbance wave length

c = complex disturbance wave velocity

He showed that the perturbation equations may be solved in exactly the same manner as for a single component gas except for the implicit effects of the foreign gas on the local flow properties for relatively small injection rates, where the boundary layer assumptions are still essentially valid. This justifies the approach used above. Covert found that the stability characteristics could be calculated for an n-component boundary layer using the steady-state velocity and density profiles. For a given range of Mach number, one may establish a boundary layer completely stable to two-dimensional subsonic disturbances simply by cooling the surface. Van Driest⁽¹¹⁾ has shown that the wall temperature required to achieve this cooling is obtained under the condition that

$$\frac{d}{dy} \left(\rho \frac{du}{dy} \right) = 0 \quad \text{at} \quad u = 1 - \frac{1}{M_e} \quad (25)$$

Covert calculated values of T_w for different Mach numbers with f_w as another parameter (see Fig. 14). It should be noted that his calculations are based on the solution of the inviscid (no viscosity) disturbance equations. Helium, carbon dioxide, and air injection were considered. Injection of any material, regardless of molecular weight, will cause a reduction in surface temperature. Since it has been established that cooling exerts a stabilizing influence on the boundary layer, we may expect an improvement with respect to a single-component gas. This should be particularly true for the injection of heavy molecules since these will act in a cooling manner by increasing the density near the surface. However, it is obvious that the act of injection introduces a disturbance in the boundary layer by decelerating the flow. This will certainly be destabilizing at high injection rates. Therefore, we may expect a counterbalancing of stabilizing and destabilizing effects. The net result will depend upon the efficiency of the injected material in cooling the boundary layer. Figure 14 shows the minimum temperature ratio for the injection of helium

as a function of Mach number with f_w as a parameter. It is indeed so that for a Mach number below 3.5, the injection reduces the stability character of a single component layer. However, as the Mach number increases, the adiabatic wall temperature rises very rapidly causing a high enthalpy region near the wall. The helium, injected into the hot boundary layer acts as a coolant decreasing the enthalpy region near the wall. The helium, injected into the hot boundary layer acts as a coolant decreasing the enthalpy and the over-all effect is to increase the minimum wall-temperature ratio. An interesting point is that no amount of air or carbon dioxide injection will increase the minimum temperature ratio. This agrees with the action shown previously by the isothermal Reynolds number calculations.

Experimental results⁽³⁾ are available for helium injection in a 17° porous cone at Mach = 2.6. At $f_w = -0.11$ the profiles were not yet transitional, but for $f_w = -0.26$, the inflection point had definitely appeared. From their data, the authors conclude that $|f_w| \approx 0.15$ is the point at which transitional profiles appear for this particular case. At the same Mach number with air injection, transitional profiles appeared at $f_w = -0.28$. Leadon, et al.⁽¹²⁾ performed a series of tests on a 20° porous cone in a Mach five stream. Results showed that transition Reynolds numbers (2.5×10^6) were about half as large as those on a similar smooth model. Furthermore, the transition point seemed very sensitive to Reynolds number, although no correlation was observed between the variables.

V. TURBULENT BOUNDARY LAYER

Solutions of turbulent boundary-layers with mass injection⁽¹⁵⁾ were originally done using the simple film theory, applied to the laminar sublayer. Even though the film theory does not yield certain details of the flow, it predicts the effects of mass injection quite well. More detailed analyses have since been carried out by Dorrance and Dore,⁽¹⁶⁾ Van Driest,⁽¹⁷⁾ and Rubesin⁽¹⁸⁾ for the case of air injection and by Rubesin and Pappas⁽¹⁹⁾ for light gas injection. Experimental results for air injection have been obtained by Mickley, et al.⁽²⁰⁾ and Leadon and Scott,⁽²¹⁾ and for helium injection by Leadon and Scott.⁽²¹⁾

Figure 15 shows examples of the reduction in Stanton number due to the injection of air into the boundary-layer for various wall to free-stream temperature ratios.

The effects of heat transfer and Mach number can be correlated by division of the blowing parameters by the zero mass-transfer Stanton number corresponding to the various wall to free-stream temperature ratios and Mach numbers. This is shown in Fig. 16. A similar correlation can be expected for other Reynolds numbers and Mach numbers. The film theory of Mickley, et al.⁽²²⁾ with air injection follows very closely the dashed curve of Fig. 16.

For the case of injection of a light gas, such as helium or hydrogen, the reduction in Stanton number for a particular value of the blowing parameter, $(\rho v)_w / \rho_e u_e c_{H_0}$, is greater than the reduction for the case of air injection, just as in the case of the laminar boundary-layer. By modifying the film theory to take into account the effects of light gas injection a similar reduction in Stanton number can be shown. This has been done by approximating the weight concentration of the foreign gas in the sub-layer and taking into account the variation in sub-layer thickness due to the foreign gas injection. As a result of the inclusion of these details in the expression obtained from the film theory, the reduction in Stanton number is

shown to be dependent on the blowing parameter. $(\rho v)_w / \rho_e u_e c_{H_0}$ and the same ratio of molecular weights used for the laminar case. This variation of Stanton number reduction, with blowing parameters, can be closely approximate by division of the blowing parameter by the molecular weight ratio to the two-thirds power rather than the one-third power as obtained for the laminar case. The results for light gas injection can then be correlated with the results for air injection. The comparison is shown on Fig. 17. Here the air-injection results of Rubesin and Pappas are given by the solid line while the experimental results of Leadon and Scott for helium injection are shown by the dashed line.

For the case of a turbulent boundary-layer with mass injection, a plot similar to that made for the laminar case shown in Fig. 10 can be made. This is shown in Fig. 18. Here the ordinate is the same as that for the laminar boundary-layer case and the abscissa is again the enthalpy driving force divided by the heat of sublimation.

A comparison of Figs. 10 and 18 shows that the 'effective heat of sublimation' for the turbulent case does not increase as fast with blowing as that for the laminar case. That is, the percentage reduction in the no-mass-transfer Stanton number is less for the turbulent boundary-layer than it is for the laminar boundary-layer.

VI. SUBLIMATION COOLING

Although there has been a great deal of work done toward solving transpiration cooling problems,^(1, 2, 3) discussion of phase changes at the surface have been exploratory in nature in that a number of assumptions were made in order to indicate qualitative trends.

Sutton and Skala⁽⁴⁾ have recently published a theory of ablating surfaces which includes the simultaneous solutions of the Navier-Stokes equations for the liquid and gaseous phase (for hypersonic flow conditions). Their method is as yet restricted to the stagnation point and few real conclusions have been drawn concerning ablating surfaces because of the complexity of the physical mechanism. From an aerodynamic viewpoint, of course, a subliming surface is much to be desired. Liquid flow on the surface of the vehicle could conceivably play havoc with transition values or simply alter the aerodynamic shape so that it no longer resembles the design and hence cannot perform its function properly. If we strive to work with materials such as naphthalene which remain essentially firm even under extreme temperature conditions then the added complexity of a liquid surface is not really necessary.

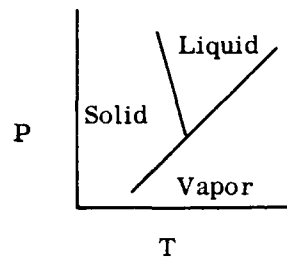
Essentially, a phase change at the surface restricts the boundary condition of the problem which is of interest here, i. e., the binary boundary layer with heat transfer. These equations have been derived and are indicated clearly on page 6. In a transpiration system in which the boundary layer is cooled by some gas, the rate at which the foreign gas enters the boundary layer is arbitrary and limited only by pumping requirements or boundary-layer separation. The temperature at the wall will then be determined from the solution of the equation. For this case, the concentration of the foreign gas at the wall will also depend only on the blowing rate for a given material (subject to the condition that no air penetrates the boundary). This situation has been solved for the case of air, nitrogen, water, helium, hydrogen, carbon dioxide, and iodine entering the boundary layer.

Sublimation covers the physical changes encountered by a substance in passing from a solid phase to a gas phase. It is characterized by the absence of any liquid phase. Referring to a p-T diagram it is at once seen that sublimation processes occur at relatively low pressure and temperature. The temperature at which the vapor pressure of the solid equals the total pressure of the gas phase in contact with it is defined as the sublimation point. The snow point is defined as that temperature at which the partial pressure of the solid is equal to the partial pressure of the substance in the gaseous phase. It is clear then that interest lies in the snow point and not in the sublimation point. In general, a foreign gas concentration of unity at the surface would imply a high blowing rate which might already have blown the boundary layer off the surface. The vapor pressure of the solid will be a function only of the temperature for equilibrium conditions. The curve below the triple point will be of concern here. The solid sublimes and creates a vapor pressure above it. These foreign molecules diffuse through the boundary layer and change the heat transfer causing a new temperature to appear on the surface. This continues until the entire system is in a steady-state condition, i. e., the heat absorbed by the subliming material and the warpage of the boundary layer profiles caused by the rate of foreign material entering no longer changes.

The equation relating the sublimation vapor pressure of a particular material to its temperature is :

$$\ln p_i = \frac{-\Delta H_s}{RT} + B \quad (26)$$

Here ΔH_s is the latent heat of sublimation and it is taken as independent of temperature for this case (this is true for almost all practical cases and certainly good for approximate calculations). B is another constant dependent upon the material and the region of integration and T is the absolute temperature of the material. Now, in



the case of low pressures, an ideal gas assumption will be valid and the concentration of the subliming material above the solid is:

$$c_1 = \frac{\frac{m_1 B' e^{-\Delta H_s / RT}}{m P_e}}{(27)}$$

Noting that the m is a function of wall concentration:

$$\frac{c_{1w}}{m - (m - 1)c_{1w}} = \frac{B'}{P_e} e^{\frac{-\Delta H_s}{RT_w}} \quad (28)$$

It has been shown previously, however, that for the case of an impermeable wall, the relationship between the velocity of the foreign gas and its concentration at the wall can be derived from the conservation of air molecules at the wall. This is:

$$\rho_2 v_w = - \rho_w D_{12} \left(\frac{\partial c_2}{\partial y} \right)_w \quad (29)$$

If, therefore, a solution is required, it must be noted that only one temperature will satisfy a given heat load. In the case of transpiration cooling, it is possible at a given heat load to vary the wall temperature by varying the amount of material blown through the surface. The problem now is to find the proper wall temperatures and concentrations for given heat loads, i. e., free stream conditions.

Eckert and Hartnett⁽¹³⁾ have indicated an approach to this problem for the case of constant fluid properties. This has been extended by Sziklas⁽³⁾ to include varying property solutions for the case of liquid coolants being injected. Possible vaporization and/or chemical reaction was taken into account in the H_s term.

Baron⁽¹⁴⁾ also made a study of the effect of phase changes by assuming a linear relationship between the heat absorbtion and the temperature at which the phase change occurs. In this way a generalized chart, relating T_w , f_w , and the molecular weight was obtained. It cannot be predicted, however, from the chart whether the physical conditions for the sublimation are feasible. Sziklas, using a constant Pr found dimensionless recovery factors greater than one for blowing with helium. When the variable property solution was included, then none of the recovery factors went above one. The same results as were used for hydrogen gas cannot be used for a carbon or plastic wall. Earlier it was shown that the friction and heat transfer coefficients for the different transpiration systems can be correlated using a molecular weight ratio term.

Rather than attempt new solutions, a preliminary study should be made to determine the usefulness of soutions now existing. The heat which is being transferred to the surface is

$$q_w = h(T_w - T_{aw}) = -k_w \left(\frac{\partial T}{\partial y} \right)_w \quad (30)$$

The amount of heat must be absorbed by the material in the form of sublimation heat.

$$q_w = -(\rho v)_w \Delta H_s \quad (31)$$

Now, equating these terms, the equation can be modified to include more common variables; the Stanton number and the Reynolds number and

$$c_H \sqrt{Re_x} (T_{aw} - T_w) = \frac{(\rho v)_w \Delta H_s \sqrt{Re_x}}{c_{p_e} \rho_e u_e} \quad (32)$$

where

$$Re_x = \frac{xu_e}{\nu_e} \quad (33)$$

$$c_H = \frac{h}{c_p e \rho_e u_e} \quad (34)$$

Introducing the blowing parameter which has been defined in many earlier works as

$$f'_{w} = - \frac{2}{\sqrt{c_w}} \frac{(\rho v)_w}{(\rho_e u_e)} \sqrt{Re_x} \quad (35)$$

Equation (7) is now:

$$-\frac{f'_{w}}{2} \frac{\Delta H_s}{c_p e} = \sqrt{Re_x} c'_H (T_{aw} - T_w) \quad (36)$$

Equation (36) may now be rewritten by multiplying and dividing the right sides by $c_{H_0} \sqrt{Re_x}$ and rearranging terms:

$$\Delta H_{eff} = \frac{c_{H_0}}{c_H} \Delta H_s = \frac{2(c_{H_0} \sqrt{Re_x}) (-T_{aw} + T_w) c_p e}{f'_{w}} \quad (36a)$$

The ΔH_{eff} is now an effective heat of sublimation which includes the blocking action of the diffusion process.

A design problem would probably designate a maximum surface temperature and then require a suitable ablating material. First of all, it is necessary to consider the adaptability of the material to withstanding severe structural strain and

thermal shock. This could prove to be the deciding factor in the choice of a material. Nevertheless, hastening the sublimation and resultant heat-transfer reduction through the mass-transfer process is to be desired. At the low pressures and temperatures encountered in the upper atmosphere, it would seem that the conditions for sublimation are quite in order. The thermal level in Eq. (9) is quite important for it indicates if a point has been reached at which the material will actually begin to sublimate. First, the relationships existing between H_s and the material and temperature should be investigated.

Previously, an approximate result was obtained which related the net heat transfer to the surface with the blowing parameter and the molecular weight:

$$\frac{c'_H}{\sqrt{Re_x}} = 0.4 \frac{f'_w}{(\bar{m})^{1/3}} + 0.407 \quad (18)$$

Equation (36) can be rewritten as:

$$-\frac{f'_w}{2} \frac{\Delta H_s}{c_p e} = 0.4 \frac{f'_w}{(\bar{m})^{1/3}} + 0.407 \quad (T_{aw} - T_w) \quad (37)$$

Substituting the expression for the recovery temperature, T_{aw} , of the wall in the last equation:

$$-\frac{f'_w}{2} \frac{\Delta H_s}{c_p e} = \left[0.4 \frac{f'_w}{(\bar{m})^{1/3}} + 0.407 \right] (T_e + r \frac{\gamma_e - 1}{2} M_e^2 T_e - T_w) \quad (38)$$

Previously, it was shown that an expression for the recovery factor was:

$$r = 0.031 \frac{f'_w}{(\bar{m})^{4/3}} + 0.885 \quad (21)$$

The final equation gives:

$$-\frac{f'_w}{2} \frac{\Delta H_s}{c p_e} = \left[0.4 \frac{f'_w}{(m)^{1/3}} + 0.407 \right] \left[T_e + \left\{ \frac{0.031 f'_w}{(m)^{4/3}} + 0.885 \right\} \frac{\gamma_e - 1}{2} M_e^2 T_e - T_w \right] \quad (39)$$

Combining this with the relationship for the concentration at the wall for a given temperature now uniquely defines a blowing rate for a given material and presumed flight conditions.

This equation is awkward but requires only algebraic manipulation for its solution. Once, having specified the flight conditions (M_e , T_e), the designer may choose different materials until one particular one suits the surface temperature requirements or heat transfer which will be specified to him. Choosing a material essentially fixes the heat of sublimation and the temperature of the surface for given geometry and flight conditions. The calculated f_w will now indicate the erosion or sublimation rate and permit an analysis of surface thickness.

Charts may be set up in the following manner. For different altitudes (specifying T_e and p_e and geometry) and velocities (M_e), the wall temperature may be plotted against the blowing parameter. In fact, such solutions have been obtained for ice, carbon dioxide, and ferrous chloride for a whole range of flight conditions. The results (Fig. 19) show that the equilibrium wall temperature, or snow temperature, approaches the sublimation temperature asymptotically as the Mach number is increased. It should be noted that the wall temperature increases much more rapidly with decreasing altitude than with the Mach number. This is what one would expect from examination of the Clausius-Clapryon Equation for wall concentration and temperature. Changes in altitude, and hence external pressure, govern the range of possible temperatures through the wall concentration. Once the altitude has been specified, however, the temperature variation on the surface is rather small and is limited by the sublimation temperature. The increased heat load brought about by increasing the Mach number is absorbed by larger blowing parameters (increased surface sublimation) rather than by large temperature increase.

Equation (26) is, of course, dependent on the condition of equilibrium. As the external pressure decreases, the sublimation pressure is reached very quickly and at extremely low wall concentrations. This implies that only very high blowing rates are possible at extreme altitudes. This is not true because different conditions are applicable at high altitudes. As the pressure is reduced, the surface molecules see fewer and fewer air molecules. Consequently, the region over the surface becomes less crowded until a situation is reached where essentially all the molecules escape which leave the surface. In this case the sublimation rate will no longer be limited by diffusion, but will tend toward the absolute rate of sublimation⁽¹⁰⁾

$$\dot{m}_e = h_f p_i \sqrt{\frac{g_e m_1}{2\pi R T_w}} \quad (40)$$

g_e = gravitational constant
 h_f = condensation coefficient

All the quantities here may be calculated with the exception of h_f , the condensation coefficient. This is usually determined experimentally and it has been found that it is relatively small in the case of polar compounds and close to unity for non-polar materials. The absolute temperature of the surface will also be an important factor for it will determine if a truly 'clean' surface exists. For $T = 1000^\circ K$ we may assume that the absorbed layer is no longer present for extremely low pressures. Therefore the maximum blowing rate we may expect is:

$$f_w = \frac{-2h_f p_1}{\rho_e u_e} \sqrt{\frac{g_e m_1 R e_x}{2\pi R T_w}} \quad (41)$$

However, in this case of rarefied flow, the heating rate is no longer affected by the efflux of vapor from the surface. That is, the heating rate is independent of the sublimation rate. The surface temperature and consequently the sublimation rate, however, adjust themselves so as to balance the heat input by heat absorption through sublimation. That is:

$$q = - \dot{m}_e \Delta H_s \quad (42)$$

where q is determined by flight velocity and altitude and vehicle geometry.

VII. ABLATION COOLING

We have just considered some simple solutions to the sublimation cooled system. The results which have accrued as a result of our analysis hold only in the region which satisfies the rather strict assumptions that we made. There may be other phenomena occurring simultaneously. Ablation then is also a self-controlled cooling system. However, the rate of injection and the consequent reduction heat transfer are no longer dependent first upon the flight conditions and material in the simple manner described for the sublimating system. Ablation cooling includes the effects of pyrolysis, erosion, dissociation, and chemical reactions. Finally, if we consider temperatures high enough, the air ionizes and the thermal conductivity increases orders of magnitude for small temperature intervals.

Because of the extreme complexity of this problem, an empirical approach may be used.

An effective heat of ablation can be defined as the heat transfer rate for the no-blowing case at the actual wall temperature divided by the experimentally determined mass injection. Now, using this definition and considering only sublimation, one obtains the effective heat of sublimation which was defined in Eq. (36a). We have already indicated relationships between f_w and T_w for the sublimation of certain materials (see Fig. 19). For a blunt body it is a simple matter to calculate $T_e(x)$ and $M_e(x)$. This enables us to obtain $H_a(x)$ along the geometry of the body. Such a calculation could then be compared with experimental data and any discrepancies might then account for side effects such as physical erosion, for instance.

REFERENCES

1. Baron, J. R., The Binary-Mixture Boundary Layer Associated with Mass Transfer Cooling at High Speeds, MIT NSL Tech. Rpt. 160, May, 1956.
2. Eckert, E. R. G., P. J. Schneider, and F. Koehler, Mass Transfer Cooling of a Laminar Air Boundary Layer by Injection of a Light Weight Gas, University of Minnesota Heat Transfer Laboratory Technical Report No. 8, April, 1956.
3. Sziklas, E. A., and C. M. Banas, Mass Transfer Cooling in Compressible Laminar Flow, RAND Symposium on Mass-Transfer Cooling for Hypersonic Flight.
4. Eckert, E. R. G., and P. J. Schneider, Diffusion Effects in a Binary Isothermal Boundary Layer, University of Minnesota Heat Transfer Laboratory Technical Report No. 5, November, 1955.
5. Gross, J. F., The Laminar Binary Boundary Layer, The RAND Corporation, Research Memorandum RM-1915, September 1, 1956.
6. Lees, L., Convective Heat Transfer with Mass Addition and Chemical Reactions, Third Combustion and Propulsion Colloquium, AGARD, NATO, Palermo, Sicily, March 17-21, 1958.
7. Low, G. M., The Compressible Boundary Layer with Fluid Injection, NACA TN 3404, March, 1955.
8. Lin, C. C., The Theory of Hydrodynamic Stability, Cambridge University Press, 1956.
9. Covert, E. E., Stability of the Binary Boundary Layer, MIT NSL TR 217, June, 1957.
10. Balekjian, G., and D. L. Koltz, Heat Transfer from Superheated Vapors to a Horizontal Tube, A. I. Ch. E. Journal, March, 1958.
11. Van Driest, E. R., Calculation of the Stability of the Laminar Boundary Layer in a Compressible Fluid on a Flat Plate with Heat Transfer, North American Aviation Aerophysics Laboratory Report AL-1334, September, 1951.
12. Leadon, B. M., C. J. Scott, and G. E. Anderson, Transpiration Cooling of a 20° Porous Cone at M=5, RAND Symposium on Mass-transfer Cooling for Hypersonic Flight.

13. Eckett, E. R. G., and J. P. Hartnett, Mass Transfer Cooling in a Laminar Boundary Layer with Constant Fluid Properties, University of Minnesota Heat Transfer Laboratory Tech. Rpt. No. 4, October 1955.
14. Baron, J. R., The Heterogeneous Laminar Boundary Layer, RAND Symposium on Mass-Transfer Cooling for Hypersonic Flight.
15. Rannie, W. D., A Simplified Theory of Porous Wall Cooling, Prog. Rpt. 4-50, Power Plant Lab. Proj. No. MX801, Jet Prop. Lab., C. I. T., November 24, 1947.
16. Dorrance, W. H., and F. J. Dore, 'The Effects of Mass Transfer on Compressible Turbulent Boundary-Layer Skin-Friction and Heat Transfer,' J. of the Aero. Sci., Vol. 21, No. 6, June 1954.
17. Van Driest, E. R., On Mass Transfer Near the Stagnation Point, RAND Symposium on Mass-Transfer Cooling for Hypersonic Flight.
18. Rubesin, M. W., An Analytical Estimation of the Effect of Transpiration Cooling on the Heat Transfer and Skin-Friction Characteristics of a Compressible, Turbulent Boundary Layer, NACA TN 3341, 1954.
19. Rubesin, M. W., and C. C. Pappas, An Analysis of the Turbulent Boundary-Layer Characteristics on a Flat-Plate with Distributed Height-Gas Injection, NACA TN 4149, February 1958.
20. Mickley, H. S., et al., Heat, Mass, and Momentum Transfer for Flow Over a Flat Plate with Slowing on Suction, Massachusetts Institute of Technology, Cambridge, Mass., September 1952.
21. Leadon, B. M., and C. J. Scott, Measurement of Recovery Factors and Heat Transfer Coefficients with Transpiration Cooling in a Turbulent Boundary Layer at M = 3 Using Air and Helium as Coolants, Rosemount Aero. Lab., University of Minnesota, Tech. Rpt. 126, February 1956.

EQUATIONS FOR A LAMINAR, COMPRESSIBLE
BINARY BOUNDARY LAYER

$$\frac{\partial(\rho u)}{\partial x} + \frac{\partial(\rho v)}{\partial y} = 0 \quad (1)$$

$$\rho \left(u \frac{\partial u}{\partial x} + v \frac{\partial u}{\partial y} \right) = \frac{\partial}{\partial y} \left(u \frac{\partial u}{\partial y} \right) \quad (2)$$

$$\rho c_p \left(u \frac{\partial T}{\partial x} + v \frac{\partial T}{\partial y} \right) = u \left(\frac{\partial u}{\partial y} \right)^2 + \frac{\partial}{\partial y} \left(k \frac{\partial T}{\partial y} \right) + \rho D_{12} \frac{\partial c_1}{\partial y} (h_1 - h_2), \quad (3)$$

$$\rho \left(u \frac{\partial c_1}{\partial x} + v \frac{\partial c_1}{\partial y} \right) = \rho D_{21} \frac{\partial c_1}{\partial y} \quad (4)$$

Figure #1

BINARY-BOUNDARY-LAYER PARAMETERS

$$x_w \approx - \frac{2(\rho v)_w}{\sqrt{c_w} (\rho u)_e} \sqrt{Re_x} \quad (11)$$

$$B^* = \frac{-x_w (\bar{m})^{-0.33}}{2\sqrt{Re_x} c_{H_2O}} \quad (12)$$

$$B^{**} = \frac{-x_w (\bar{m})^{-0.33}}{2\sqrt{Re_x} c_H} \quad (13)$$

$$c_H = \frac{h}{\rho_e u_e c \rho_e} ; \quad \bar{m} = \frac{m}{m_{air}} \quad (14)$$

Figure #2

VARIATION OF LAMINAR HEAT TRANSFER WITH HELIUM INJECTION

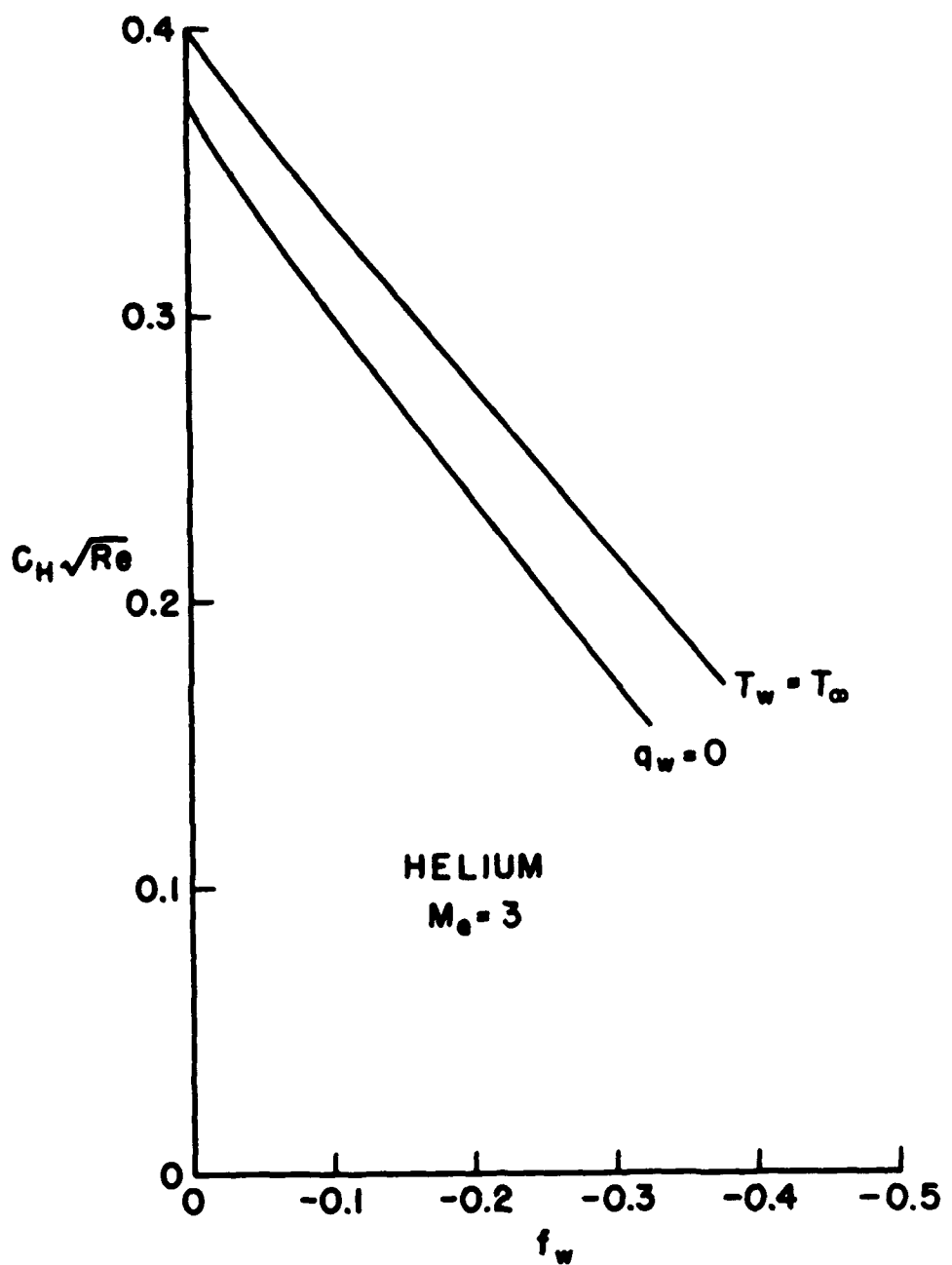


Figure #3

LAMINAR VARIATION OF HEAT TRANSFER WITH HELIUM INJECTION

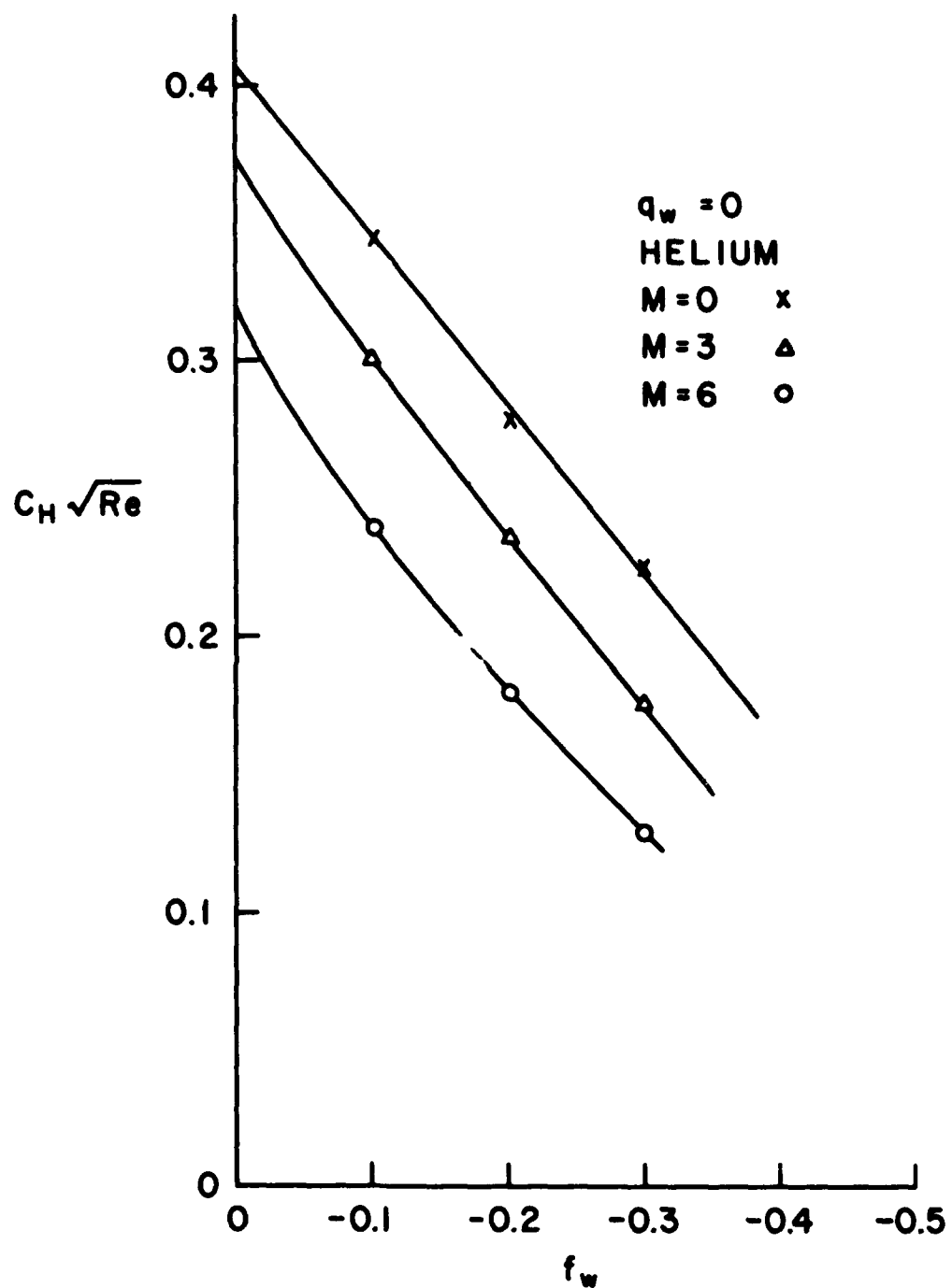


Figure #4

LAMINAR HEAT TRANSFER WITH HELIUM INJECTION

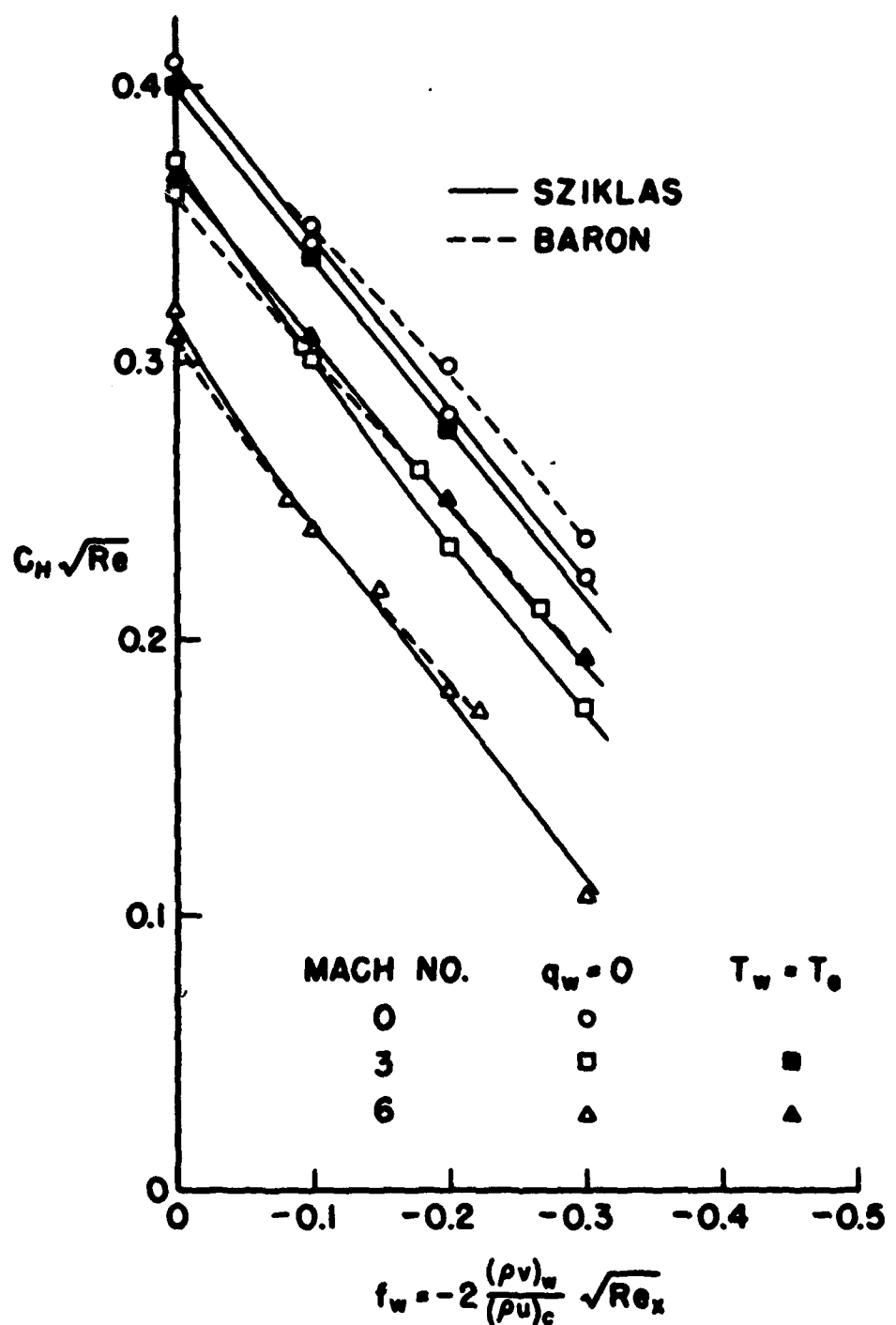


Figure #5

LAMINAR HEAT TRANSFER WITH HELIUM INJECTION

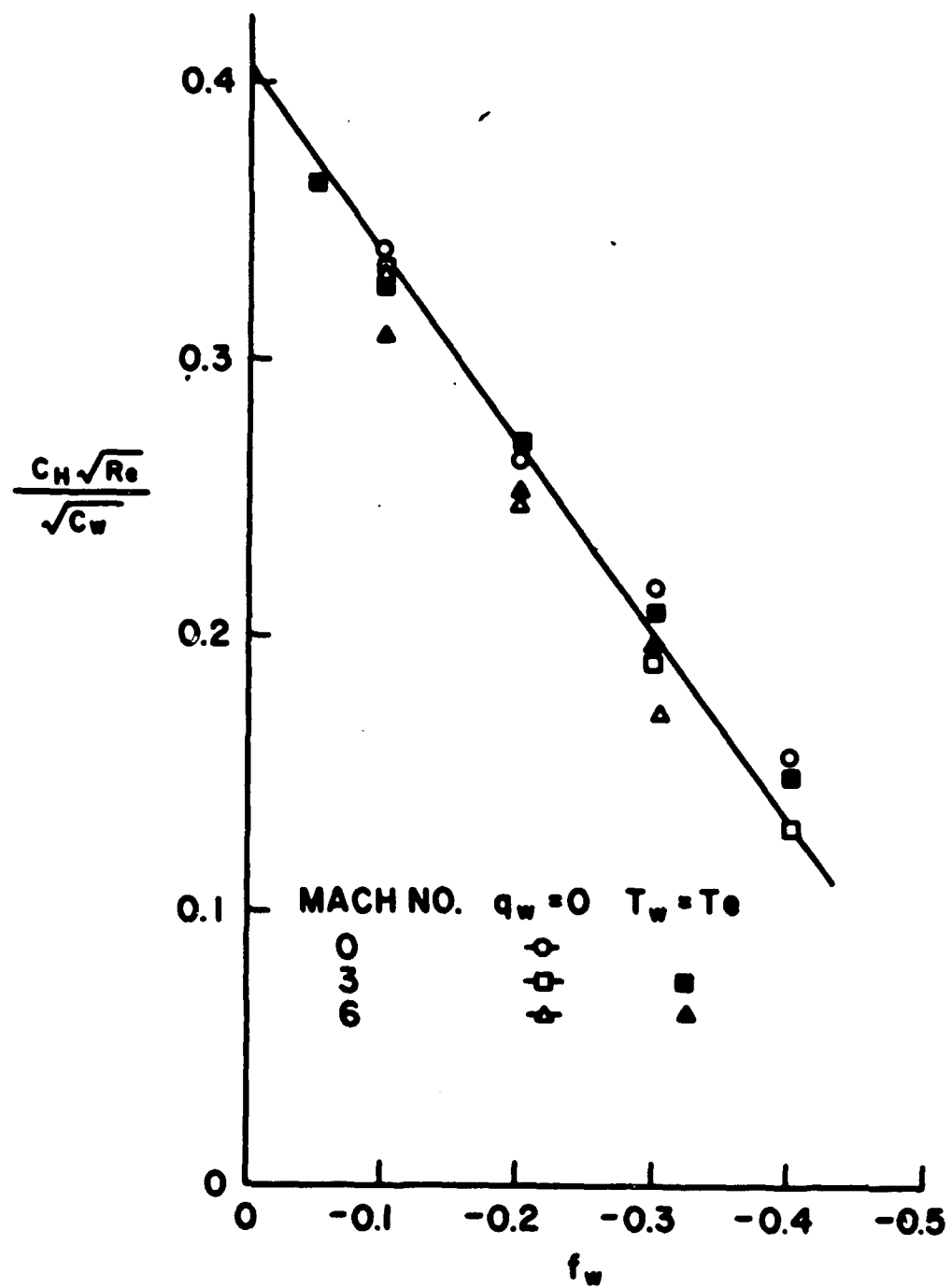


Figure #6

LAMINAR HEAT TRANSFER WITH HELIUM INJECTION

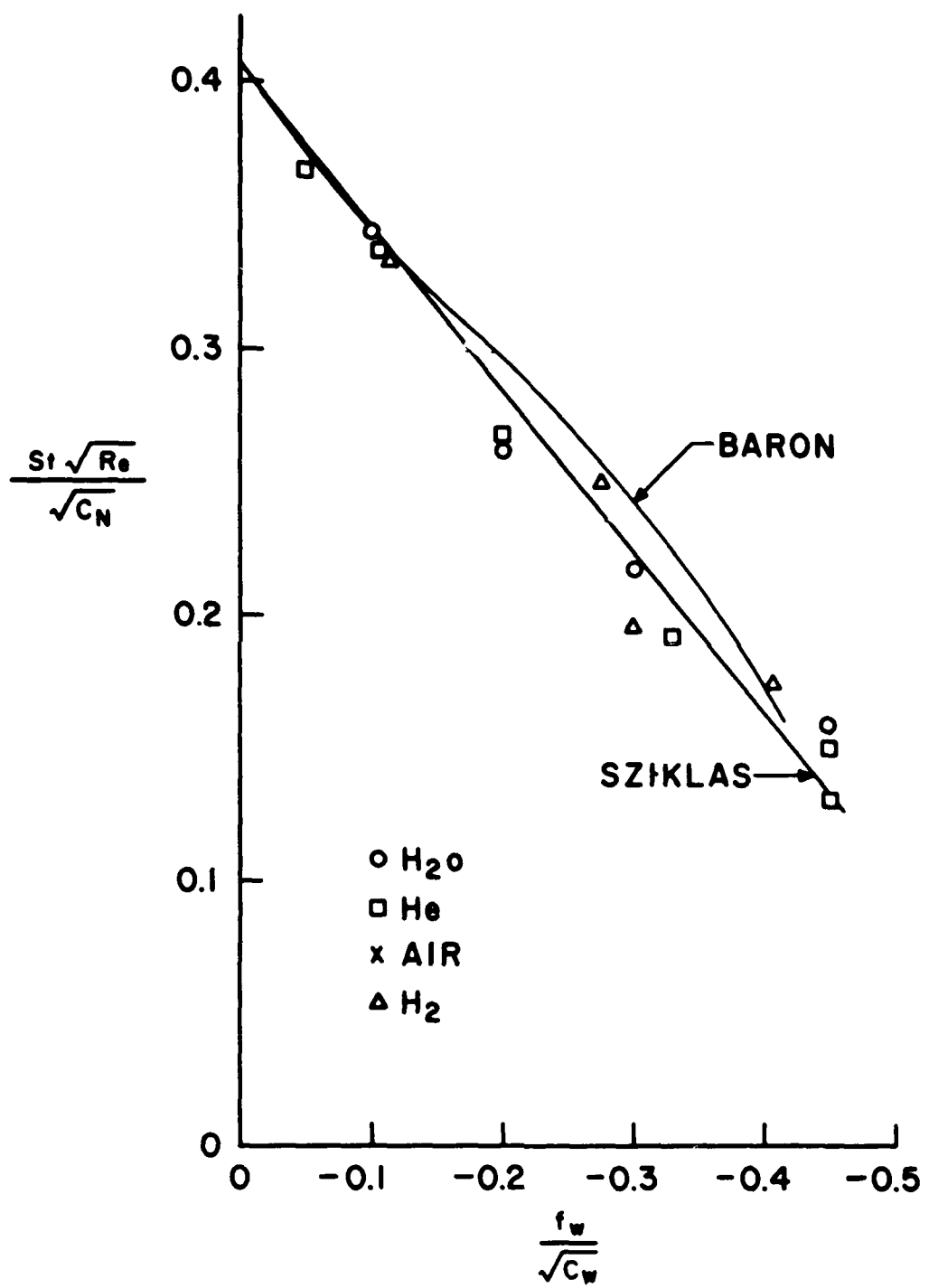


Figure #7

GENERALIZED CORRELATION OF HEAT TRANSFER AND SKIN FRICTION

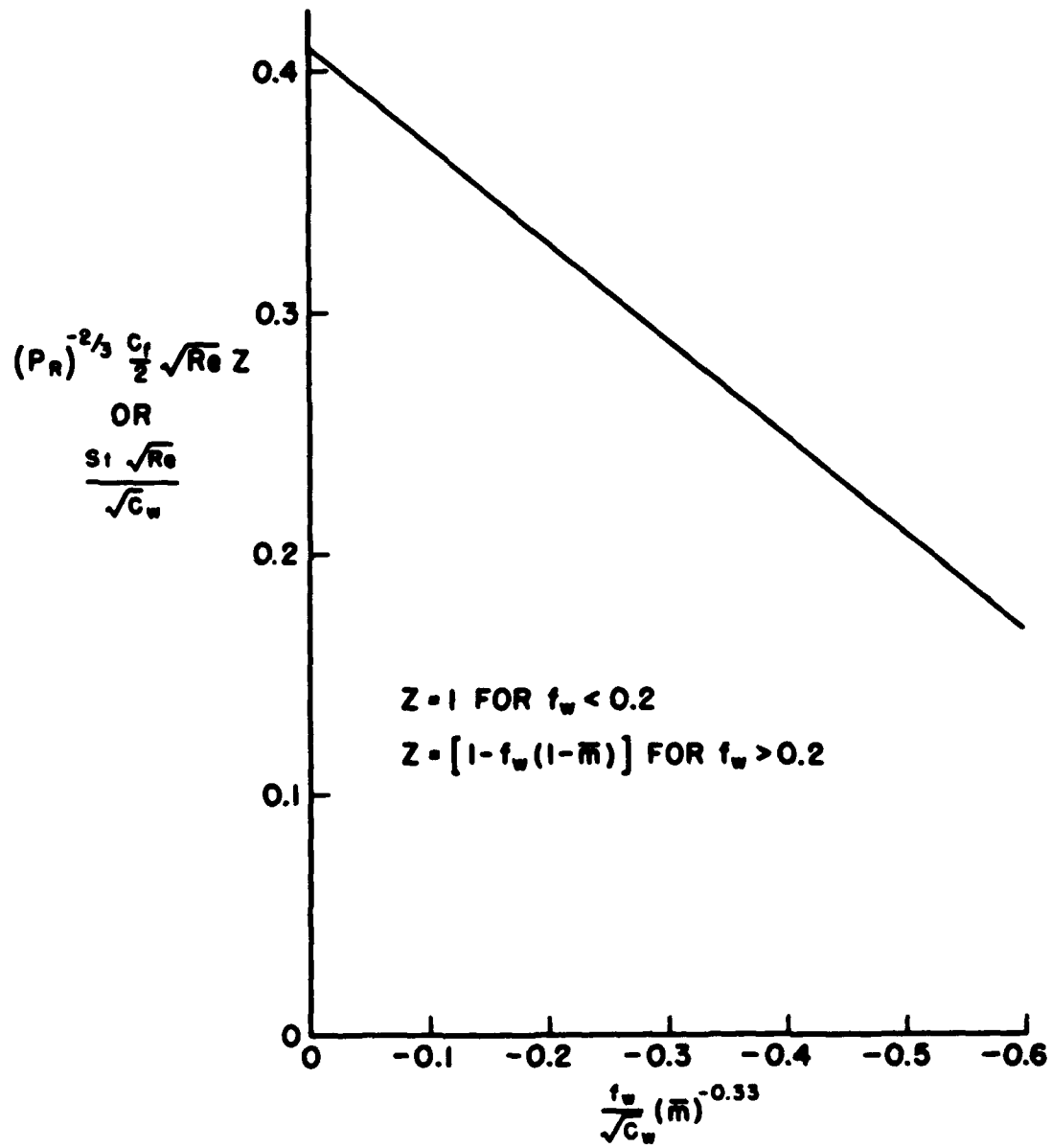


Figure #8

LAMINAR STANTON NUMBER RATIO
WITH MASS TRANSFER

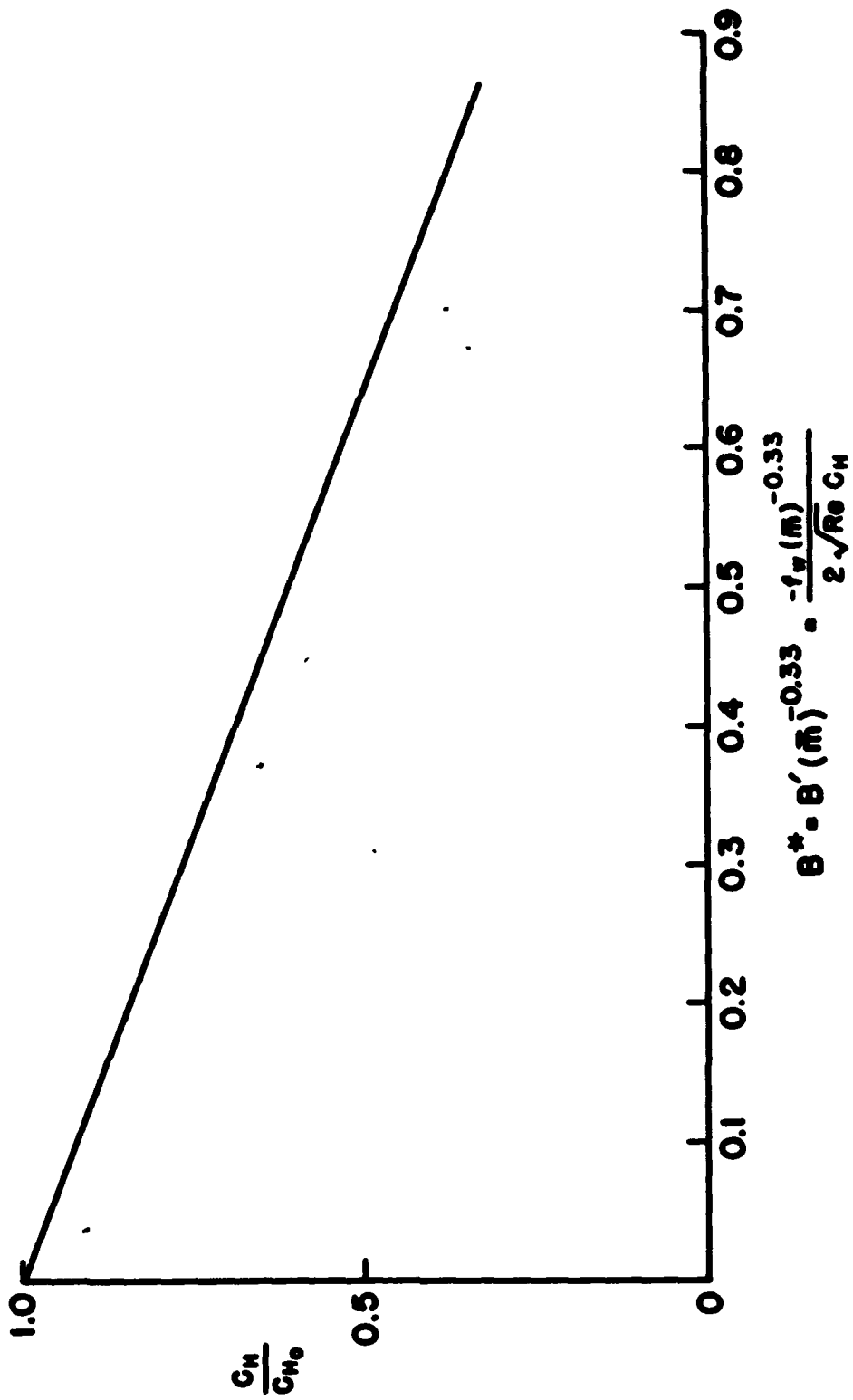


Figure #9

GENERALIZED CORRELATION OF LAMINAR RECOVERY FACTOR

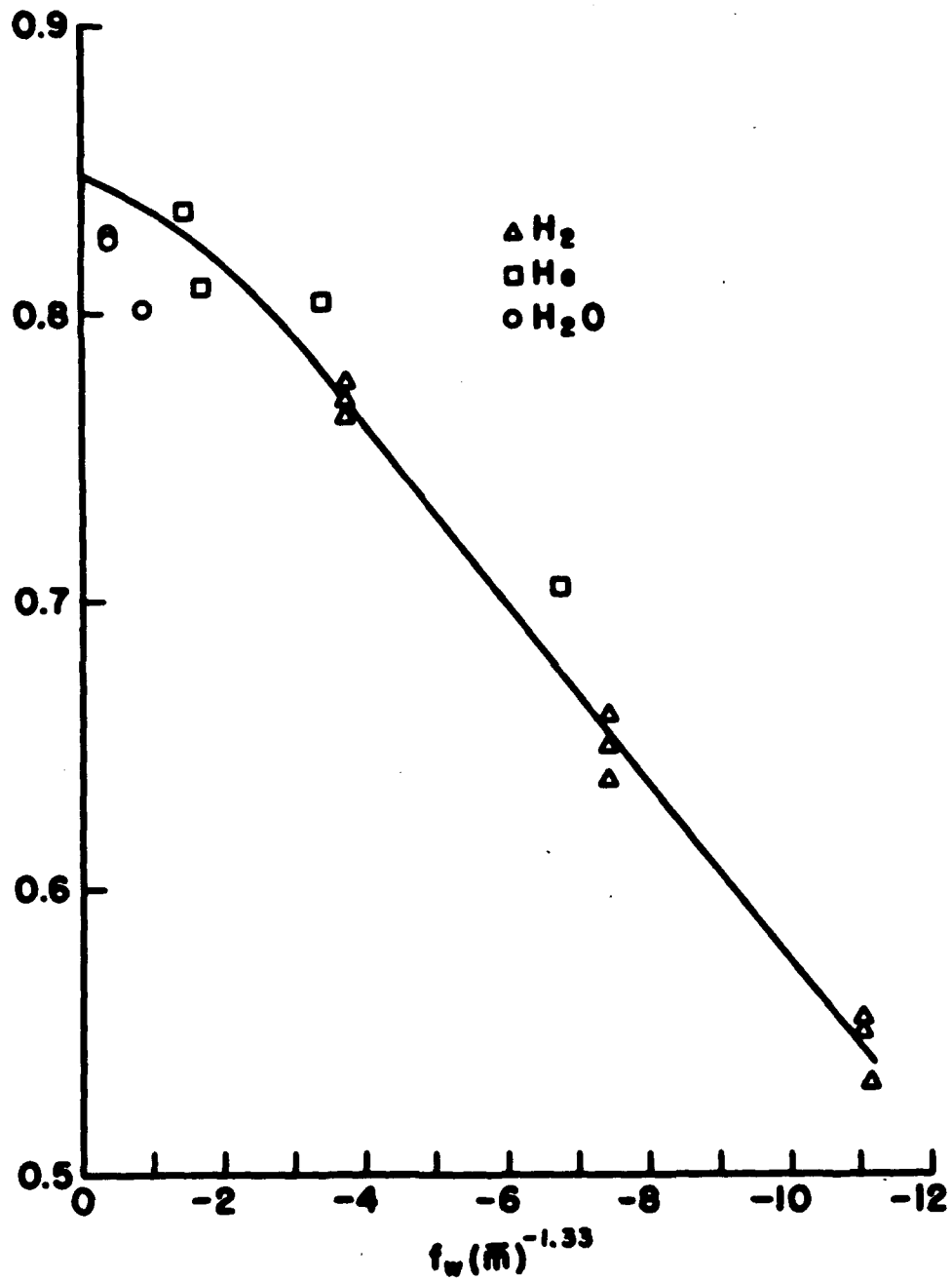


Figure #10

REDUCTION IN LOCAL TURBULENT STANTON
NUMBER DUE TO MASS INJECTION OF AIR

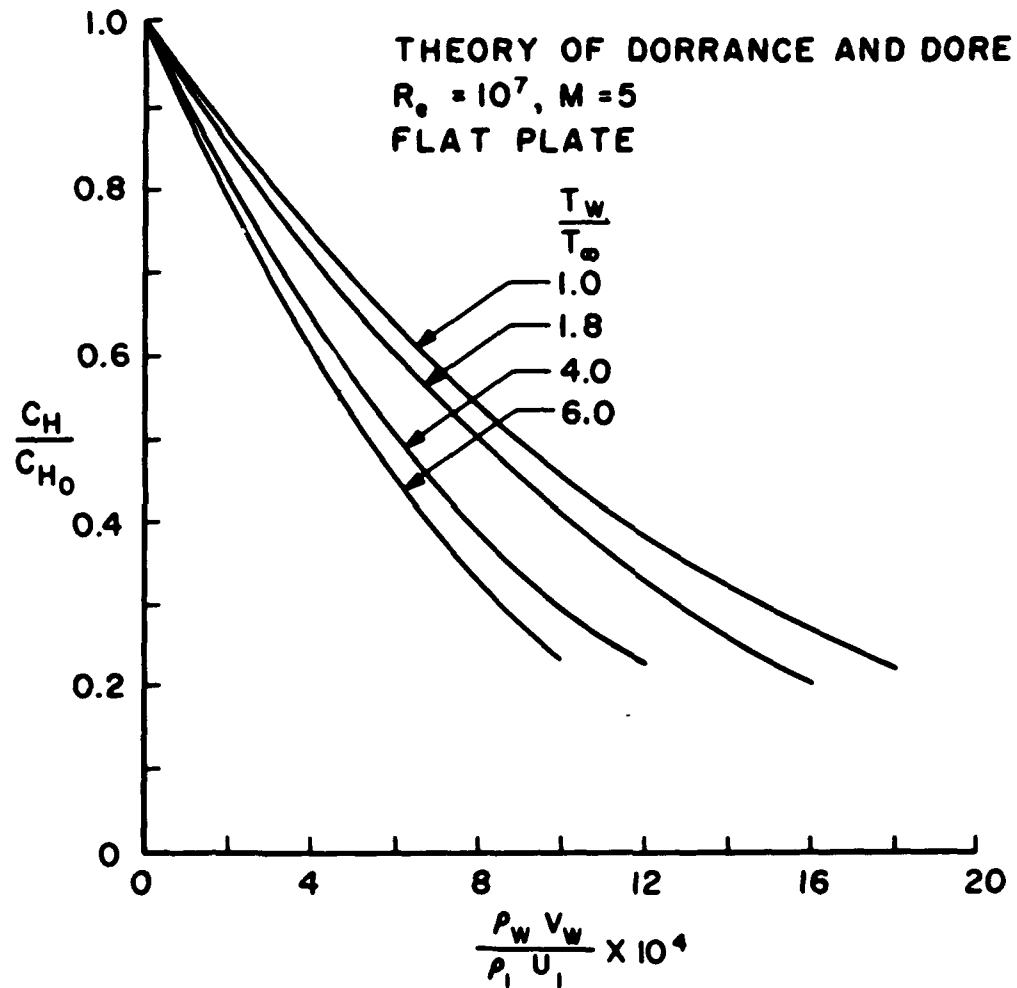


Figure #11

COMPARISON OF REDUCTION IN LOCAL
TURBULENT STANTON NUMBERS FOR
COMPRESSIBLE AND INCOMPRESSIBLE
FLOW DUE TO MASS INJECTION OF AIR

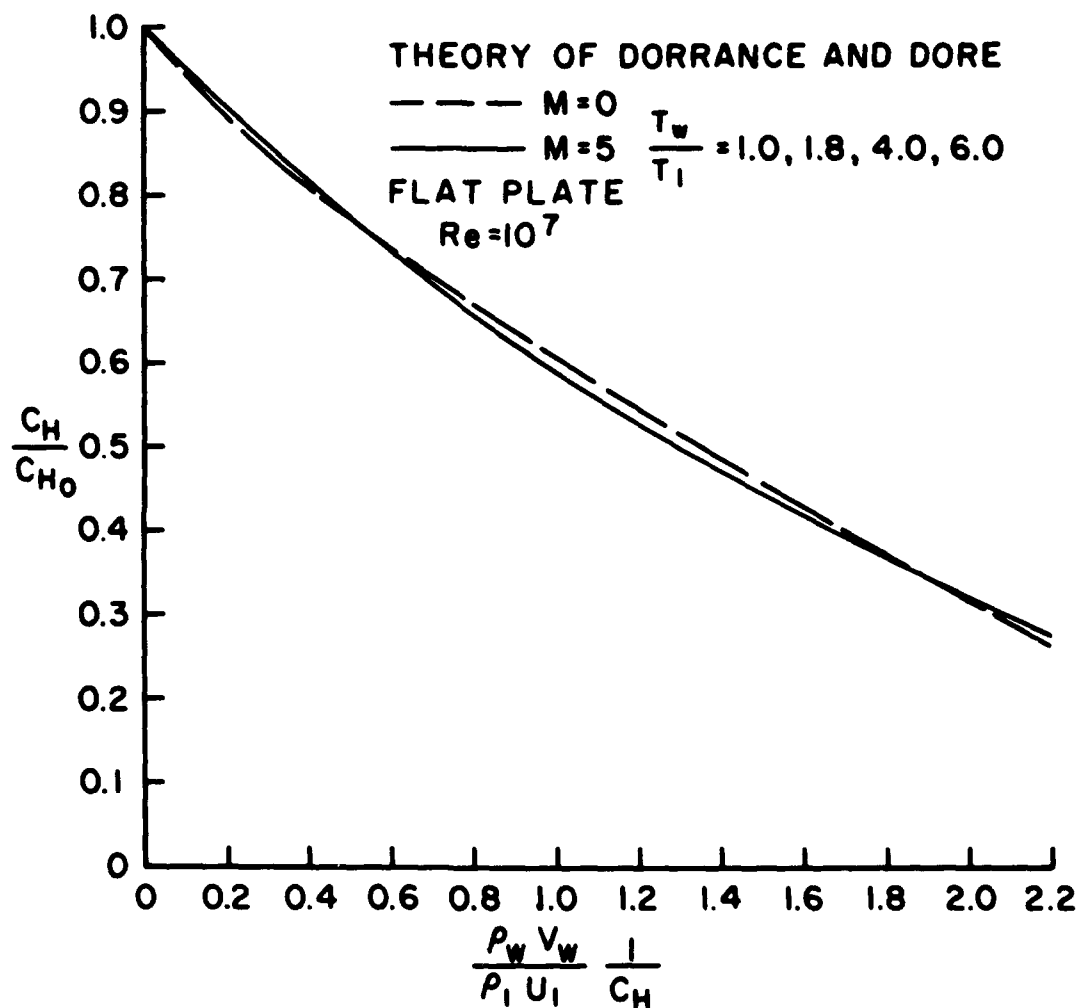


Figure #12

COMPARISON OF REDUCTIONS IN LOCAL TURBULENT
STANTON NUMBERS FOR MASS INJECTION
OF DIFFERENT GASES

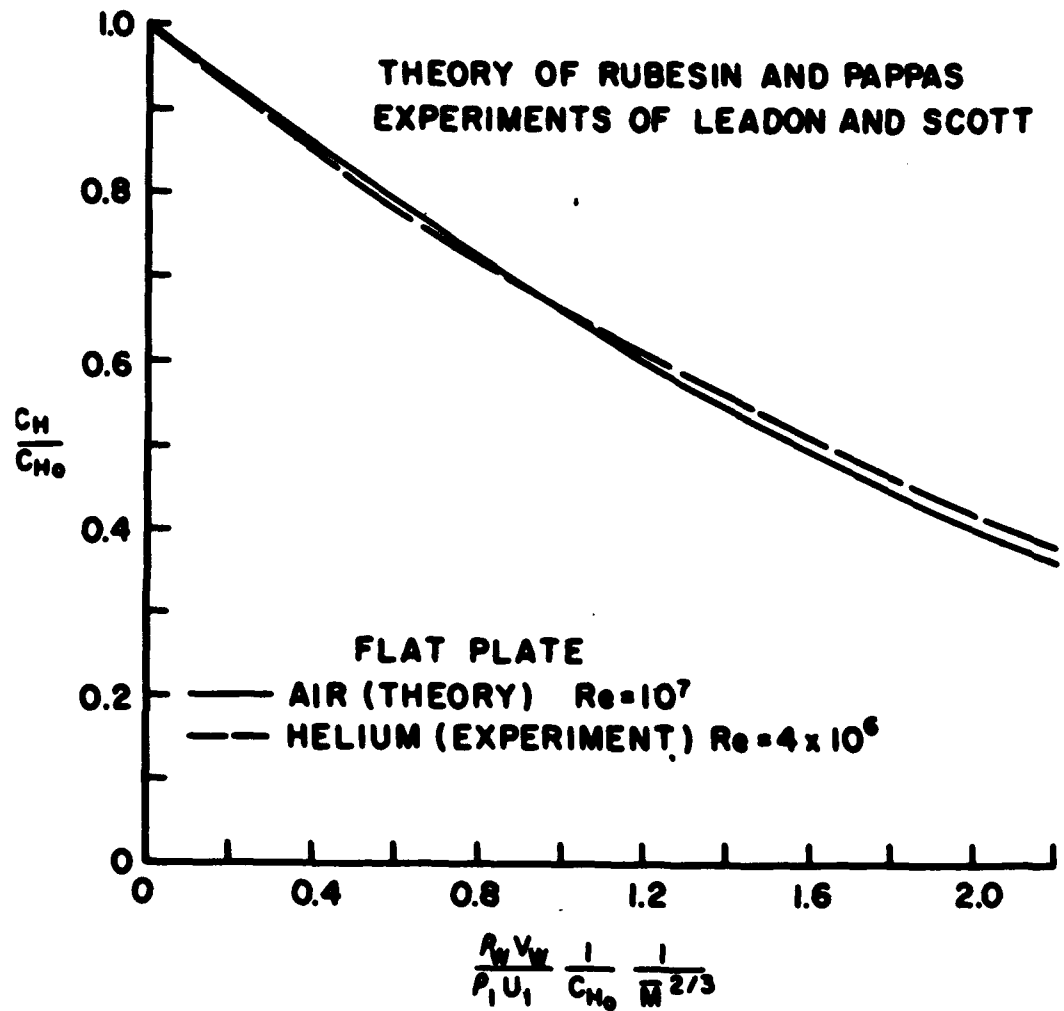


Figure #13

RELATIONSHIPS BETWEEN THE WALL TEMPERATURE AND
THE WALL CONCENTRATION OF THE FOREIGN SUBSTANCE

$$\log p = \frac{A}{T} + k \quad (15)$$

$$\frac{c_{1w}}{\frac{\pi - (\pi - 1)c_{1w}}{c_{1w}}} = e^{\frac{A}{T_w} + k} = e^{\frac{A}{T_w} - \frac{k}{p_e}} \quad (16)$$

$$\rho_{2w}^v = -\rho_w D_{12} \left(\frac{\partial c_2}{\partial y} \right)_w \quad (17)$$

Figure #14

**GENERALIZED EQUATIONS FOR THE LAMINAR,
COMPRESSIBLE BINARY BOUNDARY LAYER**

$$S_t \sqrt{R_e} x = 0.8 \frac{f_w}{(\bar{m})^{1/3}} + 0.407$$

$$r = 0.125 \frac{f_w}{(\bar{m})^{1/3}} + 0.885$$

$$\frac{f_w}{(\bar{m})^{1/3}} + 0.407 \Big] \left(T_e + \left\{ 0.125 \frac{f_w}{(\bar{m})^{1/3}} + 0.885 \right. \right.$$

$$\cdot \frac{\gamma-1}{2} M_e^2 T_e - T$$

Figure #15

GENERALIZED EFFECTIVE HEAT OF SUBLIMATION
LAMINAR FLOW

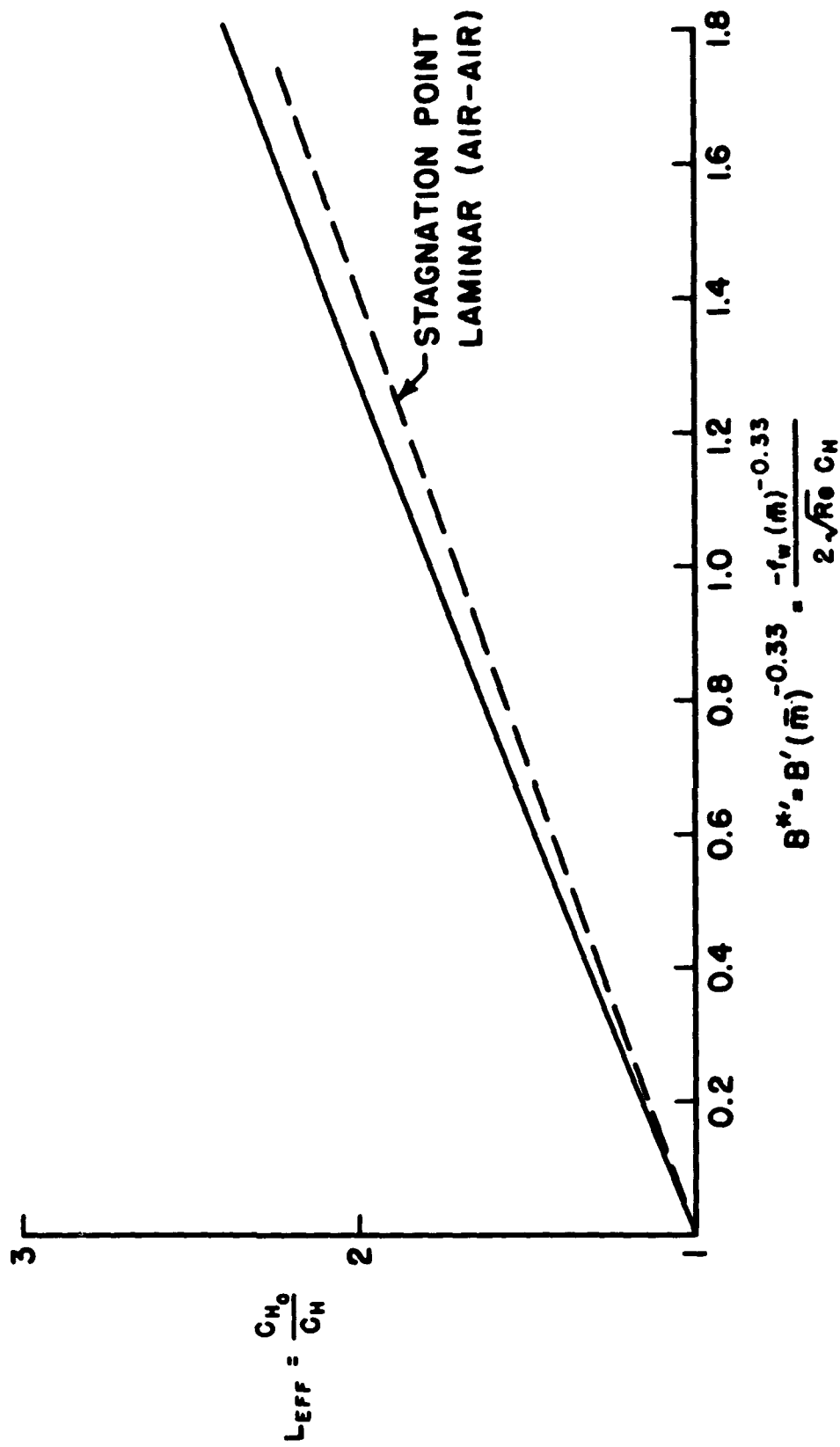


Figure #16

A TECHNIQUE FOR EXPERIMENTAL INVESTIGATION OF HEAT TRANSFER
FROM A SURFACE IN SUPERSONIC FLOW AT LARGE SURFACE-TO-FREE-
STREAM TEMPERATURE RATIOS

W. S. Brattick
Convair Scientific Research

A. R. Hansen
J. J. Scappare
R. E. Larson
University of Minnesota

A TECHNIQUE FOR EXPERIMENTAL INVESTIGATION OF HEAT TRANSFER FROM A SURFACE IN SUPERSONIC FLOW AT LARGE SURFACE-TO-FREE-STREAM TEMPERATURE RATIOS - W. S. Bradfield, A. R. Hanson, J. J. Sheppard, R. E. Larson

INTRODUCTION

The work to be discussed here was supported by OSR from its inception at the University of Minnesota. After Bradfield and Sheppard joined Convair this research was jointly supported by OSR and the Convair Scientific Research Department. The experimental investigations were carried on at the University of Minnesota.

The object of the present investigation was to produce an experimental technique suitable for attacking problems of heat transfer at high surface temperatures and high surface to free stream temperature ratios with the heat flux direction from the surface to the boundary layer in contrast to the usually, but not always, encountered free flight case. In addition, it was desired to produce a technique which would be useful in attacking problems involving chemical surface reactions in high speed boundary layer flows under the circumstances just mentioned.

In doing this we utilized a one inch free jet discharging from a storage vessel which could be charged with helium or nitrogen or any other gas of interest and we used conical graphite heated models. The power for heating was supplied electrically; it was possible to restrict the instrumentation to standard wind tunnel instrumentation with the exception of an optical pyrometer with microscope optics, the latter giving the necessary resolution in surface temperature mapping.

At this stage of the investigation we feel that the apparatus has been checked out satisfactorily. It has been possible to establish a moderately hot surface in a cooling gas stream which is chemically homogeneous and of known composition and to make detailed surface temperature and heat flux and mass loss rate measurements.

Preliminary values of local convective and radiative heat transfer at surface temperatures as high as 3440°R have been determined. Maximum surface temperatures reached in a stagnant inert atmosphere have exceeded 6200°R and in the free jet at Mach number 2.3 have exceeded 4700°R. The maximum heat flux measured to date has been 333 Btu/ft²-sec at a surface temperature of 3300°R. The maximum surface to free stream temperature ratio was 20.

APPARATUS

The small open jet was chosen as a flow producer primarily because it is inexpensive, experimentally flexible, accessible, and easy to instrument. The high temperature of the test surface was expected to predominate the flow situation and so the Mach number of the free stream was considered of relative secondary importance. It was chosen to be 2.3 for air. Conical geometry was chosen for the model because of the symmetry of such a surface with respect to the flow, easy access to model and instrumentation and because such models are comparatively easy to construct. After a comprehensive search, graphite was chosen as the model material because of its favorable chemical, electrical and structural high temperature properties and because those properties are comparatively well established experimentally. Furthermore, graphite is easy to obtain and is easy to fabricate into models.

Figure 1 presents a diagram of the free jet test setup. In the upper left hand corner is shown a storage tank which had a volume of approximately 125 cubic feet and could be pressurized to 250 lbs/in² gage. It was charged with either nitrogen or helium for the present investigations. At the exit

of the storage tank there was a connection from the blowdown wind tunnel dry air supply system into the nozzle which is shown in the center of the diagram. Thus it was possible to supply the jet with either nitrogen, helium or air for these experiments. The nozzle itself was of 1.1" exit diameter and the discharge Mach number was 2.3 with nitrogen and approximately 2.5 with helium. A model is shown as placed in the flow and power connections are indicated schematically with power being taken from the 110 volt line through a powerstat and step-down transformer. The maximum power used during these investigations was less than 5 kw. The flow gases were exhausted through the side wall of the building by means of a bell mouth as shown in the bottom center of Figure 1.

Figure 2 is a view of one of the first model configurations used. In the upper part of the picture is shown a graphite model with a graphite center electrode and, in this particular configuration, a blunted tip. It was found during the early cold blast-erosion tests of graphite that the very sharp tipped cone stood up better under blast erosion than did the rounded tip. Therefore the sharp tip configuration was adopted and used in the later parts of the investigation. The lower portion of Figure 2 shows a section through the graphite model with the threaded tip into which the center electrode fits. The thin portion of the skin is the test section or the region of controlled high temperature for these models. Figure 3 shows the latest model configuration which consists of a graphite skin, a copper center electrode and a stainless steel tip. This particular model failed at a surface temperature someplace between 4000°R and 4500°R and it failed at the thinnest point ($t = 0.007$ inches) of the test section at the rear of the test surface shown typically in Figure 2. The copper center

electrode was used because of its combined characteristics of low electrical resistivity and high thermal reflectivity. A stainless steel tip was used in this case since the different coefficients of thermal expansion for stainless steel and copper permitted the assembly of the model without using special wrenches.

Figure 4 shows the installation of the graphite model at the jet exit. In the right foreground is the jet nozzle with the model mounted on a micro-manipulator and with the heavy current leads attached to the model. Maximum current used in this series of investigations was 350 amps. The bell mouth discharging to the exterior of the building is shown on the left; in the left foreground the Schlieren optical head with the objective lens mount can be seen.

Figure 5 shows a view of the tungsten voltage pickoff probe developed for use in obtaining the detailed surface voltage distribution necessary to permit the determination of local values of heat flux. In the heat transfer determinations reported herein, the control region investigated was not more than 0.2 inch long. The voltage pickoff probe was adjustable not only vertically but also horizontally by means of micrometer barrels one of which is shown in the figure, the other having been attached after the picture was taken. By this means, it was possible to make an accurate determination of position of the tungsten tip of the voltage pickoff probe. With the probe output connected to the electronic voltmeter, it was possible to obtain detailed voltage distributions over the model surface during the heat transfer runs. Knowing what the current flow was to the model it was then possible to obtain values of electrical power dissipated in relatively small segments of the model skin.

Figure 6 shows a typical run setup with the four-man crew in position. The micrometer barrel is seen here to the right center of the picture with the tungsten voltage probe under it, the output being read on the voltmeter shown in the foreground. The gas bottle shown is a helium bottle which permitted a steady flow of helium to be directed into the interior of the model at all times between runs in order to prevent the trapping of oxygen in the interior of the model with subsequent oxidation of the interior surfaces of the model during heated runs.

The method of running for making heat transfer determinations was to set the voltage probe, adjust the optical pyrometer filament on the voltage probe position, start the blast of gas and once flow was established turn on the current, take the temperature and voltage measurements, turn off the current and then turn off the blast. These runs were generally of about 10 seconds in duration, the length of run being dictated primarily by the necessity of changing the position of the voltage probe between runs. To get a complete distribution of voltage axially along the model surface took as many as 15 or 16 runs.

Figure 7 shows a Schlieren color photograph (shown here in black and white) of the model heated in the jet. In this case the model test section boundaries are clearly shown. The maximum model surface temperature for this run was approximately 4000°R and the lip shock seen intersecting the boundary layer and causing local separation was of a strength such that an increase in pressure of 70% occurred across it going downstream. The port hole shown in the darker region of the surface was provided to give access to the interior of the model for purpose of measuring the center electrode temperature in this particular run. The non-uniform distribution of surface

temperature seen here is due to the fact that in the preliminary developmental model runs a straight taper was used in forming the skin. This gives a parabolic resistance distribution axially over the test surface and consequently a non-uniform surface temperature. This situation can be changed simply by using contoured reamers for future models where uniform surface temperature or special distributions are desired.

HEAT FLUX DETERMINATIONS

In order to make heat transfer determinations with this particular set-up, it is necessary to consider heat balance shown as Figure 8. The convective cooling of the test surface shown in Figures 2 and 7 must be determined from the difference between the electrical power dissipated in local segments of skin and the other losses from the selected skin segment. Those losses consist of the heat radiated to the model exterior, the heat radiated to the center electrode, the heat conducted from the ends of the skin element, the heat necessary for any graphite vaporization and the heat of reaction of any reaction between the carbon and the boundary layer gas.

The electrical power dissipated is given by the product of the local voltage drop across the skin segment and the current flow. The heat radiated to the exterior involves knowledge of the total emissivity of the model surface, the angle factor, the surface temperature and environmental temperature. Similarly, the heat radiated to center electrode involves knowledge of the exchange factor, the angle factor, the control surface temperature and the center electrode temperature. In cases when heat conduction is important, it is necessary to know the conductivity of the skin and the axial temperature gradient. The last terms require knowledge of the heat of vaporization and the mass loss rate.

For these measurements, the surface temperature distribution was determined by an optical pyrometer, the voltage distribution by a voltage probe, and the mass loss rate by weighing. Values so obtained together with measured values of model geometry were substituted into the equation shown in Figure 8 to determine the convective cooling rate.

Two physical cases were investigated: one with undisturbed boundary layer, and the other with a shockwave impingement upon the boundary layer.

Figure 9 is a schlieren in a black and white of the unheated and heated flow over a cone model in undisturbed boundary layer flow. In this case the jet lip disturbance has been weakened by adjusting the jet exit pressure so that there is no appreciable disturbance of the boundary layer growth rate in the impingement region.

The lower portion of this figure shows the heated region. For this particular run the test surface temperature was 3440°R. The variation of pressure across the lip disturbance was a net decrease of 0.6 lb/in^2 (going downstream). Since the film was fogged by radiation from the model surface, the unheated surfaces ahead of and behind the heated surface were connected by a solid line and the boundary layer by a dashed line. The thermal boundary layer was increased by a factor of about 70% by the heating.

Figure 10 shows a locally separated boundary layer in both the unheated and heated cases. In this instance the increase in pressure across the lip shock disturbance was 70% (in the downstream direction). Heating resulted in a strong increase in both thickness and extent of separated region as can be seen in the lower picture. The shock impingement region was approximately one inch downstream from the tip of the model, which was inserted into the nozzle about $1/2"$ for these runs.

The temperature distribution for the heated case in Figure 10 is shown as Figure 11. On the abscissa of the plot is shown a cross-section of the model to scale with a copper center electrode in the graphite shell as run. Conditions just outside the boundary layer in this case were Mach number 2.1 with a T_1 of 240°R. The free stream Mach number is 2.3 for this case (nitrogen) and the relation of the model to the nozzle is shown also with the lip shock emanating from the nozzle exit to impinge upon the graphite surface. The control region for this set of calculations was selected as extending from 0.7 inch to 0.9 inch. Checkpoints are seen at the leading and trailing edges on the selected section showing a scatter of about 50 degrees which is within 1% of the surface temperature level.

The heat transfer results are shown in Figure 12. The reference enthalpy method of Eckert¹, was used in calculating theoretical values for comparison with the measured results. In the case of the laminar theory the method of Lighthill² was used for evaluating the surface temperature gradient effect which gave a factor of 1.3 times the constant surface temperature case. In the turbulent case, both the method of Seban³ and that of Rubesin⁴ were used. These methods yielded factors of 1.09 and 1.11 times the constant surface temperature case respectively. For the shock impingement boundary layer, the experimental value of the convective heat flux was 268 Btu/ft²-sec as compared to a predicted laminar value of only 62 Btu/ft²-sec, a factor of about 4.5 times the predicted laminar value and a factor of about 3 times the turbulent value. This is an indication of the strong increase in local convective heat flux which can be expected under the circumstances of a locally separated boundary layer region.

These results are incomplete but they do show a strong effect of heating on boundary layer thickness and they show likewise a strong effect of local boundary layer separation on local values of heat flux. The agreement

of the un-separated laminar boundary layer convective heat flux measurement with laminar theory may be fortuitous at this stage of the investigation and one should be cautious about drawing any general conclusions relative to the applicability of the reference enthalpy method from these data.

SURFACE DETERIORATION STUDIES

Surface deterioration from models operating in an environment such as that just presented could be due to blast erosion, evaporation, chemical reactions or combinations of all three. Early in the program studies were made of cold blast erosion and it was found, using sharp tipped conical models, that cold blast erosion was a negligible problem. In addition to these tests, studies of coatings of Al_2O_3 , Si_3N_4 , and SiC were made in helium and nitrogen and in air. The aluminum oxide and silicon nitride models never progressed beyond the stage of testing with free convection cooling because the coating spalled from the alundum coated model at temperature less than 2500°R , and for the silicon nitride model at a temperature less than 4200°R .

It was possible to make meaningful tests with the silicon carbide coated model in comparison with uncoated graphite models in these gases and the results for air are shown in Figure 13. Two runs of the uncoated model are presented here. The first of these was run at a surface temperature of 2250°R and the second at a considerably higher temperature. The ratio of carbon mass loss to free stream mass flux is $.224 \times 10^{-5}$, and the mass flux parameter proposed by Eckert and Hartnett⁵ is .00291 which

is considerably below the blow-off velocity predicted for either carbon monoxide or carbon dioxide formation.*

The second series of runs was started at 3250°R. The current was held constant throughout the run and the surface temperature increased throughout the run. The pyrometer observer noted a rapid and continuous increase in temperature from 3250 - 4100°R during the 10 seconds of running time. During this period the surface appeared to be sloughing off in waves proceeding from the leading edge to the trailing edge of the test region as viewed through the telescope of the optical pyrometer. The mass loss rate was 500×10^{-5} lbs/ft²-sec, a factor of 10 higher than in the previous run. The mass loss parameter in this case was .0306.*

Run for comparison with the uncoated graphite cone was a silicon carbide coated graphite cone. It was run at 3100°R with constant power. In this case the surface temperature remained constant and the surface remained stable. The surface to free stream temperature ratio was 12; the mass loss rate was 21×10^{-5} lbs/ft²-sec as compared to 500×10^{-5} lbs/ft²-sec for the uncoated graphite cone starting at the same surface temperature, a factor of 25. The mass loss parameter value in the coated case is about .001.

The sum total of the results of the deterioration investigation showed a correlation of increasing mass loss rate with increasing Mach number, surface temperature and oxygen content of the gas for uncoated graphite models, although data points were sparse.

*The blow-off limit proposed was

$$\frac{\dot{m}_c}{\rho_{1u} u_1} \sqrt{\frac{R}{x_1}} = \begin{cases} 0.03 \text{ for } C + O_2 = CO_2 \\ 0.05 \text{ for } C + O = CO \end{cases}$$

Alundum and silicon nitride coatings spalled from graphite models at temperatures of less than 2500 and 4200°R respectively in free convection flow.

Silicon carbide coating of a graphite model slowed mass removal by a factor of almost 25 for the present investigation. A total of 2-1/2 minutes running time at temperatures up to 3500°R was accumulated on this model.

CONCLUSIONS

In summary it may be said that the experimental technique presented provides a surface of controlled moderately high temperature in a flow of homogeneous and chemically determined gas at high speeds.

With this technique it is possible to make detailed temperature and power dissipation surveys over the controlled surface.

Detailed Schlieren studies of processes occurring in the boundary layer at the heated surface under these circumstances may be obtained.

It is possible to determine mass flux rates from small surface areas with comparatively good accuracy.

Thus it is possible to make local heat transfer determinations and mass loss determinations by this technique for comparison with the theories which are available.

The present laminar result shows reasonable correlation with the reference enthalpy method of predicting local values of heat flux but the correlation of this data with the theory must be substantiated by additional

information. The investigation of heat flux in a region of a strong boundary layer shock wave interaction gives values approximately 4.5 times higher than those predicted by the laminar theory.

Surface deterioration studies indicate that a silicon carbide coating on a graphite surface may be a practical inhibitor of surface deterioration at temperatures up to 3200°R in air.

REFERENCES

1. Eckert, E.R.G., "Engineering Relations for Friction and Heat Transfer to Surfaces in High Velocity Flow", *J. Aero. Sc.* 22, August 1955.
2. Lighthill, M. J., "Contributions to the Theory of Heat Transfer Through a Laminar Boundary Layer", *Proc. Roy-Soc. London, Series A*, Vol. 202, 7 August 1950.
3. Scesa, S., "Experimental Investigation of Convective Heat Transfer to Air From a Flat Plate with a Stepwise Discontinuous Surface Temperature", M. S. Thesis, Univ. of Calif., Berkeley, 1949.
4. Rubesin, M. W., "The Effect of an Arbitrary Surface Temperature Variation Along a Flat Plate on the Convective Heat Transfer in an Incompressible Turbulent Boundary Layer", NACA TN 2345, April 1952.
5. Eckert, E.R.G. and Hartnett, J. P., "The Effect of Combustion on Heat Transfer to the Skin of a Vehicle Re-Entering The Atmosphere", *Proc. Rand Symposium on Mass-Transfer Cooling for Hypersonic Flight*, 24 June 1957.

NOMENCLATURE

Symbols

A_s	Control region surface area
A_{xx}	Control region cross sectional area
$\Delta \phi$	Axial voltage drop across skin segment
F_1	Angle factor between external surface of control region and environment
F_2	Angle factor between internal surface of control region and center electrode
ΔH_{vap}	Heat of vaporization per unit mass
ΔH_{reac}	Heat of chemical reaction per unit mass
I	Current
k	Model control region thermal conductivity
\dot{m}	Control region mass loss rate (subscript c indicates carbon)
M	Mach number
\dot{q}	Convective heat transfer rate
R_x	Reynolds number
R_x^*	Reynolds number based on reference enthalpy
t	Model control region skin thickness
T	Temperature
u	Flow velocity parallel to surface
X	Distance from tip along model surface
ϵ_t	Total emissivity of model surface
s^2	Radiation exchange factor between control region surface and model center electrode
ρ	Density
σ	Stefan Boltzmann constant

NOMENCLATURE

Subscripts

- 1 Conditions at outer edge of boundary layer
- 2 Conditions at surface of center electrode
- ∞ Conditions in stream ahead of shock wave
- s Conditions at model surface
- d Downstream of control region segment
- u Upstream of control region segment

FIGURES

1. Diagram of free jet installation.
2. Blunted graphite cone model.
3. Final model configuration (after failure)
4. Installation of model in free jet.
5. Tungsten voltage measuring probe in contact with cone surface.
6. Run setup with crew.
7. Color Schlieren of shock impingement heated run.
8. Heat balance equation.
9. Schlieren of unheated and heated undisturbed flow.
10. Schlieren of unheated and heated shock impingement flow.
11. Surface temperature distribution for shock impingement case.
12. Heat transfer results.
13. Surface deterioration results in air.

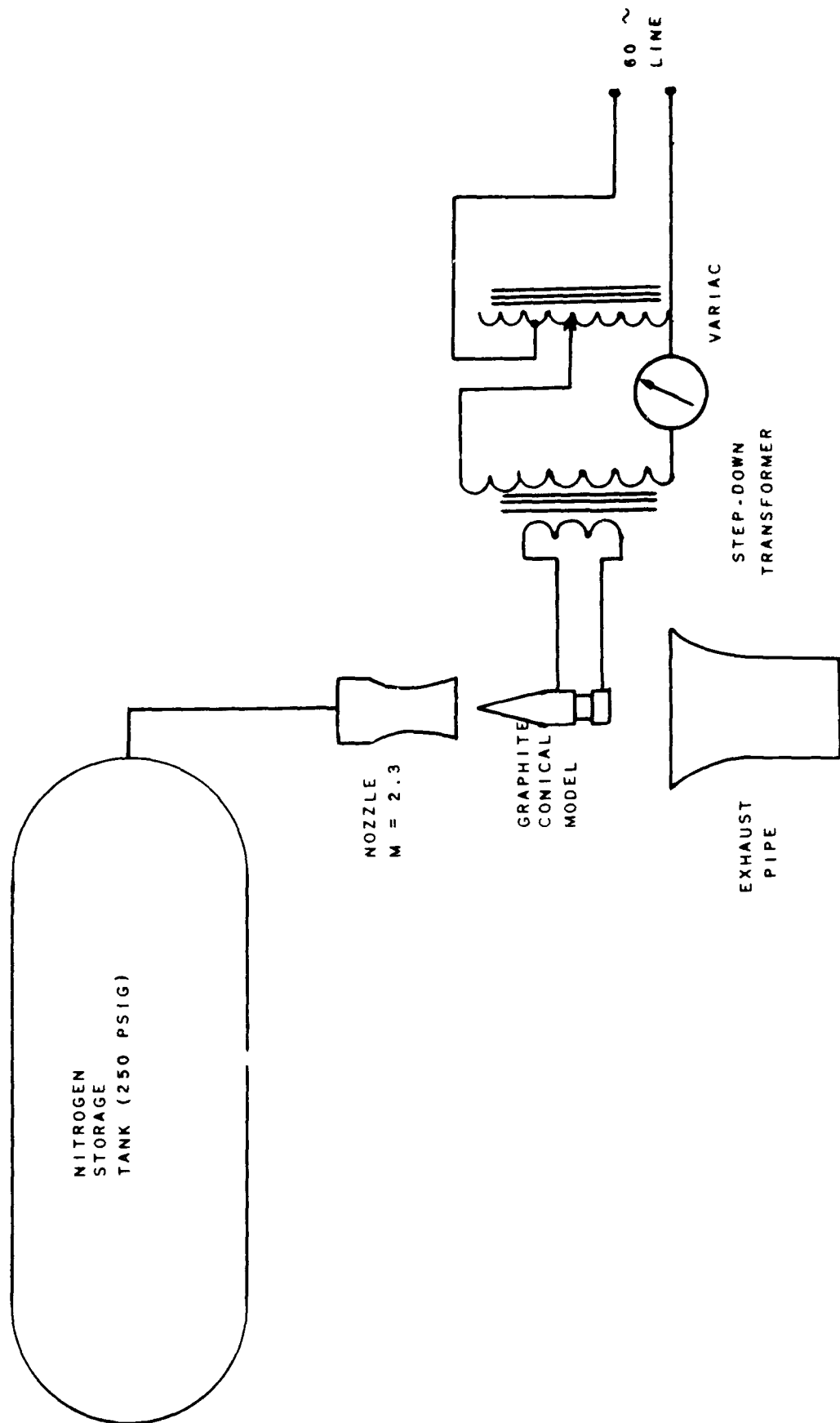


Figure #1

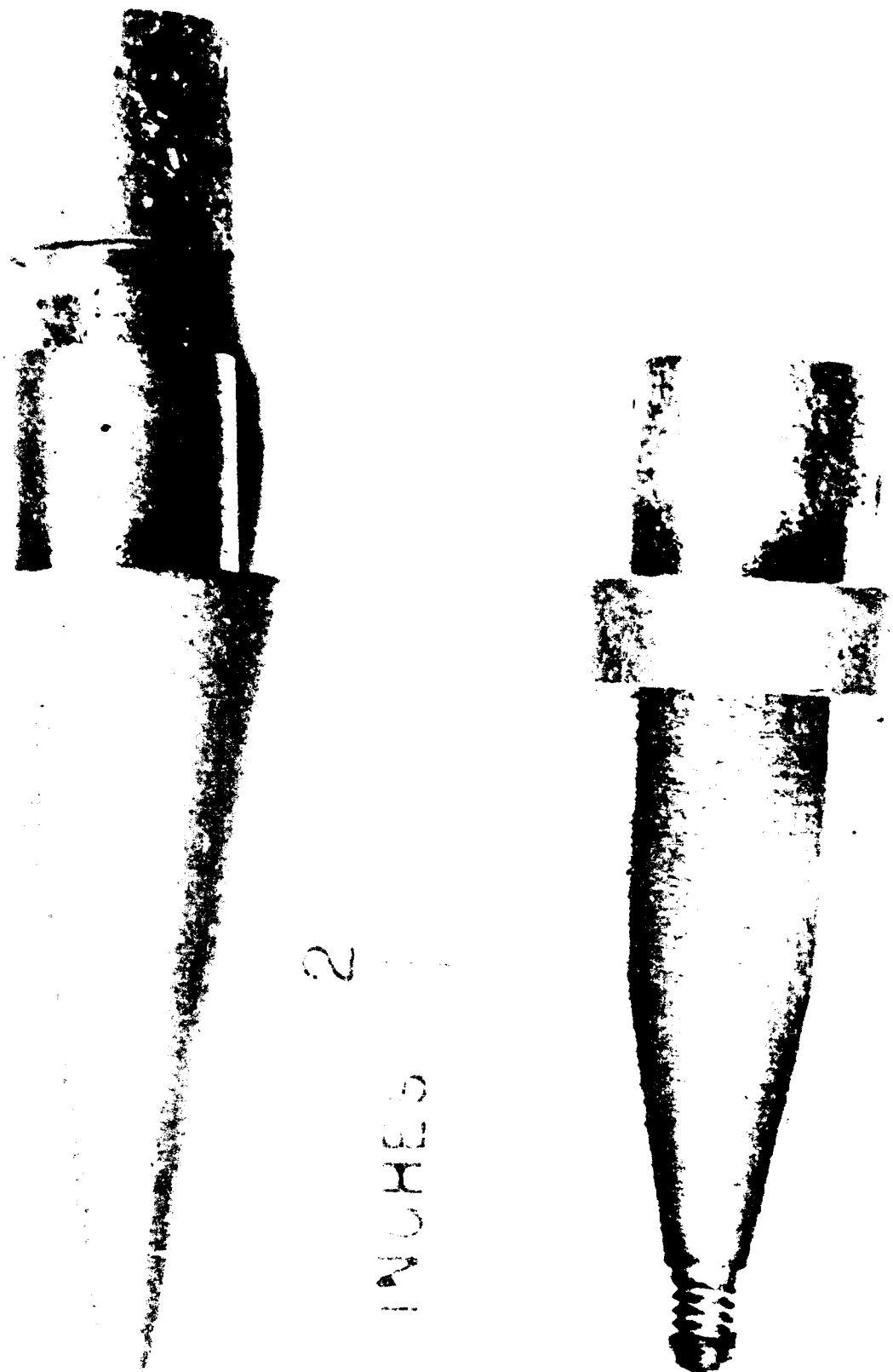


Figure #2

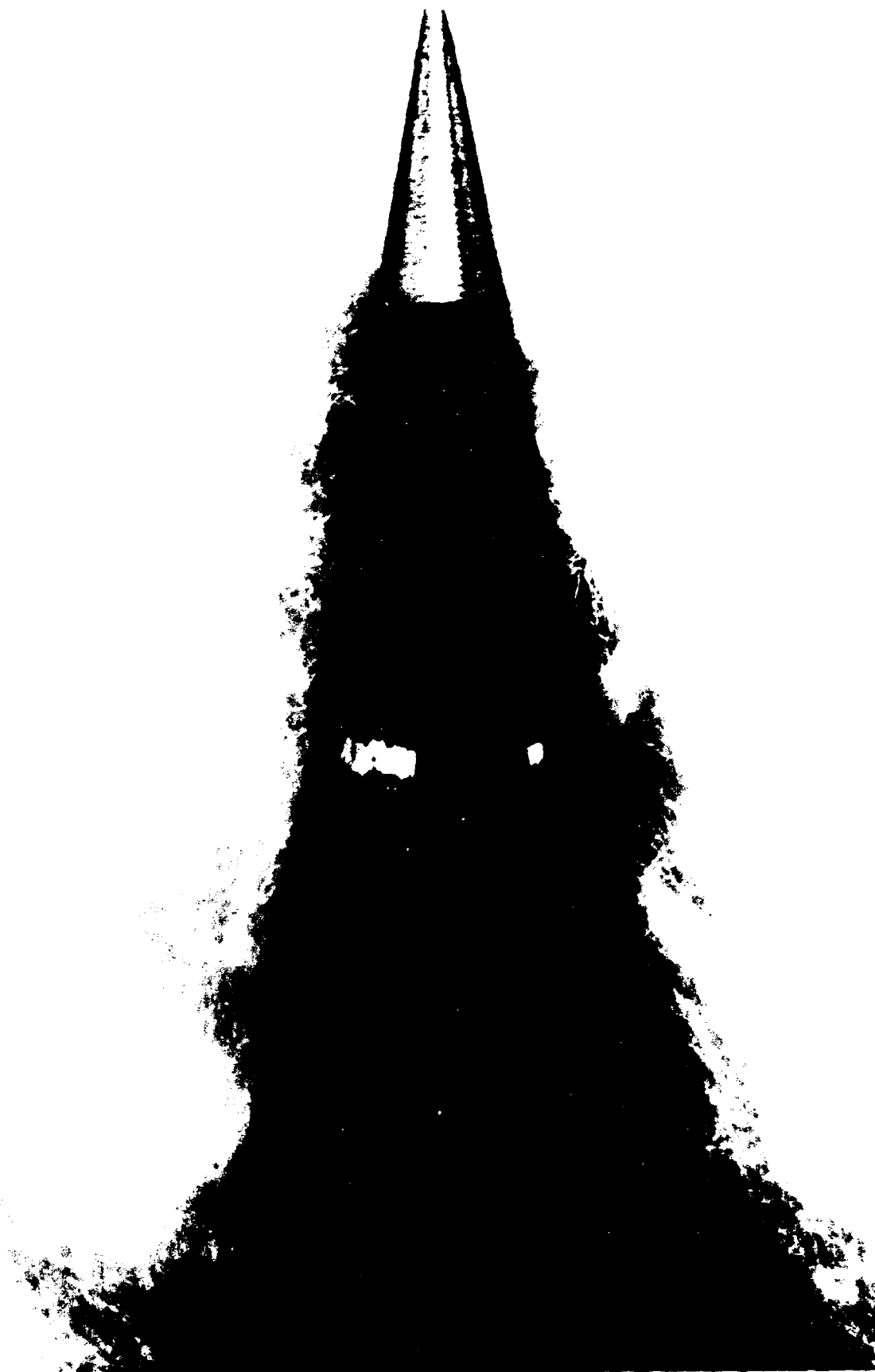


Figure #3



Figure #4

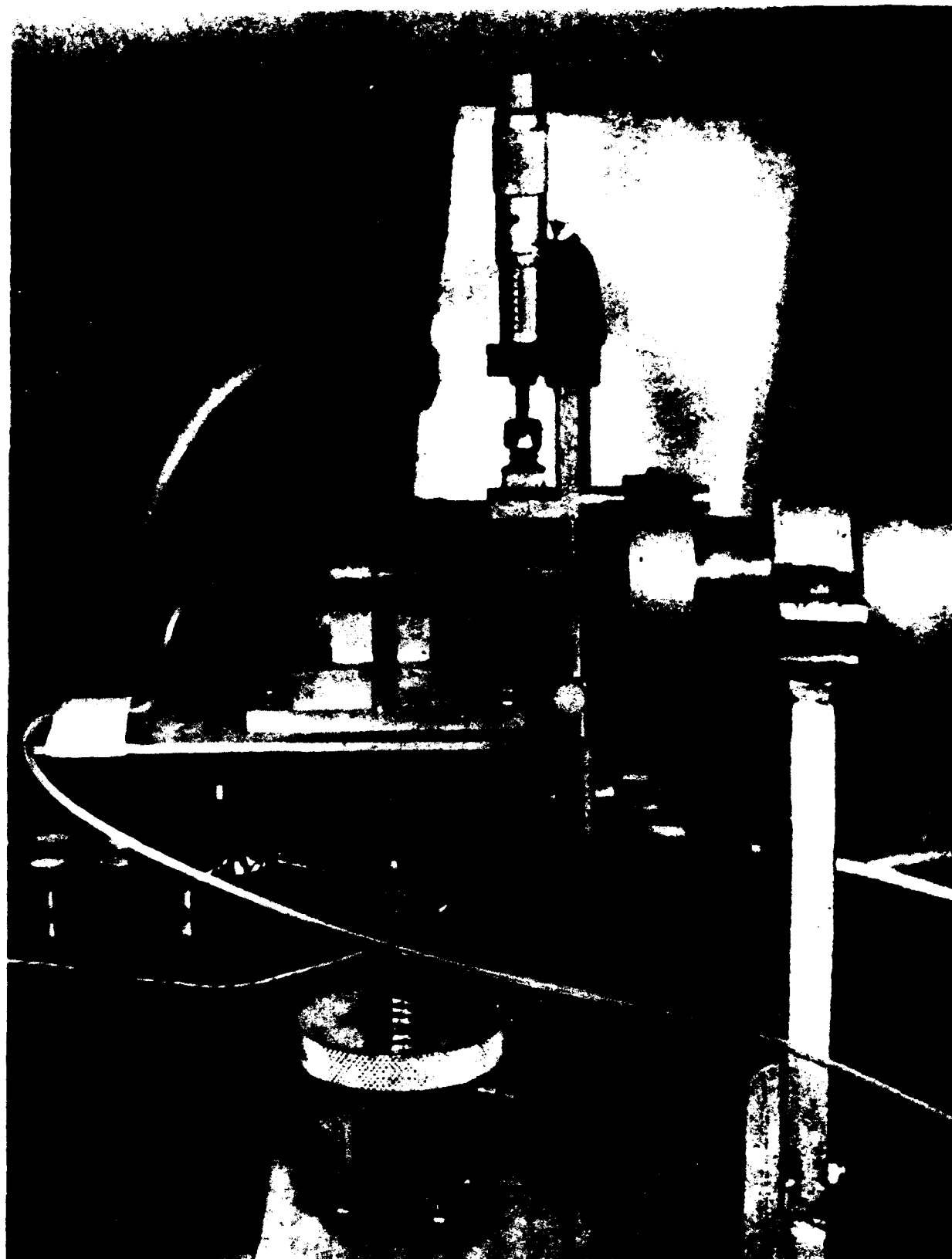


FIGURE 5. TUNGSTEN VOLTAGE MEASURING PROBE IN CONTACT WITH CONDUCTOR.

Figure #5

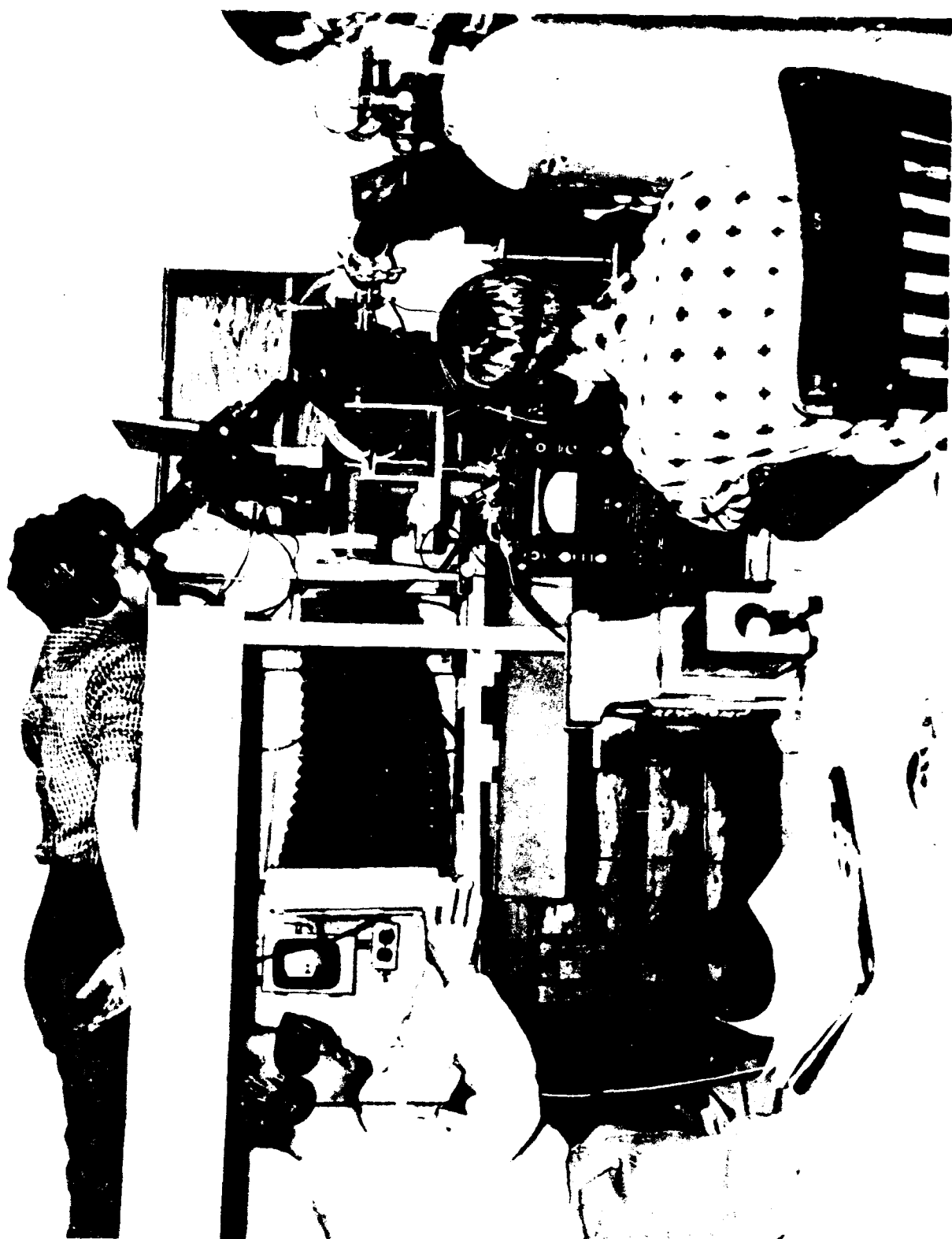


Figure #6



Figure #7

HEAT BALANCE

$$\dot{Q}_{\text{conv.}} A_s = (\Delta e) I - \left[\sigma \varepsilon_e s F_i A_s [T_s^4 - T_i^4] \right]$$

$$+ \sigma_s \varepsilon_2 F_2 A_s [T_s^4 - T_2^4]$$

$$+ \left(K_u \frac{dT}{dx} \right)_u A_{xx_u} + \left(K_d \frac{dT}{dx} \right)_d A_{xx_d} \right] \\ + \Delta H_{\text{vap}} \dot{m} + \Delta H_{\text{REAC.}} \dot{m} \left. \right\}$$

Figure #8

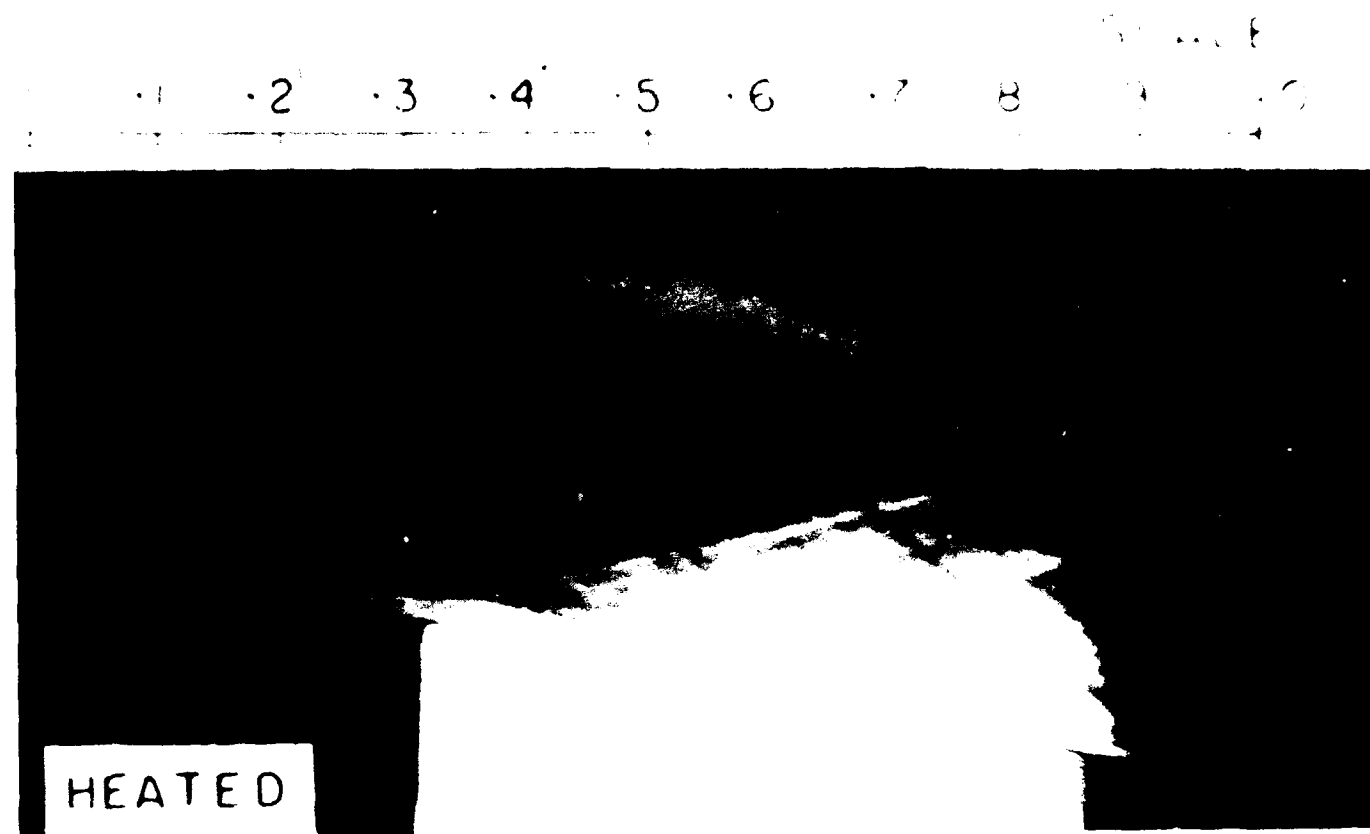


Figure #9



SCALE

0 .1 .2" .3" .4" .5" .6" .7" .8" .9" 1.0"



Figure #10

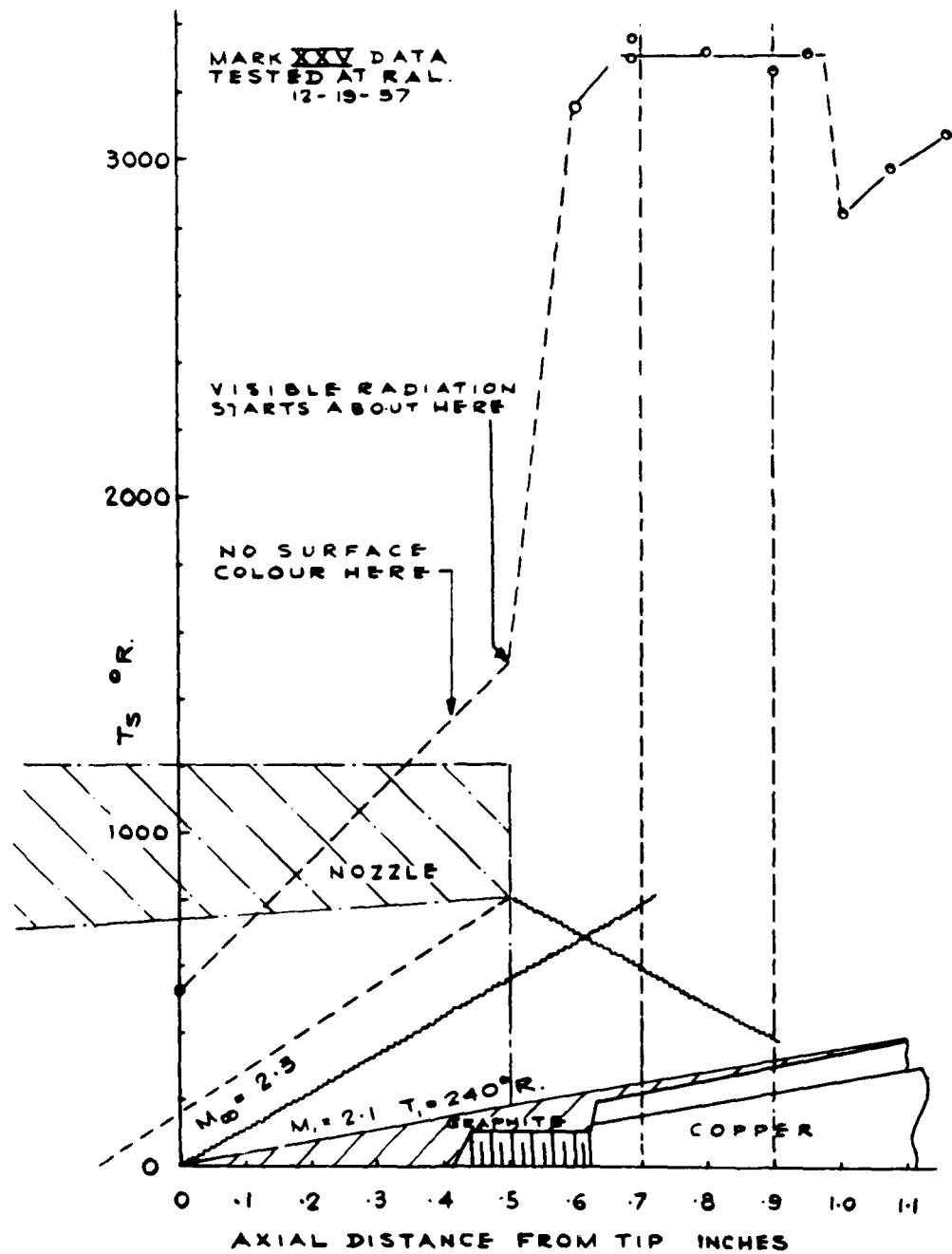


FIGURE 1

Figure #11

HEAT TRANSFER RESULTS

$$M_\infty = 2.3 \quad \text{NITROGEN} \quad \Delta x = 0.1'$$

BOUND'Y LAYER	$R_x \times 10^{-6}$	$R^* \times 10^{-6}$	$T_s - \infty R$	T_s/T_1	$\dot{q}_{\text{CONV.}} - \text{BTU/FT}^2\text{-SEC}$	
					EX.P.	THEORY
LAMINAR	3.05	.112	3440	13.0	123	130
SHOCK IMPINGEMENT	1.80	.055	3300	12.0	268	62

Figure #12

SURFACE DETERIORATION IN AIR

$M_1 = 2.3$ $R_{x_1} = 1.7 \times 10^6$

MATERIAL	T_s OR T_s / T_1	$\dot{m} \times 10^5$ lbm/FT ² SEC	$\dot{m} \times 10^5$ $\rho_{u_1} \sqrt{R_{x_1}}$
GRAPHITE CONE	2250	8.7	48
	3250	12.5	224
	4100	15.8	00291
SiC COATED CONE	3100	12.0	21
			.098 .00127

Figure #13

STRUCTURES

HIGH TEMPERATURE STRUCTURES

N. J. Hoff
Stanford University

HIGH TEMPERATURE STRUCTURES

by N. J. Hoff

Stanford University

INTRODUCTION

If we compare the multiplicity of beams, struts, wire cross bracings, axles and attachments of an early Wright biplane (Fig. 1) whose gross weight was well under a thousand pounds with the smooth monolithic appearance of a ballistic missile (Fig. 2) weighting a few hundred thousand pounds, we begin to wonder whether the relative importance of the structural analyst is not on the wane. The biplane transports and bombers of the early days of aviation consisted of complex girders which had to be analyzed very much in accordance with the procedures used by civil engineers in the design of bridges. The thin-walled reinforced monocoques which succeeded them after 1930 had, and still have, tens of thousands of parts in their skin panels and longitudinal and transverse stiffeners, attached to one another by millions of rivets. The analysis of this complex and highly redundant structure requires the services of several hundred experts in structural or stress analysis.

In contrast a ballistic missile is essentially an assembly of true monocoque shells with a minimum number of reinforcements in locations where concentrated loads have to be transmitted. The questions arise therefore whether it is still necessary to train large numbers of engineers as experts in aircraft and missile structures; if trained, will these men have enough to do in determining the strength of the few and simple structural elements of the missiles of the future; or will they be replaced by a small number of experts in the more erudite (that is more mathematical) phases of theoretical and applied mechanics aided by a few aero-thermodynamicists?

A partial answer to these questions was of course given by the technical committee of this Symposium. Had its members thought that structural problems were unimportant, they would not have invited me to talk about them. A more complete answer can be found if one examines in some detail the structural problems that arise from the new factor in structural behavior, the high temperature caused by aerodynamic heating. A broad survey of these new problems is the major purpose of this paper.

Even before such a survey is presented we should realize that shifts in the importance of various activities are inevitable, and even undesirable, if progress is to be made. For instance, the services of no electrical engineers were needed when the Wright planes were designed. In the development of the transports of the early thirties the effort that went into the design of the electric and electronic equipment was an insignificant part of the total design work. On the other hand, the electronic guidance, control and communication systems of some of the recent missiles are of such complexity and importance that the modern missile designer often wonders whether he is not just an aid to the electronics expert. On this basis we should perhaps investigate whether aeronautical engineers as a group will not soon be replaced by electrical engineers and physicists.

THE NEW LOOK IN AVIATION

With newspapers and technical journals showing photographs of firings of new missiles in almost every issue, it is easy to get the impression that the present-day conventional airplane will be entirely superseded in the near future by conical-cylindrical flying objects which at most will have a few small fins attached to them. This impression is false in

the sense that short-range transport and personal planes are certain to remain relatively unchanged by new developments. They will have to be analyzed by structures men in the future as they had to be in the past.

The major effort in aircraft construction, however, will be in the military field, at least as long as warfare is not eliminated as a means of settling differences of opinion between nations. Thus the majority of engineers working on aircraft structural analysis will have to deal with military airplanes and in particular, with missiles.

Some of the slower missiles do not differ very much from airplanes in their structural arrangement. The very high-speed missiles, however, do not need much in the way of lifting surfaces to keep them flying; their wings degenerate to small fins which are very simple from the structural standpoint. Finally the ballistic missile disposes entirely of wings and often also of aerodynamic control surfaces; it is essentially a cylindrical shell in which are housed the integral fuel and oxidizer tanks, the rocket motors, control and communication equipment and the payload, that is the bomb.

But outside the ballistic missile there are other possible means for flight over long distances. One of them is the boost glider recently advocated by H. Julian Allen (Ref. 1). In Allen's opinion a properly designed vehicle of this kind is competitive with the conventional airplane over ranges of the order of onehalf the circumference of the earth. It is boosted by a chemical rocket to a suitable speed and altitude, the latter being perhaps 100,000 to 200,000 feet, depending upon the prescribed range, and glides from there to its destination. As the wing loading of such a glider cannot be very high (say between 10 and 100 lb. per sq. ft.), the wind is likely to be large and complex structurally. Here again a task awaits the structural analyst.

What the job of the structures man will be in connection with the design of manned satellites, space platforms and vehicles for interplanetary or interstellar travel is yet to be seen. Entirely different problems have to be faced by him in connection with the design of vehicles bringing back passengers from space platforms to the earth.

HIGH TEMPERATURES IN STRUCTURES

As is well known, the new phenomenon that has to be taken into account in the structural design of hypersonic vehicles, is the heating of the surface of the vehicle by the boundary layer of the flow. It is certainly not the duty of the structures man to minimize this heating through suitable aerodynamic design and the choice of an optimal flight path. Aerodynamicists are willing to take care of this problem, and have found, according to Allen, two satisfactory solutions. With the blunt nose of the ballistic missile the drag necessary to decelerate the vehicle is largely form drag and only to a small extent frictional drag. As only the latter is responsible for the aerodynamic heating, most of the kinetic energy is dissipated in the shock wave and heats the air away from the missile. The energy balance is quite different for the boost glider which can operate efficiently only if it has a small form drag. But the flight path of this glider is so chosen that the structure is heated slowly over an extended period of time at high altitudes and is capable of radiating most of the heat energy into empty space.

It is not quite so clear who is responsible for the solution of the next problem, that of the distribution of the heat in the structure. As the details of the heating of the surface depend upon the temperature distribution in the structure, the aerodynamicist cannot carry out the calculations unaided by persons who know about the design of the structure. The interaction between the properties of the boundary layer and those of the structure necessitates a

collaboration between aerodynamicists and structures men. Both of them have to learn a great deal about thermodynamics or else they cannot solve their common problems.

Once in the structure, the heat begins to flow toward regions of lower temperature. The laws governing this flow have been studied by thermodynamicists for almost 150 years. Many of the details of the heat transfer process in an airplane or missile structure however, differ to such an extent from those to which heat transfer experts in the field of heat exchangers are accustomed, that either these experts must study airplane structures, or the airplane structures men must learn the fundamentals of thermodynamics before either one can calculate efficiently the temperature distribution in the structure.

The best-known mode of heat transfer is heat conduction. This alone was considered in a calculation of the temperature distribution in a shear web which I published seven years ago (Ref. 2). The results are shown in Fig. 3. The shear web was part of a multiweb supersonic wing (Fig. 4) suddenly accelerated to $M = 3.1$ at an elevation of 50,000 ft. Figure 3 shows that the two edges of the web (at 0 and 9 ins.) are heated up rapidly to the adiabatic wall temperature of 600° F while the temperature of the middle of the web (at 4.5 in.) lags behind.

The analysis was carried out with the aid of a number of assumptions, one of which, at least, can be eliminated if the structures man is willing to use more complex mathematics (see Ref. 3). There remain, however, a number of assumptions which can be replaced only if a better understanding of the physical phenomena and better methods of analysis become available.

First among them is the assumption that no heat is transmitted through the interior of the wing by convection. A rough estimate made in Ref. 2 indicated that the total heat transferred by convection was of the same order of magnitude as that transferred by conduction. It is important therefore that methods be developed for the analysis of this phase of the heat transfer problem.

A second simplification in the original analysis was the omission of the heating of the shear web by radiation from the hotter coverplates. Radiation is governed by the Stefan-Boltzman law which can be written for a perfectly black body in the approximate form

$$q = (1/2) (T/1000)^4 \quad (1)$$

where T is the temperature of the body in $^{\circ}$ R and q is the heat emitted in BTU per square foot per second.

Because of the fourth-power law, radiation must play a significant role in heat transfer at high temperatures, even if it is unimportant at low temperatures. This was confirmed by a simple analysis published in 1956 (Ref. 4). In one set of calculations it was assumed that conduction was absent and heat was transferred only by radiation. This analysis yielded a practically uniform temperature distribution over the web of a multiweb wing in which the distance between the webs was twice the depth of the web. Next radiation was disregarded and heat transfer by conduction alone was taken into account. This, of course, resulted in entirely non-uniform web temperatures. The total heat gained by the web through the two separate and independent processes was then compared. The results are presented in Table 1 in which the average web temperature is given for a steel web of

0.0625 in. thickness when the distance between coverplates is 8 in., the initial temperature of the structure is -60° F, and the coverplates are suddenly heated to and subsequently maintained at the constant temperature T_c .

According to the table, the crossing over point is at about 830° F; if the sudden increase in the coverplate temperature is less than this value, conduction is more important than radiation while the opposite is true when the increase is greater than 830° F.

TABLE I
Comparison of Heating by Conduction
and by Radiation

Jump in coverplate temperature: T_c $^{\circ}$ F	340	540	740	940	1140	1340
Time of heating t min.	8.51	4.87	3.04	2.02	1.4	1.015
T_{ave} $^{\circ}$ F radiation only	200	300	400	500	600	700
T_{ave} $^{\circ}$ F conduction only	264	361	390	412	419	418

Perhaps it is even more important to notice that the average increase in web temperature because of radiation alone is as high as three-quarters of that caused by conduction alone when the coverplate temperature is only 340° F. This indicates that the effect of radiation is practically never negligible if the emissivity of the surfaces is close to unity and if the space between the coverplates is not filled with opaque material.

The fact that much heat is transferred by radiation is a nuisance to the analyst since the Stefan-Boltzman law adds a nonlinear term to the differential equation governing heat transfer. Consequently analytical solutions of the

complete problem of heat transfer by simultaneous conduction, radiation and convection in a structure do not appear feasible. Fortunately finite difference methods are capable of yielding solutions, particularly if large electronic computers are available. Such methods are particularly useful when the structure has to be treated essentially as it is, that is without any substantial idealization. For complex shapes rigorous solutions have not yet been found even in the case of pure conduction.

An added complication arises from the resistance of structural joints to the transfer of heat. Barzilay (Ref. 5) has investigated this problem, but a complete understanding of the phenomenon is not yet forthcoming.

THERMAL STRESSES AND THERMAL BUCKLING

This history of the analysis of thermal stresses also dates back more than a hundred years. Fortunately for the structural analyst the fundamental physical facts are well understood in this case and the mathematical apparatus is available. The computations of course may become tedious if the structure is complicated and if inelastic strains develop during the heating, or during a simultaneous heating and loading process.

The simplest problem, and at the same time one of considerable practical significance, is that of a very long multiweb wing in which the temperature is constant through the wall thickness and in the spanwise direction. In consequence of the variable temperatures, as shown for instance in Fig. 3, the individual spanwise fibers would like to elongate unevenly. They cannot do so because plane sections perpendicular to the spanwise direction before heating must remain plane after heating. The pull exerted by the warmer fibers on the colder ones and the compression caused by the colder fibers in the warmer ones represent a state of thermal stress that can be easily calculated.

Let us assume that the stress is given by

$$\sigma^* = -\alpha E(T - T_i) \quad (2)$$

where α is the coefficient of thermal expansion (strain per $^{\circ}$ F), E is Young's modulus of elasticity (lb. per sq. in.), T is the temperature after heating and T_i is the initial uniform temperature before heating (both in $^{\circ}$ F). A negative stress is a compressive stress. It is easy to see that these stresses just compensate for the thermal expansion because the strain σ^*/E caused by them is equal and opposite to the strain $(T - T_i)$ caused by the heating.

The stress σ_{th}^* would actually prevail in a long web if the end sections of the web were not allowed to move because they were attached to rigid walls. The modulus E multiplied by the area under the temperature curve would be the reaction exerted by the walls on the long shear web. If in reality the ends of the web are free, no such reaction force can exist. This end condition can be satisfied if the average of σ_{th}^* is subtracted from σ_{th}^* . In this manner one obtains

$$\sigma_{th} = \alpha E(T - T_i) = \int_{-b}^b \alpha E(T - T_i) dy \quad (3)$$

where y is the direction of the depth of the web and $2b$ is the total depth.

This is actually the thermal stress in the major portion of the web. In the immediate vicinity of the end sections deviations must occur from this pattern because only the average stress vanishes there but not the stress in every point of the end section. The remaining stresses of the analysis are self-balancing. In view of St. Venant's theorem their effect can extend only over a limited region.

The exact calculation of these disturbance stresses is in principle rather difficult. Fortunately a set of orthogonal functions was derived recently by Horvay (Ref. 6) which reduces the task to operations not more difficult than multiplication and addition. An earlier experimental and theoretical study of the problem is due to Heldenfels and Roberts (Ref. 7). The two methods were compared and extended to apply to plates of variable thickness by Josef Singer (Ref. 8), a doctoral student of the writer at the Polytechnic Institute of Brooklyn. A useful result obtained by Singer is that deviations from the simple pattern of Eq. 3 are significant only in a region extending from the free end of the shear web over a distance equal to the depth $2b$ of the web.

The magnitude of the thermal stresses so calculated is considerable. If the restraining effect of the coverplates is disregarded, Young's modulus is taken as 29×10^6 psi and the coefficient of thermal expansion as 6.5×10^{-6} per $^{\circ}\text{F}$, the curves of Fig. 3 yield maximum thermal stresses of about 35,000, 54,000, 50,000 and 40,000 psi after 50, 100, 200, and 400 sec. of heating, respectively (see Ref. 2). What is the effect of these high thermal stresses?

If the temperature is high enough, the thermal stresses are likely to cause yielding. This is particularly true if external loads are applied at the same time. In an actual missile or supersonic airplane high heating rates and high loadings are likely to occur simultaneously. The yielding is useful because it prevents the thermal stresses from increasing too rapidly; it is not very likely with structural steel or aluminum alloys that the limit of ductility of the metal is exceeded. The situation is quite different when refractories are used as the material of structural elements at high temperature. In these, thermal stresses may cause fracture.

With ductile materials the danger is one of buckling. Figure 5 is a photograph of a sheet steel model of a wing heated in 100 sec. to a temperature of 1100° F in the 20 KW induction heater of the Polytechnic Institute of Brooklyn. As only the coverplates are heated by induction and the web receives no heat except by conduction from the coverplates if the inside of the box girder is filled with insulating material, the coverplate is essentially in compression while the web is essentially in tension. The non-uniform compressive stresses acting on a flat plate, as indicated in Fig. 6, cause buckling if they reach a critical value. The critical value was calculated in Ref. 10. A particularly simple formula was obtained for the case when the stress distribution can be represented accurately enough by the zeroth and the second terms of a Fourier cosine series:

$$\sigma_{\text{cr. ave}} = \frac{\sigma_{0, \text{cr}}}{1 - (p/2)} \quad (4)$$

where $\sigma_{\text{cr. ave}}$ is the critical value of the average of the variable compressive stress acting on the plate, $\sigma_{0, \text{cr}}$ is the critical uniform stress given by

$$\sigma_{0, \text{cr}} = \{ \pi^2 E / [3(1 - \nu^2)] \} (t/b)^2 \simeq 3.6 E (t/b)^2 \quad (5)$$

with ν Poisson's ratio and t and b the thickness and the width of the simply supported plate, and p is the ratio of the second harmonic of the stress distribution to the average stress in accordance with the expression

$$\sigma_{\text{ave}} = \sigma_{0, \text{cr}} [1 + p \cos(2\pi x/b)] \quad (6)$$

Three critical stress distributions calculated from these equations for the same plate are compared in Fig. 7. An experimental confirmation of the theory is presented in Ref. 8.

The control surfaces of some missiles can be thought of as rectangular plan-form, constant thickness plates. As these plates are non-uniformly heated, non-uniform thermal stresses develop in them. These stresses are capable of reducing significantly the torsional rigidity of the surface with adverse consequences regarding flutter. Simple formulas expressing this reduction in rigidity were derived by several authors. (Refs. 11, 12, 13).

SHELL ANALYSIS

The forward portions of missiles that are exposed to rapid aerodynamic heating are generally built according to the true monocoque principle with a minimum of reinforcing elements. In this analysis the customary simplifying assumption of the aeronautical engineer, namely that the skin carries only shear, and the normal stresses are supported by the stiffeners, cannot be maintained. Use must be made therefore of that branch of the theory of elasticity which is known as shell theory.

Shell theory has a very large and rather mathematical literature. As far as those problems are concerned in which the deformations are small compared to the shell thickness, all fundamental considerations have been established with finality and the only difficulty in the way of new solutions is the complexity of the equations. Unfortunately the mathematical difficulties are great indeed; as a consequence, the only shell for which solutions are known for all kinds of loading is the one whose median surface is a circular cylinder.

But even for the circular cylindrical shell the buckling problem is far from a complete solution. According to Batdorf (Ref. 15) critical stresses predicted by the classical small-deflection theory are in good agreement with test results in the case of lateral loads, in fair agreement in the case of hydrostatic pressure or torsion, and they differ considerably from the experimental values when the load is axial compression. From investigations initiated by von Karman (Ref. 16) it is known that the non-linear load-deflection relationship characterizing curved plate elements is responsible for this discrepancy. In spite of considerable research activity in this field (see, for instance, Ref. 17) many aspects of the jump phenomenon observed in the buckling of shells have yet to be explained satisfactorily on the basis of theory. A recent addition to the list of non-linear shell buckling problems is the effect of internal pressure (Refs. 18 and 19) which is of considerable importance in connection with the pressurized fuel tanks of missiles.

Thermal stresses in and thermal buckling of circular cylindrical shells subjected to temperature changes in the axial direction only were investigated in Ref. 20. Equation 4 was again found to represent in good approximation the critical value of the average stress when the compressive hoop stress varied in accordance with Eq. 6. However, Eq. 5 must be replaced by one expressing the buckling stress of a simply supported circular cylindrical shell under uniform lateral pressure.

Comparison of the critical stress values with thermal stress distributions caused by rather unfavorable conditions of heating and support has shown that elastic buckling is most unlikely to occur when the temperature varies only in the axial direction. Similarly, temperature variations in the radial direction do not lead to buckling. On the other hand, buckling can occur when the temperature varies in the circumferential direction.

For the stress analysis of missiles many new solutions of elastic shell theory will be needed, particularly solutions for conical and cylindrical shells. In their derivation it is well to remember that the shell equations should not be more accurate than is warranted by the use of the results to be obtained. It makes little sense to talk about rigorous shell equations; they are the general equations of the three-dimensional theory of elasticity. The term "shell theory" means a simplified set of equations derived from the general theory of elasticity with the aid of the assumption that the wall thickness is small compared to the other dimensions. In this sense every shell theory is approximate.

CREEP

The least explored and most controversial issue in the design of structures for high temperatures is the creep phenomenon. The easiest thing for the stress analyst to do is to recommend the replacement of any material that creeps at the temperature to be encountered by a better material that does not creep. Unfortunately the designer will run out of materials very soon if he tries to adopt this attitude. Moreover, creep strains of the order of magnitude of the elastic strains should not often interfere with the proper functioning of the structure. Yet they suffice to alter considerably the stress distribution in statically indeterminate structural elements.

The reason for this effect of creep is that the creep strains are not linear functions of the stress. As the stress distribution is governed equally by the equations of equilibrium and by the law of deformations, naturally replacement of Hooke's linear relationship between stress and strain by one that involves in a non-linear manner the quantities stress, strain, strain rate, temperature and time must result in a modification of the stress distribution.

This is one of the reasons why the very convenient appearing presentation of creep data in the form of curves representing the time necessary to reach a prescribed strain under the action of a given stress is not sufficient for a complete structural analysis. The information would suffice if an analysis based on elasticity theory would yield the correct stresses in the structure, and if these stresses would remain unchanged while creep took place. But the initial elastic stress distribution keeps changing during the creep process and thus creep data under variable, rather than constant, stress conditions are needed.

Results obtained from the conventional tensile creep test have other shortcomings also. These results must be generalized in a number of ways before they can be considered satisfactory for structural analysis.

Figure 8 shows the shape of the usual creep curve obtained from a tensile creep test carried out at constant stress and constant temperature. Load application at $t = 0$ causes an instantaneous elastic, and sometimes also plastic, deformation which is followed by creep elongations whose time rate decreases rapidly with time. This phase of creep is the primary phase. In the secondary phase the rate of change of the length of the test specimen is a constant, and in the tertiary phase the rate increases again until the bar ruptures (see Ref. 21).

Perhaps the most popular representation of the dependence of the steady creep rate on the applied stress is the formula

$$\dot{\epsilon} = (\sigma/\lambda)^n \quad (7)$$

where $\dot{\epsilon}$ is the rate of change of the strain with time, σ is the applied stress, and λ and n are material constants. On the basis of logic there is no objection to a

generalization of this formula to apply not only when σ is constant but also when it varies with time, although it would be a little rash to assume that all structural materials are willing to submit to this law. But an entirely different kind of a difficulty arises when one wants to generalize the most popular law of primary creep, namely

$$\epsilon = (\sigma/\lambda)^n t^{1/p} \quad (8)$$

Here ϵ is the creep strain, σ the stress, t the time counted from the load application, and n , p and λ are constants. Just to give the order of magnitude of these quantities one may quote 10,000 to 50,000 psi for λ , 3 to 10 for n and 2 to 3 for p .

If this law were assumed to be valid even for a variable σ , logically inconsistent results would be obtained. Assume that during the period $0 < t < t_1$ the applied stress is σ_1 , and this value is changed to σ_2 when $t = t_1$. Just before the change in stress the creep strain is

$$(\sigma_1/\lambda)^n t_1^{1/p}$$

and immediately after the change it is

$$(\sigma_2/\lambda)^n t_1^{1/p}$$

At t_2 the creep strain changes therefore suddenly, and if $\sigma_2/\sigma_1 = 2$ and $n = 3$, its value jumps to 8 times its original value in an extremely short time. As creep strains can develop only gradually, the predictions of Eq. 8 are incompatible with our experience. As a matter of fact any creep strain law containing time in an explicit form is logically inconsistent.

A logically correct interpretation of Eq. 8 can be given if it is assumed that it defines uniquely the creep rate at a given stress and a given strain. Assume that the loads are applied to the specimen in accordance with Fig. 9. If the creep curves of Fig. 10 are established in tests with the constant stresses σ_A , σ_B and σ_C , the strain history of our variable stress specimen can be found in the following manner: from $t = 0$ to $t = t_1$ the creep strain develops in accordance with the curve labeled σ_A . At that time the stress is suddenly changed to σ_B and with it the strain rate suddenly changes to that corresponding to the slope of the σ_B curve at the intersection with the horizontal dotted line $\epsilon = \epsilon_1$ but the strain itself remains continuous. From $t = t_2$ to $t = t_3$ the strain history is represented by the curve labeled σ_B . At $t = t_2$ a second jump occurs in stress and strain rate in accordance with the horizontal dotted line $\epsilon = \epsilon_2$. From there on the strain follows curve σ_C .

This interpretation of the primary creep phenomenon leads to a simple expression for the creep rate. The slope of the $\sigma = \text{constant}$ curve can be obtained from Eq. 8 through differentiation with respect to t with σ held constant:

$$\dot{\epsilon} = (1/p) (\sigma/\lambda)^n t^{(1-p)/p} \quad (9)$$

If Eq. 8 is solved for t and the value obtained is substituted in Eq. 9, the result is:

$$\dot{\epsilon} = \frac{1}{p} \frac{(\sigma/\lambda)^{np}}{\epsilon^{p-1}} \quad (10)$$

Equation 10 represents the relationship sought between the creep rate, the instantaneous value of the creep strain, and the instantaneous value of the stress. It is logically consistent to assume that this formula is valid for variable stress because the assumption does not lead to illogical conclusions. When the material follows such a law in its creep behavior it is said that for it a mechanical equation of state exists. Equation 10 is indeed a useful tool in the hands of the airplane structural analyst although he should not believe that every structural material will comply with the equation.

Indeed it is just as correct from the standpoint of pure logic to stipulate that at $t = t_1$ the strain rate changes along a vertical rather than along a horizontal, but the strain remains constant. Physically this means that the mechanical changes in the material (the elongation) do not have an effect upon the strain rate; what counts is simply the time of exposure to the high temperature. It is certainly known that this latter effect is very important with all the precipitation-hardened aluminum alloys.

If this second hypothesis is maintained, the creep rate is given logically correctly by Eq. 9 rather than Eq. 10. (Note that in Eq. 9 time appears explicitly in a strain rate formula, not in a strain formula). Of course, in reality both the time of exposure and the creep strain may influence the creep rate and much more theoretical and experimental work is needed before the issue can be settled. Notably a better understanding of the solid-state physical aspects of the creep process is desirable.

As in plate and shell structures the state of stress is two-, and sometimes even three-dimensional, the uniaxial empirical creep laws must be generalized to apply to these more complex situations. This can be done purely formally in a mathematically consistent manner, and as a matter of fact, such a generalization was proposed by Odqvist in 1936

(see Ref. 22). In a more recent article Prager (Ref. 23) established the most general three-dimensional deformation laws for an incompressible plastic material that strain-hardens isotropically. This approach was taken over by the author (Ref. 24) to describe creep deformations.

The general creep law can be given in the form

$$E = f(J_2, J_3) [g(J_2, J_3)T + r(J_2, J_3)S] \quad (11)$$

where E is the strain rate tensor, S the stress deviation tensor and the tensor T is defined as

$$T = S^2 - (2/3) J_2 I \quad (12)$$

The second and third invariants of the stress deviation tensor are denoted by J_2 and J_3 , f is an arbitrary function and g and r are polynomial functions of the invariants of the stress deviation tensor.

We are still very far from having sufficient theoretical or experimental information regarding the functions f , g , and r . For the time being it appears satisfactory therefore to replace the general relationship of Eq. 11 by the much simpler one

$$E = k J_2^m S \quad (13)$$

The situation looks a little brighter when it comes to establishing the effect of temperature upon the creep rate. Of the various suggestions made it should suffice to quote the one advocated by Dorn (Ref. 25):

$$\dot{\epsilon} = f(\sigma) e^{-\Delta H/RT} \quad (14)$$

where $\dot{\epsilon}$ is the creep strain rate with time, $f(\sigma)$ an empirical function of the stress σ the base of natural logarithms, ΔH the activation energy, R the universal gas constant, and T the absolute temperature. For aluminum alloys $\Delta H/R$ is about $10,000^{\circ}R$.

In the foregoing pages the shortcomings of our knowledge of the creep process were emphasized and not our achievements. Yet considerable progress has been made in establishing tools for stress analysis in the form of elastic and plastic analogues and minimal principles. With their aid a number of stress problems have been successfully solved. Concise summaries of some of these developments are given in Refs. 21, 24 and 26.

CREEP BUCKLING

Buckling analysis, in general, can be carried out in one of several different ways. In one approach, the column is assumed to be perfectly straight and homogenous, and perfectly centered. At a time $t = 0$ the perfect equilibrium of the system is disturbed, for instance by a sudden application of a large lateral load which is permitted to act for only a very short time. This impact gives the column a lateral velocity; if after the lapse of a reasonable length of time this lateral velocity subsides and the column returns close enough to its original equilibrium position, the equilibrium is considered stable. On the other hand, if the deviations from the initial straight-line configuration increase with time, the column is unstable.

In the light of a very strict interpretation of this criterion every column is unstable if its material is subject to creep. If the initial impact brings its centerline into the position indicated by y_0 in Fig. 11, the bending moment Py_0 gives rise to creep in bending, and when the elastic forces start to swing the column back toward the straight-line position, the natural (stress-free) state

of the column is no longer straight but slightly curved. When the column swings over into the opposite maximum position, the amplitude of this maximum is smaller than that of the first oscillation. Because of the bias built into the column by the first oscillation, a little more permanent curvature develops in consequence of creep during every right-hand swing then during the corresponding left-hand swing. Hence the column becomes more and more distorted as time passes. The amplitude of the oscillations may decrease, become zero, or increase depending on the conditions. But the average position moves to the right monotonically, and the deviations from straightness increase with time. Consequently the column is unstable however small the compressive force may be.

The analysis of columns by this dynamic approach is usually too difficult. It is more customary therefore to assume that the column is slightly curved initially; this slightly curved position can again be represented by the line marked y_0 in Fig. 11. Such an assumption is justified because no practical column is ever perfectly straight, nor is it centered perfectly in the testing machine. In this static, or quasi-static approach, the place of the disturbance is taken by the initial deviations from straightness. They are the cause of the appearance of bending moments Py_0 which cause bending creep to take place. Thus the curvature of the column is increased, the lever arm y of the load P becomes greater, the creep rate increases, and the vicious circle ends in collapse. Again the conclusion is that every column is unstable, however small is the axial compressive load P .

The engineer is now faced with the necessity of relaxing his buckling criterion. Obviously it would be unwise to abstain from using a reinforced concrete column because one knows that it would collapse in consequence of creep in two or three hundred years. The important problem to be solved is therefore how long it is safe to make use of the column.

The answer can be given accurately if the initial shape of the column, the creep behavior of its material and the maximum permissible deviation from straightness are exactly known. But often an approximate value of the limit of usefulness of the column can be given even without such an accurate knowledge.

It has been observed in column creep tests that the initial deviations from straightness increase very slowly at first, and that the motion of the column accelerates very rapidly when a critical value t_{cr} of the time is approached closely. This critical time can serve as a milestone in creep buckling analysis in much the same way as the Euler buckling load in elastic column analysis.

The existence of a critical time can be proved analytically also. Calculations show that the deviations from straightness of an initially slightly curved column approach infinity when the time approaches the critical time t_{cr} . This critical time is finite, and it may actually be a few seconds or minutes only, if the creep strain increases more rapidly than linearly with stress. This is always the case when the material of the column is one of our structural metals.

There is however a second explanation of the finite critical time which seems to be closer to physical facts in many cases (see Refs. 26, 27, 28, and 29). This can be given most conveniently if the cross-sectional shape of the column is idealized as indicated in Fig. 11.

If the stress-strain relationship of the material, as obtained from a rapid enough test to prevent creep, is not straight but curved (see Fig. 12), a small increment in stress is accompanied by a small increment in strain in such a manner that the tangent to the stress-strain curve is followed. On the other hand, when the stress is decreased the strain decreases along a

straight line parallel to the initial straight-line portion of the stress-strain curve because only the elastic part of the deformation can be regained. In the column test the load is constant. Hence an increase $\Delta\sigma$ in the compressive stress in the concave flange of the column must always be accompanied by a decrease of an equal amount in the concave flange. The resistance of the column to a small increment in the bending moment is therefore characterized by the quantity

$$\frac{2EE_t}{E+E_t} \frac{Ah^2}{4} = E_{red} I \quad (15)$$

where I is the moment of inertia of the idealized section and E , E_t and E_{red} are Young's modulus, the tangent modulus and the reduced modulus of the material.

At the beginning of the creep process under the load P the column is almost straight and the stresses in the two flanges are almost equal. The value of the reduced modulus can be easily calculated from Eq. 15 under these conditions. As the creep deformations increase the initial deflections, the stress in the convex flange decreases and that in the concave flange increases. The change in the strain in the convex flange is always governed by the same Young's modulus, but with increasing compressive stress in the concave flange the slope of the stress-strain curve, and thus the tangent modulus E_t decreases. Hence the bending rigidity $E_{red} I$ of the column decreases with time.

It should now be remembered that the buckling load of an inelastic column is given by the von Karman formula

$$P_{cr} = \frac{\pi^2 EI_{red}}{L^2} \quad (16)$$

where P_{cr} is the buckling load and L is the length of the column. The interesting situation arises therefore that the load P acting on the column is constant, but the critical load P_{cr} decreases with time. If the load P is permitted to act long enough on the initially slightly curved column, eventually the critical load will be reduced sufficiently to be equal to the applied load P . At that moment the column collapses. There is enough evidence available today to indicate that the phenomenon just described is the usual cause of creep buckling.

For a fixed value of the load P and for a given stress-strain diagram the value of E_{red} depends only on the deflection of the column. A critical value of the deflection can therefore be defined at which $P_{cr} = P$. In Fig. 13 a_{crit} is the critical deflection divided by the radius of gyration $h/2$ of the column; its value is plotted against the load P for three different slenderness ratios of the column. The material properties are those presented in Fig. 12.

Calculations similar to those presented can also be carried out for plates and shells but the mathematical difficulties increase. Fig. 15, taken from Ref. 28, shows the creep buckling of a circular cylindrical shell. In Fig. 16 the theoretical critical times are compared with the experimental values.

STRUCTURAL SAFETY

When the structures man is confronted with the task of establishing the safety of a structure operating at high temperature, a number of new problems arise. Should he apply a safety factor to the calculated temperature or does the safety factor for loads, if properly selected, include the effect of unpredictable variations in temperature? It is known that structural elements simultaneously loaded and heated fail under any load that is maintained for a sufficiently long time. Should a new safety factor for lifetime be created, or do the safety factors for loads and temperatures take care of this matter?

The answers to these questions are not obvious at all. In earlier papers (Refs. 24 and 30) I have called attention to the fact that a change in absolute temperature of 1 per cent can cause a change in the steady creep rate of about 40 per cent. In a similar manner, a change in stress of 1 per cent may lead to a change in creep rate amounting to 10 per cent. As all these relationships are non-linear, it is not easy to assess in advance the ultimate effects of errors made in the prediction of the loading conditions or in the manufacture of the hardware. These data refer to aluminum alloys in the temperature range from 400° F to 500° F.

The failure of tensile specimens subjected to constant loads for extended periods of time at high temperatures is known as creep rupture. With aluminum alloys in the temperature range mentioned, a safety factor of 2 applied to the stress may increase the lifetime by a factor of 32, while a safety factor of 2 applied to the lifetime would require a ratio of 1.15 of the ultimate stress to the limit stress.

These figures should suffice to prove that we are faced with a bewildering situation. In my opinion, the only way out is to establish statistically on the one hand the frequencies of the occurrence of various loads and temperatures, and on the other hand the frequencies of the occurrence of instantaneous fracture under loads and of various creep rates at all the temperatures of interest. From these frequency curves the laws of probability theory can predict the probability of failure. The acceptable probability of failure must be established by the purchaser of the airplane or missile. He may be guided in reaching his decision by probability values to be calculated for existing and already proven aircraft or missiles.

CONCLUSIONS

Even though some missiles of the future will be composed of significantly fewer structural elements than today's bomber and transport airplanes, the number of structural problems to be solved is increasing at the present time. To take care of them, the structures man will have to acquire a working knowledge in some disciplines which used to be far from his field of interest. In this category are supersonic aerodynamics, thermodynamics, the physics of the solid state and the theory of probability.

If he is dismayed by this prospect, he should remember that his aerodynamic co-worker has already gone through a similar transformation. He has been studying thermodynamics, quantum mechanics, the kinetic theory of gases and just now he is on the way to becoming a physical chemist in order to solve the problems of very high-speed, high-temperature flow.

There is no reason to believe that the structural problems are harder to solve than their aerodynamic counterparts. The more research-minded ones among structures men will broaden their interests considerably and the more hardware-minded ones will be able to use new routine methods which will be established in the future.

In conclusion we may safely say that the structures man is here to stay.

REFERENCES

1. Allen, H. Julian, Hypersonic Flight and the Re-entry Problem, Twenty-First Wright Brothers Lecture, Institute of the Aeronautical Science, December 17, 1957.
2. Hoff, N. J., Structural Problems of Future Aircraft, Third Anglo-American Aeronautical Conference 1951, The Royal Aeronautical Society, London, England, p. 77.
3. Pohle, Frederick V., and Oliver, Henry, Temperature Distribution and Thermal Stresses in a Model of a Supersonic Wing, Journal of the Aeronautical Sciences, Vol. 21, No. 1, p. 8, January 1954.
4. Hoff, N. J., Comparison of Radiant and Conductive Heat Transfer in a Supersonic Wing, Journal of the Aeronautical Sciences, Vol. 23, No. 7, p. 694, July 1956.
5. Barzelay, Martin E.; Tong, Kin Nee; and Hollo, George, Thermal Conductance of Contacts in Aircraft Joints, NACA Tech. Note 3167, March 1954.
6. Horvay, G., The End Problem of Rectangular Strips, Journal of Applied Mechanics, Vol. 20, No. 1, p. 87, March 1953.
7. Heldenfels, R. R., and Roberts, W. M., Experimental and Theoretical Determination of Thermal Stresses in a Flat Plate, NACA Tech. Note 2769, 1952.

REFERENCES (Cont)

8. Singer, Josef; Anliker, M.; and Lederman, S., Thermal Stresses and Thermal Buckling, WADC Tech. Report 57-69, December 1956.
9. Hoff, N. J., The Structural Effects of Aerodynamic Heating, Proceedings of the Third General Assembly of AGARD (NATO), AG 6/P3, p. 47, September 1953.
10. Hoff, N. J., Thermal Buckling of Supersonic Wing Panels, Journal of the Aeronautical Sciences, Vol. 23, No. 11, p. 1019, November 1956.
11. Bisplinghoff, R. L., Some Structural and Aeroelastic Considerations of High-Speed Flight, The Nineteenth Wright Brothers Lecture, Journal of the Aeronautical Sciences, Vol. 23, No. 4, p. 289, April 1956.
12. Hoff, N. J., Approximate Analysis of the Reduction in Torsional Rigidity and of the Torsional Buckling of Solid Wings under Thermal Stresses, Journal of the Aeronautical Sciences, Vol. 23, No. 6, p. 603, June 1956.
13. Budiansky, Bernard, and Mayers, J., Influence of Aerodynamic Heating on the Effective Torsional Stiffness of Thin Wings, Journal of the Aeronautical Sciences, Vol. 23, No. 12, p. 1061, December 1956.

REFERENCES (Cont)

14. Singer, Josef, and Hoff, N. J., Effect of the Change in Thermal Stresses due to Large Deflections on the Torsional Rigidity of Wings, *Journal of the Aeronautical Sciences*, Vol. 24, No. 4, p. 310, April 1957.
15. Batdorf, S. B., A Simplified Method of Elastic Stability Analysis for thin Cylindrical Shells, *NACA Report No. 874*, 1947.
16. von Karman, Th.; Dunn, Louis G.; and Tsien, Hsue-Shen, The Influence of Curvature on the Buckling Characteristics of Structures, *Journal of the Aeronautical Sciences*, Vol. 7, No. 7, p. 276, May 1940.
17. Kempner, Joseph; Pandalai, K. A. V.; Patel, Sharad A.; and Crouzet-Pascal, Jacques, Post Buckling Behavior of Circular Cylindrical Shells under Hydrostatic Pressure, *Journal of the Aeronautical Sciences*, Vol. 24, No. 4, p. 253, April 1957.
18. Lo, Hsu; Crate, Harold; and Schwartz, Edward B., Buckling of Thin-Walled Cylinder under Axial Compression and Internal Pressure, *NACA Report No. 1027*, 1951.
19. Fung, Y. C., and Sechler, E. E., Buckling of Thin-Walled Circular Cylinders under Axial Compression and Internal Pressure, *Journal of the Aeronautical Sciences*, Vol. 24, No. 5, p. 351, May 1957.

REFERENCES (Cont)

20. Hoff, N. J., Buckling of Thin Cylindrical Shell under Hoop Stresses Varying in Axial Direction, *Journal of the Aeronautical Sciences*, Vol. 24, No. 3, p. 405, September 1957.
21. Hoff, N. J., Rapid Creep in Structures, *Journal of the Aeronautical Sciences*, Vol. 22, No. 10, p. 661, October 1955.
22. Odqvist, Folke K. G., Theory of Creep under the Action of Combined Stresses with Applications to High-Temperature Machinery, *Proceedings of the Royal Swedish Institute for Engineering Research*, No. 141, Stockholm, Sweden, 1936.
23. Prager, W., Strain Hardening under Combined Stresses, *Journal of Applied Physics*, Vol. 16, No. 12, p. 837, December 1945.
24. Hoff, N. J., Stress Distribution in the Presence of Steady Creep, *Proceedings of the Conference on High-Speed Aeronautics*, edited by A. Ferri, N. J. Hoff and P. A. Libby, Polytechnic Institute of Brooklyn, Brooklyn, N. Y., 1955, p. 271.
25. Dorn, John E., Some Fundamental Experiments on High-Temperature Creep, *Journal of Mechanics and Physics of Solids*, Vol. 3, No. 2, p. 85, January 1955.

REFERENCES (Cont)

26. Hoff, N. J., Effets thermiques dans le calcul de la resistance des structures d'avions et d'engins, Report 52 of Advisory Group for Aeronautical Research and Development (AGARD) of NATO, Paris, France, January 1956.
27. Fraeijns de Veubeke, Baudouin, Creep Buckling, Chapter 11 of High Temperature Effects in Aircraft Structures, edited by N. J. Hoff, to be published by Pergamon Press under the sponsorship of AGARD, 1958.
28. Hoff, N. J., Buckling at High Temperature, Journal of the Royal Aeronautical Society, Vol. 61, No. 563, p. 756, November 1957.
29. Chapman, J. C.; Erickson, Burton; and Hoff, N. J.; A theoretical and Experimental Investigation of Creep Buckling, paper presented at the Annual Meeting of the Institute of the Aeronautical Sciences in New York, N. Y., January 1958.
30. Hoff, N. J., Philosophy of Safety in the Supersonic Age, Advisory Group for Aeronautical Research and Development (AGARD) of NATO, Report 87, Paris, France, August 1956.

FIGURES

Fig. 1. Wright Model R, or Roadster, Racing plane of 1910.

(From the Sherman Fairchild Collection of the
Institute of the Aeronautical Sciences.)

Fig. 2. Convair Atlas Intercontinental Ballistic Missile of

1958. (Courtesy of the Convair Division of
General Dynamics Corp.)

Fig. 3. Temperature Distribution in Shearweb of Supersonic

Wing. (From Third Anglo-American Aeronautical
Conference, The Royal Aeronautical Society, 1951).

Fig. 4. Multiweb Supersonic Wing

Fig. 5. Buckling of Model of Wing Caused by Heating. (From
Proceedings, 3rd General Assembly of AGARD).

Fig. 6. Rectangular Flat Plate Subjected to Non-Uniform Edge Compression

Fig. 7. Three Critical Stress Conditions of a Flat Rectangular Plate
Drawn to the Same Scale. (From Journal of the
Aeronautical Sciences).

Fig. 8. Tensile Creep Curve

Fig. 9. Load History of Tensile Creep Test Specimen.

FIGURES (Cont)

Fig. 10. Creep Curves for Three Stresses

Fig. 11. Column

Fig. 12. Properties of the Material of the Column

Fig. 13. Critical Deflections of Columns

Fig. 14. Creep Buckling of Circular Cylindrical Shell.

(From Journal of the Royal Aeronautical Society).

Fig. 15. Comparison of Experimental and Theoretical Creep Buckling

**Times of Cylinder. (From Journal of the Royal
Aeronautical Society).**

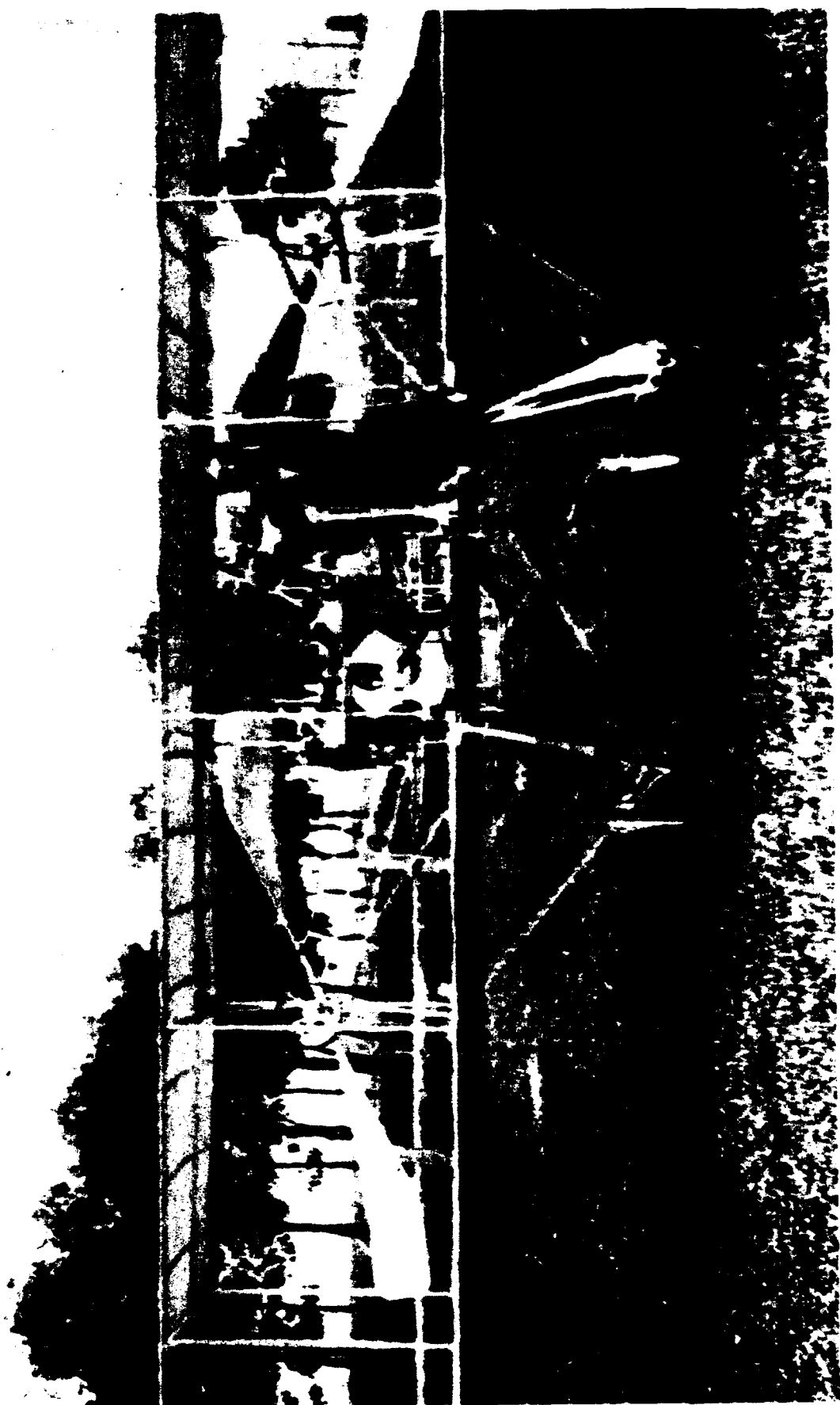


Figure #1

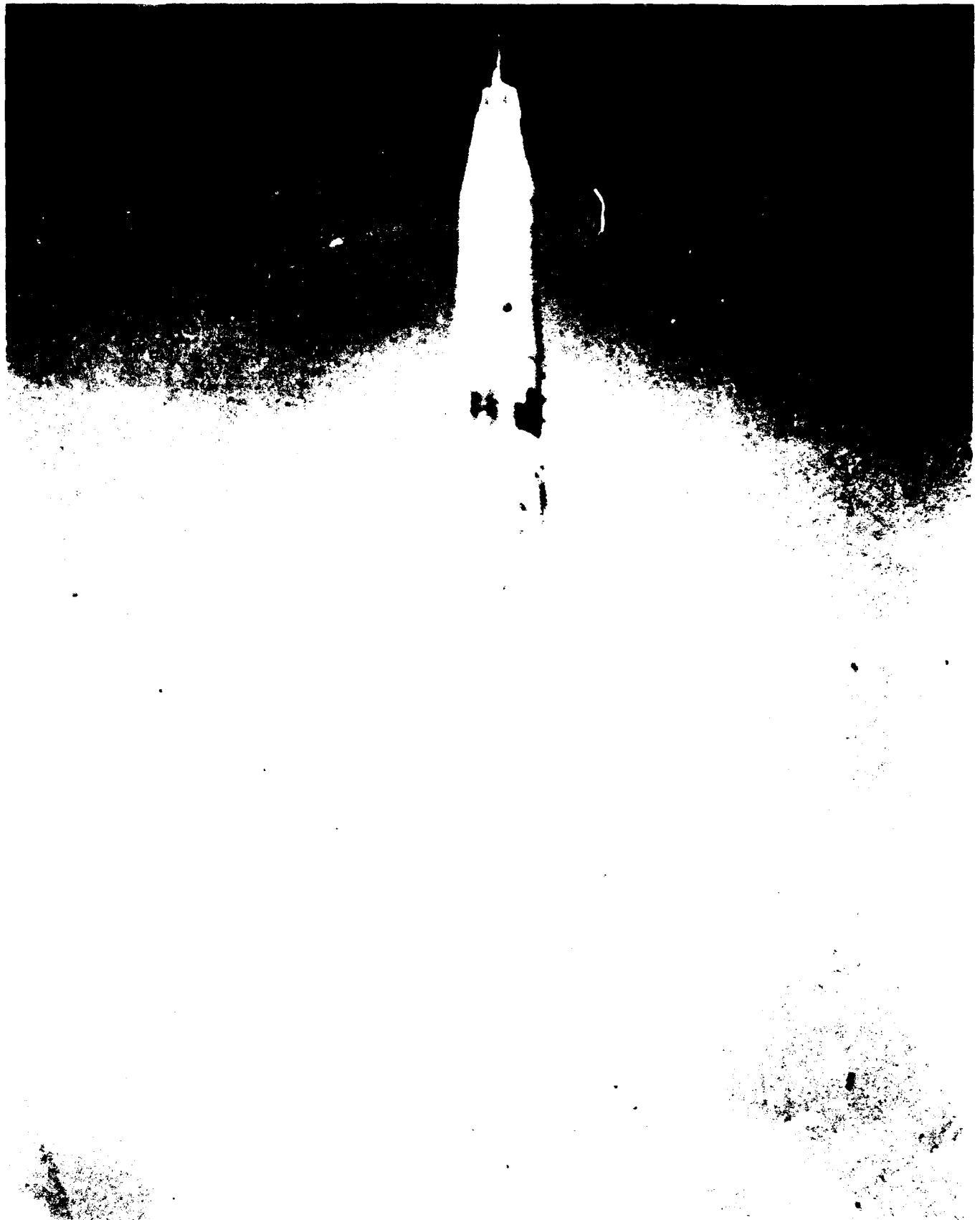


Figure #2

N. J. HOFF

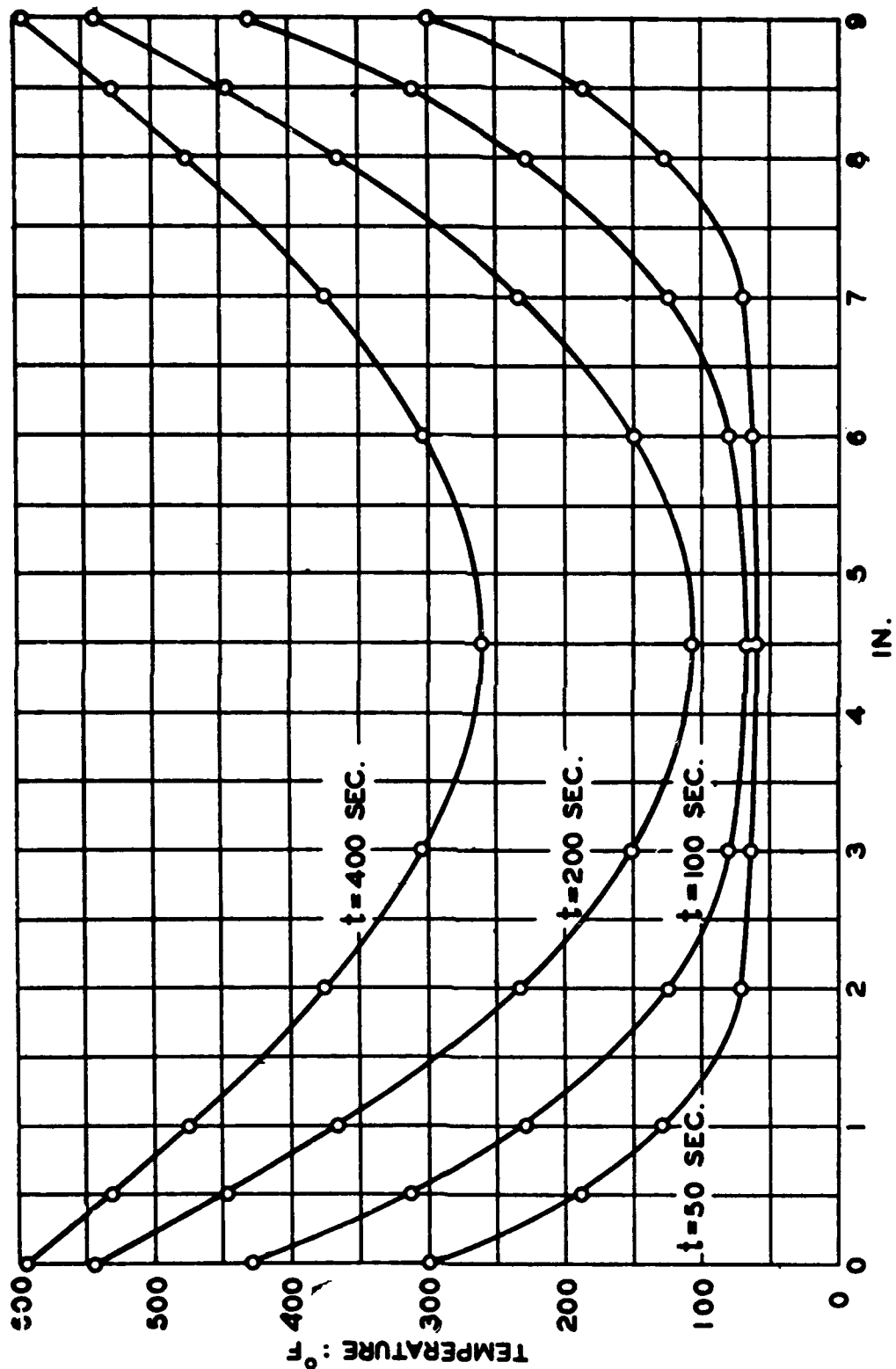


Fig. 8.

Figure #3

**FIG. 2 SCHEMATIC CROSS SECTION
OF WING**

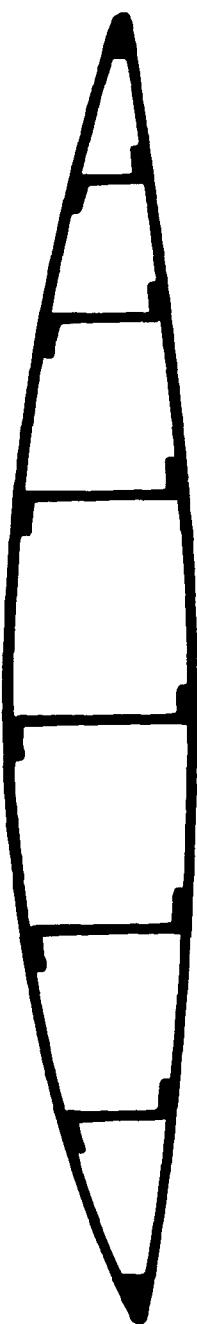


Figure #4



Figure #5

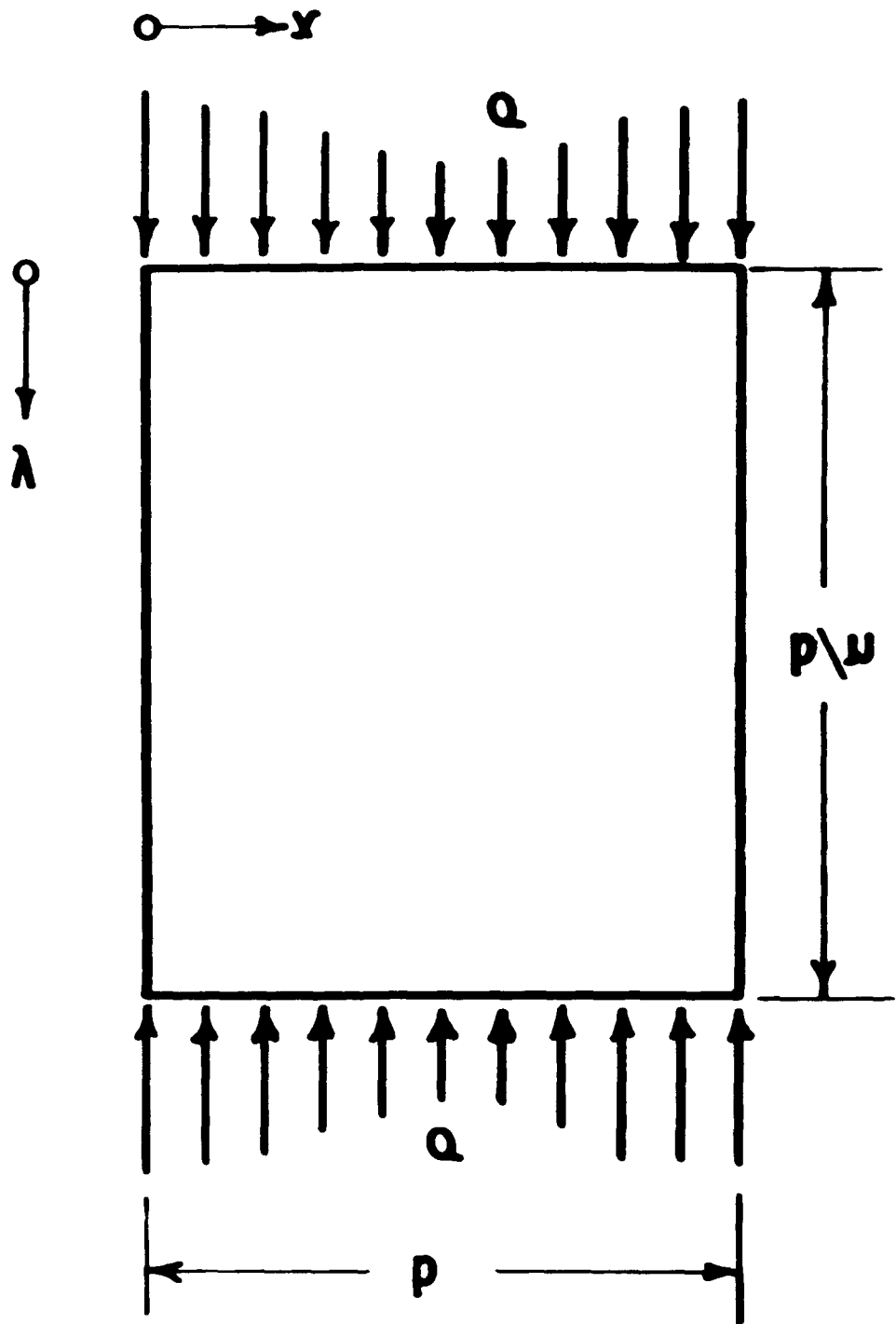


Figure #6

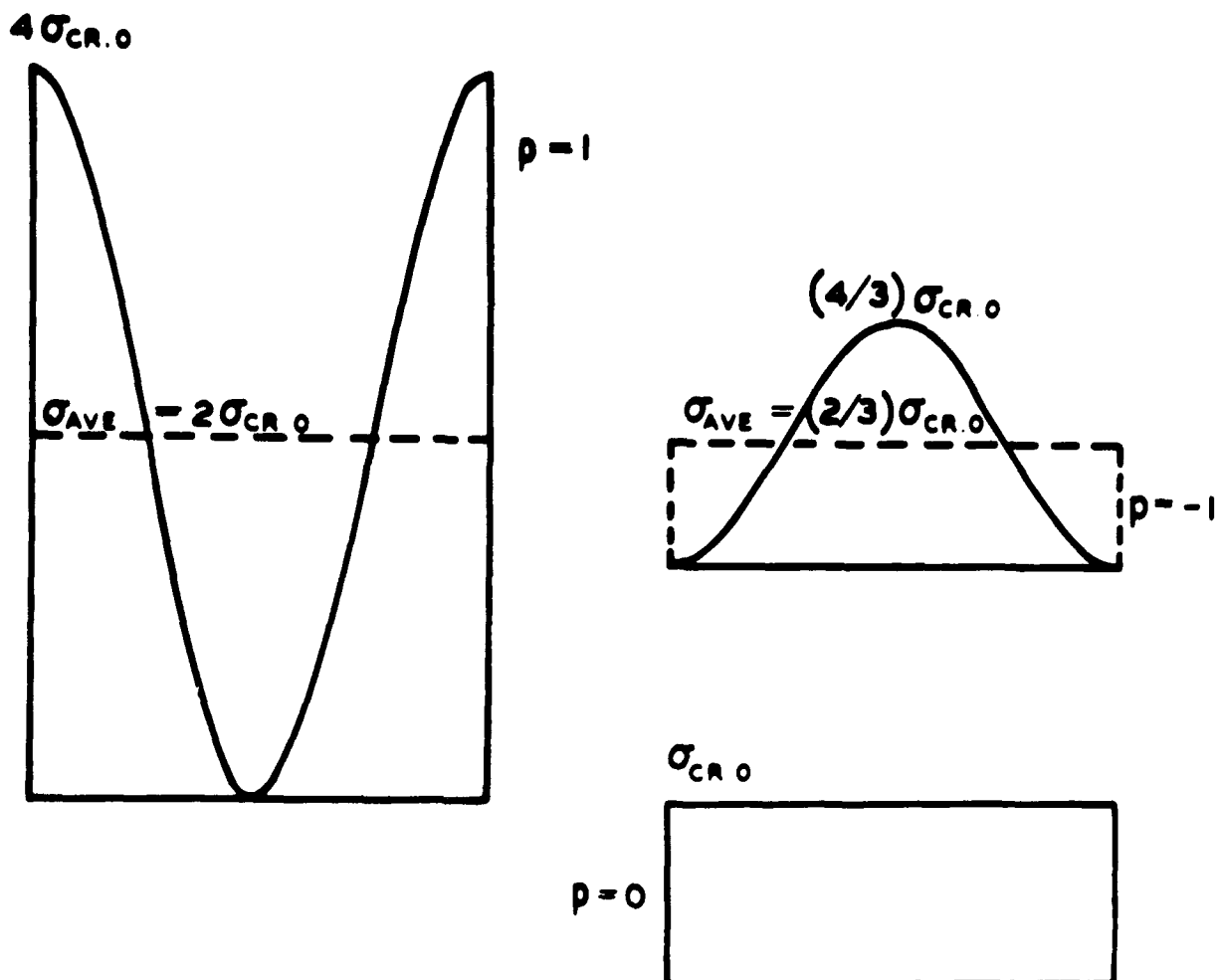


Figure #7

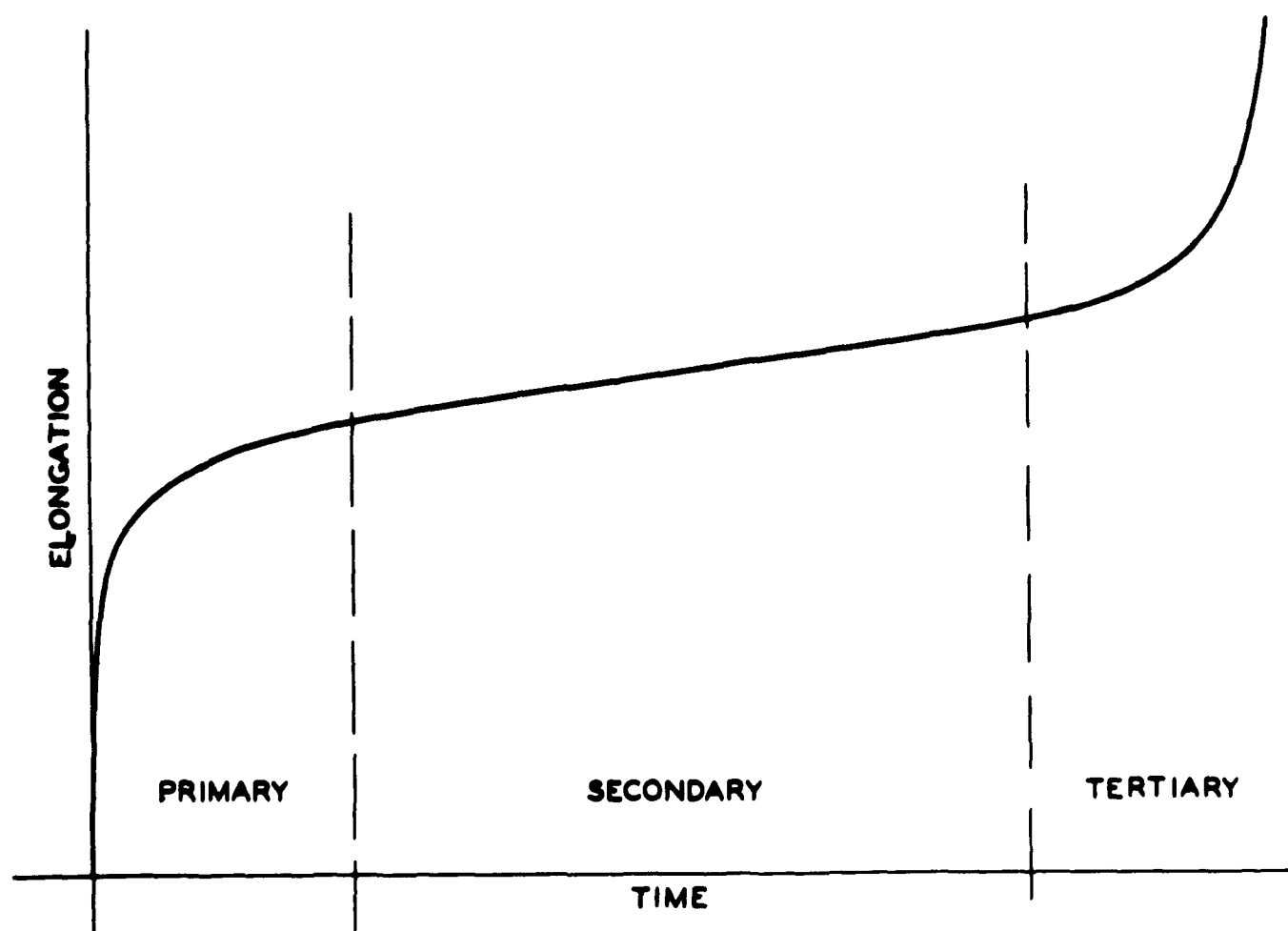


FIG. I CREEP OF METAL ROD IN TENSION

Figure #8

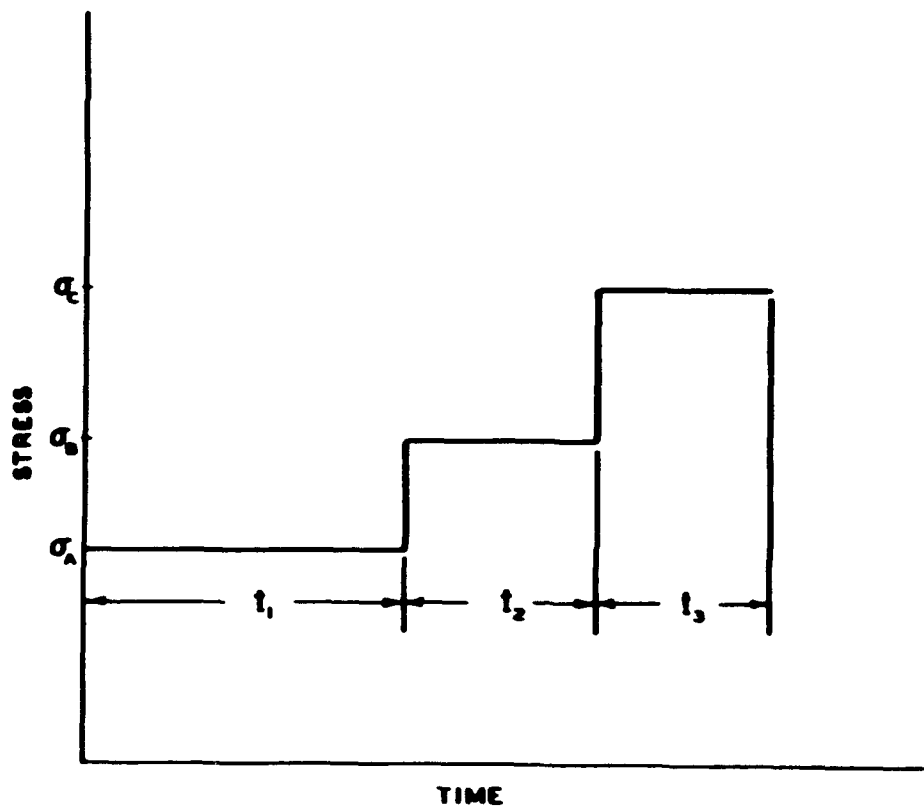


FIG. 5 STRESS HISTORY

Figure #9

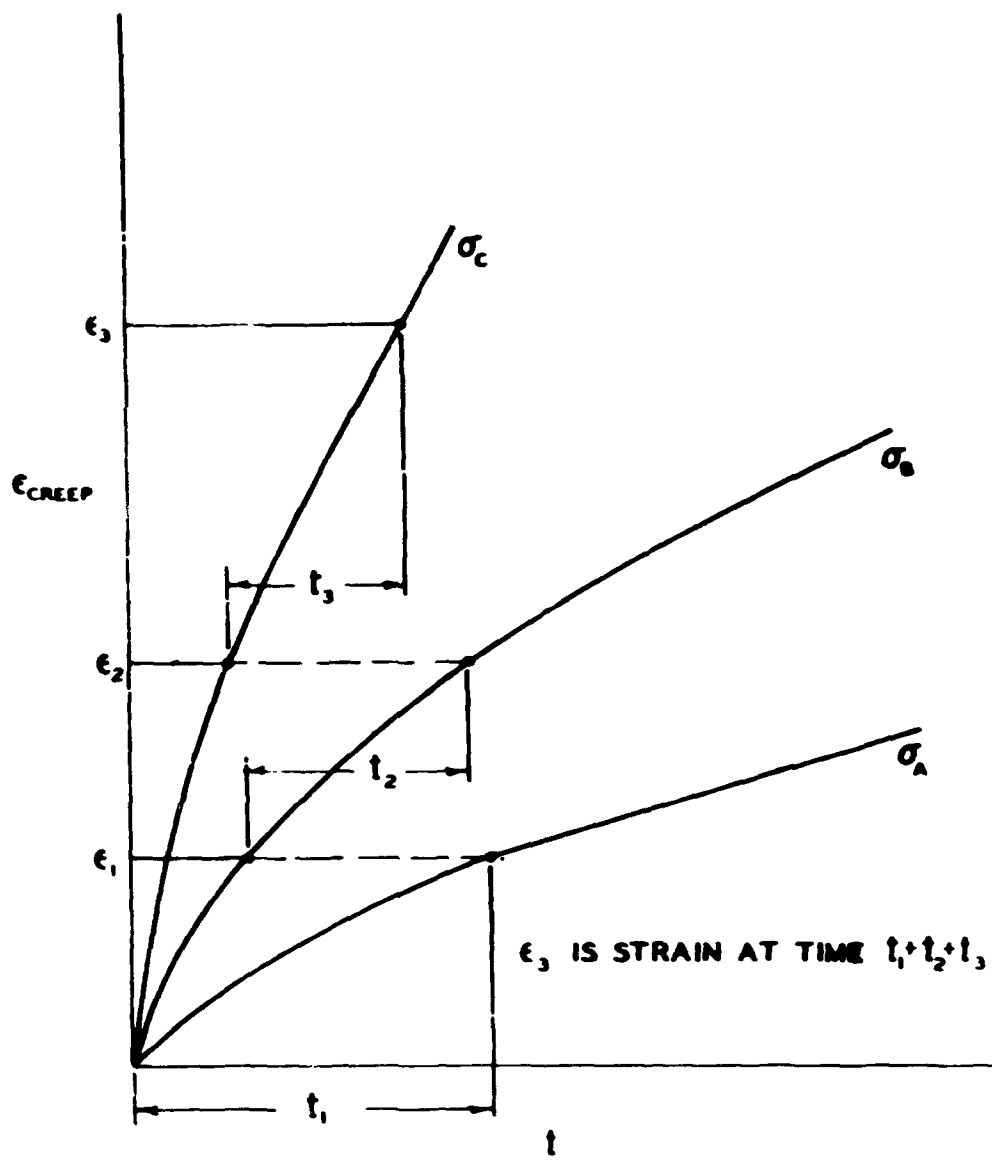


FIG. 6 CREEP STRAIN CURVE CORRESPONDING TO STRESS HISTORY OF FIG.

Figure #10

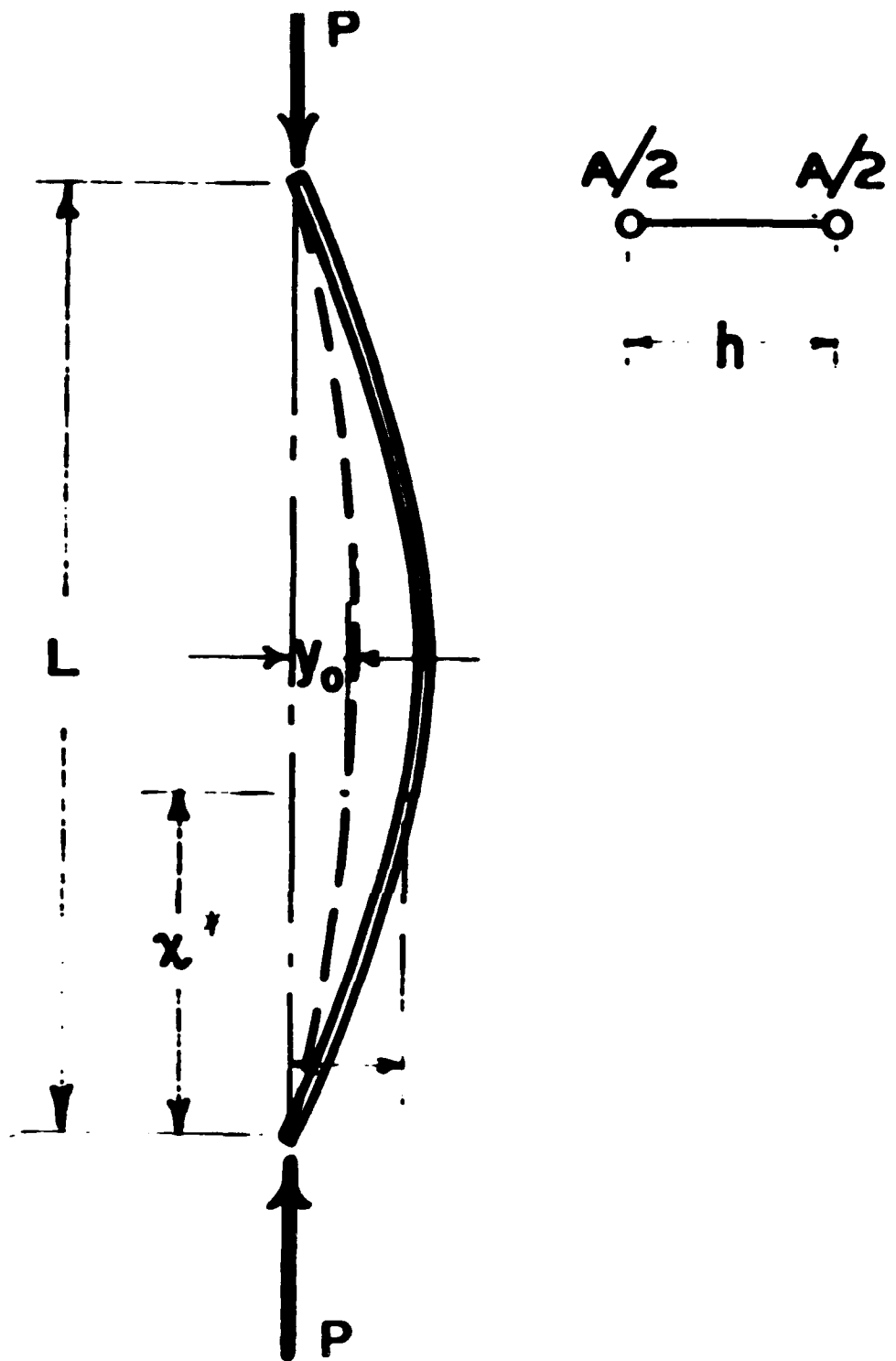


Figure #11

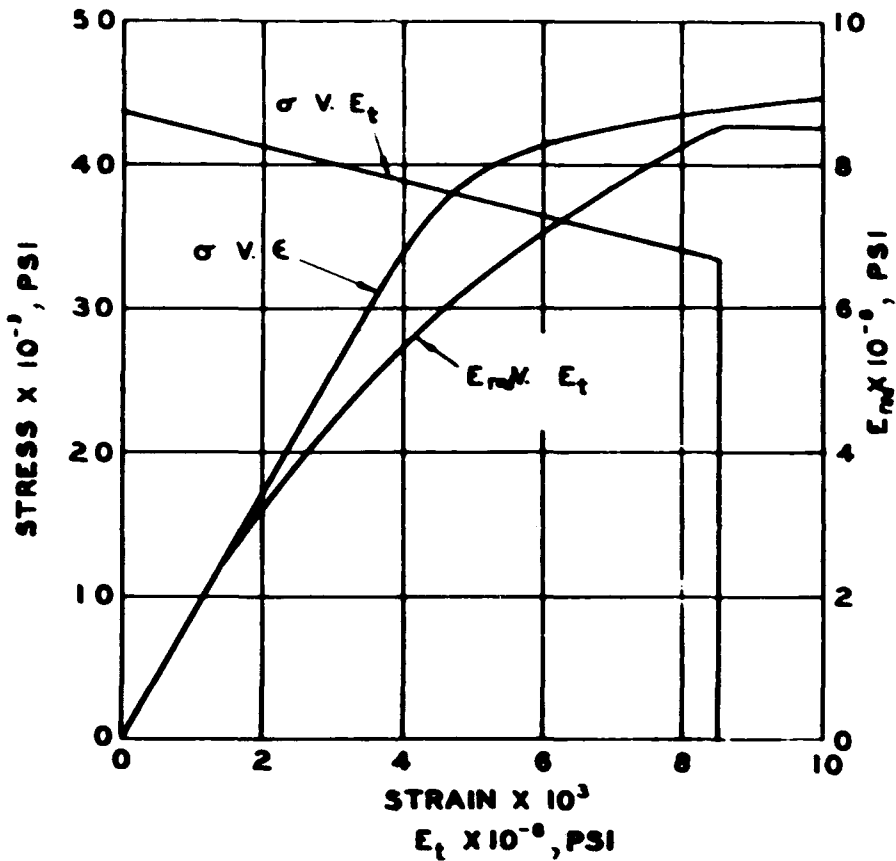


FIG. 1 CORRECTED STRESS-STRAIN CURVE
AS DETERMINED FROM INSTANTANEOUS
BENDING TESTS AT 500°F
1/2" X 1/4" SECTION AL ALLOY 2024-T4

Figure #12

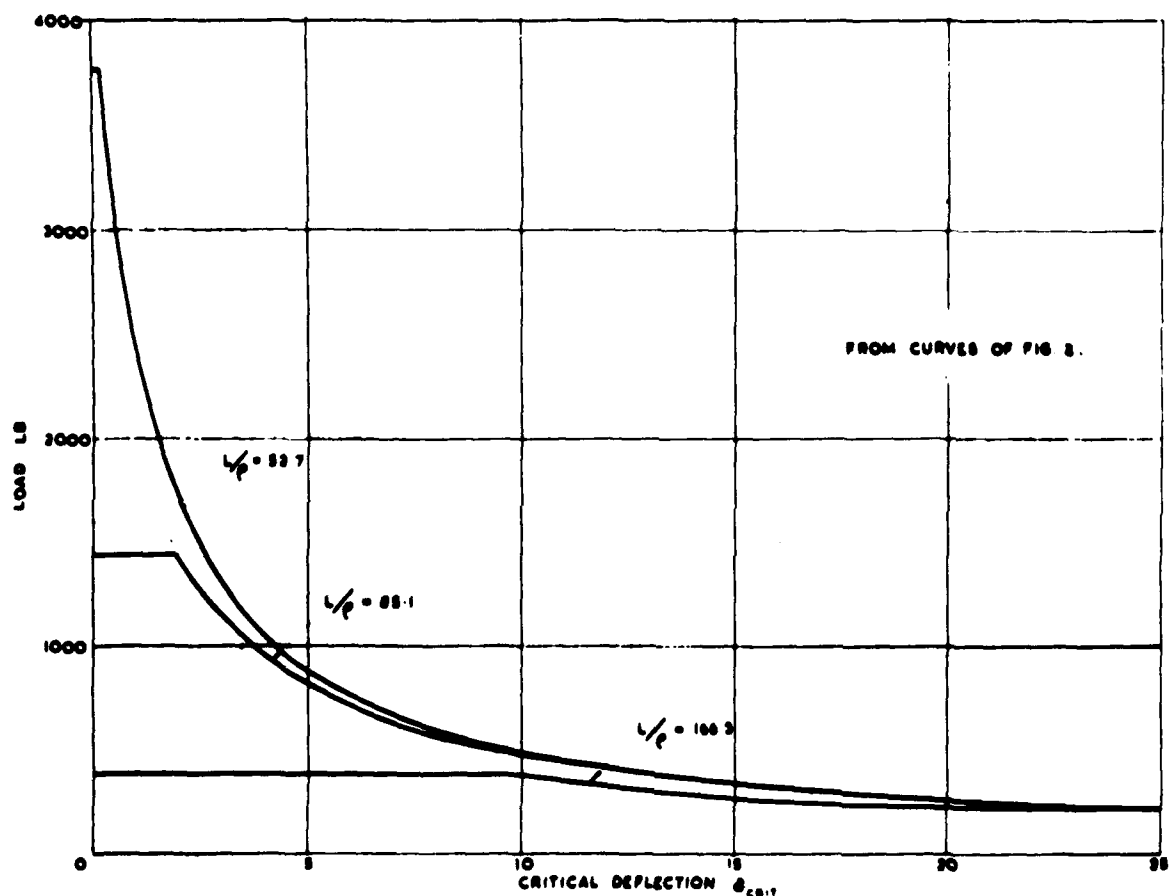


Figure #13



Figure #14

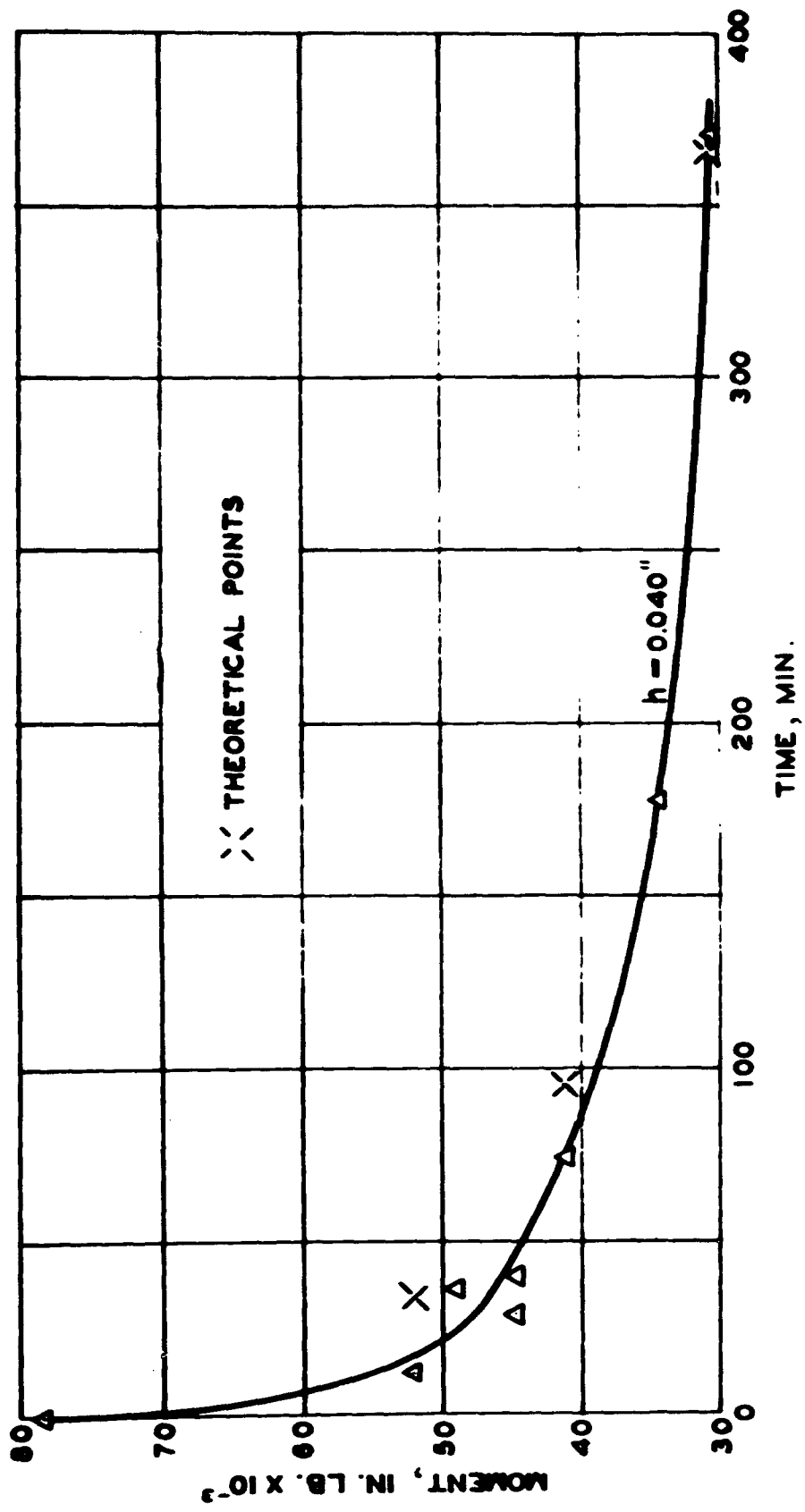


Figure #15

<p>AF Cambridge Research Laboratories, Bedford, Mass. Electronics Research Directorate. ON TWO MATRIX SYSTEMS DERIVED FROM A POLYNOMIAL OF EVEN ORDER WITH REAL COEFFICIENTS, by Kurt H. Haase. December 1961. 51 pp incl. tables. AFCRL 983</p> <p>Unclassified report</p>	<p>UNCLASSIFIED</p> <p>1. Polynomials I. Haase, Kurt, H.</p>	<p>A polynomial $f(z)$ of even order n and real coefficients $A_n = 1, A_{n-1}, \dots, A_1, A_0$, has $n/2$ pairs of roots, each pair yielding a square polynomial $z^2 + y_1 z + x_1$ with real coefficients y_1 and x_1. Hence there is a summation form and a product form for $f(z)$. From a comparison of the coefficients for any power of z, $n+1$ equations can be derived, each consistent for any pair y_1 and x_1. These equations involve the elements Z_{ik} of an $(n+1) \times (n+1)$ square matrix with columns multiplied by the A coefficients. Simultaneous polynomials in x and y defined as real variables, the elements of this 'Z matrix' depend only on the order n of $f(z)$. (over)</p>	<p>UNCLASSIFIED</p>	<p>UNCLASSIFIED</p>
<p>AF Cambridge Research Laboratories, Bedford, Mass. Electronics Research Directorate. ON TWO MATRIX SYSTEMS DERIVED FROM A POLYNOMIAL OF EVEN ORDER WITH REAL COEFFICIENTS, by Kurt H. Haase. December 1961. 51 pp incl. tables. AFCRL 983</p> <p>Unclassified report</p>	<p>UNCLASSIFIED</p> <p>1. Polynomials I. Haase, Kurt, H.</p>	<p>A polynomial $f(z)$ of even order n and real coefficients $A_n = 1, A_{n-1}, \dots, A_1, A_0$, has $n/2$ pairs of roots, each pair yielding a square polynomial $z^2 + y_1 z + x_1$ with real coefficients y_1 and x_1. Hence there is a summation form and a product form for $f(z)$. From a comparison of the coefficients for any power of z, $n+1$ equations can be derived, each consistent for any pair y_1 and x_1. These equations involve the elements Z_{ik} of an $(n+1) \times (n+1)$ square matrix with columns multiplied by the A coefficients. Simultaneous polynomials in x and y defined as real variables, the elements of this 'Z (over)</p>	<p>UNCLASSIFIED</p>	<p>UNCLASSIFIED</p>
<p>AF Cambridge Research Laboratories, Bedford, Mass. Electronics Research Directorate. ON TWO MATRIX SYSTEMS DERIVED FROM A POLYNOMIAL OF EVEN ORDER WITH REAL COEFFICIENTS, by Kurt H. Haase. December 1961. 51 pp incl. tables. AFCRL 983</p> <p>Unclassified report</p>	<p>UNCLASSIFIED</p> <p>1. Polynomials I. Haase, Kurt, H.</p>	<p>A polynomial $f(z)$ of even order n and real coefficients $A_n = 1, A_{n-1}, \dots, A_1, A_0$, has $n/2$ pairs of roots, each pair yielding a square polynomial $z^2 + y_1 z + x_1$ with real coefficients y_1 and x_1. Hence there is a summation form and a product form for $f(z)$. From a comparison of the coefficients for any power of z, $n+1$ equations can be derived, each consistent for any pair y_1 and x_1. These equations involve the elements Z_{ik} of an $(n+1) \times (n+1)$ square matrix with columns multiplied by the A coefficients. Simultaneous polynomials in x and y defined as real variables, the elements of this 'Z (over)</p>	<p>UNCLASSIFIED</p>	<p>UNCLASSIFIED</p>

UNCLASSIFIED

not on the coefficients, and are known for any even order. A transcription of the derived equations yields a Y matrix whose elements are multiplied by powers of x, or an X matrix whose elements are multiplied by powers of y. The elements of the Y matrix are polynomials in y only, with real coefficients that are combinations of the A coefficients. The Y matrix is immediately known for any order n of $f(z)$. The properties of these derived matrices are compiled in 12 theorems.

UNCLASSIFIED

not on the coefficients, and are known for any even order. A transcription of the derived equations yields a Y matrix whose elements are multiplied by powers of x, or an X matrix whose elements are multiplied by powers of y. The elements of the Y matrix are polynomials in y only, with real coefficients that are combinations of the A coefficients. The Y matrix is immediately known for any order n of $f(z)$. The properties of these derived matrices are compiled in 12 theorems.

UNCLASSIFIED
UNCLASSIFIED

matrix¹ depend only on the order n of $f(z)$, not on the coefficients, and are known for any even order. A transcription of the derived equations yields a Y matrix whose elements are multiplied by powers of x, or an X matrix whose elements are multiplied by powers of y. The elements of the Y matrix are polynomials in y only, with real coefficients that are combinations of the A coefficients. The Y matrix is immediately known for any order n of $f(z)$. The properties of these derived matrices are compiled in 12 theorems.

UNCLASSIFIED
UNCLASSIFIED

matrix¹ depend only on the order n of $f(z)$, not on the coefficients, and are known for any even order. A transcription of the derived equations yields a Y matrix whose elements are multiplied by powers of x, or an X matrix whose elements are multiplied by powers of y. The elements of the Y matrix are polynomials in y only, with real coefficients that are combinations of the A coefficients. The Y matrix is immediately known for any order n of $f(z)$. The properties of these derived matrices are compiled in 12 theorems.

UNCLASSIFIED

UNCLASSIFIED